

Characterising Ultracool Dwarfs in the *Gaia* Mission All Sky Survey

Author:

William J. COOPER

Supervised by:

Prof. H. R. A. JONES

Dr. R. L. SMART

Centre for Astrophysics Research
School of Physics, Engineering and Computer Science
University of Hertfordshire

*Submitted to the University of Hertfordshire in partial fulfilment of the requirements of
the degree of Doctor of Philosophy.*

October 2023

Abstract

I present here the characterisation of ultracool dwarfs having been observed through direct, ground-based campaigns. These ultracool dwarfs have been used to assist with the parameterisation of objects as observed by *Gaia*. I also present software packages and further technical skills, developed for the astronomical community.

Data observed from 2015–2016 on the OSIRIS instrument at the GTC was used to measure spectral types and radial velocities for 46 objects. This data was analysed further to ascertain if any objects had interesting features such as young moving group membership or low metallicity features. I led multiple observing proposals and observed on several nights, which resulted in a number of interesting objects being discovered. Expanding on what was known of ultracool dwarfs from direct campaigns, I helped data process the ultracool dwarfs in *Gaia* data releases. I contributed to ‘downstream’ analysis of these *Gaia* ultracool dwarfs. This, in turn, enhanced the body-of-knowledge of directly observed ultracool dwarfs.

Using *Gaia* DR3, I created a novel colour ratio to select outliers from *Gaia* RP spectra. This was a proof-of-concept work to demonstrate that one can use a large, homogeneous population like *Gaia*, to identify the most extreme outliers from low resolution data. I created multiple software tools and databases, which the community has used to observe, access, analyse and present data.

Declaration

I declare that no part of this work is being submitted concurrently for another award of the University or any other awarding body or institution. This thesis contains a substantial body of work that has not previously been submitted successfully for an award of the University or any other awarding body or institution.

The following parts of this submission have been published previously and/or undertaken as part of a previous degree or research programme:

1. Chapter 2: Cooper et al. (submitted to MNRAS), ‘The *Gaia* Ultracool Dwarf Sample – IV. GTC/OSIRIS optical spectra of *Gaia* L dwarfs’. All text and figures are my own.
2. Chapter 3: Section 5.4 of ‘*Gaia* Early Data Release 3. The *Gaia* Catalogue of Nearby Stars’ by Gaia Collaboration et al. (2021f) and Section 3 of ‘Ultracool dwarfs in *Gaia* DR3’ by Sarro et al. (2023). Gaia Collaboration et al. (2023b) is the primary work documenting the coordination unit I am part of (CU8), within the *Gaia* DPAC, although it is not specific to UCDs. Other *Gaia* works I contributed towards include the primary releases, Gaia Collaboration et al. (2021b, with corrigendum by Gaia Collaboration et al. (2021c)) and Gaia Collaboration et al. (2023i) plus the wider documentation from CU8 (Creevey et al., 2023; Fouesneau et al., 2023; Delchambre et al., 2023). Due to my contributions to the *Gaia* DPAC, I am a co-author on further works not detailed in this thesis. These include Gaia Collaboration et al. (2021e), Gaia Collaboration et al. (2021a), Gaia Collaboration et al. (2021d), Gaia Collaboration et al. (2022), Andrae et al. (2023a), Recio-Blanco et al. (2023), Lanzafame et al. (2023), Gaia Collaboration et al. (2023f), Gaia Collaboration et al. (2023a), Gaia Collaboration et al. (2023e), Gaia Collaboration et al. (2023c), Gaia Collaboration et al. (2023d), Gaia Collaboration et al. (2023g) and Gaia Collaboration et al. (2023h).
3. Chapter 4: Cooper et al. (2023, accepted by MNRAS), ‘Ultracool Spectroscopic Outliers in *Gaia* DR3’. All text and figures are my own.
4. Chapter 5: Cooper et al. (in preparation for submission to RASTI) ‘*Gaia* Ultracool Dwarf Sample – V. Database’. All text and figures are my own.

5. Chapter 6: Software packages published in Zenodo: (Cooper, 2022a,b,c). Observed targets published by Mamajek et al. (2018), González Egea et al. (2021) and Faherty et al. (2021). Contributed figures in works by Gaia Collaboration et al. (2021f), Reylé et al. (2021), Rybizki et al. (2021) and Morris et al. (2022, also contributing analysis).

Except where indicated otherwise in the submission, the submission is my own work and has not previously been submitted successfully for any award.

Acknowledgements

None of this thesis would have been actualised without the support of my supervisors directing my studies, keeping me focused and enabling me traveling around Europe. My other senior Hertfordshire colleagues have also been vital for giving me the opportunities to guide my career with the time provided for my PhD. I have also been massively supported by senior colleagues from around the world, giving me invaluable advice, research opportunities and scientific guidance. My friends and family have somehow kept me (mostly) sane and motivated to get to the finishing line.

Contents

Abstract	i
Acknowledgements	iv
Contents	v
List of Figures	viii
List of Tables	xiv
List of Abbreviations	xv
1 Introduction	1
1.1 Theory and Direct Observations	1
1.1.1 Detecting UCDS	2
1.1.2 Spectral Features	2
1.1.3 Binarity	3
1.1.4 Formation	4
1.1.5 UCD Population Statistics	8
1.2 Surveys and Missions	9
1.3 Motivation and Thesis Structure	10
2 The <i>Gaia</i> Ultracool Dwarf Sample – IV. GTC/OSIRIS optical spectra of <i>Gaia</i> L dwarfs	11
2.1 Introduction	12
2.2 Methodology	15
2.2.1 Target selection	15
2.2.1.1 Cross-matching	18
2.2.2 Observations	18
2.2.3 Reduction	19
2.3 Analysis	20
2.3.1 Spectral typing	21
2.3.1.1 GTC spectral sequence	22
2.3.2 Fundamental astrophysical parameters	22
2.3.3 Calculating the radial velocities	26
2.3.3.1 Line centre fitting	26
2.3.3.2 Cross-correlation	28

2.3.3.3	Adopted RV	29
2.3.4	Kinematics	30
2.4	Results	30
2.4.1	Spectral types	31
2.4.2	Kinematics	32
2.4.2.1	Moving groups	35
2.4.2.2	Galactic components	36
2.4.3	Astrophysical parameters	36
2.4.3.1	Individual objects	38
2.5	Summary	44
3	Ultracool Dwarfs in <i>Gaia</i>	47
3.1	<i>Gaia</i> Catalogue of Nearby Stars	47
3.1.1	New UCD candidates in <i>Gaia</i> DR3	48
3.1.2	GCNS completeness in the UCD regime	48
3.1.3	UCD empirical completeness exceptions	49
3.2	Ultracool Dwarfs in <i>Gaia</i> DR3	51
4	Ultracool Spectroscopic Outliers in <i>Gaia</i> DR3	56
4.1	Introduction	57
4.2	Method	60
4.2.1	External cross-matching	61
4.2.2	Estimating a spectral type	62
4.2.3	Creating a colour ratio	63
4.2.3.1	Determining outliers	66
4.3	Analysis	66
4.3.1	Photometry checks	68
4.3.2	Kinematics	70
4.4	Results	71
4.5	Summary	75
5	<i>Gaia</i> Ultracool Dwarf Sample – V. Database	78
5.1	Introduction	78
5.2	Database Description	79
5.2.1	Interfacing with the database	84
5.2.2	Contributing to the database	86
5.3	Conclusions	87
6	Astronomical Software and Observations	88
6.1	SIMPLE Database	88
6.2	Public Python packages	89
6.2.1	GaiaXPy Batch	89
6.2.2	RV Fitter	91
6.2.3	Target List Generator	91
6.2.4	Publication-ready Plots	91
7	Conclusions	95

A	GTC/OSIRIS optical spectra of <i>Gaia</i> L dwarfs Appendices	96
A.0.1	Supplementary Tables	96
A.0.2	Comparison with standard routines	99
A.0.2.1	Bespoke IRAF Reduction	99
A.0.3	Radial velocity method validation	102
A.0.3.1	Line centres	102
A.0.3.2	Cross-correlation	103
A.0.4	Spectral sequence	105
A.0.5	PyPeIt Configuration Files	105
A.0.5.1	Reduction	105
A.0.5.2	Sensitivity Function	109
A.0.5.3	Flux Calibration	110
A.0.5.4	Coadding	110
A.0.5.5	Telluric Correction	110
B	Ultracool Outliers in <i>Gaia</i> DR3 Appendices	112
B.1	Ultracool Outliers in <i>Gaia</i> DR3 Training Sample	112
	Bibliography	114

List of Figures

1.1	A plot by Burrows et al. (1997) showing time versus temperature. The blue lines indicate stellar objects which can fuse hydrogen, hence the constant (flat) $T(t)$. Purple lines are the brown dwarf region where they start with fusing deuterium (constant $T(t)$) but run out and begin thermally decaying. Red lines represent planets.	3
1.2	From Ryan et al. (2017), based on the evolutionary tracks from Burrows et al. (1997), a cooling curve with different masses displayed and the spectral types L and T on the right axis. The curves here show the degeneracy between age and mass, as a given T_{eff} or spectral type do not directly provide age and mass, unless one of the two parameters can be separately determined.	4
1.3	From Smart et al. (2019) – absolute <i>Gaia</i> magnitude against <i>Gaia</i> G-RP colour for UCDs. To the right, and named are specific objects suspected of being unresolved binaries with objects coloured by spectral type (colour mapped on the right axis).	5
1.4	Log projected separation against frequency for various binary detection methods at the sub-stellar boundary, from Bardalez Gagliuffi et al. (2019) and references therein.	6
1.5	A flow diagram representing the different formation mechanisms starting from a gas cloud that results in star/brown dwarf formation.	7
1.6	A flow diagram representing the different formation mechanisms starting from a protostellar disc that results in brown dwarf/planet formation.	8
1.7	Space density plot of L dwarfs and T dwarfs from Marocco et al. (2015) and references therein: A comparison between measured space densities of L and T dwarfs with simulations by Deacon and Hambly (2006) with $\alpha = +1.0, 0.0, 1.0$ and $\beta = 0.0, 0.2, 0.5$. On the top axis they show an indicative temperature scale.	9
2.1	R2500I spectra for J1745–1640, normalised at 8100–8200 Å, comparing two independent reduction procedures: PyPeIt in black and IRAF in orange. In blue, the heliocentric corrected MagE spectra (Burgasser et al., 2015) for the same object is shown (which is not telluric corrected).	21
2.2	The first 24 of the R2500I VPHG spectra with a linear offset applied, sorted by spectral sub-type. We show the short names and the spectral sub-types from this work, attached to each spectrum. At the top of the figure are grey lines denoting a selection of spectral features typical to L dwarfs, plus the two main telluric bands.	23
2.3	Same as Figure 2.2 but for the second half of the R2500I VPHG sample.	24
2.4	Same as Figure 2.2 but for the R300R grism spectra.	25

- 2.5 J1745–1640 RV calculation via different line profiles (orange: solid – Gaussian; dash-dot – Voigt) against the data (black squares) and fifth order spline fit (blue) in the regime around the eight listed line centres. The shift from the laboratory line position (vertical dashed grey line) is shown as the vertical solid black line. The horizontal black line (solid or dash-dot, depending on the fitted line profile as above) is the continuum, as is subtracted from the data. A grey band is given, corresponding to the region of data the line profiles are fitted to. The shown region is between the inner edges of the continuum regions. 27
- 2.6 J1745–1640 RV calculation via the manually shifted BT-Settl model (orange) against the data (black squares) and fifth order spline fit (blue). The laboratory line position (vertical dashed grey line) has been manually shifted by the RV given on the sub-plot title (vertical solid black line). Effective temperature, gravity and metallicity are also indicated on each features title. 28
- 2.7 J1745–1640 RV values for each given line. In the top panel, orange squares are cross-correlated RVs, blue diamonds are line centre RVs; each spectral feature has been indicated on the y axis. In the bottom panel, the orange curve is the cross-correlated PDF; the blue curve is the line centre PDF; and the black curve is the adopted PDF. The dotted vertical lines are the mean RV values as associated with each PDF. 29
- 2.8 Comparison between this works spectral types and the literature spectral types. Blue squares are spectral types from our adopted, *kastredux* method whilst orange circles are from the manual ‘by eye’ method. Grey lines connect these two methods and we show a one-to-one dashed grey line with associated ± 2 spectral sub-types confidence bands. 32
- 2.9 **[Left Panel]**: Histograms of the RVs calculated in this work (orange) and from the literature (blue) to show the relevant population densities. The dashed vertical lines indicate the means of the associated distributions. **[Right Panel]**: The RV values from the literature on the x axis with our adopted RV values, on the y . We show a one-to-one relation, over which our 19 comparison RVs are plotted as diamonds. Orange diamonds are like-for-like comparisons and blue diamonds are for the two benchmark systems, i.e., comparisons between our measured secondary RV against the literature RV of the primary. 33
- 2.10 Toomre diagram, as done by Bensby et al. (2005), using *Gaia* DR3 astrometry in combination with our calculated RVs. V is on the x axis, against the velocity dispersion ($\sqrt{U^2 + W^2}$) on the y axis. Black circles are UVW velocities calculated with the RVs from this work, with associated error-bars given. We show the respective thick disc and halo selection lines at $V_{\text{total}} > 70 \text{ km s}^{-1}$ and $V_{\text{total}} > 180 \text{ km s}^{-1}$ respectively. 37
- 2.11 The expected \widehat{T}_{eff} (calculated via spectral type through a Filippazzo relation, Filippazzo et al., 2015) on the x axis and the best-fitting BT-Settl model mean T_{eff} on the y axis. Blue crosses are for objects with a fit to the R300R spectra whilst black crosses are objects with a fit to the R2500I spectra. 38

- 2.12 Colour-absolute magnitude diagram (CAMD) including the BHAC15 model cooling tracks by Baraffe et al. (2015). The $2\text{MASS } J - K_s$ colour is on the x axis against absolute $2\text{MASS } J$ magnitude on the y axis (having been computed using the *Gaia* parallaxes). Underlying the plot as grey circles is the full UCD sequence from the GUCDS. The blue lines are the 100 Myr and 500 Myr isochrones with solid, dashed, dash-dot, and dotted line styles respectively. The orange lines are $0.05 M_{\odot}$ and $0.1 M_{\odot}$ profiles with respective line styles as above. Each object is coloured by our adopted spectral type, with error-bars shown in both axes. Diamonds are the young candidates discussed in Section §2.4.3.1. Key: a-J0453-1751, b-J0502+1442, c-J1058-1548, d-J1213-0432, e-J0953-1014, f-J1004-1318, g-J1246+4027, h-J1004+5022, i-J1441-0945. 39
- 2.13 Gravity sensitive alkali lines for a selection of young candidates as compared with a field object of a given spectral type. The first column are L0 spectral types, then L3 and L4, all corrected for RV. Black lines are for the selected field objects: J1232-0951 (L0), J0918+2134 (L3) and J1750-0016 (L4). Orange lines are objects which have been kinematically bound to young moving groups in this work. The blue lines are potentially young candidates which are either in the field or have a probability greater than 10 per cent of being in a young moving group. L0: J0502+1442 (orange), J0953-1014 (blue) and J1441-0945 (blue, dashed). L3: J0453-1751 (orange), J1058-1548 (orange, dashed), J1004-1318 (blue) and J1004+5022 (blue, dashed). L4: J1213-0432 (orange) and J1246+4027 (blue). 40
- 3.1 Left: M_G vs. $G - J$ diagram of stars in GCNS that are not found in *Gaia* DR2. The red dots are new UCD candidates, the blue points are known UCDs (spectral types between M7 and T8), and the grey points are the full GCNS sample. The new candidates are selected following the condition $M_G > -3 \times (G - J) + 25$, after removing stars whose probability of being a WD is higher than 20 %. Right: Distance distribution of the new candidates in the GCNS (red) and the known UCDs (blue). 48
- 3.2 CAMD of $G_{BP} - G_{RP}$ [mag] against M_J [mag]. The full sample is from the GUCDS, and known binaries are over plotted as squares. Points are coloured by their published spectral types. 49
- 3.3 Simulated completeness per parsec for each spectral type. Each spectral type from M7-L8 (right to left) is labelled next to its respective simulated completeness level. We skip L5 and L7 for better readability. 50
- 3.4 In dark grey, ground-based optical spectra from the GTC (Cooper et al., submitted). These spectra have been simulated from the original spectra by passing through MIOG. The objects shortnames are: J1717+6526 - L6, J1213-0432 - L5, J0453-1751 - L3, J1745-1640 - L1, J0935-2934 - L0, J0938+0443 - M9. Over-plotted are RP spectra coloured by effective temperature and labelled by spectral type. All fluxes are normalised by the area and linearly offset. 54
- 3.5 As Figure 3.4 but for externally calibrated RP spectra. The calibrated spectra were constructed using the `gaiaxy.calibrate` function. The GTC spectra as shown here have not been passed through MIOG and represent the actual spectra with resolution ≈ 2500 . A selection of features typical of late M - mid L dwarfs are shown above. 55

- 4.1 The normalised median RP fluxes for each spectral type (see Sect. 4.2.2) from M5–T6. Each spectral type is indicated by the attached text with its corresponding median effective temperature given on the auxiliary axis. Vertical dashed lines are shown for every spectrum to indicate the position of the two primary spectral peaks. The normalised spectra were multiplied by a constant value such that the fluxes sum to 100 instead of 1 and are offset by a set value. 59
- 4.2 Histogram of the number of objects in each spectral type bin from the GUCDS. The full GUCDS is shown in blue whilst over plotted in orange is the distribution of the known standards used. 62
- 4.3 Spectral type conversion from T_{eff} [K] to spectral type for the GUCDS, as a 2-D histogram. The number of objects in each bin is shown by the colour bar. Our fourth order polynomial is shown as the blue line. By comparison, we plot in orange the fifth order polynomial (equation (4): Stephens et al., 2009) relation, valid from M6–T8. A wider spread of T_{eff} can be seen in the late M and early L dwarfs. This is a natural spread as each known spectral type will have an error margin of 1–2 spectral types. 64
- 4.4 Internally calibrated RP spectra of known objects, separated by their literature optical spectral types. Magenta spectra are known young objects whilst blue spectra are known subdwarfs. Over-plotted in black is the median RP spectra for a given spectral type from known objects in the GUCDS. The blue and red bands are shown in their respective positions and colours as described in Section. 4.2.3. The normalised spectra were multiplied by a constant value such that the fluxes sum to 100 instead of 1 and are offset by a set value. 65
- 4.5 Colour ratio (CR, Sect. 4.2.3.1) against estimated spectral type (Sect. 4.2.2). We display sources only between M6–L4 (there are no later candidates). The full population is shown as small squares using a colour-code reflecting T_{eff} shown on the right-hand axis. Standards are displayed as black squares whilst known young objects are magenta diamonds (filled if very low gravity, i.e. δ / ‘vl-g’) and known subdwarfs are blue circles. Horizontal coloured lines are shown demarcating the selection criteria, magenta for $\text{CR} \leq z_{-3\sigma}$ and blue for $\text{CR} \geq z_{3\sigma}$. A black dotted line is shown at the mean CR. Candidate subdwarfs are yellow circles, candidate young objects are yellow diamonds. 67
- 4.6 Spectral comparison between internally and externally calibrated RP spectra of spectral type standards from M7–L4. Spectra are coloured by effective temperature. Internally calibrated RP spectra of spectral type standards in the upper plot. Externally calibrated RP spectra of spectral type standards in the lower plot. The normalised spectra were multiplied by a constant value such that the fluxes sum to 100 instead of 1. 69
- 4.7 Four colour-absolute magnitude diagrams with M_G on the top row, M_J on the bottom row, $G - J$ on the left column, and $J - K_s$ on the right column. The full RP spectral sample is shown as small squares using a colour-code reflecting T_{eff} , as shown in the colour bar. Standards are displayed as black squares whilst known young objects are open magenta diamonds (filled if very low gravity δ / ‘vl-g’) and known subdwarfs are open blue circles. Candidate subdwarfs are yellow circles, candidate young objects are yellow diamonds. Dashed lines are shown demarcating the cut-offs for the photometric filtering of the candidate selection. Magenta lines are for the young object candidate selection and blue lines are for the subdwarf selection. These lines represent the cuts in Table 4.2. 70

4.8	Toomre diagram (Sandage and Fouts, 1987), corrected for the LSR, of our prime candidates with thick disk and halo selection lines shown at $V_{\text{total}} > 70 \text{ km s}^{-1}$ and $V_{\text{total}} > 180 \text{ km s}^{-1}$ respectively. Standards are displayed as black squares whilst known young objects are open magenta diamonds (filled if very low gravity $\delta / \text{'vl-g'}$) and known subdwarfs are open blue circles. Candidate subdwarfs are yellow circles, candidate young objects are yellow diamonds. Error-bars in matching colours are also shown.	72
4.9	Internally calibrated RP spectra of our seven prime candidates with estimated spectral type, rounded to 0.5, indicated. Any objects with dashed lines are already known to the literature. Blue lines are subdwarfs whilst magenta lines are young objects. Over-plotted in black is the median RP spectra for the given spectral type from known objects in the GUCDS. Subdwarfs are typically over-luminous in blue and underluminous in red (the blue and red bands shown as shaded regions, as described in Sect. 4.2.3) with the inverse true for young objects. The normalised spectra were multiplied by a constant value such that the fluxes sum to 100 instead of 1.	73
4.10	The Δ SEDs for our seven prime candidates in yellow with estimated spectral type (rounded to 0.5) indicated, as compared with the mean absolute magnitudes for the given spectral type from the GUCDS. Positive values indicate over-brightness and negative values under-brightness. Blue dotted lines are shown on the objects already known to be subdwarfs in the literature. Over-plotted in dark grey at zero are the wavelengths covered. A grey shading is shown in the region covered by <i>Gaia</i> RP spectra. The photometry shown is from Pan-STARRS, <i>Gaia</i> , 2MASS and AllWISE; converted into an absolute magnitude using the <i>Gaia</i> DR3 parallax. The wavelengths plotted correspond to the mean wavelengths ($\bar{\lambda}$) of each photometric band ($g, G_{\text{BP}}, r, G, i, G_{\text{RP}}, z, y, J, H, K_s, W1, W2, W3, W4$, in increasing $\bar{\lambda}$ order), as extracted from VOSA (Bayo et al., 2008).	76
5.1	An example search for any objects with a short name like 'J1234'.	84
5.2	Example query looking for any objects which have at least four spectra in the database.	85
5.3	Example object plotting four spectra, in log space.	86
6.1	An example search performed on the SIMPLE website for any object with a name (not only the main name) including 'VHS'.	89
6.2	An example object results page, with the interactive photometry and spectra plots shown.	90
6.3	From Morris et al. (2022), "Fitted line profiles and radial velocities for the hydrogen recombination lines. Points and blue lines are the data, yellow dashed lines are the fits, using a Voigt profile, and converted into velocity space. The median radial velocity of the star was $-283.9 \pm 9.3 \text{ km s}^{-1}$, relative to the Local Standard of Rest. The individual radial velocities fitted to each line are marked with solid yellow lines. Fluxes are normalised with respect to the HI $3 \rightarrow 2$ line."	92
6.4	An example object finder chart, using Aladin and Pan-STARRS within a 5 arcminute view.	93
6.5	An example object finder chart, using Aladin and Pan-STARRS within a 1 arcminute view.	94
6.6	An example target list of UCDs interspersed with nearby A dwarf standards. This is formatted to the requirements for the Infrared Telescope Facility.	94

A.1	Same as Figure 2.2 with additional comparison spectra. Light blue shows the corresponding standard optical spectra whilst light orange is the best-fitting BT-Settl model around the relevant spectral lines.	106
A.2	Same as Figure A.1 but for the second half of the R2500I VPHG spectral sample.	107

List of Tables

2.1	The 53 targets observed at the GTC with OSIRIS and presented in this work.	16
2.2	The list of atomic alkali metal lines used when estimating astrophysical parameters and calculating radial velocities. Wavelengths are as measured by Kramida et al. (2021) and are defined in standard air.	25
2.3	Our spectral types compared with the literature optical and near-infrared types for each object.	31
2.4	RVs measured in this work and compared to the literature.	34
2.5	The UVW velocities and BANYAN Σ classification (with associated probability) from this work.	35
2.6	Effective temperatures and surface gravities from this work.	37
3.1	List of standard UCDs used to calibrate the ESP-UCD module empirical training set in effective temperature. Astrometry is from <i>Gaia</i> DR3 and the T_{eff} values are those produced by the ESP-UCD Apsis module and published as part of the Data Release.	52
4.1	Polynomial coefficients for T_{eff} to spectral type relation in equation (4.1). Valid for $1150 < T_{\text{eff}} < 2700$ K or M6–T4.	63
4.2	Photometric cuts to select subdwarfs and young objects.	68
4.3	Unsorted list of candidate subdwarfs and young objects. Astrometry is from <i>Gaia</i> DR3 and the T_{eff} values are those produced by the ESP-UCD Apsis module and published as part of the Data Release.	72
5.1	The GUCDS description.	80
A.1	Additional information for all observations carried out as part of the two programmes presented here. Note, multiple objects were observed multiple times, with either the same grism or the other. Seeing is given as a range corresponding to reverse wavelength, and is corrected for airmass.	97
A.2	Cross-matched absolute photometry from <i>Gaia</i> , 2MASS & WISE, using <i>Gaia</i> parallaxes.	99
B.1	List of subdwarfs and young objects used to train our colour ratio. Astrometry is from <i>Gaia</i> DR3 and the T_{eff} values are those produced by the ESP-UCD Apsis module and published as part of the Data Release.	113

List of Abbreviations

Acronym	What (it) Stands For
CMD	Colour-Magnitude Diagram
CR	Colour Ratio
CU	Coordination Unit
DPAC	Data Processing and Analysis Consortium
(E)DR#	(Early) Data Release #
GCNS	<i>Gaia</i> Catalogue of Nearby Stars
GTC	Gran Telescopio Canarias
GUCDS	<i>Gaia</i> Ultracool Dwarf Sample
MIOG	Mean Instrument Object Generator
OSIRIS	Optical System for Imaging and low-intermediate Resolution Integrated Spectroscopy
RV	Radial Velocity
SpT	Spectral Type
UCD	UltraCool Dwarf
VPHG	Volume Phased Holographic Grating

Chapter 1

Introduction

I discuss here the background on ultracool dwarfs (UCDs), including their discovery and history of characterisation. I also highlight the current astrophysical theory of UCDs, most notably their different formation mechanisms. All-sky surveys are also discussed, and how that relates to the completeness of known UCD populations. Finally, I break down the structure of this thesis.

1.1 Theory and Direct Observations

UCDs are the lowest-mass, coldest, and faintest products of star formation, which make them difficult to study at large distances. They were defined as objects with spectral types M7 and later (Kirkpatrick et al., 1997), through L (Kirkpatrick et al., 1999), T (Burgasser et al., 2002), and Y (Cushing et al., 2011) types, have typical masses $M \lesssim 0.1 M_{\odot}$, and effective temperatures $\lesssim 2700 \text{ K}$ (Kirkpatrick, 2005). UCDs are of particular interest since they include both low-mass stars that slowly fuse hydrogen, and brown dwarfs (BDs), which have insufficient mass (below $0.075 M_{\odot}$) to sustain hydrogen fusion in their cores, and cool with time.

Commonly known as ‘failed stars’, brown dwarfs exist in the range of ≈ 13 (Saumon et al., 1996; Chabrier et al., 2000) to 80 (Chabrier and Baraffe, 1997; Baraffe et al., 1997) Jupiter masses (M_J), they are considered ‘failed’ because they are unable to reach the ignition point of hydrogen within their cores ($\approx 13 \times 10^6 \text{ K}$), although they can burn deuterium. They, along with exoplanets are interesting because they provide insight into stellar and planetary formation.

There is an important distinction in the definitions of ultracool dwarfs and brown dwarfs. A brown dwarf is an object that cannot fuse hydrogen stably as core contraction is prevented by

electron degeneracy. Pauli's exclusion principle, then, prevents electrons with the same spin being in the same energy level. At extreme densities electrons are 'forced' into states at a higher energy (Desai, 2010), this energy equates the gravitational potential energy released by core contraction – preventing further collapse.

1.1.1 Detecting UCDs

Another cause of the disparity between predicted and observed number densities, is that UCDs are dimmer than main sequence stars. There is a detection bias in observational campaigns, as it is far easier to detect main sequence stars. UCDs emit their light predominantly at near- and mid-infrared wavelengths. Near-infrared objects like these are challenging to see with ground based telescopes. This is because of the Earth's atmosphere emitting and absorbing light at those (telluric) wavelengths. Another challenge to the detection of UCDs is that dust in the galaxy (Draine, 2003) also emits at near-infrared wavelengths so source selection difficulties amongst such a background lowers the number of UCD confirmations.

Brown dwarfs will cool over time once they deplete their supply of deuterium (Figure 1.1), most of which having only been formed within the first few minutes after the Big Bang, during primordial nucleosynthesis (Damone et al., 2018).

For the separation of the different types of ultracool dwarfs, it can be seen in Figure 1.2 that the age needs to be determined given a measured effective temperature. Young objects have lower surface gravities than normal objects while old objects typically have lower metallicities and higher velocities.

1.1.2 Spectral Features

Due to the low temperature of brown dwarfs, molecules such as water (H₂O), ammonia (NH₃) or methane (CH₄) dominate (Canty et al., 2015). I focus in this thesis on late-M and L dwarfs.

Ultracool, late-M dwarfs have spectral features typical of other M dwarfs but are cooler. L dwarfs have effective temperatures between 1400–2500 K. L dwarf spectra have lines not seen in warmer stars like chromium hydride because they have 'dusty' atmospheres. They are dim and often undetected in optical surveys, appearing red in part due to the increased scattering of blue light because of dust grains in the photosphere.

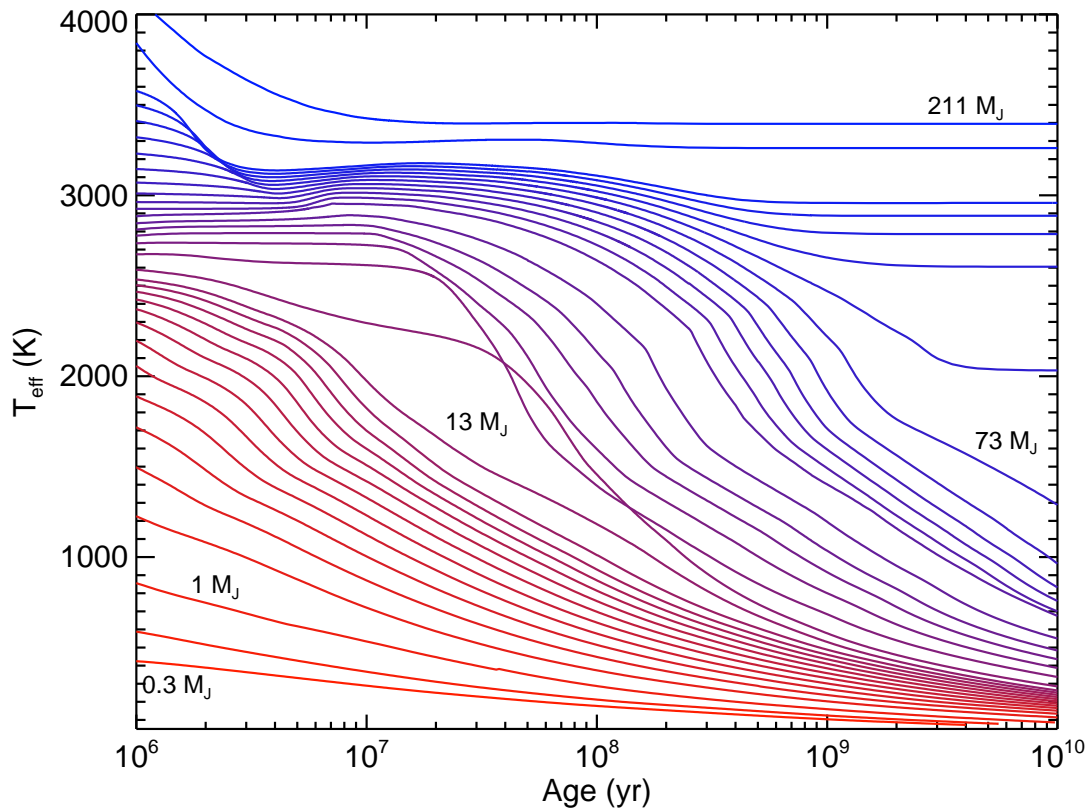


FIGURE 1.1: A plot by Burrows et al. (1997) showing time versus temperature. The blue lines indicate stellar objects which can fuse hydrogen, hence the constant (flat) $T(t)$. Purple lines are the brown dwarf region where they start with fusing deuterium (constant $T(t)$) but run out and begin thermally decaying. Red lines represent planets.

1.1.3 Binarity

There had been an increase in the number of multiple stellar systems found where one or more of the companions are UCDs (e.g., Mužić et al., 2012; Deacon et al., 2014; Baron et al., 2015; Marocco et al., 2017). Most companions, however, are found at extended separations from their host stars (see ‘brown dwarf desert’, Ranc et al., 2015; Grether and Lineweaver, 2006) where the gravitational pull is not strong. An example of a wide binary with an UCD component is GD 165B (Becklin and Zuckerman, 1988) where the primary star is a white dwarf and the companion is a brown dwarf with a separation of 120 AU.

There is still ongoing discussion on the fraction of stars with BD components. For instance, work by Pinfield et al. (2006), used simulated BD populations and the 2-Micron All Sky Survey (2MASS, Skrutskie et al., 2006) to determine $34^{+9}_{-6}\%$ as the fraction of subgiant or white dwarf stars with BD companions in 2MASS. Gomes et al. (2013) discussed the binary fraction of UCDs and found 59 L dwarfs as part of multiple systems, 35 of which with a UCD primary.

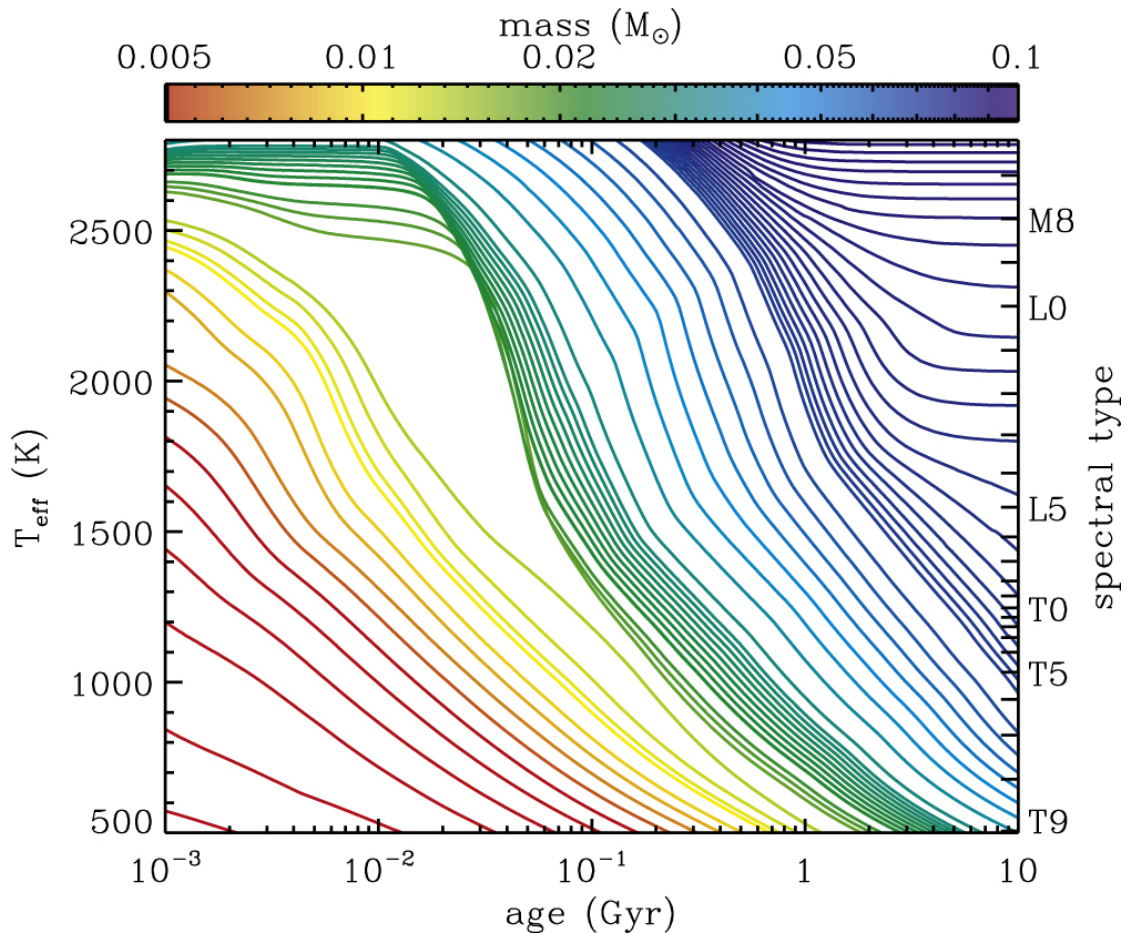


FIGURE 1.2: From Ryan et al. (2017), based on the evolutionary tracks from Burrows et al. (1997), a cooling curve with different masses displayed and the spectral types L and T on the right axis. The curves here show the degeneracy between age and mass, as a given T_{eff} or spectral type do not directly provide age and mass, unless one of the two parameters can be separately determined.

As can be seen in Figure 1.7, unresolved binarity has a key role in predicting the binary fraction, especially in the L+T transition region. Without a true binary fraction, we cannot use age models (Figure 1.1) to derive the true mass function. Figure 1.3 shows objects from Smart et al. (2019) as a colour-magnitude diagram to show how objects evolve with spectral type, unresolved binaries can contaminate the young object population. Figure 1.4 shows different methods for exploring the aforementioned ‘brown dwarf desert’.

1.1.4 Formation

There are a number of theories as to how brown dwarfs form, with recent debates still ongoing as to which method produces brown dwarfs of different masses. For example, Wagner et al. (2019) finds the gravitational disc instability model (Forgan et al., 2018) fits well with observations

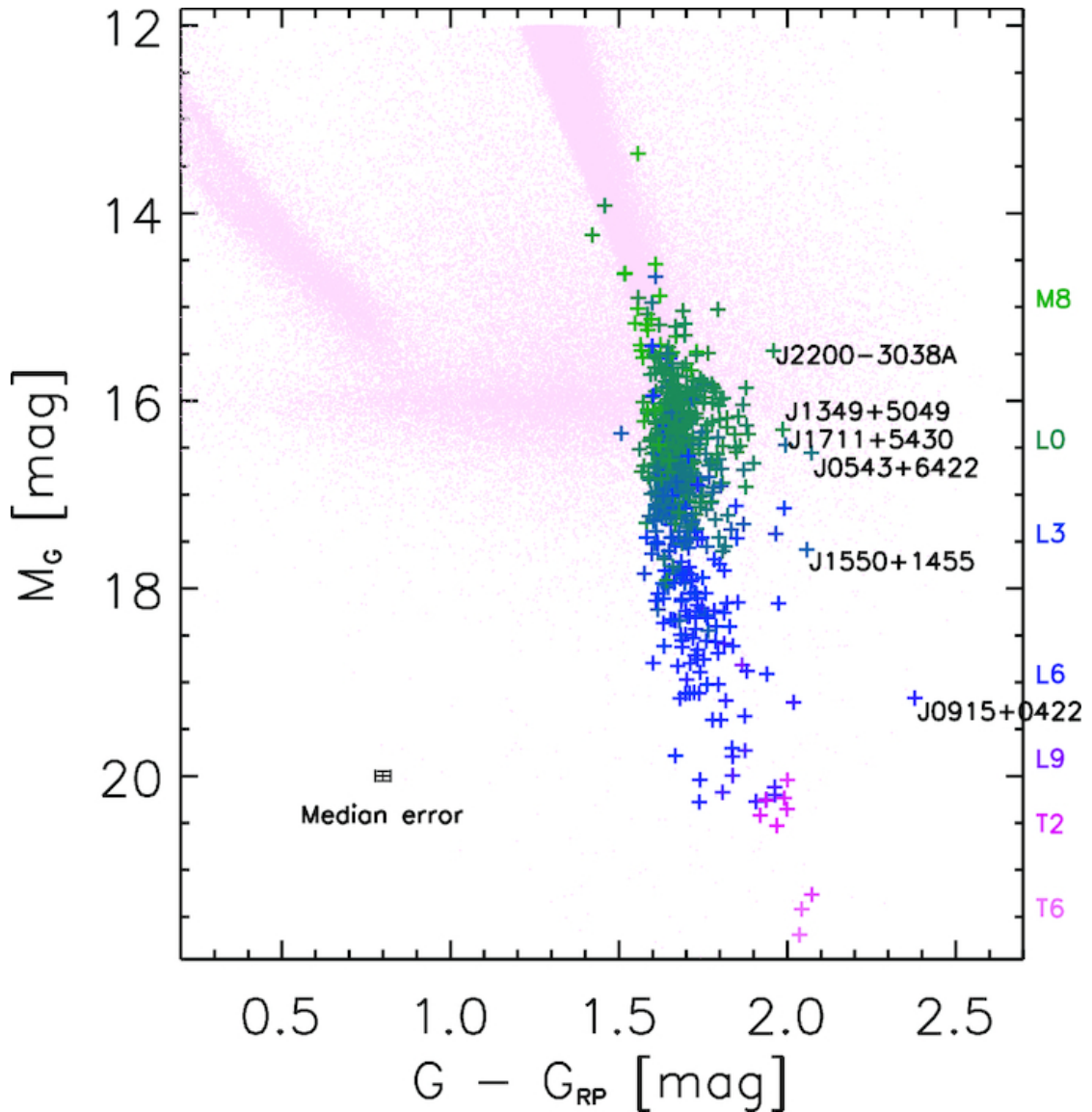


FIGURE 1.3: From Smart et al. (2019) – absolute *Gaia* magnitude against *Gaia* G-RP colour for UCDs. To the right, and named are specific objects suspected of being unresolved binaries with objects coloured by spectral type (colour mapped on the right axis).

in the $\sim 20\text{--}70 M_J$ regime while core accretion (Mordasini et al., 2009) fits better below that regime (see Figure 4 of Wagner et al., 2019) with the different models discussed below. All models tend to be related and there are still unknowns about the processes, I have attempted to show the generic hierarchy of formation methods in a flow diagram in Figures 1.5 and 1.6:

1. Gravitational Cloud Instability/Gravoturbulent fragmentation (Padoan et al., 2012): As with main sequence stars, when a gas cloud above the Jeans' Mass (Equation 1.1, assuming virial equilibrium) collapses due to the gravitational potential energy exceeding the outward thermal pressure (Carroll and Ostlie, 2007). Hydrostatic equilibrium is therefore

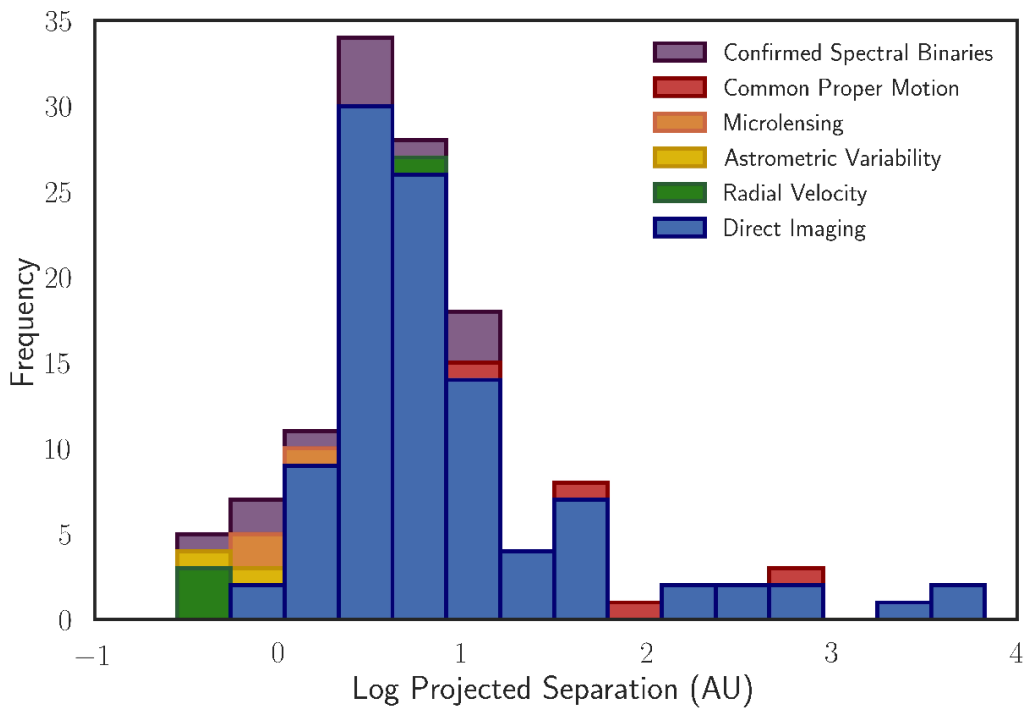


FIGURE 1.4: Log projected separation against frequency for various binary detection methods at the sub-stellar boundary, from Bardalez Gagliuffi et al. (2019) and references therein.

broken and the gas cloud collapses on a free-fall timescale ($t \approx (G\rho)^{-\frac{1}{2}}$). The key features leading to a successful collapse are the temperature and particle density of the gas. This fragmenting can potentially come from both fast (shocks) and slow (ions moving on magnetic field lines) processes. Although it is more likely a fast process due to the low typical lifetimes as observed in molecular gas clouds, $\tau \sim 3$ Myr (Elmegreen, 2000; Hartmann et al., 2001).

2. Disc fragmentation (Whitworth and Stamatellos, 2006): Initially after the birth of a young stellar object (YSO), there can be gravitational instabilities in a disc which could cause fragmentation on an orbital timescale. This timescale is directly correlated with the mass of the YSO and the position within the disc. For example, Andrews et al. (2018) used a sample of YSOs with masses between $\approx 0.5-2 M_{\odot}$ and radii from ≈ 5 AU to $\gtrsim 150$ AU. An orbital timescale can therefore range from $\approx 10^1-10^3$ years. This is considerably shorter than typical disc lifetimes with $\tau \approx 1.3-3.5$ Myr (Mamajek, 2009; Richert et al., 2018). Disc fragmentation forms objects following radiative cooling, with often H_2 dissociation causing secondary fragmentation, leading to low mass binaries in the disc.
3. Core accretion (Pollack et al., 1996): Mass accretion following disc fragmentation from the protostellar disc is limited by the amount of mass available from the disc. This tends

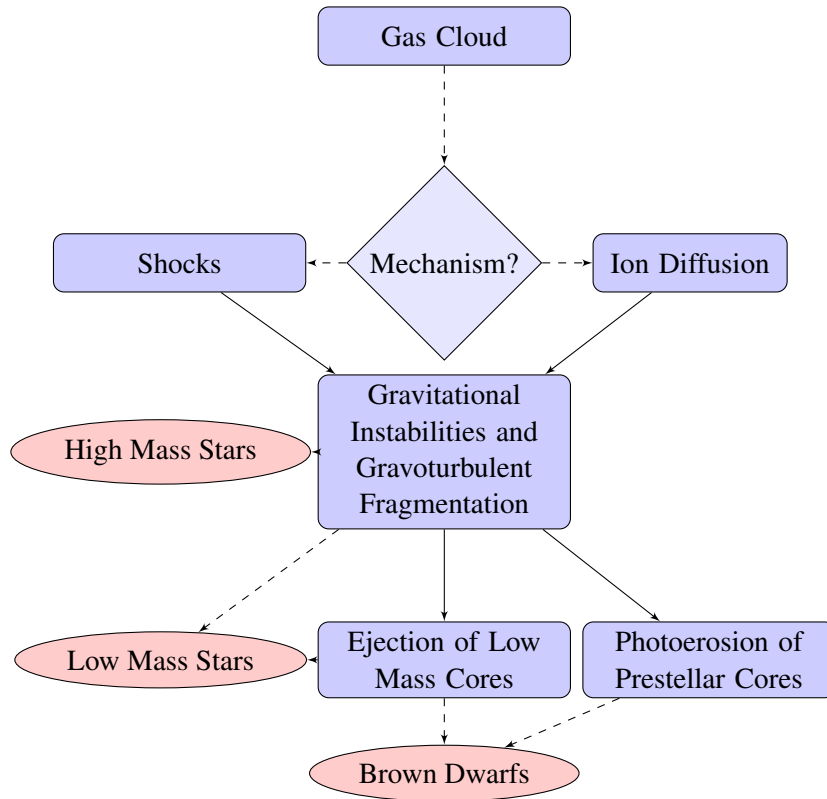


FIGURE 1.5: A flow diagram representing the different formation mechanisms starting from a gas cloud that results in star/brown dwarf formation.

to be the most common formation method for planets rather than brown dwarfs as the mass supply tends to be limited.

4. Ejection of low mass cores (Reipurth and Clarke, 2001): Following gravoturbulent fragmentation of molecular clouds, there is a period of time where the core of this collapse is accreting gas through gravitational attraction. One of the most significant ways this accretion is cut off is due to dynamical interactions providing a randomly directed velocity, which can be enough to remove the core from the molecular cloud. This truncates star formation, leading to the creation of a free floating brown dwarf.
5. Photoerosion of prestellar cores (Whitworth and Zinnecker, 2004): In both cloud and disc fragmentation there can be a scenario where a protostellar core ignites hydrogen. This ignition is from a nearby star during cloud fragmentation and the host star for disc fragmentation. This creates a radiative pressure which depletes the gas supply that other objects were accreting/fragmenting in, hence forming a brown dwarf.

$$M_{Jean} = \left(\frac{5kT}{G\mu m_H} \right)^{\frac{3}{2}} \left(\frac{3}{4\pi\rho} \right)^{\frac{1}{2}} \quad (1.1)$$

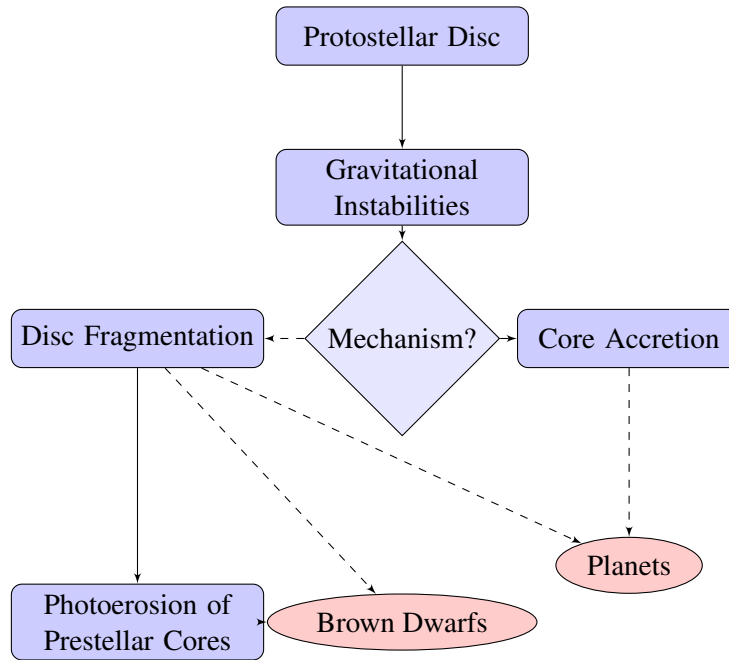


FIGURE 1.6: A flow diagram representing the different formation mechanisms starting from a protostellar disc that results in brown dwarf/planet formation.

1.1.5 UCD Population Statistics

During the process of collapse, one could expect a larger number of brown dwarfs than stellar objects, because they require less mass to form. This is a numerical relation in the form of the Salpeter Initial Mass Function (IMF, Salpeter, 1955), where $\alpha = 2.35$ (Equation 1.2). The observed mass function, when compared to the predicted IMF, is a common method for determining age. This is performed by observing a stellar cluster and calculating which mass stars have turned off of the main sequence. This is clearly visible in the Hertzsprung-Russell diagram of a cluster. For example, if high-mass stars are still dwarfs, the cluster is very young. The typical assumption is that all stars in an globular or open cluster are coeval, i.e. they have formed at the same time with the same chemical composition.

$$\xi(M) = \xi_0 \left(\frac{M}{M_\odot} \right)^{-\alpha} \quad (1.2)$$

This, however, does not match the observations, where the most numerous stars are K and M Dwarfs. A reason for this mismatch between the observed and predicted number densities is the inaccuracy of the IMFs in the substellar region. One suggested alteration to the IMF is to transfer from a single component to a multi component function. Kroupa (2002), for instance,

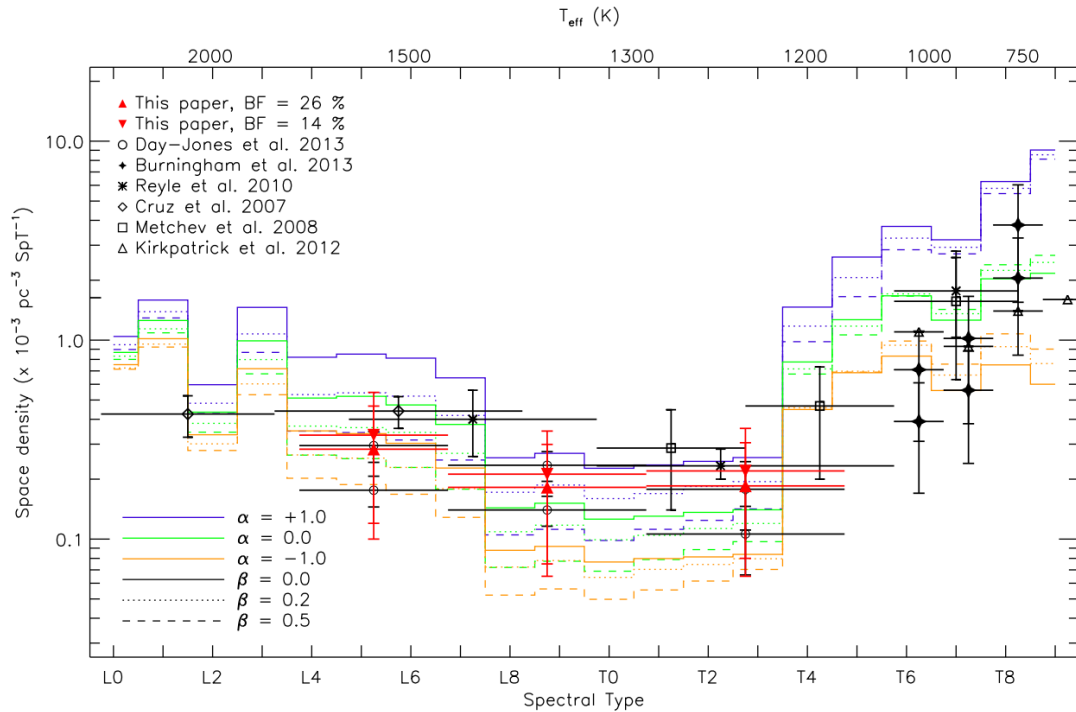


FIGURE 1.7: Space density plot of L dwarfs and T dwarfs from Marocco et al. (2015) and references therein: A comparison between measured space densities of L and T dwarfs with simulations by Deacon and Hambly (2006) with $\alpha = +1.0, 0.0, -1.0$ and $\beta = 0.0, 0.2, 0.5$. On the top axis they show an indicative temperature scale.

changes α to: 0.3 for brown dwarfs; 1.3 for $0.08 < M < 0.5 M_{\odot}$; and 2.3 for more massive stars. This appears to fit the observed distribution better (Figure 1.7).

1.2 Surveys and Missions

Although UCDs have only been observed since the mid 90s, there have been a multitude of both ground-based and space mission surveys for which the detection of UCDs was an achievable objective. Gathering positional and velocity data has historically been a challenging concept. A major space-based mission in the 80s and 90s was the Hipparcos satellite and associated catalogue (Perryman et al., 1997). This was complemented by ground-based parallax programme, such as the PARSEC programme (Andrei et al., 2011; Marocco et al., 2013; Smart et al., 2018).

The ESA *Gaia* mission launched in 2013 and is observing objects as diverse as minor planets, stars, galaxies out to QSOs and had its first data release (DR) in 2016. *Gaia* is measuring the parallaxes of all celestial objects down to $G = 20.7$ mag (complete to 20.3 mag). Reylé et al.

(2021) have published an initial foray into this discovery space, identifying 679 as-yet unconfirmed L dwarf candidates. Smart et al. (2017) estimated that in the final *Gaia* catalogue there will be over 1000 candidates and of these ~ 400 will be new. Thanks to its full sky coverage and high precision observations, *Gaia* offers the means to uncover nearby UCDs through astrometric, rather than purely photometric, selection (e.g., Reyl e, 2018; Smart et al., 2019; Scholz, 2020) and provides a large and homogeneous sample. The most recent data release, *Gaia* DR3, also provided spectra and astrophysical parameters. Sarro et al. (2023) discussed the 94 158 UCDs selected in *Gaia* DR3.

Although UCDs have their peak flux towards the infrared, a lot of useful information can be gathered from optical surveys. These include *Gaia*, Pan-STARRS (PS1, Chambers et al., 2016) and SDSS (York et al., 2000; Abazajian et al., 2009). Infrared surveys, where UCDs are considerably brighter than in the optical, consist of 2MASS (Cutri et al., 2003; Skrutskie et al., 2006), DENIS (Epchtein et al., 1997), VISTA’s VVV/VIRAC/VHS (Minniti et al., 2010; Smith et al., 2018; McMahon et al., 2021), UKIDSS (Lawrence et al., 2007) and the unWISE/catWISE (Schlafly et al., 2019; Marocco et al., 2021; Meisner et al., 2023) catalogues, which used WISE (Wright et al., 2010)

1.3 Motivation and Thesis Structure

In this thesis, I discuss the gathering of ground-based spectra for the confirmation and analysis of UCDs in Chapter 2. This is tied to my contributions to *Gaia* in Chapter 3. I then discuss in Chapter 4 my work on detecting outlying *Gaia* RP spectra. In Chapter 5, I show the ongoing work in generating a database including all available information on objects in the GUCDS. Chapter 6 discusses my creation of software and further technical work, for use by the astronomical community. My conclusions are then provided in Chapter 7.

Chapter 2

The *Gaia* Ultracool Dwarf Sample – IV. GTC/OSIRIS optical spectra of *Gaia* L dwarfs

I present here the work into deriving radial velocities, spectral types, spectral indices, effective temperatures, and surface gravities for objects observed with the OSIRIS instrument on the GTC. This work was predicated by a continuing series of observing proposals designed for completing the UCD 30 pc sample. The data from these programmes are presented in the GUCDS series of papers (Smart et al., 2017, 2019; Marocco et al., 2020). I have additionally contributed to the publication of interesting targets through this observation campaign, chiefly as a telescope observer, see Mamajek et al. (2018), González Egea et al. (2021) and Faherty et al. (2021). This chapter constitutes my ‘The *Gaia* Ultracool Dwarf Sample – IV. GTC/OSIRIS optical spectra of *Gaia* L dwarfs’ submitted paper where ‘we’ refers to myself, and the co-authors.

Abstract

As part of our comprehensive, ongoing characterisation of the low-mass end of the main sequence in the Solar neighbourhood, we used the OSIRIS instrument at the 10.4 m Gran Telescopio Canarias to acquire low- and mid-resolution optical spectroscopy of 53 late M and L ultracool dwarfs. Most of these objects are known but poorly investigated and lacking complete kinematics. We measured spectral indices, determined spectral types (6 of which are new) and

inferred effective temperature and surface gravity from BT-Settl synthetic spectra fits for all objects. We were able to measure radial velocities via line centre fitting and cross correlation for 46 objects, 29 of which lacked previous radial velocity measurements. Using these radial velocities in combination with the latest *Gaia* DR3 data, we also calculated Galactocentric space velocities.

From their kinematics, we identified two candidates outside of the thin disc and four in young stellar kinematic groups. Three ultracool dwarfs are potential young moving group candidates with low surface gravity spectral features. Two further ultracool dwarfs are apparently young field objects: 2MASSW J1246467+402715 (L4 β), which has a potential, weak lithium absorption line, and G 196–3B (L3 γ), which was already known as young due to its well-studied primary companion.

2.1 Introduction

The majority of known UCDs are within the Solar neighbourhood (e.g. Smart et al., 2019; Kirkpatrick et al., 2021; Sarro et al., 2023) with typically dim apparent optical magnitudes (*Gaia* $G \gtrsim 17$ mag). The closest stars to the Sun have been catalogued throughout the history of astronomy. For example, the Catalogue of Nearby Stars (CNS) from Gliese (1957) has been updated with every all-sky photometric and astrometric survey, including the most recent release using *Gaia* DR3 data (CNS5, Golovin et al., 2023). This Solar neighbourhood has been further described in the ‘The Solar Neighborhood’ series by the Research Consortium on Nearby Stars (RECONS) team with publications from Henry et al. (1994) to Vrijmoet et al. (2022). Specifically, M dwarfs within 30 pc were covered in another series of articles from Delfosse et al. (1999) to Crifo et al. (2005). Volume limited samples such as the recent *Gaia* Collaboration et al. (100 pc, 2021f), Kirkpatrick et al. (20 pc, 2021) and Reyl   et al. (10 pc, 2021) works provide important constraints on the initial mass function (Salpeter, 1955; Scalo, 1986; Kroupa, 2001; Chabrier, 2003), which underpins all aspects of astrophysics from stars to galaxies to cosmology.

Several features of youth, e.g. a weak sodium doublet, $\lambda\lambda 8183,8195$   (Schiavon et al., 1997a), are apparent in mid- to high-resolution optical spectra. Additionally, in the optical regime features such as the $\lambda 9850$ – 10200   FeH Wing-Ford band (Schiavon et al., 1997b) can be seen, which is a direct trace of low or high metallicity. Optical spectra have an advantage in that there

are fewer and weaker telluric absorption bands than in ground-based infrared spectra, where water bands can dominate (Reiners et al., 2007; Smette et al., 2015). However, only the closest and brightest UCDs can be observed with optical spectroscopy due to the low relative flux; further and fainter UCDs require large aperture telescopes and long exposure times.

The photometry of UCDs is important because the change in colour across the optical and NIR regime (Leggett et al., 2002) correlates with physical and atmospheric properties. These changing processes, such as dust, condensate cloud formation and subsequent clearing as an atmosphere cools, are well covered in the literature (e.g. Marley et al., 2002; Dahn et al., 2002; Saumon and Marley, 2008). Understanding a changing atmosphere for different ages with a range of masses has allowed the computing of ‘cooling tracks’ (Burrows et al., 1997; Baraffe et al., 2015). Accounting for theoretical atmospheric physics has been used in traditional model grids such as BT-Settl (Allard et al., 2011), or Sonora (Marley et al., 2021; Karalidi et al., 2021), and when interpreting the results of modern retrieval techniques (e.g. Burningham et al., 2017; Calamari et al., 2022). Having the ability to constrain mass and age whilst fitting observations to a selection of astrophysical parameters has underpinned modern observational low-mass astronomy. The metallicity and surface gravity of a subtype specific object are the major variables affecting the photometric colour (Stephens et al., 2009), see references to ‘blue’ and ‘red’ L dwarfs (Leggett, 1992; Faherty et al., 2009; Schmidt et al., 2010). Any works that infer spectral type, surface gravity and effective temperature must take into account the atmospheric physics, as these directly correlate with observable features.

Obtaining the full 6D (right ascension, declination, proper motions, parallax, radial velocity: $\alpha, \delta, \mu_\alpha \cos \delta, \mu_\delta, \varpi, v_r$) positional and kinematic information is fundamental to fully characterise the populations of UCDs within a volume limited sample (e.g. Best et al., 2021). Precise measurements of radial velocities (RVs) are obtained from high signal-to-noise observations taken with high resolution spectrographs with resolving powers of $R \sim 100\,000$, leading to uncertainties $\sim 1\text{--}5 \text{ m s}^{-1}$. This has only been achievable for the nearest, brightest UCDs (e.g. Zechmeister et al., 2019). Blake et al. (2010) achieved $\delta v_r \approx 50\text{--}200 \text{ m s}^{-1}$ with the Keck Near-Infrared Spectrometer (NIRSPEC), which has a resolution of $R \approx 25\,000\text{--}35\,000$ (post-upgrade). The ‘Brown Dwarf Kinematics Project’ has gathered further UCD RVs (Burgasser et al., 2015; Hsu et al., 2021) with both the NIRSPEC and the Magellan Echellette (MagE, $R \sim 4100$, $\delta v_r \approx 2\text{--}3 \text{ km s}^{-1}$) spectrographs. By comparison, low-resolution spectroscopy such as those discussed in this work is only capable of theoretical minimum uncertainties of $\gtrsim 5 \text{ km s}^{-1}$; this is still useful when constraining the kinematics of the Solar neighbourhood. Parallaxes and proper motions

of UCDs were historically gathered from ground based time-domain campaigns (e.g. PARSEC: Andrei et al., 2011; Marocco et al., 2013; Smart et al., 2018) that have been generally superseded by *Gaia* for the brightest objects, $G \lesssim 20$ mag. In the case of most late-L and T dwarfs, ground-based astrometry is still the predominant source (e.g. Vrba et al., 2004; Dupuy and Liu, 2012; Liu et al., 2016; Best et al., 2018). For even dimmer objects, beyond mid-T dwarfs, parallaxes and proper motions are gathered by space-based infrared surveys and are analysed in-depth by Kirkpatrick et al. (2021). Young moving groups are constrained using these complete kinematics. See the BANYAN Σ series and references therein for detail on nearby young moving groups and clusters (Gagné et al., 2014b, to Gagné and Faherty 2018) or similarly, the LACEwing code (Riedel et al., 2017), designed around young objects in the Solar neighbourhood. Subdwarfs, meanwhile, are characterised by their statistically higher space velocities indicative of the older population (e.g. Lodieu et al., 2005; Burgasser et al., 2007; Lodieu et al., 2017; Zhang et al., 2017b).

This is the fourth item in the *Gaia* Ultracool Dwarf Sample series (GUCDS, Smart et al., 2017, 2019; Marocco et al., 2020) and is an ongoing, international, multi-year programme aimed at characterising all of the UCDs visible to *Gaia*. *Gaia* DR3 produced astrophysical parameters for ≈ 470 million sources (Creevey et al., 2023), including effective temperatures, T_{eff} . The $\approx 94\,000$ *Gaia* DR3 T_{eff} values relating to UCDs by Creevey et al. (2023) were provided under the `teff_espucd` keyword. The full sample of UCDs detected by *Gaia* with *Gaia* DR3 T_{eff} values were documented and analysed by Sarro et al. (2023). In our analysis, we will use the values from these *Gaia* DR3 derivative works to compare with the equivalent values directly measured by us. There is significant overlap between the Sarro et al. (2023) sample and the GUCDS, although the majority of UCD sources as seen by *Gaia* are as yet not characterised through spectroscopic follow-up. A subset of this Sarro et al. (2023) sample has public *Gaia* RP spectra (see the *Gaia* `xp_summary` table), which covers the G_{RP} passband ($\Delta\lambda \approx 6200\text{--}10420\text{Å}$, Riello et al., 2021). The internally calibrated *Gaia* RP spectra and processing were discussed thoroughly by Carrasco et al. (2021), De Angeli et al. (2023) and Montegriffo et al. (2023).

The aim of this work is to complement the literature population with measurements and inferences from low- and mid-resolution optical spectroscopy. In Section §2.2 we explain the target selection (§2.2.1), observation strategy (§2.2.2) and different reduction techniques with a test case (§2.2.3). Section §2.3 explains our techniques for determining spectral types (§2.3.1), astrophysical parameters (§2.3.2), and kinematics (§2.3.3) including membership in moving groups (§2.3.4). Section §2.4 follows a discussion of our results for spectral types (§2.4.1),

kinematics (§2.4.2) and astrophysical parameters (§2.4.3). We also discuss individual objects (§2.4.3.1) before summarising the overall conclusions in Section §2.5.

2.2 Methodology

We obtained optical spectroscopy of 53 unique UCDs using the OSIRIS (Optical System for Imaging and low-intermediate Resolution Integrated Spectroscopy – Cepa, 1998) instrument on the 10.4 m Gran Telescopio Canarias (GTC) at El Roque de los Muchachos in the island of La Palma, Spain, under proposal IDs GTC54-15A and GTC8-15ITP (PIs Caballero and Marocco, respectively). The objects were observed in semesters 2015A, 2015B and 2016A. We aimed to determine spectral types, spectral indices and radial velocities from directly measuring the GTC spectra. Furthermore, we inferred astrophysical parameters (effective temperature, T_{eff} [K]; surface gravity, $\log g$ [dex]; and metallicity, [Fe/H] [dex]) from comparisons with atmospheric models.

The observed data from the GTC were complemented with *Gaia* DR3. *Gaia* also carries a radial velocity spectrometer, although this was unsuitable for our purposes as all of our targets were fainter than the *Gaia* selection limit (Katz et al., 2023, $G < 14$ mag,).

We acquired 63 spectra in which we observed 53 unique objects, shown in Table 2.1. These 63 observations are shown in Table A.1, including the air mass and humidity of the observation. Of the 63 spectra, 46 were observed with the R2500I volume phased holographic grating (hereafter VPHG), whilst 17 were observed with the R300R grism. Ten of the 53 objects were observed with both dispersive elements.

Twenty of the 53 objects already had full 6D positional and kinematic information in the literature. Fifty-one had proper motions, 43 had parallaxes, and two had only α and δ . All values along with their provenance are given in Table 2.1. In the next sub-sections we discuss the target list selection, observation and reduction procedures.

2.2.1 Target selection

Our targets were drawn from a combination of two samples: benchmark systems (system with a star and a UCD, Pinfield et al., 2006) and known L dwarfs with poor or no available spectroscopy. The targets were selected by Marocco et al. (2017) and Marocco et al. (2020), and

TABLE 2.1: The 53 targets observed at the GTC with OSIRIS and presented in this work.

Object short name	Gaia DR3 source ID	α [hms]	δ [dms]	ϖ [mas]	G [mag]	J [mag]	Grism/VPHG
J0028–1927	2363496283669200768	0 28 55.6	-19 27 16	25.742	18.97	14.19	R2500I
J0235–0849	5176990610359832576	2 35 47.5	-8 49 20	21.742	20.35	15.57	R2500I
J0428–2253	4898159654173165824	4 28 51.1	-22 53 20	39.398	18.72	13.51	R2500I
J0453–1751	297956628523332608	4 53 26.5	-17 51 55	33.064	20.14	15.14	R2500I
J0502+1442	3392546632197477248	5 02 13.5	+14 42 36	21.746	18.90	14.27	R2500I
J0605–2342	2913249451860183168	6 05 01.9	-23 42 25	30.185	19.31	14.51	R2500I
J0741+2316	867083081644418688	7 41 04.4	+23 16 38	13.019	20.83	16.16	R2500I
J0752+4136	920980385721808128	7 52 59.4	+41 36 47	11.734	17.71	14.00	R2500I
J0809+2315	...	8 09 10.7 ¹	+23 15 16 ¹	16.72	R2500I
J0823+0240	3090298891542276352	8 23 03.1	+2 40 43	...	21.18	16.06	R2500I
J0823+6125	1089980859123284864	8 23 07.3	+61 25 17	39.467	19.66	14.82	R2500I
J0847–1532	5733429157137237760	8 47 28.9	-15 32 41	57.511	18.38	13.51	R300R
J0918+2134	...	9 18 38.2 ²	+21 34 06 ²	15.66	R2500I
J0935–2934	5632725432610141568	9 35 28.0	-29 34 58	29.969	19.00	14.04	R2500I
J0938+0443	3851468354540078208	9 38 58.9	+4 43 43	15.448	19.89	15.24	R2500I
J0940+2946	696581955256736896	9 40 47.7	+29 46 52	17.961	20.30	15.29	R2500I
J0953–1014	3769934860057100672	9 53 21.2	-10 14 22	28.022	18.44	13.47	R2500I
J1004+5022	824017070904063488	10 04 20.4	+50 22 56	46.195	20.13	14.83	R300R & R2500I
J1004–1318	3765325471089276288	10 04 40.2	-13 18 22	40.438	19.84	14.68	R2500I
J1047–1815	3555963059703156224	10 47 30.7	-18 15 57	35.589	19.01	14.20	R300R & R2500I
J1058–1548	3562717226488303360	10 58 47.5	-15 48 17	55.098	19.24	14.16	R300R & R2500I
J1109–1606	3559504797109475328	11 09 26.9	-16 06 56	24.161	19.65	14.97	R2500I
J1127+4705	785733068161334656	11 27 06.5	+47 05 48	23.758	19.94	15.20	R2500I
J1213–0432	3597096309389074816	12 13 02.9	-4 32 44	59.095	19.86	14.68	R2500I
J1216+4927	1547294197819487744	12 16 45.5	+49 27 45	...	20.92	15.59	R2500I
J1221+0257	3701479918946381184	12 21 27.6	+2 57 19	53.812	17.86	13.17	R2500I
J1222+1407	...	12 22 59.3 ³	+14 07 50 ³	R300R
J1232–0951	3579412039247581824	12 32 18.1	-9 51 52	34.5 ⁴	18.74	13.73	R2500I
J1246+4027	1521895105554830720	12 46 47.0	+40 27 13	44.738	20.28	15.09	R300R & R2500I
J1331+3407	1470080890679613696	13 31 32.6	+34 07 55	34.791	19.01	14.33	R300R & R2500I
J1333–0215	3637567472687103616	13 33 45.1	-2 16 02	26.599	20.10	15.38	R2500I
J1346+0842	3725064104059179904	13 46 07.2	+8 42 33	23.339	20.47	15.74	R2500I
J1412+1633	1233008320961367296	14 12 24.5	+16 33 10	31.278	18.67	13.89	R300R & R2500I
J1421+1827	1239625559894563968	14 21 30.6	+18 27 38	52.862	17.84	13.23	R2500I
J1439+0039	...	14 39 15.1 ¹	+0 39 42 ¹	18.00	R300R
J1441–0945	6326753222355787648	14 41 36.9	-9 46 00	32.505	19.22	14.02	R300R & R2500I
J1527+0553	...	15 27 22.5 ¹	+5 53 16 ¹	17.63	R300R
J1532+2611	1222514886931289088	15 32 23.3	+26 11 19	...	21.08	16.12	R2500I
J1539–0520	4400638923299410048	15 39 42.6	-5 20 41	59.266	18.98	13.92	R2500I
J1548–1636	6260966349293260928	15 48 58.1	-16 36 04	37.535	18.54	13.89	R2500I
J1617+7733B	1704566318127301120	16 17 06.5	+77 34 03	13.705	16.55	13.10	R300R & R2500I
J1618–1321	4329787042547326592	16 18 44.9	-13 21 31	21.86 ⁵	19.34	14.25	R2500I
J1623+1530	4464934407627884800	16 23 21.8	+15 30 39	10.301	20.59	15.94	R2500I
J1623+2908	...	16 23 07.4 ²	+29 08 28 ²	16.08	R2500I
J1705–0516	4364462551205872000	17 05 48.5	-5 16 48	53.122	18.19	13.31	R300R
J1707–0138	4367890618008483968	17 07 25.3	-1 38 10	25.976	19.25	14.29	R300R & R2500I
J1717+6526	1633752714121739264	17 17 14.5	+65 26 20	45.743	20.26	14.95	R300R & R2500I
J1724+2336	4569300467950928768	17 24 37.4	+23 36 50	14.625	20.19	15.68	R300R
J1733–1654	4124397553254685440	17 33 42.4	-16 54 51	54.935	18.50	13.53	R300R
J1745–1640	4123874907297370240	17 45 34.8	-16 40 56	50.918	18.44	13.65	R2500I
J1750–0016	4371611781971027268	17 50 24.4	-0 16 12	108.581	18.29	13.29	R2500I
J2155+2345	1795137592033253888	21 55 58.6	+23 45 30	...	20.93	15.99	R2500I
J2339+3507	2873220249284763392	23 39 25.5	+35 07 16	36.230	20.46	15.36	R2500I

References – Positions all at 2016.5 except at the indicated epochs: 1. Lawrence et al. (2007) – 2008, 2. Skrutskie et al. (2006) – 1998–2000, 3. Chambers et al. (2016) – 2012–2013, 4. Best et al. (2020) – 2014–2018, 5. Weinberger et al. (2016) – 2007–2013.

here we briefly summarise their selection criteria. Both samples were chosen with the aim of gathering low- and mid-resolution spectra, mostly to achieve radial velocities and to confirm their status as L dwarfs. Benchmark system selection used the procedure of Marocco et al. (2017, their section 4). To summarise, primary systems consisting of possibly metal-rich or metal-poor stars were selected with metallicity cuts of $[\text{Fe}/\text{H}] < -0.3$ and $[\text{Fe}/\text{H}] > 0.2$ dex from a number of catalogues (Marocco et al., 2017, their table 2). If more than one value of $[\text{Fe}/\text{H}]$ was available, the one with the smallest uncertainty was used; Marocco et al. (2017) did not investigate if there were any systematic offsets between different catalogues, as this was beyond the scope of that work. The companions to these systems were filtered by a series of colour, absolute magnitude and photometric quality cuts from 2MASS, SDSS (the Sloan Digital

Sky Survey, York et al., 2000) and ULAS (United Kingdom Infrared Telescope Deep Sky Survey, Large Area Survey, Lawrence et al., 2007) photometry in equation (2.1). These colour cuts in equation (2.1) are taken directly from Marocco et al. (2017) as that work created part of the target list used in this work. Magnitudes from 2MASS were converted into UKIRT/WFCAM magnitudes via the equations of Stephens and Leggett (2004).

$$\begin{aligned}
 Y - J &> 0.85; \\
 J - H &> 0.50; \\
 z - J &> 2.1; \\
 \sigma_J &< 0.1; \\
 [2.5 \times (z - J) + 4] &< M_J < [5 \times (z - J) + 1]; \\
 M_J &> 11.5; \\
 1.6 &< i - z < 6.0; \\
 11.5 &< M_z < [3.5714 \times (i - z) + 9.286]; \\
 M_z &\geq 15; \\
 M_z &\geq [3.5714 \times (i - z) + 6.5]; \\
 i - z &\leq 2.1.
 \end{aligned} \tag{2.1}$$

These companions were determined as being candidate benchmark systems with a maximum matching radius of 3 arcmin, i.e. the maximum separation to the primary object. The remaining targets, known L dwarfs, were already spectroscopically confirmed bright L dwarfs that were predicted to be visible to the astrometry and photometry in (at the time, upcoming) *Gaia* data releases. These known L dwarfs should be single systems. They would, however, not be bright enough for the *Gaia* radial velocity spectrometer (Katz et al., 2023), and thus were chosen to determine radial velocities for, as a complement to the 30 pc volume-limited sample. This list was complemented with additional targets too dim for *Gaia* photometry and astrometry, which were detected in UKIDSS, and by a few well-known L dwarfs, such as G 196–3B, which could serve as template standards.

2.2.1.1 Cross-matching

All observed targets (Table 2.1) were cross-matched with *Gaia*, Pan-STARRS, 2MASS, and ALLWISE. These surveys were chosen because they are all-sky and we were aiming for completeness in this process. This sample of 53 objects was then also cross-matched against the astrophysical parameter and `xp_summary` tables from *Gaia* DR3¹. Thirty-eight of these objects had a `teff_espuccd` value, and 28 had a public RP spectrum. Internally calibrated *Gaia* RP spectra were then extracted from the *Gaia* archive with a linearly dispersed grid from 6000 Å to 10500 Å using the `gaiaxy.convert` (Ruz-Mieres, 2022) and `gaiaxy-batch` (Cooper, 2022a) codes. We also searched for common proper motion systems within Simbad (Wenger et al., 2000) with the selection criteria given in the GUCDS, specifically equation (1) of Marocco et al. (2020):

$$\rho < 100\varpi; \tag{2.2}$$

$$\Delta\varpi < \max[3\sigma_\varpi, 1];$$

$$\Delta\mu < 0.1\mu;$$

$$\Delta\theta < 15 \text{ deg}.$$

In equation (2.2), ρ is the separation in arcseconds, θ is the proper motion position angle in degrees, whilst ϖ (milli-arcseconds) and μ (milli-arcseconds per year) are our target list's *Gaia* DR3 parallax and proper motion, respectively. Like with the photometric selection, equation (2.1), the common proper motion selection was taken directly from Marocco et al. (2020). This is because the target list in this work is drawn from the same wider target list used in the GUCDS. In effect, this selection is creating a widest possible physical separation of 100 000 AU (see the discussion on binding energies by Caballero, 2009).

2.2.2 Observations

The OSIRIS instrument used a 2×1 mosaic of 2048×4096 pixel (photosensitive area) red-optimised CCDs (Marconi MAT-44-82 type) with a 7.8×7.8 arcmin² unvignetted field of view. We used the standard operational mode of 2×2 binning, which has a physical pixel size of

¹These tables are logically distinct from the main *Gaia* table in terms of schema and completeness.

0.254 arcsec pixel⁻¹. For our purposes, we used the 7.4 arcmin long slit with a width of 1.2 arcsec. We had variable seeing between 0.6 and 2.5 arcsec, with the vast majority having seeing < 1.2–1.5. We used the R300R and R2500I grisms and purely read off CCD 2 due to the instrument calibration module having a strong gradient from CCD 1 to 2 in the flat fields. The R300R grism has a wavelength range of $\approx 4800\text{--}10000\text{ \AA}$ with a dispersion of $\approx 7.74\text{ \AA pix}^{-1}$ for a resolution of ≈ 350 whilst the R2500I VPHG has a wavelength range of $\approx 7330\text{--}10000\text{ \AA}$ with a dispersion of $\approx 1.36\text{ \AA pix}^{-1}$ for a resolution of ≈ 2500 , as per the online documentation. Both dispersive elements experience an increase in fringing at wavelengths $\gtrsim 9200\text{ \AA}$ to ≥ 5 per cent. The R300R grism however, had second order light from 4800 to 4900 \AA contaminating the 9600 to 9800 \AA region. This is because standards, but not UCDs, have flux in the blue regime, hence affecting the flux calibration in the red regime. As a result, the R300R spectra were conservatively truncated to 9000 \AA . Our standards were a selection of white dwarfs plus two well-studied bright main sequence dwarf stars, all with literature flux calibrated spectra and spectral types: Ross 640 (DZA6, Oke, 1974; McCleery et al., 2020); Hilt 600 (B1, Hamuy et al., 1992, 1994); GD 153 (DA1, Bohlin et al., 1995, 2014); G191-B2B (DA1, Oke, 1990; Bohlin et al., 1995, 2014); GD 248 (DC5, Tremblay et al., 2011; McCleery et al., 2020), GD 140 (DA2, Tremblay et al., 2011; McCleery et al., 2020) and G 158-100 (dG-K, Oke, 1990). We took a series of short exposures for the brightest objects to avoid saturation and non-linearity. The majority of observations had a bright moon whilst the sky condition varied from photometric to clear with humidity typically $\lesssim 50$ per cent. All calibration frames were taken at the start and end of each night, the arc lamps being used were: Hg-Ar, Ne and Xe. The full observing log is given in Table A.1.

2.2.3 Reduction

Our adopted PypeIt (Prochaska et al., 2020) reduction procedure applied to every object was as follows: master calibration files were created by median stacking the relevant flat, bias and arc frames. Basic image processing was performed including bias subtraction, flat fielding, spatial flexure correction and cosmic ray masking via the L.A. Cosmic Rejection algorithm (van Dokkum, 2001). We then manually identified the arc lines using the median stacked master arc. These arc lines were used to manually create a wavelength solution through `pypeit.identify` with an $\text{RMS} = 0.0804 \pm 0.0005\text{ \AA}$ for the R2500I VPHG and $\text{RMS} = 0.1394 \pm 0.0000\text{ \AA}$ for the R300R grism. Note here that the lower standard deviation of RMS values for the R300R grism are due to it being a lower polynomial order (3) than the R2500I VPHG (6), over a much

wider wavelength range. The information inside the object headers (observation date, object sky position, longitude and latitude of the observatory) was used to heliocentric correct the wavelength solution. The `PypeIt` wavelength solution was defined in vacuum.

The standard frames were median stacked before the global sky was subtracted and corrected for spectral flexure. Both the stacked standard and object were then extracted using both box-car (5 pixel) and optimal (Horne, 1986) extraction methods, with the latter being the presented spectra.

We then fitted a function to account for the sensitivity, CCD quantum efficiency and zeropoint. The telluric regions listed by Reiners et al. (2007) and Smette et al. (2015) were masked out. We divided each standard by its corresponding flux calibrated spectrum from the literature, as listed above. This sensitivity function was then applied to the reduced standard and object to flux calibrate the extracted spectra. If an observation had more than one science frame, those were co-added after wavelength and flux calibration.

The standards observed under the R2500I VPHG were used to create a telluric model from a high resolution atmospheric grid derived at Las Campanas. This telluric model was applied back to the flux calibrated standard and object. The configuration files used in our reduction procedure are given in Appendix A.0.5. A comparison between this reduction, and that which used standard IRAF routines, is shown in the normalised spectra of J1745–1640 in Figure 2.1. The full, bespoke IRAF reduction is described in Appendix A.0.2.1.

We show good agreement in the flux profile up to $\sim 8900 \text{ \AA}$. The IRAF reduced spectra is brighter in the broad H_2O region (the MagE spectrum is not telluric corrected), due to the differing telluric correction methods. This difference does not affect the model fitting of the spectra, as this is done in localised, small, chunks. All spectra then agree at wavelengths $\gtrsim 9800 \text{ \AA}$.

2.3 Analysis

Here, we discuss the analysis of the reduced spectra, in order to produce spectral types, astrophysical parameters and kinematics. We discuss our measurements of astrophysical parameters first because the cross-correlation technique used to measure RV requires the use of a best-fitting model derived template, obtained from the best fit of astrophysical parameters. The code used for both estimating astrophysical parameters and calculating RV is `rvfitter` (Cooper, 2022b).

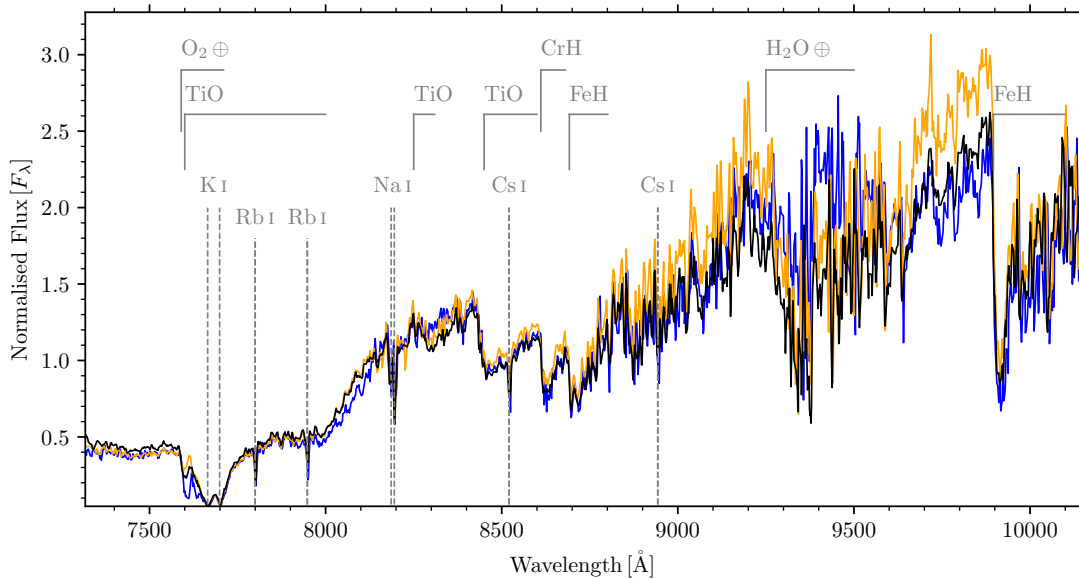


FIGURE 2.1: R2500I spectra for J1745–1640, normalised at 8100–8200 Å, comparing two independent reduction procedures: PypeIt in black and IRAF in orange. In blue, the heliocentric corrected MagE spectra (Burgasser et al., 2015) for the same object is shown (which is not telluric corrected).

This program was developed to effectively recreate in python older codes (e.g. `IRAF.Fxcorr`, `IRAF.Splot`, `IDL.gaussfit`) designed for allowing a user to manually cross-correlate spectra and fit line centres with different profiles. All wavelengths discussed in this Section are in standard air, hence we converted our PypeIt spectra from vacuum to air. This was performed via the `specutils` package, using the corrections by Edlen (1953).

2.3.1 Spectral typing

We spectral typed both the R300R and R2500I spectra using the `classifyTemplate` method of the `kastredux` (Burgasser, 2021) package. This compared each spectrum against SDSS standards (Bochanski et al., 2007; Schmidt et al., 2010; Kesseli et al., 2017), from M0–T0, and selected the spectral type with the minimum difference in scaled fluxes (ΔF : equations (2.3 - 2.4)) with equally weighted (W) points.

$$\Delta F = \sum \frac{W(F_{\text{object}} - KF_{\text{standard}})^2}{\sigma_{\text{object}}^2} \quad (2.3)$$

$$K = \sum \frac{WF_{\text{object}}F_{\text{standard}}}{\sigma_{\text{object}}^2} \bigg/ \sum \frac{WF_{\text{standard}}F_{\text{standard}}}{\sigma_{\text{object}}^2} \quad (2.4)$$

The spectra had all been smoothed in wavelength with a Gaussian 5σ kernel, and we only compared the regions from 8000 to 8500 Å for R2500I and 7000 to 8000 Å for R300R. This was decided through experimentation, which deliberately excluded regions with telluric features, as those features can cause poorer solutions. Each object was also visually checked against known standards (Kirkpatrick et al., 1999), the spectral sub-types by which we refer to as ‘by eye’. Any spectra with indicators of youth are given optical gravity classes as defined by Cruz et al. (2009), from β, γ, δ in order of decreasing surface gravity. The `kastredux` spectral types were our adopted spectral types.

2.3.1.1 GTC spectral sequence

The 46 spectra from the R2500I VPHG, ordered by our adopted spectral type, are shown in Figures 2.2 and 2.3. All spectra are heliocentric corrected, such that the relative motion of the Earth has been removed. Each spectrum shown had an outlier masking routine applied such that points within a rolling ≈ 15 Å (ten data points) chunk are removed if they had a difference greater than the standard deviation from the median. Additionally, some objects had problematic O₂ A-band tellurics. In those cases, we interpolated over the region 7540–7630 Å from the maximum of the first ≈ 7.5 Å to minimum of the last ≈ 7.5 Å. Where appropriate, spectra were co-added. All spectra appear noisy in the primary H₂O band of ≈ 9200 – 9600 Å. The 17 heliocentric corrected, reduced spectra from the R300R grism are shown in Figure 2.4. The R300R spectra were trimmed from $6500 < \lambda < 9000$ Å due to (a) the lack of signal in the blue regime and (b) to constrain to purely the first order light. Unlike the R2500I spectra, the R300R spectra were not telluric corrected.

2.3.2 Fundamental astrophysical parameters

We used the `rvfitter.crosscorrelate` code on our R300R and R2500I spectra with BT-Settl CIFIST model grids from $1200 \leq T_{\text{eff}} \leq 4000$ K and $4.5 \leq \log g \leq 5.5$ dex (Allard et al., 2011). These models assume a solar metallicity with no variation and are linearly dispersed in steps of 100 K and 0.5 dex. This code allowed us to visually select the best fitting model from the array of model grids and for each spectral line from Table 2.2.

We used these chosen lines rather than correlating against the entire model because the models do not exactly match the flux profile of ground based spectra. For efficiency purposes, each

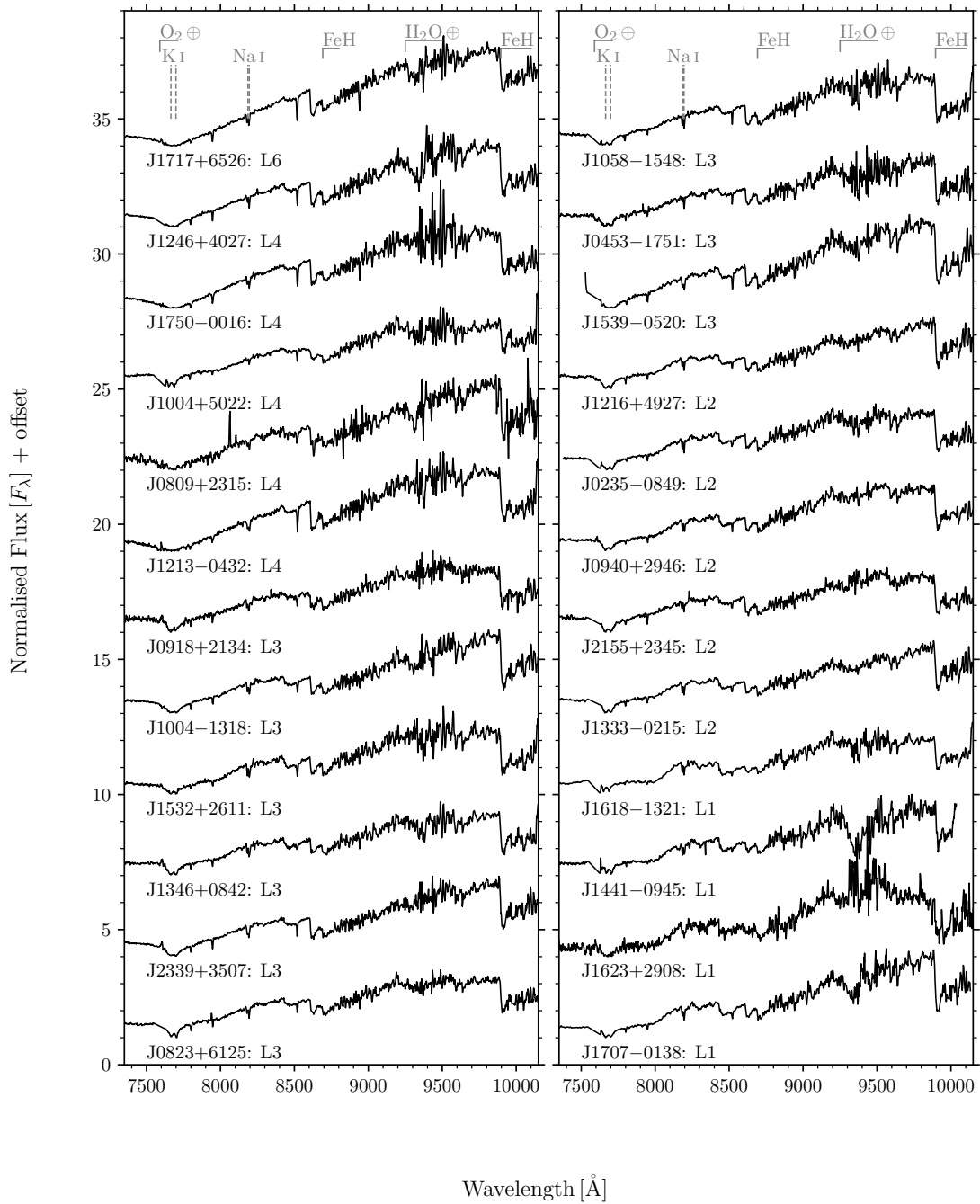


FIGURE 2.2: The first 24 of the R2500I VPHG spectra with a linear offset applied, sorted by spectral sub-type. We show the short names and the spectral sub-types from this work, attached to each spectrum. At the top of the figure are grey lines denoting a selection of spectral features typical to L dwarfs, plus the two main telluric bands.

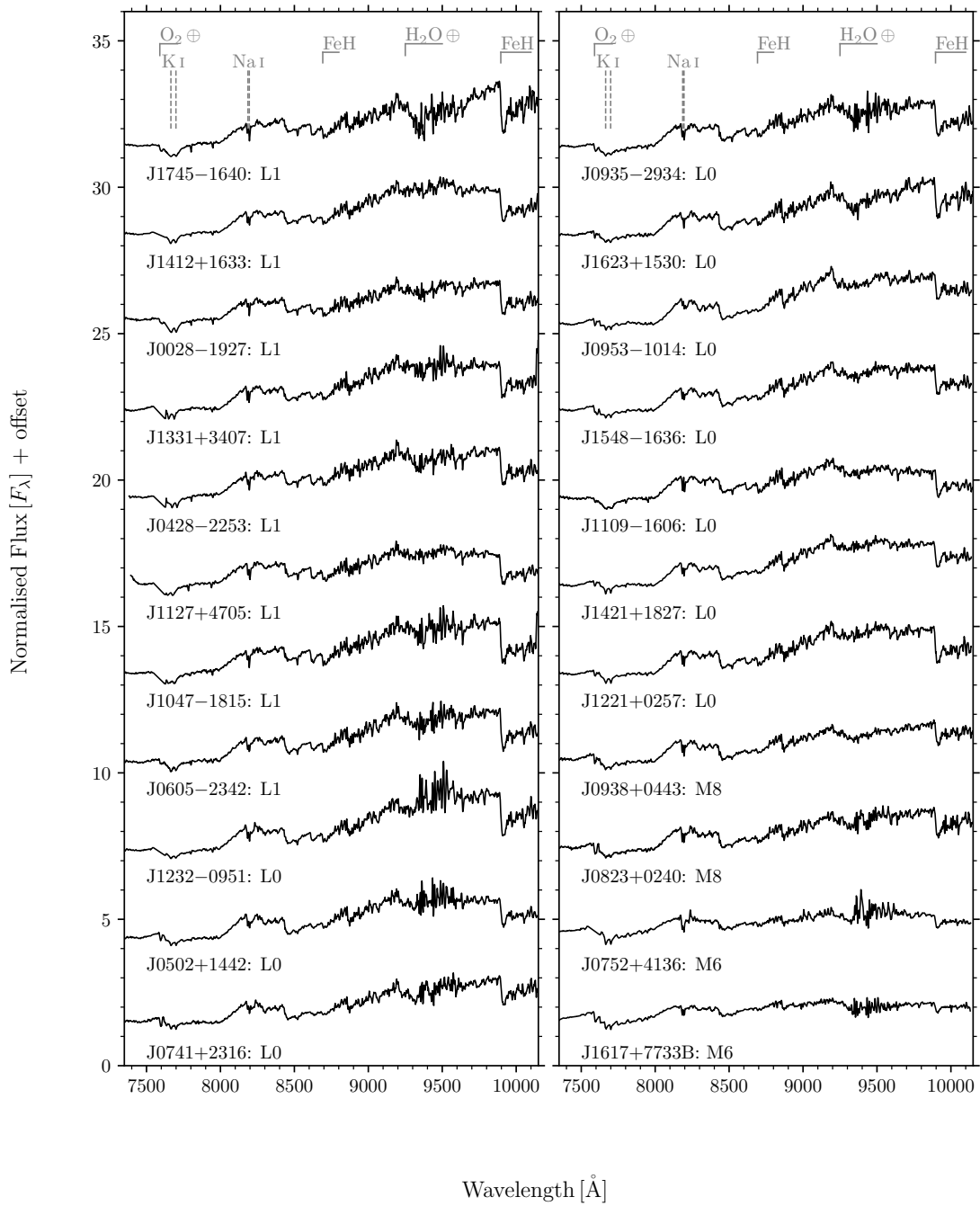


FIGURE 2.3: Same as Figure 2.2 but for the second half of the R2500I VPHG sample.

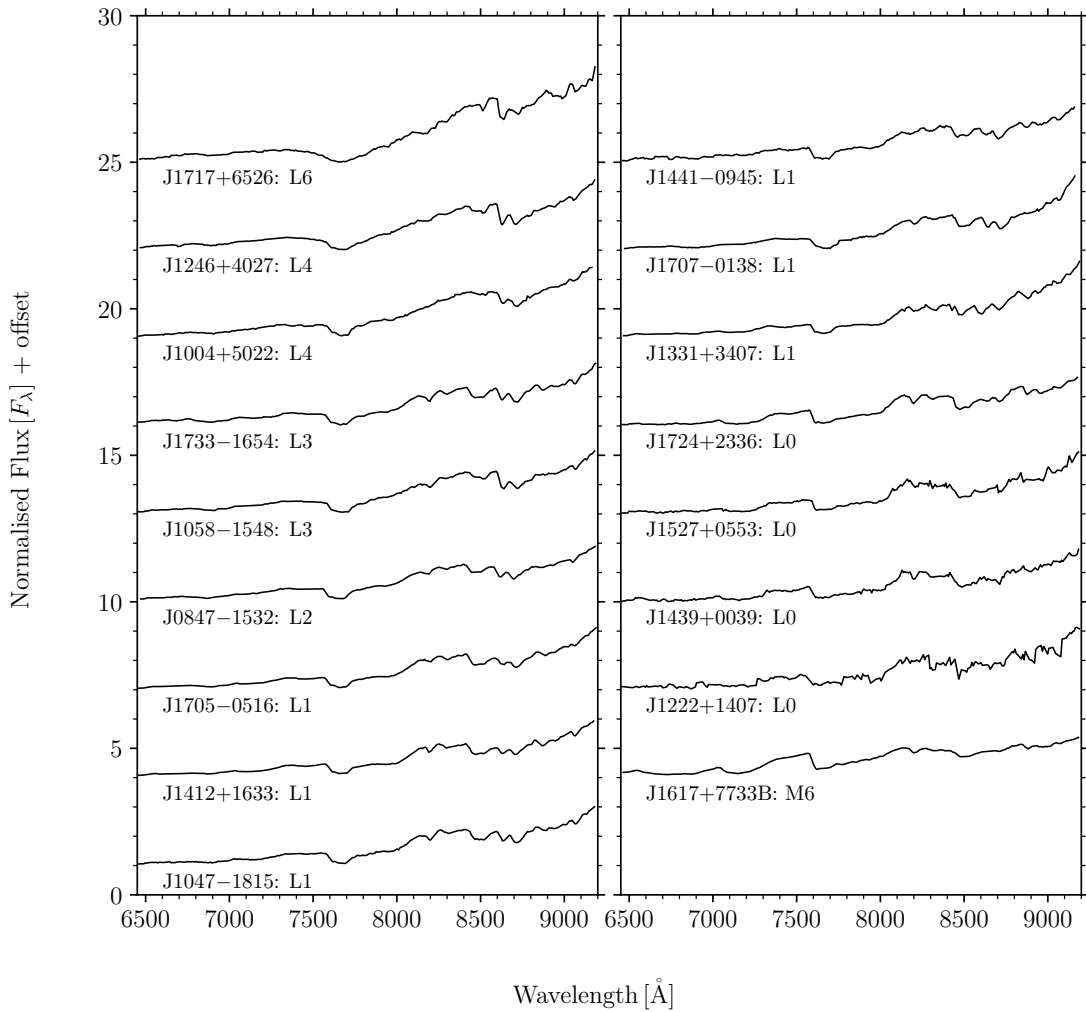


FIGURE 2.4: Same as Figure 2.2 but for the R300R grism spectra.

Line	λ [Å]
K I-a	7664.8991
K I-b	7698.9646
Rb I-a	7800.268
Rb I-b	7947.603
Na I-a	8183.2556
Na I-b	8194.824
Cs I-a	8521.13165
Cs I-b	8943.47424

TABLE 2.2: The list of atomic alkali metal lines used when estimating astrophysical parameters and calculating radial velocities. Wavelengths are as measured by Kramida et al. (2021) and are defined in standard air.

model when being loaded into the code, was interpolated onto the wavelength array of the object being compared against. The models could optionally be Gaussian smoothed, which was helpful for fitting any ‘messy’ models (e.g. $\gtrsim 2000$ K). We normalised the model and data by their respective medians in a given variably sized ‘chunk’ around each spectral line. We noted that around certain lines, particular models appeared almost identical to each other, e.g. around 7000–8000 Å, the 1900 and 2000 K models are not visually distinct. This means there is a higher uncertainty for effective temperatures within the 1900–2000 K region. Not every spectral line was used for each object as some have poorly resolved features or low signal-to-noise. Our selected T_{eff} was the mean T_{eff} from each line measurement, as was $\log g$. To determine the error on each T_{eff} and $\log g$ final value, we chose to use the standard deviation from each independent line fit divided by the square root of the number of lines used. This error was added in quadrature with half of the separation between each grid, i.e. 50 K for T_{eff} and 0.25 dex for $\log g$.

Additionally, we created an ‘expected’ effective temperature, \widehat{T}_{eff} , using the Filippazzo, sixth order field T_{eff} relation (Filippazzo et al., 2015) and our adopted spectral types. The errors on \widehat{T}_{eff} correspond with the mean difference in T_{eff} across ± 0.5 spectral sub-types (our spectral sub-type uncertainty).

2.3.3 Calculating the radial velocities

Only our R2500I spectra were used to determine RVs as the features in R300R spectra are mostly blended/unresolved. We used two methods by which to measure an adopted RV: line centre fitting and cross correlation. We note that our seeing (Table A.1, corrected for airmass) was almost always smaller than the slit width, which affects the RV offset as the slit is not fully illuminated. The full width at half-maximum was typically 3–4 pixels, corresponding to ≈ 0.75 –1 arcseconds. Most observations were seeing-limited, whilst a few, taken in poorer conditions, were slit-limited. The following methods were performed only on heliocentric corrected spectra, hence any quoted RV values are heliocentric corrected.

2.3.3.1 Line centre fitting

Using the same atomic absorption lines listed in Table 2.2, we applied the `rvfitter.linecentering` code to interactively fit Gaussian, Lorentzian and Voigt profiles with the minimum possible width. This minimum possible width is equal to the number of free

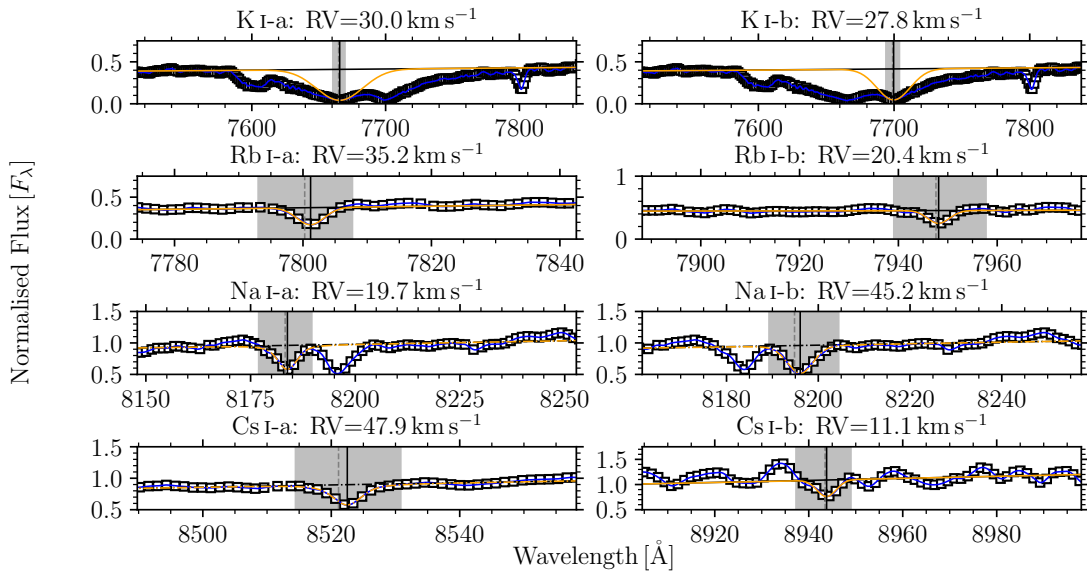


FIGURE 2.5: J1745–1640 RV calculation via different line profiles (orange: solid – Gaussian; dash-dot – Voigt) against the data (black squares) and fifth order spline fit (blue) in the regime around the eight listed line centres. The shift from the laboratory line position (vertical dashed grey line) is shown as the vertical solid black line. The horizontal black line (solid or dash-dot, depending on the fitted line profile as above) is the continuum, as is subtracted from the data. A grey band is given, corresponding to the region of data the line profiles are fitted to. The shown region is between the inner edges of the continuum regions.

parameters plus one (although this does not guarantee a successful fit). We used these different profiles to obtain the best fit for a particular line given its underlying absorption characteristics and the available signal-to-noise of the spectral region. The fitting technique used was least-mean-square minimisation. For each spectral line, we subtracted a linear continuum from the data. The continuum corresponds to the medians of selected regions to the blueward and redward sides of the spectral line. Each continuum region is chosen to follow the shape of the spectra with a minimum width of $\approx 50 \text{ \AA}$ within $100\text{--}200 \text{ \AA}$ of the spectral line. Also shown during the fitting routine is a fifth order spline, as a visual aid; the minima of the spline does not necessarily correspond to the line position. An example of this routine is given for J1745–1640 in Figure 2.5. The fits were only accepted if they appeared to accurately represent the spectral lines profile upon visual inspection. The uncertainty for each line, was the value in the diagonal of the covariance matrix corresponding to centroid position from the least-squares fit, plus the wavelength calibration RMS for that object, Doppler shifted into RV space.

After measuring every line, we then calculated the overall mean (μ_{LC}) and standard deviation (σ_{LC}). The uncertainty from the vacuum to air conversion was negligible ($\ll 0.1 \text{ km s}^{-1}$) compared to the fitting uncertainties calculated from the eight (or less, if rejected) aforementioned lines. We use the standard deviation of the mean for the uncertainty in the final line centre

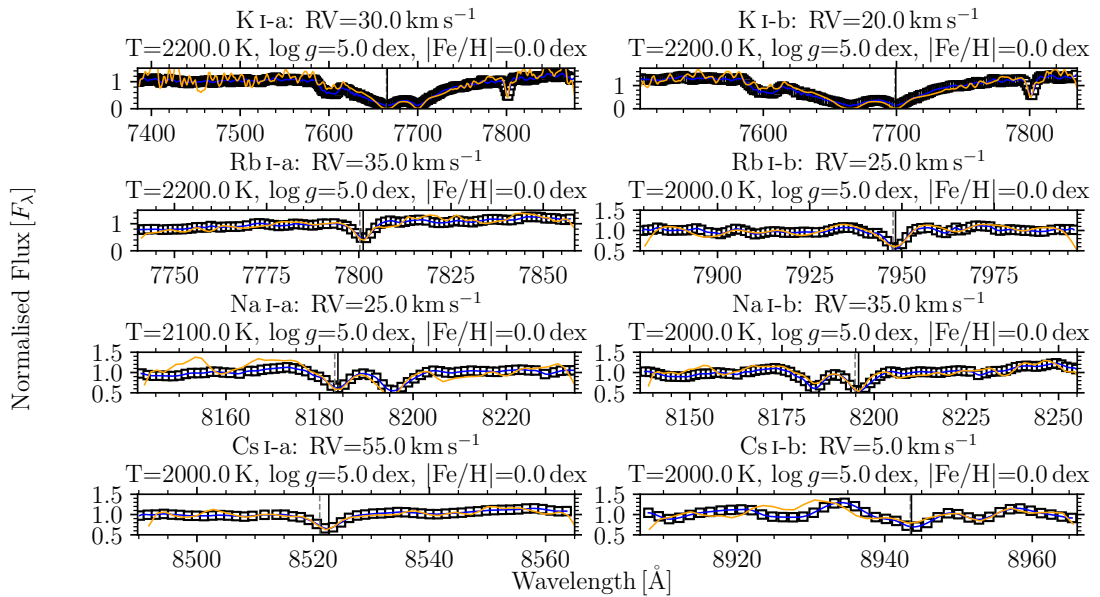


FIGURE 2.6: J1745–1640 RV calculation via the manually shifted BT-Settl model (orange) against the data (black squares) and fifth order spline fit (blue). The laboratory line position (vertical dashed grey line) has been manually shifted by the RV given on the sub-plot title (vertical solid black line). Effective temperature, gravity and metallicity are also indicated on each features title.

derived RVs, by dividing the standard deviation by the square root of the number of lines successfully fit.

2.3.3.2 Cross-correlation

In addition to estimating the astrophysical parameters with `rvfitter.crosscorrelate` in Section §2.3.2, we also used the same package to measure RV by manually shifting the best fitting BT-Settl model as a template. No smoothing was applied to the model template to match the spectral resolution of the object spectrum. Likewise, there was no continuum subtraction applied to the object spectrum. The RV shift was in steps of 5, 10, 100 km s^{-1} , which in turn defined the RV uncertainty on each line (2.5, 5, 50 km s^{-1} , i.e. the margin of error). These RV errors are added to the wavelength calibration RMS for the given object (Doppler shifted into an RV error). Not all atomic lines were always used, only in the cases where the model appeared to closely match the apparent line profile. The typical technique was to select a broad region ($\Delta\lambda = 100\text{--}200 \text{ \AA}$) around each spectral line, find the best fitting template in terms of T_{eff} and $\log g$, then narrow that region ($\Delta\lambda \approx 50 \text{ \AA}$) to then find an RV. We also show a fifth order spline, as with the line centering method, as a visual aid. This initial broad region is shown for J1745–1640 in Figure 2.6.

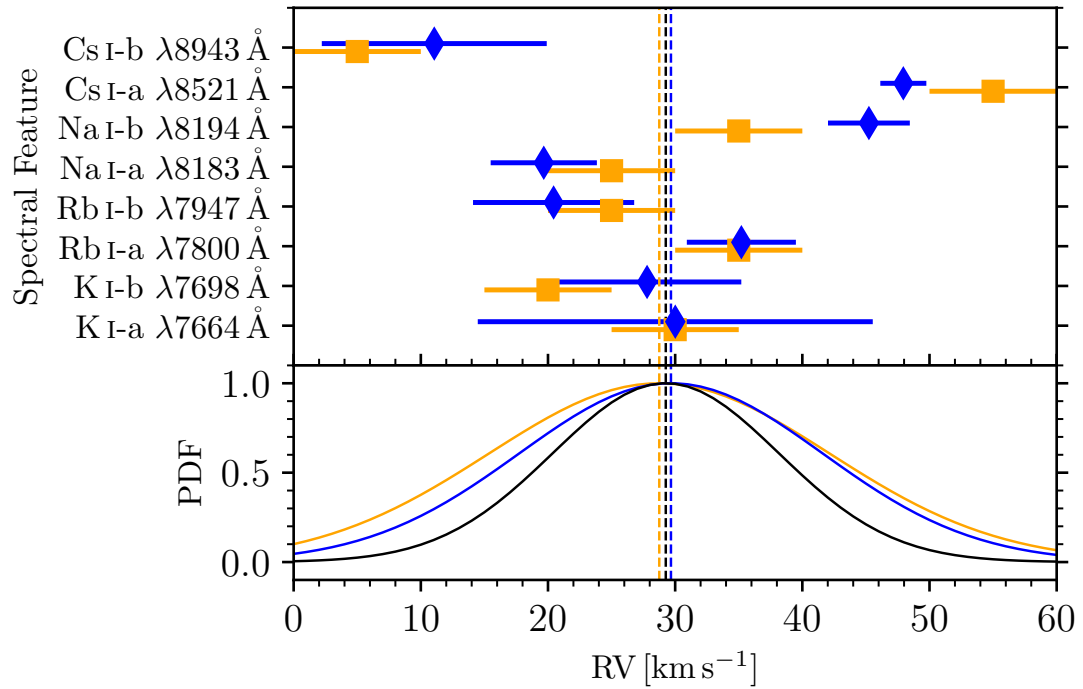


FIGURE 2.7: J1745–1640 RV values for each given line. In the top panel, orange squares are cross-correlated RVs, blue diamonds are line centre RVs; each spectral feature has been indicated on the y axis. In the bottom panel, the orange curve is the cross-correlated PDF; the blue curve is the line centre PDF; and the black curve is the adopted PDF. The dotted vertical lines are the mean RV values as associated with each PDF.

As in Section §2.3.3.1, the overall cross-correlated mean RV value (μ_{XC}) and standard deviation (σ_{XC}) was calculated, using all of the manually selected lines. We used the same method to estimate the uncertainty in final cross-correlation derived RVs as for the line centre results, by finding the standard error of the mean.

2.3.3.3 Adopted RV

We created an adopted RV by constructing a weighted mean, using the deviation in each method as the weighting. The different RV values for each line, method and the corresponding probability distribution functions (PDFs) are shown in Figure 2.7, for J1745–1640.

The adopted RV was the mean (μ_{RV}) whilst the standard error (δ_{RV}) was equal to the standard deviation (σ_{RV}) divided by $\sqrt{2}$. The mean and standard deviation was calculated through the inverse variance weighting equations (2.5 and 2.6).

$$\mu_{\text{RV}} = \frac{\mu_{\text{LC}}\sigma_{\text{XC}}^2 + \mu_{\text{XC}}\sigma_{\text{LC}}^2}{\sigma_{\text{LC}}^2 + \sigma_{\text{XC}}^2} \quad (2.5)$$

$$\sigma_{\text{RV}} = \sqrt{\frac{\sigma_{\text{LC}}^2\sigma_{\text{XC}}^2}{\sigma_{\text{LC}}^2 + \sigma_{\text{XC}}^2}} \quad (2.6)$$

2.3.4 Kinematics

Galactic UVW velocities were calculated using our adopted RVs plus *Gaia* astrometric measurements, using the equations from `astrolib.py`. We corrected for the Local Standard of Rest (LSR) using the values from Coşkunoğlu et al. (2011) where $U, V, W = (-8.50, +13.38, +6.49) \text{ km s}^{-1}$. These equations follow the work by Johnson and Soderblom (1987), except that U is orientated towards the Galactic anti-centre. We also used BANYAN Σ (Gagné et al., 2015a, 2018), which provided moving group classification with associated probability. When using BANYAN Σ , we checked the resultant probabilities both with and without RV. This was because RV has by far the lowest precision, thus could reduce a likely membership candidate into a field object in error. Our final values are the ones which include RV. Notably, when using velocities in the Galactic reference frame, one can select a Galactic component with V_{total} (where V_{total} is the total space velocity, $V_{\text{total}} = \sqrt{U^2 + V^2 + W^2}$). We followed the work by Nissen and Schuster (2010) and define thick disc and halo objects as having $V_{\text{total}} > 70 \text{ km s}^{-1}$ and $V_{\text{total}} > 180 \text{ km s}^{-1}$ respectively. This definition, especially for separating thin and thick disc, is very indicative and strongly correlated with metallicity; see the Besançon Galaxy models (Czekaj et al., 2014; Lagarde et al., 2021).

2.4 Results

In this Section, we present the spectral types, radial velocities and astrophysical parameters. In Table A.2, we provide photometry from the *Gaia*, 2MASS and ALLWISE catalogues. We discuss individually interesting objects and objects where our measured results differ significantly from published values.

TABLE 2.3: Our spectral types compared with the literature optical and near-infrared types for each object.

Object short name	Lit Opt sp. type	Lit NIR sp. type	By eye sp. type	kastredux sp. type	Object short name	Lit Opt sp. type	Lit NIR sp. type	By eye sp. type	kastredux sp. type
J0028–1927	L0 ¹	L0.5 ²	L0.5	L1	J0235–0849	L2 ³	L2 ²	L2	L2
J0428–2253	L0.5 ⁴	L0 ²	L0.5	L1	J0453–1751	L3 ⁵	L3 ²	L3 β	L3
J0502+1442	L0 ⁶	M9 ²	M9 β	L0	J0605–2342	L0 ⁷	L1 ²	L0.5	L1
J0741+2316	L1 ⁸	...	L0	L0	J0752+4136	M7 ⁹	...	M6	M6
J0809+2315	L4:	L4	J0823+0240	M9	M8
J0823+6125	L2 ¹	L2.5 ²	L3	L3	J0847–1532	L2 ⁵	...	L2	L2
J0918+2134	L2.5 ¹⁰	L2.5 ²	L3	L3	J0935–2934	L0 ¹	L0.5 ²	L0	L0
J0938+0443	L0 ⁶	M8 ²	M9	M8	J0940+2946	L1 ⁶	L0.5 ²	...	L2
J0953–1014	L0 ⁷	M9.5 ²	M9.5 β	L0	J1004+5022	L3VI-G ¹¹	L3Int-G ¹²	L3 γ	L4
J1004–1318	L0 ¹³	L1 ¹⁴	L3.5 β	L3	J1047–1815	L2.5 ¹⁵	L0.5 ²	L1	L1
J1058–1548	L3 ¹⁰	L3 ¹⁶	L3 β	L3	J1109–1606	L0 ⁶	...	L1	L0
J1127+4705	L1 ⁶	...	L1	L1	J1213–0432	L5 ⁵	L4 ²	L5 β	L4
J1216+4927	L1 ⁶	...	L2:	L2	J1221+0257	L0.5 ¹⁷	M9p ¹⁸	M9.5	L0
J1222+1407	M9 ⁸	...	M9::	L0	J1232–0951	L0 ¹	M9.5 ²	M9.5	L0
J1246+4027	L4 ¹⁹	L4 ²	L4 w/ Li	L4	J1331+3407	L0 ¹	L1p(red) ²⁰	L0	L1
J1333–0215	L3 ⁶	L2 ²	...	L2	J1346+0842	L2 ⁶	...	L2.5	L3
J1412+1633	L0.5 ¹⁹	L0 ²	L0	L1	J1421+1827	L0 ¹	M9 ²	M9.5	L0
J1439+0039	L0	J1441–0945	L0.5 ¹¹	L0.5 ²	L0.5	L1
J1527+0553	L0	J1532+2611	L1 ⁶	L3
J1539–0520	L4 ¹¹	L2 ²¹	L4.5	L3	J1548–1636	...	L2 ²²	M9.5	L0
J1617+7733B	M6	J1618–1321	L0 ¹¹	M9.5 ²	L0	L1
J1623+1530	L0 ⁶	...	M9	L0	J1623+2908	L1 ⁶	...	L1::	L1
J1705–0516	L0.5 ¹	L1 ¹²	L1	L1	J1707–0138	L0.5 ¹³	L2 ²³	L1	L1
J1717+6526	L4 ³	L6 ²	L6	L5	J1724+2336	L0
J1733–1654	L0.5 ²⁴	L1 ²	L2	L3	J1745–1640	L1.5 ²⁴	L1.5 ²	L1	L1
J1750–0016	...	L5.5 ²²	L5.5	L4	J2155+2345	...	L2 ²⁰	L3	L2
J2339+3507	L3.5 ¹	...	L3.5	L3					

Literature Spectral Types: 1. Reid et al. (2008), 2. Bardalez Gagliuffi et al. (2014), 3. Hawley et al. (2002), 4. Kendall et al. (2003), 5. Cruz et al. (2003), 6. Schmidt et al. (2010), 7. Cruz et al. (2007), 8. Marocco et al. (2017), 9. West et al. (2011), 10. Kirkpatrick et al. (1999), 11. Kirkpatrick et al. (2008), 12. Allers and Liu (2013), 13. Martín et al. (2010), 14. Marocco et al. (2013), 15. Martín et al. (1999b), 16. Knapp et al. (2004), 17. Schneider et al. (2014), 18. Gagné et al. (2015a), 19. Kirkpatrick et al. (2000), 20. Kirkpatrick et al. (2010), 21. Kendall et al. (2004), 22. Kendall et al. (2007b), 23. Phan-Bao et al. (2011), 24. Phan-Bao et al. (2008).

The ‘.’ after a spectral type indicates uncertainty of ± 1 whilst ‘p’ indicates peculiarity. Surface gravity flags β and γ are given when appropriate, and are discussed in Section §2.4.3.1. The adopted spectral type is the `kastredux` method, only overwritten where there are gravity flags in the ‘by eye’ method. In addition, J1246+4027 has been typed as having a potential Li I detection ($\lambda 6708 \text{ \AA}$), which can only be seen in the R300R spectra.

2.4.1 Spectral types

In Table 2.3 we list published spectral types based on optical spectra, near-infrared spectra and the ‘by eye’ and `kastredux` methods discussed in Section §2.3.1. This work has produced the first spectral type estimates for six of the 53 objects.

The 47 objects with known spectral types have a standard deviation of 0.5 sub-types between the published values and the ‘by eye’/`kastredux` results, which we adopt as the error on the new spectral sub-types. When the literature values for a given object differ we adopted the optical spectral type. Our spectral types across the two methods are displayed against the adopted literature spectral types in Figure 2.8.

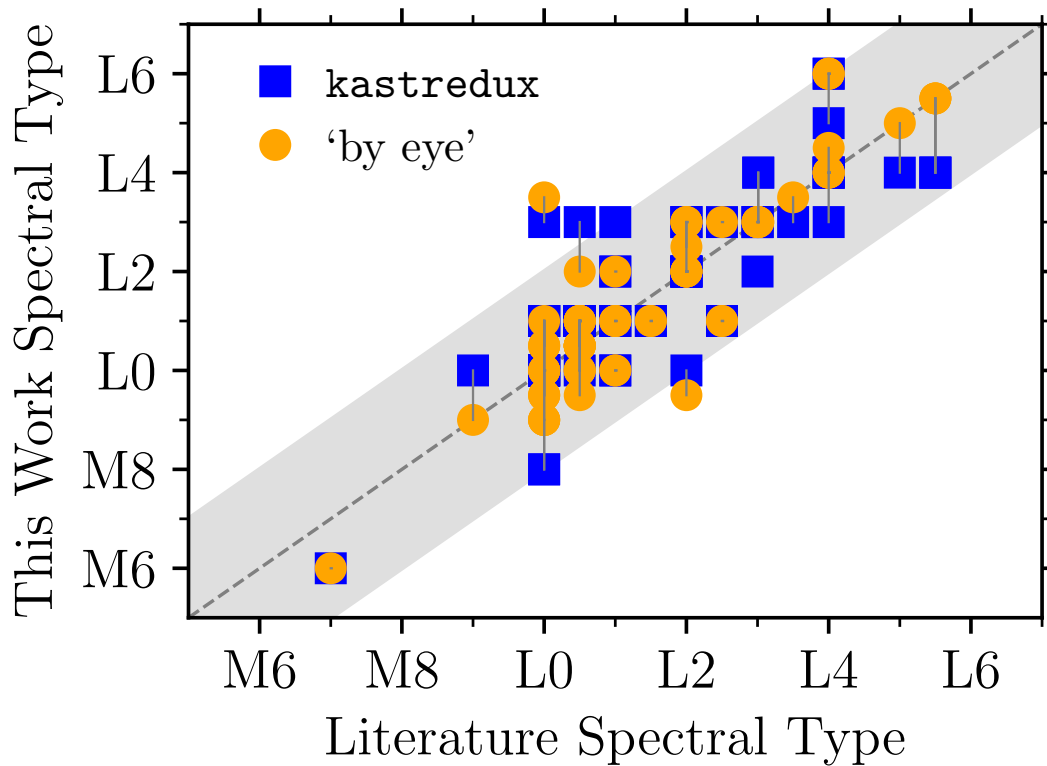


FIGURE 2.8: Comparison between this works spectral types and the literature spectral types. Blue squares are spectral types from our adopted, *kastredux* method whilst orange circles are from the manual ‘by eye’ method. Grey lines connect these two methods and we show a one-to-one dashed grey line with associated ± 2 spectral sub-types confidence bands.

All objects except J1004–1318 have sub-type differences between the spectral type derived in this work and the adopted literature spectral type of less than two sub-types. J1004–1318, has an optical (Opt) spectral sub-type of L0 (Martín et al., 2010) whilst Marocco et al. (2013) finds a sub-type of L1 using near-infrared (NIR) spectra; we find a sub-type of L3.5/L3. However, a more recent study, Robert et al. (2016), found a sub-type of L4, this is more consistent with our result. This is discussed further in Section §2.4.3.1.

2.4.2 Kinematics

We have derived RVs for 46 of the observed 53 objects, the seven objects that we did not measure RVs were only observed with the R300R grism. For 20 of the 53 objects, there are published RVs and for 17 of these we have measured RVs. The objects J1004+5022 and J1617+7733B are candidate members of benchmark systems (Section §2.2.1), and we adopt the RVs of their primary stars as a comparison with our measured values for the secondary, for a total of 19 comparison RVs. In Figure 2.9 left panel, we plot histograms of the 20 published and the 46

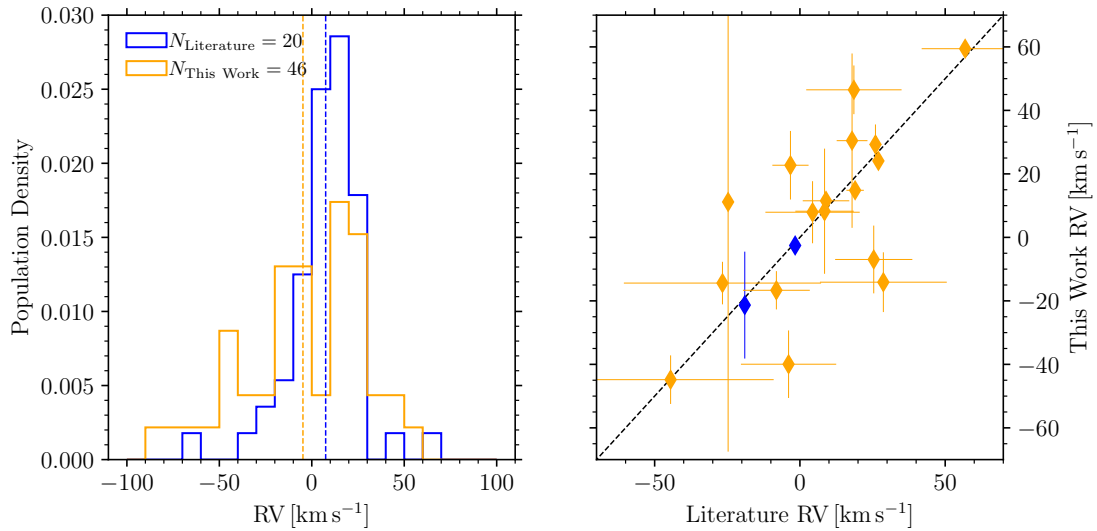


FIGURE 2.9: **[Left Panel]:** Histograms of the RVs calculated in this work (orange) and from the literature (blue) to show the relevant population densities. The dashed vertical lines indicate the means of the associated distributions. **[Right Panel]:** The RV values from the literature on the x axis with our adopted RV values, on the y . We show a one-to-one relation, over which our 19 comparison RVs are plotted as diamonds. Orange diamonds are like-for-like comparisons and blue diamonds are for the two benchmark systems, i.e., comparisons between our measured secondary RV against the literature RV of the primary.

measured values. In the right panel, we plot the difference between the published and measured values of the 19 overlapping objects. If there is more than one literature value, we take the weighted mean RV and standard error on the mean, to compare against the adopted RV from this work. The error used to define σ are the quadrature summed errors from the literature and our adopted RV.

Our 46 RVs in the heliocentric reference frame are presented in Table 2.4. This reference frame has been experimented with, in that the heliocentric/barycentric correction via `pypeit` has been compared with a manual barycentric correction using `barycorrpy` (Kanodia and Wright, 2018). Resultant RV differences from the manual barycentric correction to the pipeline barycentric correction differ by $\approx 0.1 \text{ km s}^{-1}$. The difference between heliocentric and barycentric correction is 0.5 km s^{-1} (~ 2 per cent) in the case of J1745–1640.

All objects except J1221+0257 have an adopted and literature RV difference less than two times the sum of the respective errors in quadrature. J1221+0257 is 2.08σ from the weighted mean literature value. Any objects in Table 2.4 which have known primary stars with literature RVs are discussed below:

J1004+5022: G 196–3B is the binary companion to G 196–3A. G 196–33A has a mean RV

TABLE 2.4: RVs measured in this work and compared to the literature.

Object short name	Literature RV [kms ⁻¹]	Line Centre RV [kms ⁻¹]	Cross Correlation RV [kms ⁻¹]	Adopted RV [kms ⁻¹]
J0028–1927	...	24.6 ± 10.6 ^{abcde}	26.2 ± 13.2 ^{abcde}	25.2 ± 15.8
J0235–0849	15.3 ± 11.2 ¹ , 22.8 ± 6.1 ²	35.5 ± 26.5 ^{cd}	26.7 ± 21.0 ^{cd}	30.5 ± 27.5
J0428–2253	...	118.9 ± 48.7 ^{abcde}	16.0 ± 6.1 ^{de}	17.1 ± 9.5
J0453–1751	...	10.7 ± 6.3 ^{df}	13.3 ± 5.9 ^{cd}	11.7 ± 6.2
J0502+1442	...	43.4 ± 5.9 ^{abc}	41.2 ± 5.4 ^{abcde}	42.4 ± 7.4
J0605–2342	...	28.5 ± 7.0 ^{de}	25.0 ± 8.8 ^{abcde}	27.6 ± 8.7
J0741+2316	...	30.9 ± 0.2 ^{de}	38.0 ± 3.3 ^{ab}	31.0 ± 0.2
J0752+4136	8.5 ± 10.1 ¹	1.7 ± 23.4 ^{be}	14.2 ± 15.7 ^{abc}	8.2 ± 19.7
J0809+2315	...	-32.5 ± 7.3 ^{de}	-38.0 ± 9.5 ^{de}	-34.2 ± 8.5
J0823+0240	...	-19.8 ± 9.6 ^{ef}	-4.3 ± 4.5 ^{abcde}	-9.4 ± 6.8
J0823+6125	...	-35.7 ± 11.5 ^{de}	-12.9 ± 12.7 ^{abcde}	-28.5 ± 13.4
J0918+2134	...	-95.1 ± 7.6 ^{ef}	-80.0 ± 7.5 ^{de}	-89.3 ± 7.3
J0935–2934	...	-7.8 ± 10.7 ^{ae}	-22.5 ± 6.1 ^{abcde}	-16.8 ± 9.5
J0938+0443	25.4 ± 13.3 ¹	-10.4 ± 14.7 ^{de}	-5.7 ± 6.7 ^{abcde}	-7.0 ± 10.7
J0940+2946	27.3 ± 11.8 ¹ , 4.1 ± 7.1 ²	48.9 ± 6.0 ^{de}	35.0 ± 9.2 ^{abcde}	46.5 ± 7.7
J0953–1014	...	26.9 ± 17.2 ^{bgh}	10.0 ± 7.5 ^{abcde}	15.7 ± 12.2
J1004+5022	-1.7 ± 1.5 ^{†3} , -1.6 ± 0.9 ^{†4} , -0.7 ± 1.2 ^{†5} , -2.8 ± 0.9 ^{†6}	1.1 ± 11.4 ^f	-3.0 ± 1.8 ^{de}	-2.6 ± 2.7
J1004–1318	...	17.2 ± 6.0 ^{de}	13.3 ± 8.4 ^{cd}	16.0 ± 7.9
J1047–1815	...	-19.2 ± 7.9 ^{ef}	-18.0 ± 6.6 ^{de}	-18.5 ± 7.6
J1058–1548	...	0.7 ± 9.7 ^{de}	-1.0 ± 5.7 ^{de}	-0.6 ± 7.8
J1109–1606	48.7 ± 16.1 ¹ , 69.9 ± 10.0 ²	61.1 ± 2.2 ^{gh}	48.8 ± 2.8 ^{abcde}	59.4 ± 2.0
J1127+4705	-23.7 ± 11.1 ¹ , -26.4 ± 6.5 ²	12.4 ± 71.4 ^{de}	10.0 ± 69.3 ^{de}	11.2 ± 78.6
J1213–0432	...	-12.2 ± 14.2 ^{de}	-40.0 ± 24.7 ^{cd}	-17.2 ± 18.2
J1216+4927	4.3 ± 16.2 ¹	7.1 ± 6.9 ^{abcde}	8.8 ± 6.9 ^{abcde}	7.9 ± 9.8
J1221+0257	2.0 ± 10.1 ¹ , -8.0 ± 3.0 ⁷ , -12.6 ± 4.1 ² , -8.8 ± 0.1 ⁸	24.9 ± 7.2 ^{abcde}	20.0 ± 8.1 ^{abcde}	22.7 ± 10.8
J1232–0951	...	-8.6 ± 6.3 ^{abcde}	-8.6 ± 7.3 ^{abcde}	-8.6 ± 9.3
J1246+4027	...	-46.1 ± 14.4 ^{cd}	-46.7 ± 15.0 ^{cd}	-46.3 ± 18.0
J1331+3407	4.1 ± 10.2 ¹ , 15.4 ± 7.8 ²	-5.6 ± 24.0 ^f	12.0 ± 1.8 ^{de}	11.5 ± 2.8
J1333–0215	28.7 ± 21.8 ¹	-19.0 ± 7.2 ^{cd}	-7.5 ± 7.2 ^{abcde}	-14.1 ± 9.4
J1346+0842	-67.9 ± 12.2 ¹ , -17.7 ± 10.6 ²	-48.7 ± 5.3 ^{cd}	-35.6 ± 7.0 ^{abcde}	-44.8 ± 7.7
J1412+1633	...	-77.4 ± 19.9 ^{abcde}	-81.4 ± 20.5 ^{abcde}	-79.5 ± 27.6
J1421+1827	...	-7.0 ± 8.5 ^{abcde}	-10.0 ± 9.1 ^{ab}	-8.5 ± 11.2
J1441–0945	...	21.4 ± 42.5 ^{ef}	21.7 ± 28.0 ^{de}	21.6 ± 37.8
J1532+2611	-38.8 ± 36.6 ¹ , 9.2 ± 12.4 ²	-24.6 ± 9.2 ^{de}	-11.7 ± 4.4 ^{cd}	-14.4 ± 6.7
J1539–0520	27.3 ± 0.2 ⁹ , 27.0 ± 4.0 ⁷	27.0 ± 11.1 ^{de}	24.0 ± 1.7 ^{de}	24.1 ± 2.6
J1548–1636	...	21.0 ± 8.4 ^{abcde}	21.2 ± 7.4 ^{abcde}	21.1 ± 11.1
J1617+7733B	-19.0 ± 0.8 ^{†4}	-30.4 ± 20.5 ^{de}	-18.0 ± 12.5 ^{ade}	-21.3 ± 16.8
J1618–1321	...	-39.4 ± 11.3 ^{de}	-75.0 ± 48.0 ^{ce}	-41.7 ± 17.3
J1623+1530	-17.8 ± 11.5 ¹ , 5.4 ± 17.2 ²	-49.7 ± 8.4 ^{cd}	-28.8 ± 7.8 ^{abcde}	-40.0 ± 10.6
J1623+2908	-8.1 ± 11.5 ²	-14.7 ± 5.4 ^{ef}	-26.0 ± 9.2 ^{de}	-16.7 ± 6.0
J1707–0138	...	15.5 ± 9.0 ^{abcde}	18.3 ± 9.6 ^{cd}	17.0 ± 12.2
J1717+6526	...	-65.0 ± 3.4 ^{cd}	-76.7 ± 6.1 ^{cd}	-66.5 ± 3.9
J1745–1640	26.0 ± 2.0 ⁷	29.7 ± 4.2 ^{abcde}	28.8 ± 4.7 ^{abcde}	29.3 ± 6.3
J1750–0016	19.0 ± 3.0 ⁷	8.5 ± 4.4 ^{cd}	16.0 ± 1.7 ^{cd}	14.8 ± 2.4
J2155+2345	...	-47.9 ± 11.3 ^{cd}	-46.7 ± 11.0 ^{cd}	-47.3 ± 13.6
J2339+3507	...	-64.8 ± 10.0 ^{de}	-47.1 ± 10.4 ^{bcde}	-58.7 ± 11.5

Literature Radial Velocities: 1. Kiman et al. (2019), 2. Schmidt et al. (2010), 3. Binks and Jeffries (2016), 4. Gaia Collaboration et al. (2018b), 5. Shkolnik et al. (2012), 6. Schlieder et al. (2012b), 7. Burgasser et al. (2015), 8. Hsu et al. (2021), 9. Blake et al. (2010).

Indices: a – K I-a; b – K I-b; c – Rb I-a; d – Rb I-b; e – Na I-a; f – Na I-b; g – Cs I-a; h – Cs I-b. Quoted RVs are already heliocentric corrected. A ‘†’ symbol next to an RV means the RV is that of the primary star in the common proper motion system a given object is part of.

of $-1.6 \pm 0.4 \text{ km s}^{-1}$. This mean RV of the primary is 0.4σ away from the RV of the secondary companion from this work.

J1617+7733B: TYC4571-1414-1B is the binary companion of TYC4571-1414-1A. TYC4571-1414-1A has an RV of $-19 \pm 0.8 \text{ km s}^{-1}$ (Gaia Collaboration et al., 2018b), this RV is 0.1σ from the companion RV.

TABLE 2.5: The UVW velocities and BANYAN Σ classification (with associated probability) from this work.

Object short name	V_{tan} [kms $^{-1}$]	V_r [kms $^{-1}$]	U [kms $^{-1}$]	V [kms $^{-1}$]	W [kms $^{-1}$]	V_{total} component	Galaxy component	BANYAN Σ classification	Probability [per cent]
J0028–1927	20.5	25.2	10.7	10.9	-19.6	24.8	Thin	Field	100.0
J0235–0849	6.0	30.5	4.0	17.9	-21.6	28.3	Thin	Field	100.0
J0428–2253	23.3	17.1	19.5	6.9	9.7	22.9	Thin	Field	100.0
J0453–1751	7.0	11.7	-1.6	1.9	4.0	4.7	Thin	β Pictoris	97.9
J0502+1442	17.1	42.4	33.2	-5.2	4.3	33.9	Thin	Hyades	99.4
J0605–2342	19.4	27.6	20.7	7.0	-9.2	23.7	Thin	Field	100.0
J0741+2316	10.1 ¹	31.0	22.8	4.3	8.0	24.5	Thin	Field	100.0
J0752+4136	10.3	8.2	2.5	19.9	3.2	20.3	Thin	Field	100.0
J0823+6125	61.6	-28.5	10.7	-12.8	-53.1	55.7	Thin	Field	100.0
J0847–1532	19.8	-1.0 ²	-26.2	4.5	5.6	27.2	Thin	Field	100.0
J0935–2934	11.1	-16.8	-3.6	32.7	8.9	34.1	Thin	Field	100.0
J0938+0443	13.1	-7.0	-16.6	7.0	-4.3	18.5	Thin	Field	100.0
J0940+2946	38.2	46.5	44.4	-13.4	16.6	49.3	Thin	Field	100.0
J0953–1014	18.0	15.7	0.9	-7.5	-0.1	7.6	Thin	Field	80.3
J1004+5022	25.3	-2.6	0.7	-9.6	0.7	9.6	Thin	Field	99.9
J1004–1318	27.1	16.0	-5.9	-14.9	-7.0	17.5	Thin	Field	60.8
J1047–1815	49.0	-18.5	34.8	18.5	-22.5	45.4	Thin	Field	100.0
J1058–1548	22.4	-0.6	11.9	8.7	-1.5	14.8	Thin	Argus	92.9
J1109–1606	105.0	59.4	43.3	-91.0	-24.8	103.8	Thick	Field	100.0
J1127+4705	13.2	11.2	3.5	4.5	15.2	16.2	Thin	Field	100.0
J1213–0432	29.6	-17.2	18.3	6.6	-13.8	23.8	Thin	Carina Near	98.2
J1221+0257	13.3	22.7	-1.9	-5.1	24.0	24.6	Thin	Field	100.0
J1232–0951	30.2 ³	-8.6	7.7	-5.9	-12.3	15.7	Thin	Field	99.8
J1246+4027	17.6	-46.3	-32.2	3.1	-35.8	48.3	Thin	Field	100.0
J1331+3407	55.8	11.5	14.6	-33.9	28.4	46.6	Thin	Field	100.0
J1333–0215	52.5	-14.1	24.9	-27.0	-8.2	37.6	Thin	Field	100.0
J1346+0842	52.6	-44.8	34.2	-26.2	-30.8	52.9	Thin	Field	100.0
J1412+1633	17.9	-79.5	7.7	-2.4	-71.8	72.3	Thick	Field	100.0
J1421+1827	69.2	-8.5	31.2	-42.5	19.1	56.1	Thin	Field	100.0
J1441–0945	30.7	21.6	-5.0	-13.5	32.5	35.5	Thin	Field	65.7
J1539–0520	47.9	24.1	-45.6	51.0	-2.6	68.5	Thin	Field	100.0
J1548–1636	30.3	21.1	-19.5	-17.6	23.3	35.2	Thin	Field	100.0
J1617+7733B	18.7	-21.3	1.3	-11.8	-2.1	12.1	Thin	Field	95.8
J1618–1321	29.3 ⁴	-41.7	31.9	-15.5	-4.8	35.8	Thin	Field	100.0
J1623+1530	14.7	-40.0	15.6	-15.7	-13.1	25.7	Thin	Field	100.0
J1705–0516	14.9	12.2 ⁵	-25.4	14.2	-2.8	29.2	Thin	Field	100.0
J1707–0138	5.8	17.0	-26.0	17.6	7.8	32.3	Thin	Field	100.0
J1717+6526	20.1	-66.5	-27.6	-32.3	-42.4	60.0	Thin	Field	100.0
J1733–1654	7.0	17.0 ²	-26.1	16.5	2.1	31.0	Thin	Field	100.0
J1745–1640	13.7	29.3	-39.1	16.1	-3.6	42.4	Thin	Field	100.0
J1750–0016	19.4	14.8	-17.7	17.2	28.8	37.9	Thin	Field	100.0
J2339+3507	23.4	-58.7	-5.1	-47.8	22.1	52.9	Thin	Field	100.0

Literature astrometry used to generate UVWs: 1. Smith et al. (2014), 2. Burgasser et al. (2015), 3. Best et al. (2020), 4. Weinberger et al. (2016), 5. Blake et al. (2010).

U is in the direction of the Galactic anti-centre. Derived using this work’s adopted radial velocity in combination with *Gaia* DR3 kinematics unless otherwise indicated. We also show the predicted Galaxy component, taken from the UVW velocities and V_{total} cuts in Nissen and Schuster (2010).

2.4.2.1 Moving groups

Our results for UVW Galactic kinematic components are presented in Table 2.5 with each object’s moving group classification and associated probability from BANYAN Σ . When accounting for RV in BANYAN Σ , the resultant probability was often lower than the calculation without RV. This was due to the Bayesian probabilities being designed for a higher recovery rate (moving from 82 per cent to 90 per cent) when accounting for the RV (see the BANYAN Σ cautionary note, Gagné et al., 2018). In addition, the RV uncertainties from this work are much higher than proper motion or parallax uncertainties from *Gaia*.

We find four objects are members of the following young moving groups and clusters: Argus (30–50 Myr, Makarov and Urban, 2000); β Pictoris (Zuckerman et al., 2001), 20–26 Myr (Majek and Bell, 2014; Couture et al., 2023, and references therein); Carina-Near (\sim 200 Myr, Zuckerman et al., 2006); and the Hyades cluster (600–800 Myr, Perryman et al., 1998; Martín et al., 2018; Lodieu et al., 2018). These are discussed below in Section §2.4.3.1.

2.4.2.2 Galactic components

Thin disc objects were differentiated from thick disc and halo objects using the LSR corrected UVW Galactic velocities; the thick disc and halo objects were those with $V_{\text{total}} > 70 \text{ km s}^{-1}$ and $V_{\text{total}} > 180 \text{ km s}^{-1}$ respectively (Nissen and Schuster, 2010). V_{total} is the total space velocity. We calculated upper and lower bounds for UVW Galactic velocities using the propagated parallax, proper motion, and RV errors; these UVW velocities with associated uncertainties are shown in Figure 2.10. The objects J1109–1606 ($V_{\text{total}} = 103.8 \text{ km s}^{-1}$) and J1412+1633 ($V_{\text{total}} = 72.3 \text{ km s}^{-1}$) are found using the above criteria to be most likely thick disc objects, and are shown in Figure 2.10. However, without metallicity information, this is not a direct inference on age. We note additionally that J1412+1633 is a marginal classification due to its high uncertainty. Both of these objects are worth visiting with higher resolution spectroscopy to gain metallicity information, to confirm any potential subdwarf candidacy. This future work would also involved gathering NIR spectra, as in work by Zhang (2018); Zhang et al. (2018b, and references therein).

2.4.3 Astrophysical parameters

We present the T_{eff} and $\log g$ values from the model fitting (Section §2.3.2) in Table 2.6 along with \widehat{T}_{eff} , assuming our adopted spectral type and equation (4) by Stephens et al. (2009) and `teff_espucd` values from *Gaia* DR3. In Figure 2.11, we plot the difference between our value and the Stephens value. In the cases of objects with both R2500I and R300R spectra available, we default to the higher resolution result.

Only J1724+2336 had a T_{eff} difference greater than 2σ . The measurement of T_{eff} for this object was based on the lower resolution spectra, R300R. Although the best-fitting surface gravity values are interesting, they are quite degenerate and without corresponding metallicity values,

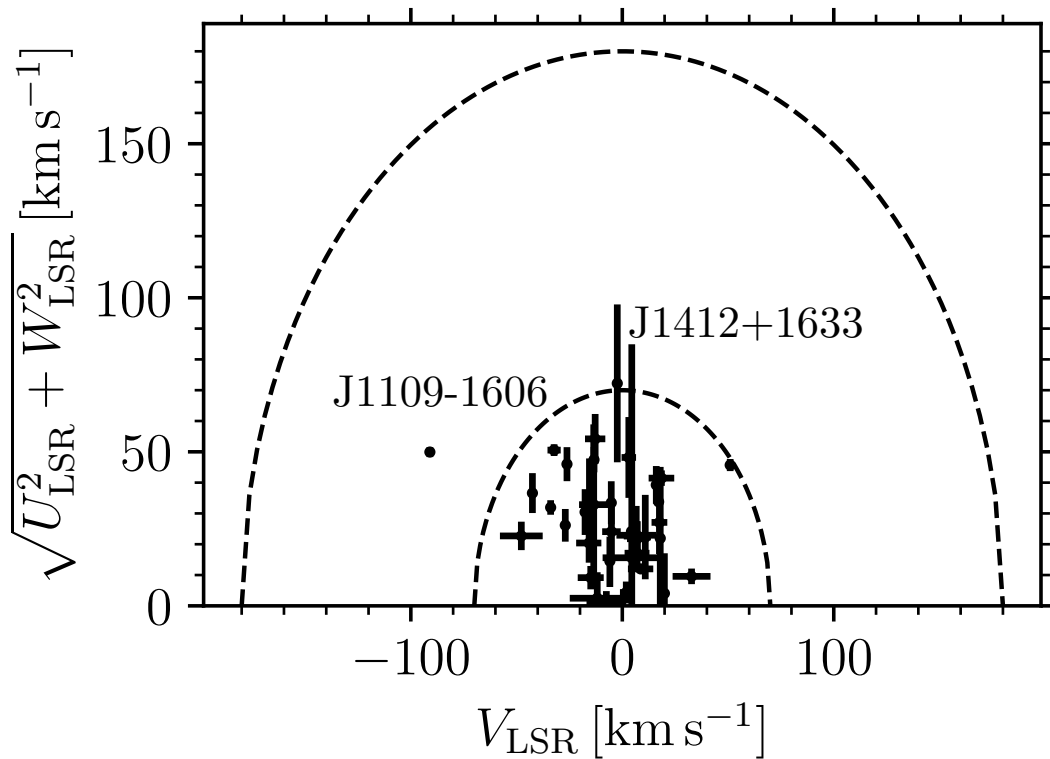


FIGURE 2.10: Toomre diagram, as done by Bensby et al. (2005), using *Gaia* DR3 astrometry in combination with our calculated RVs. V is on the x axis, against the velocity dispersion ($\sqrt{U^2 + W^2}$) on the y axis. Black circles are UVW velocities calculated with the RVs from this work, with associated error-bars given. We show the respective thick disc and halo selection lines at $V_{\text{total}} > 70 \text{ km s}^{-1}$ and $V_{\text{total}} > 180 \text{ km s}^{-1}$ respectively.

TABLE 2.6: Effective temperatures and surface gravities from this work.

Object short name	\widehat{T}_{eff} [K]	T_{eff} [K]	<i>Gaia</i> T_{eff} [K]	$\log g$ [dex]	Object short name	\widehat{T}_{eff} [K]	T_{eff} [K]	<i>Gaia</i> T_{eff} [K]	$\log g$ [dex]
J0028–1927	2099±133	1988±116	2115±112	4.8±0.4	J0235–0849	1967±130	1983±62	2035±190	5.0±0.3
J0428–2253	2099±133	1980±64	2322±71	5.0±0.3	J0453–1751	1839±124	1850±70	1921±176	5.0±0.3
J0502+1442	2234±136	2212±126	2285±80	4.9±0.3	J0605–2342	2099±133	2088±136	2121±82	4.8±0.4
J0741+2316	2234±136	2020±190	...	5.0±0.3	J0752+4136	2808±159	2817±62	...	4.9±0.4
J0809+2315	1717±116	1820±64	...	5.5±0.3	J0823+0240	2512±142	2500±287	...	5.1±0.4
J0823+6125	1839±124	1843±70	1951±93	4.7±0.4	J0847–1532	1967±130	1950±70	2040±50	5.0±0.3
J0918+2134	1839±124	1880±110	...	5.2±0.4	J0935–2934	2234±136	2162±121	2316±39	5.0±0.3
J0938+0443	2512±142	2486±228	2364±88	5.1±0.4	J0940+2946	1967±130	1950±70	2144±164	4.6±0.4
J0953–1014	2234±136	2100±150	2181±70	4.6±0.4	J1004+5022	1717±116	1740±70	1899±100	4.5±0.3
J1004–1318	1839±124	1850±70	1886±197	5.0±0.3	J1047–1815	2099±133	1980±64	2103±81	5.0±0.3
J1058–1548	1839±124	1900±102	1834±109	5.0±0.3	J1109–1606	2234±136	2175±82	2104±112	5.0±0.3
J1127+4705	2099±133	2060±94	2136±120	4.9±0.4	J1213–0432	1717±116	1783±143	1580±152	5.0±0.3
J1216+4927	1967±130	2012±59	...	4.8±0.4	J1221+0257	2234±136	2250±295	2210±41	5.0±0.3
J1222+1407	2234±136	2150±70	...	5.0±0.3	J1232–0951	2234±136	2114±144	...	5.0±0.3
J1246+4027	1717±116	1750±91	1780±162	4.6±0.4	J1331+3407	2099±133	2040±70	2170±71	4.9±0.4
J1333–0215	1967±130	2075±96	2104±76	4.8±0.4	J1346+0842	1839±124	1888±78	1889±349	4.8±0.4
J1412+1633	2099±133	2014±97	2104±55	4.6±0.4	J1421+1827	2234±136	2133±157	2233±69	4.9±0.4
J1439+0039	2234±136	2325±139	...	5.0±0.3	J1441–0945	2099±133	2033±106	2240±60	5.0±0.3
J1527+0553	2234±136	2100±50	...	5.0±0.3	J1532+2611	1839±124	1917±84	...	4.8±0.4
J1539–0520	1839±124	1840±70	1804±109	5.4±0.4	J1548–1636	2234±136	2125±147	2272±82	4.9±0.3
J1617+7733B	2808±159	2860±94	...	4.9±0.4	J1618–1321	2099±133	2050±100	...	5.0±0.3
J1623+1530	2234±136	2112±105	2339±147	4.8±0.4	J1623+2908	2099±133	2080±90	...	5.2±0.4
J1705–0516	2099±133	1950±70	2065±35	5.0±0.3	J1707–0138	2099±133	2100±180	2019±78	5.0±0.3
J1717+6526	1606±106	1550±168	1589±63	4.7±0.4	J1724+2336	2234±136	2550±70	2320±88	5.0±0.3
J1733–1654	1839±124	1800±50	2055±63	4.8±0.4	J1745–1640	2099±133	2088±105	2008±49	5.0±0.3
J1750–0016	1717±116	1660±113	1542±71	5.1±0.4	J2155+2345	1967±130	1900±76	...	5.0±0.3
J2339+3507	1839±124	1871±86	1855±138	5.0±0.3					

These T_{eff} values are generated using fits to preferentially R2500I spectra if available, else R300R. Model fits assume solar metallicities. \widehat{T}_{eff} represents the expected effective temperature, based on an object’s spectral type. *Gaia* T_{eff} are the `teff_espucd` effective temperatures from *Gaia* DR3.

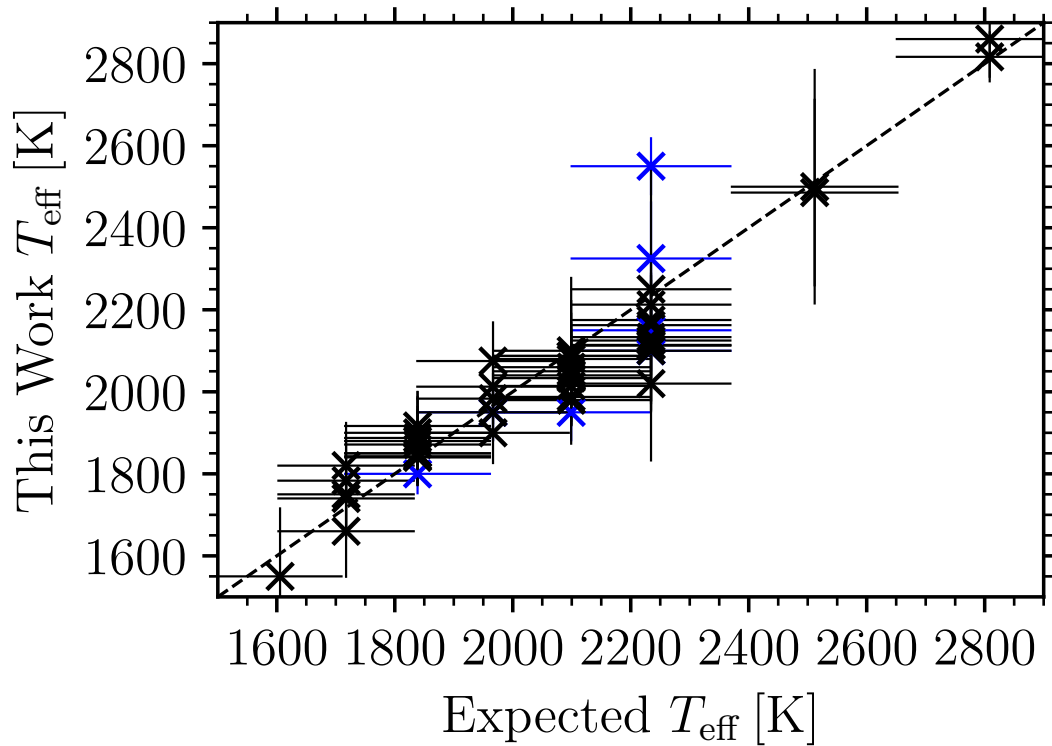


FIGURE 2.11: The expected \widehat{T}_{eff} (calculated via spectral type through a Filippazzo relation, Filippazzo et al., 2015) on the x axis and the best-fitting BT-Settl model mean T_{eff} on the y axis. Blue crosses are for objects with a fit to the R300R spectra whilst black crosses are objects with a fit to the R2500I spectra.

therefore they are not used in our discussion below. The best fitting spectral sub-types and BT-Settl models are shown in a spectral sequence for R2500I VPH spectra in Figures A.1 and A.2.

Figure 2.12 is a 2MASS $J - K_s$ Colour-absolute magnitude diagram (CAMD) with UCD cooling tracks by Baraffe et al. (2015). These tracks are shown as either a fixed age or fixed mass as given in the legend. The ages plotted along the mass tracks are from 100–500 Myr, the masses plotted along the isochrones are from 0.05–0.1 M_{\odot} . This selection of masses and ages is restrictive because lower mass objects are not computed to field ages. Highlighted here as diamonds are the objects with spectral features that are indicative of youth.

2.4.3.1 Individual objects

We further discuss here objects we have indicated as being non-typical, with interesting features or results. Plotted in Figure 2.13 are the gravity sensitive alkali lines Rb I, Na I and Cs I (see Table 2.2), following discussion by Gorlova et al. (2003), McGovern et al. (2004), McLean et al. (2007) and Cruz et al. (2009). Note that some less populated bins such as M9.5 or L5 are

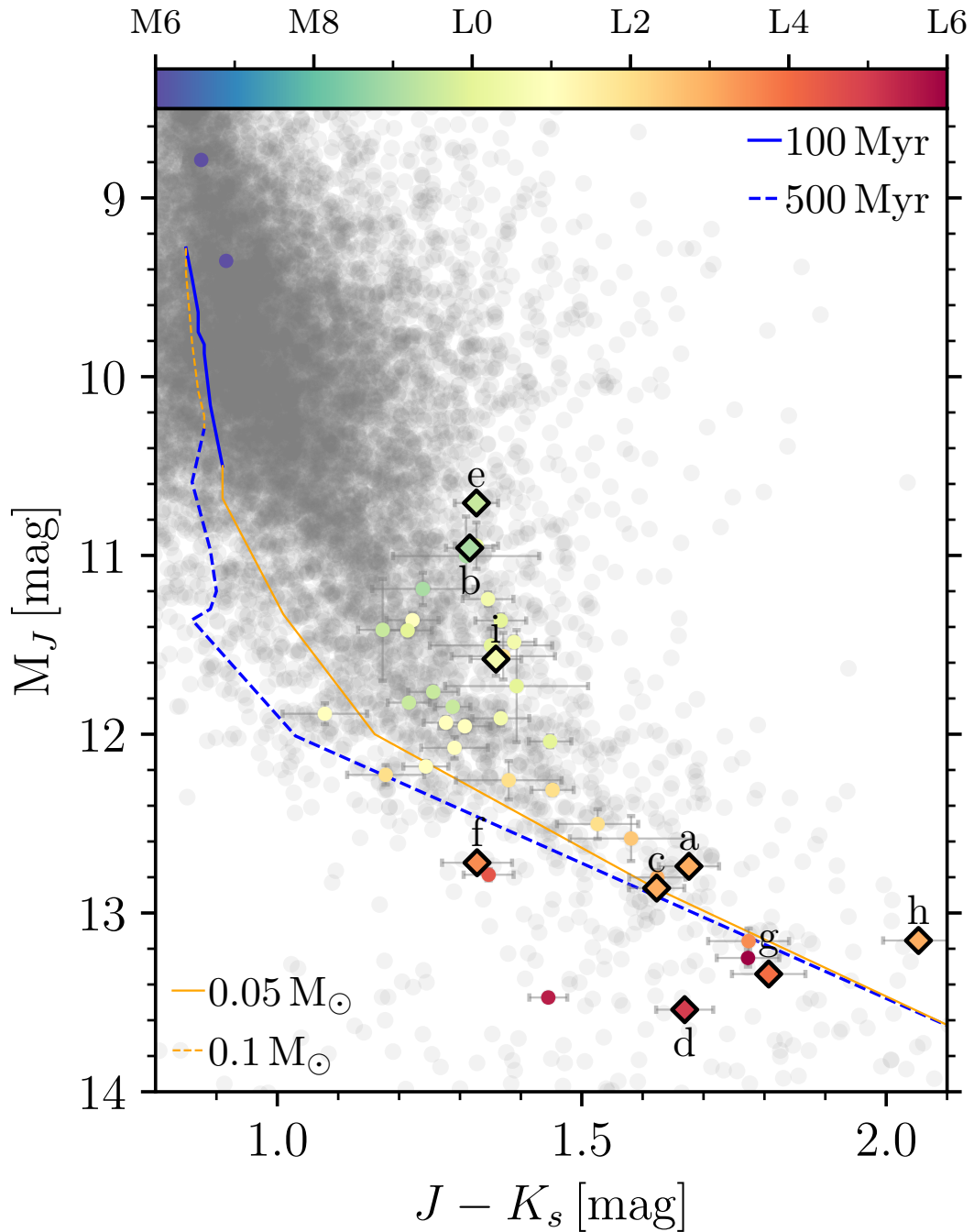


FIGURE 2.12: Colour-absolute magnitude diagram (CAMD) including the BHAC15 model cooling tracks by Baraffe et al. (2015). The $2MASS J - K_s$ colour is on the x axis against absolute $2MASS J$ magnitude on the y axis (having been computed using the *Gaia* parallaxes). Underlying the plot as grey circles is the full UCD sequence from the GUCDS. The blue lines are the 100 Myr and 500 Myr isochrones with solid, dashed, dash-dot, and dotted line styles respectively. The orange lines are $0.05 M_{\odot}$ and $0.1 M_{\odot}$ profiles with respective line styles as above. Each object is coloured by our adopted spectral type, with error bars shown in both axes. Diamonds are the young candidates discussed in Section §2.4.3.1. Key: a–J0453–1751, b–J0502+1442, c–J1058–1548, d–J1213–0432, e–J0953–1014, f–J1004–1318, g–J1246+4027, h–J1004+5022, i–J1441–0945.

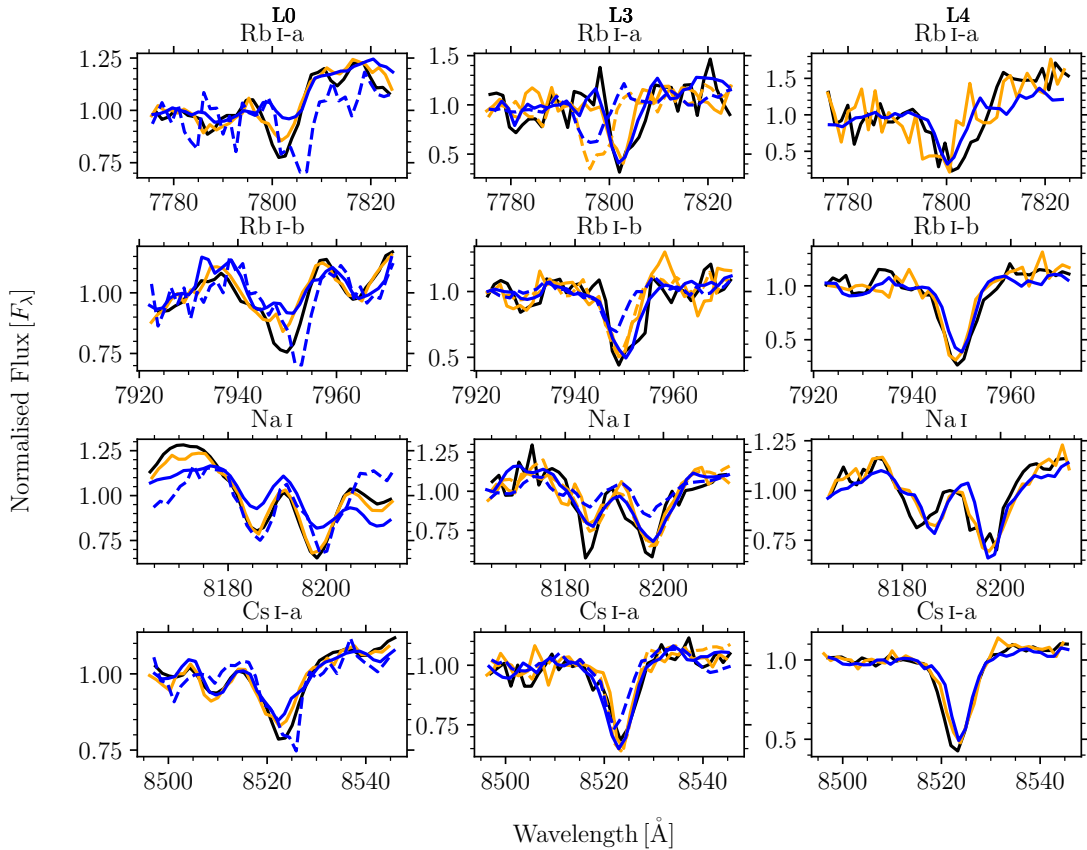


FIGURE 2.13: Gravity sensitive alkali lines for a selection of young candidates as compared with a field object of a given spectral type. The first column are L0 spectral types, then L3 and L4, all corrected for RV. Black lines are for the selected field objects: J1232–0951 (L0), J0918+2134 (L3) and J1750–0016 (L4). Orange lines are objects which have been kinematically bound to young moving groups in this work. The blue lines are potentially young candidates which are either in the field or have a probability greater than 10 per cent of being in a young moving group. L0: J0502+1442 (orange), J0953–1014 (blue) and J1441–0945 (blue, dashed). L3: J0453–1751 (orange), J1058–1548 (orange, dashed), J1004–1318 (blue) and J1004+5022 (blue, dashed). L4: J1213–0432 (orange) and J1246+4027 (blue).

compared with field objects of a close as possible spectral sub-type, hence only showing L0, L3 and L4.

We check for any age classifications, based on the moving group membership and isochrones from Figure 2.12. There are additional objects which exist in the same colour space as our highlighted objects in Figure 2.12 which are not discussed below. This is because there can be large implicit colour scatter due to unresolved binarity, metallicity and dust. Hence, only objects which are interesting either spectrally or kinematically are discussed. The following four objects were found to be members of the moving groups listed above, in Section §2.4.2.1.

J0453–1751: This L3 object, 2MASS J04532647–1751543, is a probable member of β Pic-toris with a 98 per cent confidence. Gagné et al. (2015b) by comparison found this object

as a member (96 per cent) of the similarly aged Columba association (20–40 Myr, Torres et al., 2008), where there is a lot of overlap in sky position with β Pictoris. As we using more precise updated kinematic information from *Gaia* DR3 plus RV, we would argue that our identification is more reliable. From Figure 2.12, we see J0453–1751 (a) is not immediately consistent with the age of these moving groups, although it is dimmer than where the young isochrones cease. As compared with a field object in Figure 2.13, J0453–1751 has a weaker sodium doublet, which would be expected for a young object. Its T_{eff} of 1850 ± 79 K is in good agreement with \widehat{T}_{eff} and `teff_espucd`. We can conclude that this object is an L3 β within β Pictoris.

J0502+1442: 2MASS J05021345+1442367, an M9/L0, we find as a member of the Hyades cluster with a 99 per cent probability. This improves the membership confidence by Gagné and Faherty (2018, 75 per cent) and concurs (at 100 per cent) with the classifications by *Gaia* Collaboration et al. (2018a); Cantat-Gaudin et al. (2020, using the Melotte 25 name). It also agrees with the classification by Lodieu et al. (2019), which had a ‘c parameter’ of 5.88, well within their Hyades membership limit, $c < 25.9$. Figure 2.12, places J0502+1442 (b) as very young, younger than the age of the Hyades cluster, on the ≈ 10 Myr isochrone. It has weaker alkali lines than a field object in Figure 2.13, except for Na I. However, this featural analysis is not valid for objects at the age of the Hyades, see discussion by Barrado Y Navascués (2006, and references therein). With a T_{eff} of 2212 ± 126 K and an understanding of its youthful features, J0502+1442 is an M9 β object in the Hyades cluster.

J1058–1548: Another L3 object, SIPS J1058–1548, is classified with 93 per cent confidence as a member of Argus. Gagné et al. (2015b) had the same classification with a much lower probability (35 per cent). As with J0453–1751, this increase in probability is due to the improved astrometric measurements of *Gaia* DR3 and inclusion of RV. Also like J0453–1751, J1058–1548 is clearly substellar and has a $T_{\text{eff}} = 1900 \pm 102$ K, see (c) in Figure 2.12. It is also not immediately consistent with the age of Argus, although colours for theoretical isochrones can be inconsistent (Baraffe et al., 1998). For the gravity sensitive alkali lines, J1058–1548 is much akin to the similarly aged J0453–1751. Almendros-Abad et al. (2022) notes that early-L UCDs like these can have some field-like alkali lines whilst still being young. We can therefore type this as an L3 β member of Argus.

J1213–0432: 2MASS J12130336–0432437 (L4/L5) we classify as a member of Carina-Near (98 per cent), which is an improvement on the 75 per cent classification by Gagné and Faherty (2018). Curiously, Figure 2.12 (d) has this object as dimmer than the oldest isochrones, as would not be expected of a Carina-Near member with a T_{eff} of 1783 ± 143 K. J1213–0432 has comparable alkali lines in Figure 2.13 to a field L4, although as with J0502+1442, for an age like Carina-Near, the alkali lines not being weaker is not necessarily surprising. This object can be classified then as an $L5\beta$ member of Carina-Near.

There are an additional three objects with probabilities of being non-field objects >10 per cent:

J0953–1014: 2MASS J0953212–101420, an M9.5 object, has a 16 per cent of being in the Columba association. This is in disagreement with the 65 per cent classification of being in Carina (Torres et al., 2008, 20–40 Myr) by Gagné et al. (2015b) and the 91 per cent probability of TW Hya (de la Reza et al., 1989; Kastner et al., 1997, 5–15 Myr) membership (Gagné et al., 2015a). Gagné et al. (2017) had reduced the probability of TW Hya membership to 81.1 per cent, having used features of youth, photometry and proper motion to do so. If it is indeed a bona fide member of Columba, its age could be constrained to 20–40 Myr. Its photometry places it as the youngest object in the sample in Figure 2.12 (e). This object has been spectrally typed several times, all from M9–L0 (bar one L2 measurement by Marocco et al., 2013), one of which also carries the β gravity classification (Faherty et al., 2016). Additionally, our mean best fitting model had $\log g = 4.6 \pm 0.4$ dex ($T_{\text{eff}} = 2150 \pm 150$ K). J0953–1014 has considerably weaker alkali lines in Figure 2.13 and is therefore classified as an $M9.5\beta$ member of one of the similarly aged moving groups discussed above.

J1004–1318: The L3.5 object, 2MASS J10044030–1318186, was classed here with a 33 per cent probability of being in the AB Doradus moving group (Zuckerman et al., 2004, ~ 50 Myr). It is not known as a member of any young association in the literature. We fit a best-fitting model $T_{\text{eff}} = 1850 \pm 70$ K. Figure 2.12 places J1004–1318 (f) on the ≈ 1 Gyr isochrone. Metallicity and dust can confuse these photometric analyses, as in work by Marocco et al. (2014) and Hiranaka et al. (2016). In Figure 2.13, J1004–1318 is much more akin to J0453–1751 than a field object. The inconsistent spectral types in the literature as compared with this work indicate that this is a peculiar object. This implies

that this object is a L3.5 β and a potential candidate member of AB Doradus. Follow up work with high resolution spectroscopy would be beneficial to explore the peculiarity of this object, this would also confirm how affected J1004–1318 is by dust.

J1441–0945: DENIS J144137.2-094558, has a spectral sub-type L0.5 and a 36 per cent probability of being in Carina-Near; it has no memberships known to the literature. We find a T_{eff} of 2033 ± 106 K, which is somewhat cooler than the `teff_espucd` value of 2240 ± 60 K. In Figure 2.12, J1441–0945 (i) is closest to the 50 Myr isocrone, which is not in exact agreement with the age of Carina-Near. Additionally, in Figure 2.13, it resembles more a field object than a known young object like J0502+1442. As previously discussed, this featural analysis is not wholly valid (see Smith et al., 2015) for objects of the age of Carina-Near. It is a potentially young object but improved kinematics and metallicity information would resolve this.

There are two further field objects that we have highlighted as interesting due to their spectral features:

J1246+4027: The L4 dwarf, 2MASSW J1246467+402715, observed at the two resolutions, is of interest due to the potential Li I detection at ≈ 6708 Å. As this feature is only in the wavelength regime of the R300R spectra, this is not definitive enough a detection to confirm lithium (see discussion by Martín et al., 2018, using the equation from Cayrel (1988)). Higher resolution ($R \gtrsim 2000$) spectra would be required for confirmation (Gálvez-Ortiz et al., 2014). Assuming a true detection, employing the lithium test (Rebolo et al., 1992) alongside our fitted effective temperature of $T_{\text{eff}} = 1750 \pm 91$ K would identify this object as being substellar. This T_{eff} is in good agreement with the expected temperature of $\widehat{T}_{\text{eff}} = 1717 \pm 116$ K and the *Gaia* DR3 T_{eff} of 1780 ± 162 K. This substellar argument is in line with discussion by Basri (1998), Martín et al. (1999a) and Kirkpatrick et al. (1999), because our T_{eff} is in the range $2670 > T_{\text{eff}} > 1400$ K. Figure 2.12 suggests J1246+4027 (g) is well below the stellar/substellar boundary and young (although the youngest isochrones are not computed to this point). The best fitting model had a surface gravity of $\log g = 4.6 \pm 0.3$ dex, although we have no complementary metallicity information. BANYAN Σ finds no correlation with any known young moving groups. J1246+4027 has weaker alkali lines still than the known young object J1213–0432 so could also be classed as an L4 β field object.

J1004+5022: G 196–3B is known to be a low gravity brown dwarf (Kirkpatrick et al., 2008; Allers and Liu, 2013), to which we concur, with a spectral sub-type of L3 γ . Our $\log g$ value is 4.5 ± 0.2 dex ($T_{\text{eff}} = 1740 \pm 113$ K), as would be expected from the already known young nature. As with J1246+4027, this object sits clearly below the stellar/substellar boundary in Figure 2.12 (h) in a very young position. It is a companion to the well known G 196–3A M3 star, to which we compared our kinematics in Section §2.4.2, finding a 0.4σ difference. There is much deeper discussion on this benchmark system by Zapatero Osorio et al. (2010), which measures an angular separation of $\rho = 15.99 \pm 0.06$. Combined with a *Gaia* DR3 parallax of $\varpi = 46.1952 \pm 0.5452$ mas, this implies a projected separation of $s = 739 \pm 1$ AU through equation (2.7, where ρ is angular separation in arcseconds, ϖ is the parallax in milli-arcseconds, and s is the projected physical separation in AU). This is slightly more than the projected physical separation range calculated by Zapatero Osorio et al. (2010), 285–640 AU.

$$s = \frac{\rho}{\varpi} \tag{2.7}$$

$$\sigma_s = \sqrt{\sigma_\rho^2 + \sigma_\varpi^2}$$

We found a probability of the secondary being a field object of 99.9 per cent, which is an increase on the 32 per cent probability of being a member of AB Doradus by Gagné et al. (2014b). This is also in agreement with the 50 per cent classification of the primary being a member of AB Doradus by Schlieder et al. (2012a), which was later downgraded to 0 per cent by Binks and Jeffries (2016); however, the primary was also classified as being a member of the Castor moving group (Barrado y Navascues, 1998) with 75 per cent confidence (Klutsch et al., 2014). Figure 2.13 strongly indicates that J1004+5022 is consistently weaker in the alkali lines, as would be expected for an L3 γ object.

2.5 Summary

We have presented the low and mid resolution optical GTC/ OSIRIS spectra of 53 objects observed between 2015 and 2016. Our data reduction was non-standard, using a pipeline package, `PyPeIt`; this reduction was validated with an independent IRAF spectral extraction and calibration for one of the objects. We used `kastredux` to create 53 automated spectral types, six of

which are for objects not yet spectrally typed, alongside the established technique of comparing against spectral standard template spectra. We found that our chosen spectral reduction package, PypeIt, introduced some non-optimal artefacts during reduction. One example is a spike appearing near the O₂ A band from the telluric correction procedure, which required interpolating over for visualisation purposes (it does not affect wavelength solutions).

In addition to using new data reduction software, we also used novel analysis software, `rvfitter`, that we developed to perform manual line centering and cross-correlation (against BT-Settl CIFIST models). The `rvfitter` code also used an uncertainty-weighted mean to create an adopted RV. This produced 46 radial velocities, 29 of which are new, which we have validated against standard IRAF and IDL software techniques. The cross-correlation also produced mean T_{eff} and $\log g$ values for all 53 objects.

In this work, we performed further analysis on our spectral types, RVs and T_{eff} values by making comparisons to the literature where appropriate and ensuring all results were within two spectral sub-types, $\Delta RV < 2\sigma$ and $\Delta T_{\text{eff}} < 2\sigma$ (against \widehat{T}_{eff} and *Gaia* DR3 `teff_espucl`). We then discussed any measurements which did not conform with these standards. There were four objects that we classified through BANYAN Σ as being a member of a young moving group; we continued with the same discussion on objects that had potential young moving group classifications (>10 per cent). There were two objects we placed as members of the thick disc, one of which we deemed as a statistically likely member.

Finally, by relating to gravity sensitive alkali lines and the aforementioned young moving group members, we discuss the interesting young candidates J1246+4027 and J1004+5022. 2MASSW J1246467+402715 (J1246+4027) has a potential lithium indication and is otherwise an L4 β field object. G 196-3B (J1004+5022) is confirmed as a young object, as was known from its primary companion.

In conclusion, this work was part of the GUCDS series of papers. The kinematic analysis of the spectra observed and presented here is a sizeable contribution to the total number of 6-D complete L dwarfs. A number of interesting objects were identified or confirmed, either into young moving groups or young field objects. We used novel open-source techniques at all stages of our procedure, which we make available to the astronomical community. These techniques have been compared with established and accepted techniques in order to generate a baseline of trust. The observation campaign to complete the 30 pc sample is ongoing, with predominantly

NIR spectrographs. This campaign will continue to produce work discussing, expanding and exploring this 30 pc sample.

Data availability

The data underlying this article will be available in CDS VizieR, the GUCDS Data Browser, and the SIMPLE Database. The code used to generate the reduced spectra and analysis is available either through open-source repositories (see Cooper, 2022b, and the acknowledgements) or upon any reasonable request.

Chapter 3

Ultracool Dwarfs in *Gaia*

Although I am listed as a co-author on most *Gaia* papers from EDR3 onwards; my contribution to *Gaia* was part of CU8 (Astrophysical Parameters), notably Creevey et al. (2023). I had a larger role in the *Gaia* EDR3 validation, through the ‘*Gaia* Catalogue of Nearby Stars’ (GCNS, Gaia Collaboration et al., 2021f); and, the ‘Ultracool Dwarfs in *Gaia* DR3’ publication (Sarro et al., 2023), discussing the UCD population of *Gaia* DR3. I led the section on the stellar to substellar boundary in Gaia Collaboration et al. (2021f, Section 3.1) and the discussion of *Gaia* RP spectra in Sarro et al. (2023, Section 3.2).

3.1 *Gaia* Catalogue of Nearby Stars

The full sky coverage and high-precision observations of *Gaia* offer the means of uncovering nearby UCDs through astrometric rather than purely photometric selection (Reyl , 2018; Smart et al., 2019; Scholz, 2020). *Gaia* provides a large homogeneous sample. The capability of *Gaia* to study the stellar to substellar boundary is illustrated in Sect. 5.2 (Gaia Collaboration et al., 2021f), where the luminosity function can be computed for the first time with one unique dataset throughout the main sequence down to the brown dwarf regime. It nicely shows a dip in the space density at spectral type L3, defining the locus of the stellar to substellar boundary.

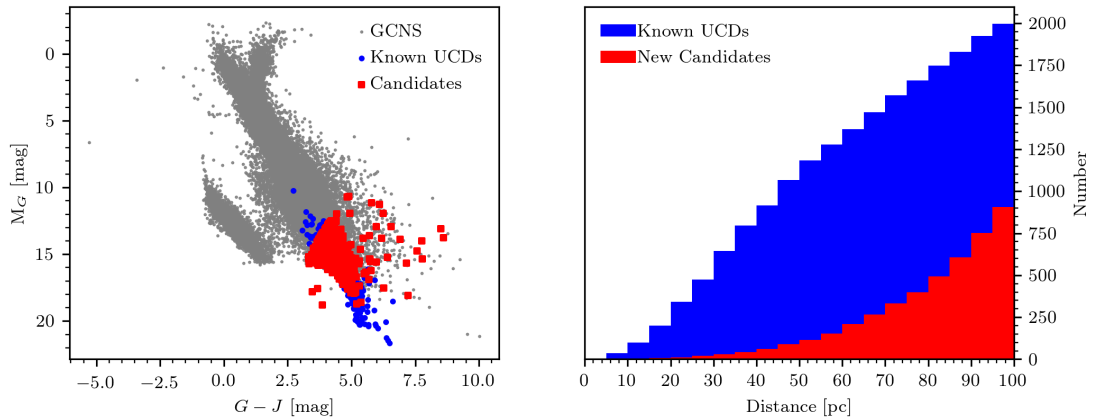


FIGURE 3.1: Left: M_G vs. $G - J$ diagram of stars in GCNS that are not found in *Gaia* DR2. The red dots are new UCD candidates, the blue points are known UCDs (spectral types between M7 and T8), and the grey points are the full GCNS sample. The new candidates are selected following the condition $M_G > -3 \times (G - J) + 25$, after removing stars whose probability of being a WD is higher than 20%. Right: Distance distribution of the new candidates in the GCNS (red) and the known UCDs (blue).

3.1.1 New UCD candidates in *Gaia* DR3

As mentioned in Sect. 4.2 (Gaia Collaboration et al., 2021f), the GCNS contains thousands of faint stars (WDs and low-mass stars) that have no parallax from *Gaia* DR2. We investigate the potential new UCD candidates in the GCNS in more detail. Following the selection procedure from Reylé (2018), we selected UCD candidates from the M_G versus $G - J$ diagram (Fig. 3.1, left panel). The GCNS contains 2879 additional candidates compared to *Gaia* DR2, 1016 of which have a median distance inside 100 pc. This is a valuable contribution to complete the solar neighbourhood census in the region of the stellar to substellar boundary, as shown in the right panel of Fig. 3.1.

In Fig. 3.2 we examine $G_{BP} - G_{RP}$ versus M_J for known UCDs taken from the *Gaia* Ultracool Dwarf Sample (Smart et al., 2017, 2019). The non-monotonic decrease of M_J with $G_{BP} - G_{RP}$ indicates that G_{BP} is unreliable in the UCD regime, in agreement with the conclusions in Smart et al. (2019). For a full discussion and explanation of the limits on G_{BP} , see Riello et al. (2021).

3.1.2 GCNS completeness in the UCD regime

We show the simulated completeness for M7-L8 in Fig. 3.3. This was calculated using median absolute magnitudes M_G and standard deviations for each spectral type derived from the GCNS sample (in Sect. 4.2 Gaia Collaboration et al., 2021f) and assuming a sky-isotropic G apparent

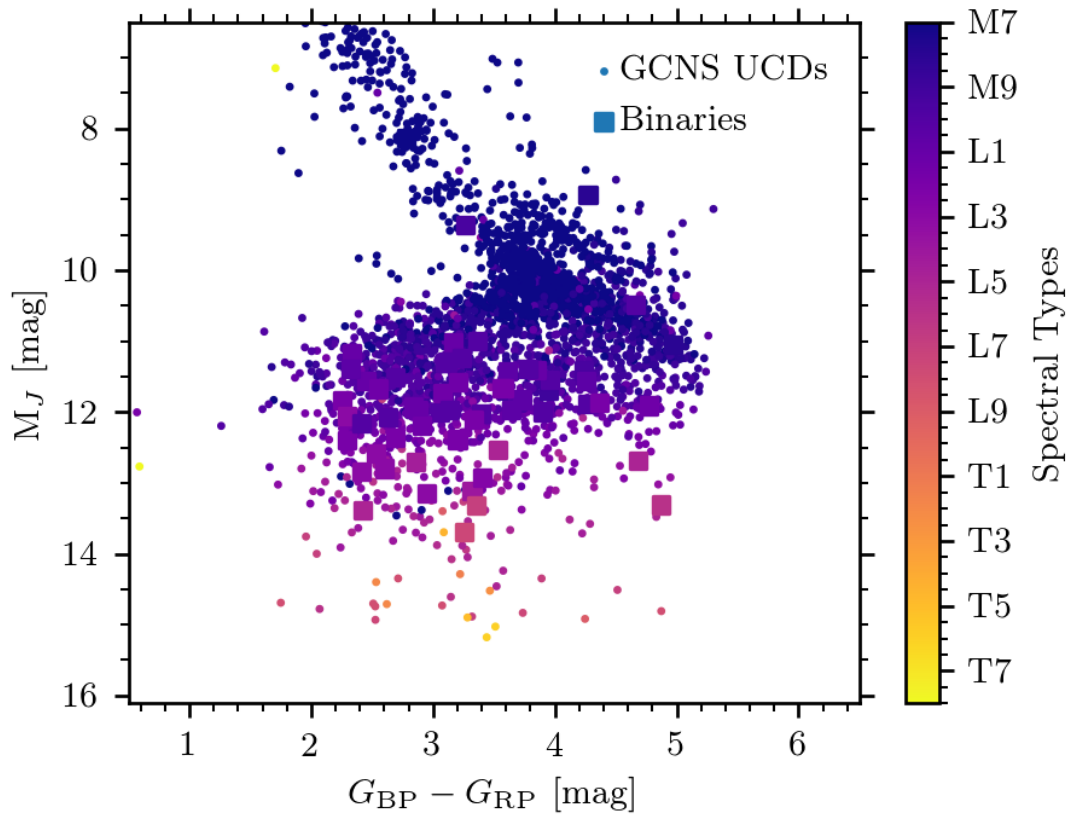


FIGURE 3.2: CAMD of $G_{BP} - G_{RP}$ [mag] against M_J [mag]. The full sample is from the GUCDS, and known binaries are over plotted as squares. Points are coloured by their published spectral types.

magnitude limit of 20.4 mag with Monte Carlo sampling. Fig. 3.3 indicates that an incompleteness begins at spectral type M7 and increases until L8, where the catalogue is only complete for the first 10 pc. The standard deviations of absolute magnitudes per spectral type bin are large (0.5 to 1 mag) and often have small sample sizes; therefore, the noise in these simulations was quite large, which explains the crossing of the mean relation for some sequential spectral types.

3.1.3 UCD empirical completeness exceptions

We considered the simulated completeness from Fig. 3.3 with respect to a known sample, objects in the GUCDS identified in one of the *Gaia* releases, and spectral type from M7 to T6. This corresponds to 2925 sources. We find that 98 objects were not included in the GCNS that are in *Gaia* DR3, but they either do not have parallaxes (34) or failed our probability selection (25), and 39 had parallaxes < 8 mas. Of the 34 objects that did not have parallaxes, 21 did have parallaxes in *Gaia* DR2 but the five-parameter solutions in *Gaia* DR3 were not published because their

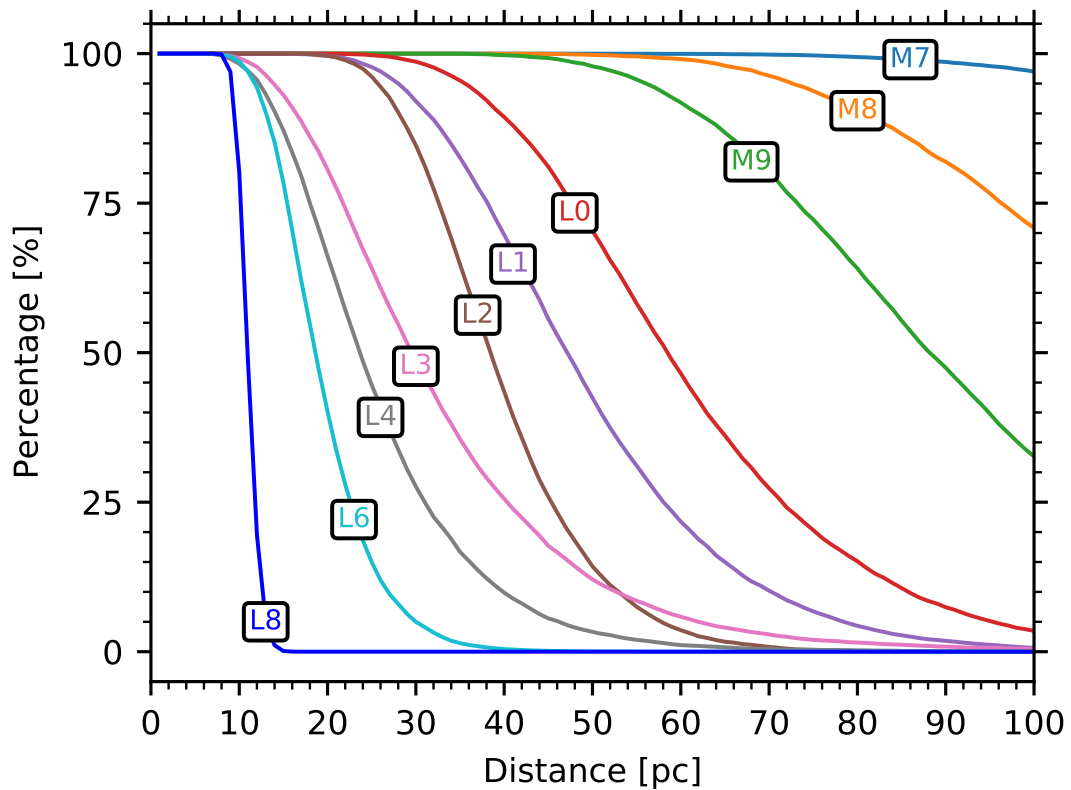


FIGURE 3.3: Simulated completeness per parsec for each spectral type. Each spectral type from M7-L8 (right to left) is labelled next to its respective simulated completeness level. We skip L5 and L7 for better readability.

$\text{astrometric_sigma5d_max} > 1.2 \text{ mas}$. This could be because these objects are non-single or simply because they are very faint and at the limit of our precision.

An example of a system that we would expect to be in the GCNS is the nearby L/T binary Luhman 16 AB; *Gaia* DR2 5353626573555863424 and 5353626573562355584 for A and B, respectively, with $\pi = 496 \pm 37 \text{ mas}$ (Luhman, 2013) and $G = 16.93$ & $G = 16.96 \text{ mag}$. The primary is in *Gaia* DR2 and *Gaia* DR3 (without complete astrometric solution in either), whilst the secondary is only in *Gaia* DR2. This is a very close binary system with a short period, so that the use of a single-star astrometric solution may result in significant residuals that may have resulted in its exclusion in the current release.

3.2 Ultracool Dwarfs in *Gaia* DR3

Gaia DR3 includes for the first time the BP and RP low-resolution spectra described in De Angeli et al. (2023). Since UCDs are intrinsically faint and very red objects, their BP spectra only contain noise in all but the brightest and hottest candidates and even there, only at the reddest wavelengths. Hence, we only discuss here the RP spectra.

Figure 5 (Sarro et al., 2023) shows in turquoise simulations of BT-Settl synthetic spectra obtained using the Mean Instrument Object Generator (MIOG, briefly described in Creevey et al., 2023). The spectral types were assigned from the BT-Settl T_{eff} using the Stephens et al. (2009) calibration. The black lines correspond to the median RP spectrum in each spectral type (assigned again using the same calibration and the ESP-UCD temperatures), and the red lines show spectral type standards defined by us starting from known optical spectral type standards within 20 pc (c.f. Table 13, Kirkpatrick et al., 2019) which have RP spectra, then increased in number with the addition of manually inspected bright objects from the GUCDS (Smart et al., 2017). These standards are shown in Table 3.1.

We endeavoured to balance maintaining an acceptable number of RP spectra for each spectral type and ensuring that the RP spectra of the selected standards were visually similar and consistent. Naturally, this is challenging as there is a very limited number of dwarfs of spectral type later than mid-L for which good quality RP spectra are available. The differences are evident and they do not simply correspond to effective temperature offsets that could be explained by a different spectral type-temperature calibration. In Sect. 6 (Sarro et al., 2023) we study UCDs in the catalogue that we identify as young and therefore potentially useful in defining low gravity diagnostics based on their RP spectra. The detection of subdwarfs in the catalogue will be addressed in a subsequent paper Cooper et al. (submitted).

At the low resolution typical of the RP spectra (50–30 in $\lambda/\Delta\lambda$ Montegriffo et al., 2022), individual features cannot be discerned since multiple nearby spectral features, both lines and bands, are blended and merged. The systematic changes and dependencies of the RP spectra with astrophysical parameters such as T_{eff} , $\log g$ or metallicity are not immediately evident due to this blending of spectral features. Also because the effects in different features appear as opposing factors that can cancel out or partially compensate each other. Figure 5 (Sarro et al., 2023) shows how these merged absorption features differ with spectral type. For example, the majority of RP spectra of L dwarfs have a peak near 800 nm, the strength of which (and its

TABLE 3.1: List of standard UCDs used to calibrate the ESP-UCD module empirical training set in effective temperature. Astrometry is from *Gaia* DR3 and the T_{eff} values are those produced by the ESP-UCD Apsis module and published as part of the Data Release.

<i>Gaia</i> DR3 Source ID	α (hms)	δ (dms)	ϖ (mas)	Object Name	Spectral Type	T_{eff} [K]
4293315765165489536	19 16 57	+5 08 39.7	169.0 ± 0.1	VB 10 ¹	M8 ²	2404 ± 8
1287312100751643776	14 28 43	+33 10 27.9	91.2 ± 0.1	LP 271-25 ³	M9 ⁴	2238 ± 9
5761985432616501376	8 53 36	-3 29 35.4	115.5 ± 0.1	LP 666-9 ³	M9 ⁴	2272 ± 26
4595127343251508992	17 31 30	+27 21 19.2	83.7 ± 0.1	LSPM J1731+2721 ⁵	L0 ⁶	2233 ± 24
31235033696866688	3 14 03	+16 03 04.6	72.6 ± 0.2	2MASS J03140344+1603056 ⁷	L0 ⁶	2201 ± 40
3701479918946381184	12 21 28	+2 57 19.1	53.8 ± 0.2	2MASS J12212770+0257198 ⁷	L0 ⁸	2210 ± 41
3457493517036545280	6 02 31	+39 10 50.5	85.8 ± 0.1	LSR J0602+3910 ⁹	L1 ¹⁰	2044 ± 24
3802665122192531712	10 45 23	-1 49 57.9	58.8 ± 0.2	2MASS J10452400-0149576 ¹¹	L1 ¹²	2073 ± 71
3808159454810609280	10 48 42	+1 11 54.5	66.6 ± 0.2	LSPM J1048+0111 ¹¹	L1 ⁸	2077 ± 38
1649407285800074240	16 58 03	+70 26 56.7	54.1 ± 0.1	LSPM J1658+7027 ¹³	L1 ¹³	2069 ± 39
3460806448649173504	11 55 40	-37 27 48.2	84.7 ± 0.1	2MASS J11553952-3727350 ¹²	L2 ¹²	1978 ± 31
4878035808244168832	4 45 54	-30 48 27.4	61.9 ± 0.1	2MASS J04455387-3048204 ¹⁴	L2 ¹⁵	2017 ± 47
5723739672264914176	8 28 34	-13 09 19.4	85.6 ± 0.1	SSSPM J0829-1309 ¹⁶	L2 ¹⁶	1981 ± 51
851053031037729408	10 51 19	+56 13 03.6	63.9 ± 0.1	2MASS J10511900+5613086 ⁷	L2 ⁶	2025 ± 81
5733429157137237760	8 47 29	-15 32 40.6	57.5 ± 0.2	SIPS J0847-1532 ¹⁴	L2 ⁸	2040 ± 50
4910850870213836928	1 28 26	-55 45 32.5	53.9 ± 0.2	SIPS J0128-5545 ¹⁷	L2 ¹⁸	1993 ± 65
11825274753387703680	15 06 53	+13 21 05.9	85.4 ± 0.2	2MASSW J1506544+132106 ¹⁹	L3 ¹³	1787 ± 56
167202325215063168	4 01 37	+28 49 51.1	80.4 ± 0.2	2MASS J04013766+2849529 ²⁰	L3 ²⁰	1872 ± 59
1329942262499164544	16 15 44	+35 58 51.1	50.2 ± 0.3	2MASSW J1615441+355900 ²¹	L3 ²¹	1791 ± 216
3238449635184620672	5 00 21	+3 30 44.5	75.6 ± 0.3	2MASS J05002100+0330501 ⁷	L3 ²²	1735 ± 119
3562717226488303360	10 58 48	-15 48 16.8	55.1 ± 0.3	SIPS J1058-1548 ²³	L3 ²⁴	1834 ± 109
6118581861234228352	14 25 28	-36 50 30.8	84.4 ± 0.3	2MASS J14252798-3650229 ²⁵	L4 ²²	1819 ± 52
5908794218026022144	17 53 45	-66 00 01.1	63.6 ± 0.3	SIPS J1753-6559 ⁷	L4 ¹⁸	1703 ± 147
6306068659857135232	15 07 48	-16 27 54.5	134.9 ± 0.3	2MASSW J1507476-162738 ¹⁹	L5 ²¹	1552 ± 102
2467182154313027712	1 44 36	-7 16 17.5	78.5 ± 0.5	2MASS J01443536-0716142 ²⁶	L5 ⁸	1603 ± 90
3698979462002285824	12 03 57	+0 15 45.6	66.3 ± 0.5	2MASS J12035812+0015500 ²⁷	L5 ²⁸	1642 ± 219
3597096309389074816	12 13 03	-4 32 44.3	59.1 ± 0.6	2MASS J12130336-0432437 ¹⁴	L5 ²⁸	1580 ± 152
4220379661283166720	20 02 51	-5 21 54.4	56.7 ± 1.4	2MASS J2002507-052152 ²⁹	L6 ⁸	1547 ± 187
4371611781971072768	17 50 24	-0 16 11.8	108.6 ± 0.2	2MASS J17502484-0016151 ³⁰	L6 ³¹	1542 ± 71
1954170404122975232	21 48 17	+40 04 06.7	123.7 ± 0.4	2MASSW J2148162+400359 ³²	L6 ⁸	1511 ± 160
4752399493622045696	2 55 05	-47 01 00.2	205.4 ± 0.2	DENIS J025503.3-470049 ³³	L8 ⁸	1365 ± 38
5052876333365036928	2 57 27	-31 05 46.7	102.7 ± 0.5	2MASS J02572581-3105523 ¹⁵	L8 ⁸	1354 ± 71
1037131492704550656	8 57 58	+57 08 45.2	72.7 ± 0.7	2MASS J08575849+5708514 ¹¹	L8 ¹¹	1361 ± 316
3426333598021539840	6 07 38	+24 29 51.7	138.1 ± 0.5	2MASS J06073908+2429574 ³⁴	L9 ²⁰	1355 ± 105
2997171394834174976	5 59 20	-14 04 54.6	95.3 ± 0.7	2MASS J05591914-1404488 ³⁵	T5 ³⁶	1147 ± 86
1267906854386665088	15 03 20	+25 25 28.7	155.8 ± 0.8	2MASS J15031961+2525196 ³⁷	T6 ³⁷	1132 ± 102

References: 1. Luyten (1955), 2. Kirkpatrick et al. (1991), 3. Luyten (1979), 4. Reid and Gizis (2005), 5. Lépine and Shara (2005), 6. Reid et al. (2008), 7. Reid et al. (2006), 8. Schneider et al. (2014), 9. Lépine et al. (2002b), 10. Salim et al. (2003), 11. Hawley et al. (2002), 12. Gizis (2002), 13. Gizis et al. (2000), 14. Cruz et al. (2003), 15. Schmidt et al. (2007), 16. Scholz and Meusinger (2002), 17. Deacon and Hambly (2007), 18. Marocco et al. (2013), 19. Reid et al. (2000), 20. Castro et al. (2013), 21. Kirkpatrick et al. (2000), 22. Gagné et al. (2015a), 23. Delfosse et al. (1997), 24. Kirkpatrick et al. (1999), 25. Kendall et al. (2004), 26. Hall (2002), 27. Fan et al. (2000), 28. Bardalez Gagliuffi et al. (2014), 29. Cruz et al. (2007), 30. Kendall et al. (2007a), 31. Burgasser et al. (2010), 32.Looper et al. (2008), 33. Martín et al. (1999b), 34. Castro and Gizis (2012), 35. Burgasser et al. (2000), 36. Geballe et al. (2002), 37. Burgasser et al. (2003)

redward trough) is affected by the pressure broadening on the K I resonance doublet (which strengthens with spectral type, Tinney and Reid, 1998), by the weakening of Na I (again with spectral type) and by a weakening of TiO (vanishing in the early L types but still present in late M). We use ground-based optical spectra to better understand the morphological features seen in *Gaia* RP spectra. This is demonstrated in Figure 3.4, which shows simulated RP spectra of mid-resolution spectra from the GTC/OSIRIS instrument for a selected sequence of objects. This same sequence is also illustrated in Figure 3.5 which shows the externally calibrated (c.f. `gaiaxy.calibrate`) RP spectra (Montegriffo et al., 2022). It shows spurious oscillations and significant discrepancies with respect to the ground-based spectra (particularly evident in the L5 case). The appearance of these oscillations is discussed in Montegriffo et al. (2022) and is

not yet fully understood. However, the apparent amplification of these wiggles at longer wavelengths is due to the fact that the externally calibrated SEDs are normalised by the inverse of the response model, which in the RP case drops quickly to very small values beyond 900 nm. These externally calibrated spectra were not used as input to Apsis or ESP-UCD. ESP-UCD and the rest of Apsis modules used only internally calibrated spectra for the prediction of astrophysical parameters.

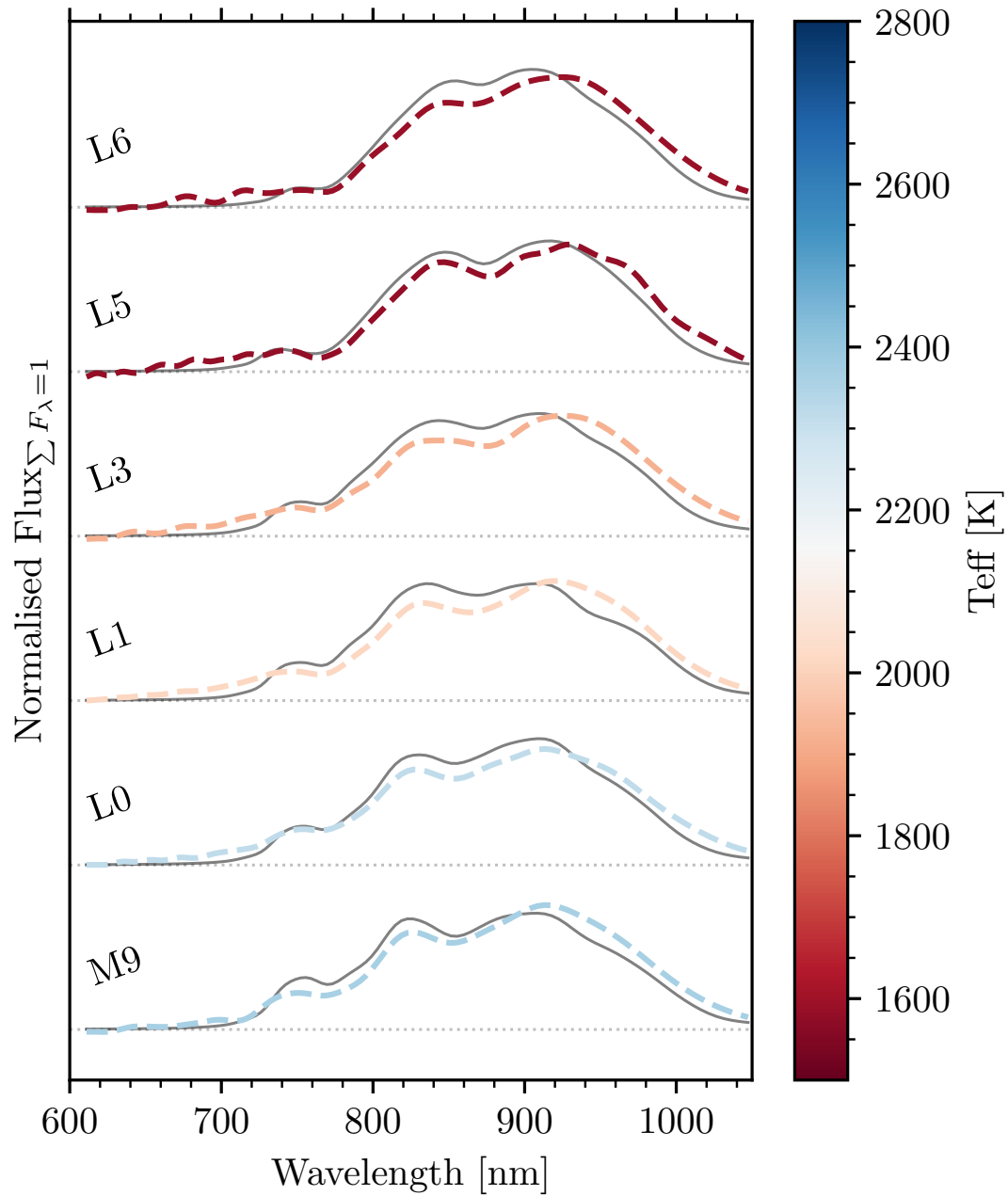


FIGURE 3.4: In dark grey, ground-based optical spectra from the GTC (Cooper et al., submitted). These spectra have been simulated from the original spectra by passing through MIOG. The objects shortnames are: J1717+6526 - L6, J1213-0432 - L5, J0453-1751 - L3, J1745-1640 - L1, J0935-2934 - L0, J0938+0443 - M9. Over-plotted are RP spectra coloured by effective temperature and labelled by spectral type. All fluxes are normalised by the area and linearly offset.

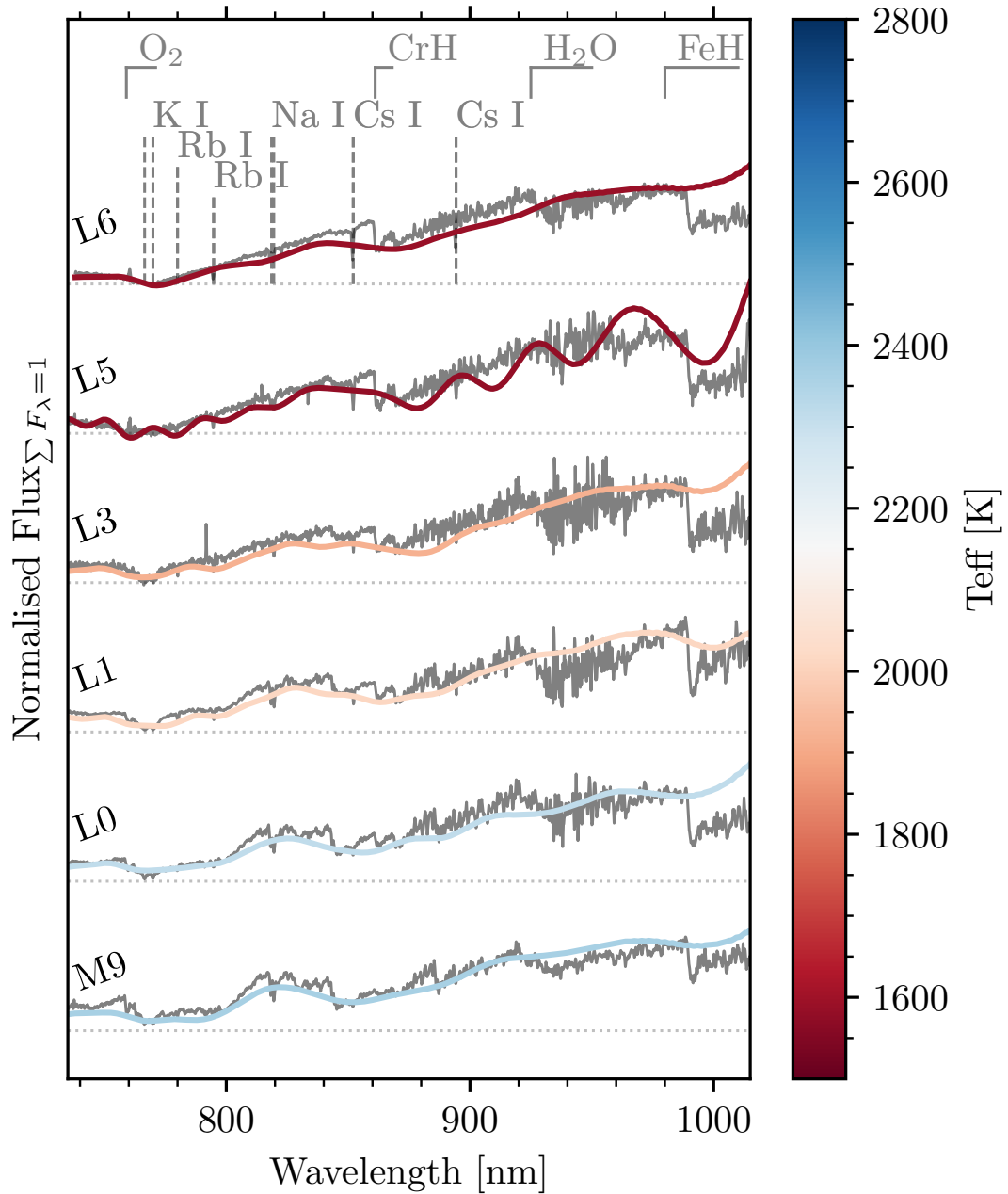


FIGURE 3.5: As Figure 3.4 but for externally calibrated RP spectra. The calibrated spectra were constructed using the `gaiaxy.calibrate` function. The GTC spectra as shown here have not been passed through MIOG and represent the actual spectra with resolution ≈ 2500 . A selection of features typical of late M - mid L dwarfs are shown above.

Chapter 4

Ultracool Spectroscopic Outliers in *Gaia* DR3

Here, I present the work on classifying *Gaia* UCDs as outlying objects, either subdwarfs or young objects. The work in this chapter constitutes my accepted ‘Ultracool Spectroscopic Outliers in *Gaia* DR3’ work (Cooper et al., 2023) where ‘we’ refers to myself, and the co-authors.

Abstract

Gaia DR3 provided a first release of RP spectra and astrophysical parameters for ultracool dwarfs. We used these *Gaia* RP spectra and astrophysical parameters to select the most outlying ultracool dwarfs. These objects have spectral types of M7 or later and might be young brown dwarfs or low metallicity objects. This work aimed to find ultracool dwarfs which have *Gaia* RP spectra significantly different to the typical population. However, the intrinsic faintness of these ultracool dwarfs in *Gaia* means that their spectra were typically rather low signal-to-noise in *Gaia* DR3. This study is intended as a proof-of-concept for future iterations of the *Gaia* data releases. Based on well studied subdwarfs and young objects, we created a spectral type-specific color ratio, defined using *Gaia* RP spectra; this ratio is then used to determine which objects are outliers. We then used the objects kinematics and photometry external to *Gaia* to cut down the list of outliers into a list of ‘prime candidates’. We produce a list of 44 *Gaia* RP spectra outliers, seven of which we deem as prime candidates. Of these, six are likely subdwarfs

and one is a known young stellar object. Four of six subdwarf candidates were known as subdwarfs already. The two other subdwarf candidates: 2MASS J03405673+2633447 (sdM8.5) and 2MASS J01204397+6623543 (sdM9), are new classifications.

4.1 Introduction

Subdwarfs are old objects, with lower metallicities than field objects. As such, multi-wavelength photometric cross-matches are an ideal method to select subdwarf candidates. Notably, optical surveys like *Gaia* (Gaia Collaboration et al., 2016) and Pan-STARRS (Chambers et al., 2016) are typically compared with near/mid-infrared surveys including 2MASS (Skrutskie et al., 2006) and AllWISE (Cutri et al., 2013). Kinematically, subdwarfs, due to their age, are much faster than field objects. Hence, subdwarfs (depending on their metallicity and age) are either thick disk or halo objects. Multiple literature sources discuss the selections and classifications of thick disk/halo dwarfs, for example, work by Leggett (1992). For purely kinematic selections of halo objects, when metallicity information is not present, Nissen and Schuster (2010) utilised either a cut of $V_{\text{total}} > 180 \text{ km s}^{-1}$ (Venn et al., 2004) or $V_{\text{total}} > 210 \text{ km s}^{-1}$ (Schönrich and Binney, 2009; Koppelman et al., 2018, depending on the Galactic model used) where V_{total} is the total space velocity, $V_{\text{total}} = \sqrt{U^2 + V^2 + W^2}$, and U, V, W are the velocities in the Galactic reference frame. Likewise, selection of thick disk objects varies from $V_{\text{total}} > 85 \text{ km s}^{-1}$ (Zhang and Zhao, 2006) to $V_{\text{total}} > 70 \text{ km s}^{-1}$ (Nissen and Schuster, 2010) and $V_{\text{total}} > 50 \text{ km s}^{-1}$ (Gaia Collaboration et al., 2023b). Without radial velocity (RV) information, tangential velocity, V_{tan} , has been often used as it is highly indicative of thick disc/halo membership. Ultracool subdwarfs follow this same detection criteria (Gizis, 1997; Gizis and Reid, 1999). We follow previous work discovering ultracool subdwarfs (e.g., Zhang et al., 2017a, 2019) which has benefit from the selection of subdwarfs using virtual observatory tools (Lodieu et al., 2012, 2017) and all-sky surveys (Lépine et al., 2002b; Lépine, 2008).

By comparison, young objects have typically lower surface gravities and are redder than field objects (Cruz et al., 2016). Unresolved binaries often occupy the same space on colour-absolute magnitude diagrams (CMDs) as young objects, hence purely photometric selections are contaminated (e.g., Marocco et al., 2017). Kinematically, young objects are slower than field objects, and are often still gravitationally bound to young moving groups (Gagné and Faherty, 2018, and references therein). Gathering spectra of UCD candidates is therefore necessary for confirming youth, especially when the objects are isolated. The spectral confirmation of youth involves

analysing the surface gravity of the UCD, where a lower gravity indicates a younger object. Optical spectra are given Greek letter classifications with α as normal, β as intermediate, γ as low gravity (Cruz et al., 2009) and δ for extreme low gravity (Kirkpatrick et al., 2006).

Gaia is a European Space Agency mission launched in 2013 and in June 2022 released *Gaia* DR3 (Gaia Collaboration et al., 2023i) which, importantly for this work, included spectra. This is referred to as ‘XP’ spectra where ‘X’ can be interchanged with either ‘B’ or ‘R’ corresponding to the blue and red filters. *Gaia* provides five dimensional astrometric measurements (two positions, two proper motions and parallax). *Gaia* also released RVs for objects with $G_{\text{RVS}} \lesssim 14$ mag (Katz et al., 2023), where G_{RVS} is the magnitude integrated across the *Gaia* RV spectrometer (RVS, Sartoretti et al., 2023). We focus here on RP spectra, which cover the far red optical regime from ≈ 600 – 1050 nm. The resolution of these internally calibrated spectra for UCDs are around 30 – $50 \frac{\Delta\lambda}{\lambda}$ (Montegriffo et al., 2023, who also discuss the external calibration). However, at the low resolution of *Gaia* RP spectra, individual features cannot be seen, leading to a merging of features (Sarro et al., 2023).

Recently, many discoveries have been using *Gaia* data with the focus of finding outlying objects and astrophysical parameters. For example, exploration of hot subdwarf stars in *Gaia* DR3 (Culpan et al., 2022) found 21 785 underluminous objects. Yao et al. (2023) uncovered 188 000 candidate metal-poor stars using *Gaia* XP spectra. Similarly, Andrae et al. (2023b), following the study by Anders et al. (2023), applied XGBoost to determine metallicities for main-sequence dwarfs and giants. Parameters of stars, forward modelled from *Gaia* XP spectra, were also determined by Zhang et al. (2023).

In UCDs, spectral feature changes due to age or metallicity are not directly seen in the RP spectra, as the spectra are too low resolution to readily be isolated, they do however change the general shape of the RP spectra, most notably the centroids and intensity of the 2–3 peaks (Fig. 4.1 in this work and fig. 5 by Sarro et al., 2023). As effective temperature decreases in Fig. 4.1, the first peak (~ 750 nm) disappears when approaching the stellar/substellar boundary ($\approx L3$, Gaia Collaboration et al., 2021f) whilst the second peak goes from being brighter than the third peak in M dwarfs, to being dimmer than the third peak in L dwarfs and being roughly equivalent in T dwarfs. In addition, the centroids of the peaks shift to the red with decreasing T_{eff} .

This work is focused on the characterisation of the *Gaia* internally calibrated RP spectra and the isolation of young and subdwarf UCDs. Section 4.2 discusses the methodology, and the creation of a colour ratio; Section 4.3 is the analysis and selection of prime candidates from

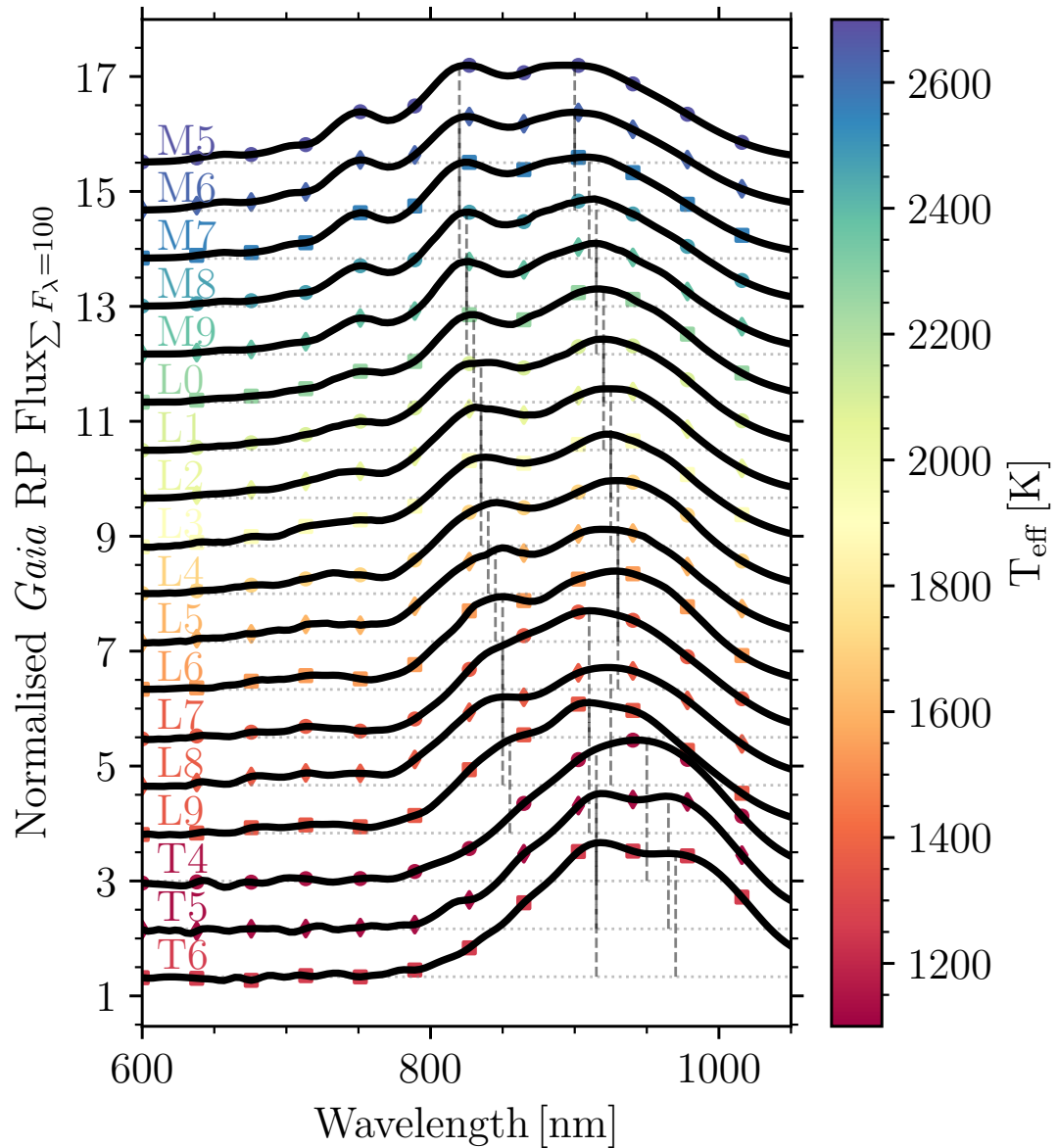


FIGURE 4.1: The normalised median RP fluxes for each spectral type (see Sect. 4.2.2) from M5–T6. Each spectral type is indicated by the attached text with its corresponding median effective temperature given on the auxiliary axis. Vertical dashed lines are shown for every spectrum to indicate the position of the two primary spectral peaks. The normalised spectra were multiplied by a constant value such that the fluxes sum to 100 instead of 1 and are offset by a set value.

external photometry and kinematics; Section 4.4 show the results of our prime candidates whilst Section 4.5 concludes and plans future work to counter the known issues.

4.2 Method

Here we discuss our iterative approach to deriving an outlier classifier. We started with the sample of UCDs in *Gaia* as discussed by Sarro et al. (2023). To summarise, the sample of *Gaia* UCDs consists of every object for which the ESP-UCD work package derived an effective temperature. The selection of UCDs from *Gaia* was: $\varpi > 1.7$ mas, $G - G_{\text{RP}} > 1$, $q_{33} > 60$, $q_{50} > 71$, $q_{67} > 83$ where q_{33} , q_{50} , q_{67} are the 33.33, 50, 66.67 percentiles of the total RP flux respectively (Creevey et al., 2023). Of these 94 158 objects, only 21 205 have public RP spectra (see the online documentation and sect. 4 by De Angeli et al., 2023, for the *Gaia* spectra publication criteria). All effective temperatures discussed were from *Gaia* DR3, from the astrophysical parameters table and specific to the UCD work package ESP-UCD. The relevant columns originating from the ESP-UCD work package are `teff_espucd` and `flags_espucd`. One part of the *Gaia* DR3 RP spectra publication criteria, important for the search of spectral outliers, was that the *Gaia* RP UCD spectra were required to be one of the highest two quality flags (0–1, not 2 in `flags_espucd`). The flagging in ESP-UCD included measuring the Euclidean distance of a *Gaia* RP spectrum from its BT-Settl model counterpart. Whilst this requirement was vital for reducing the number of published *Gaia* RP contaminants, it prejudices our results against classifying the most extreme spectral outliers, as was expected for extreme and ultra-subdwarfs. Thus, our expected number of ‘prime candidates’ was diminished.

The RP spectra of these 21 205 objects were extracted with `gaiaxy.convert` (Ruz-Mieres, 2022) through the `gaiaxy-batch` package (Cooper, 2022a). The absolute sampling of the retrieved spectra is a linearly dispersed grid from 600–1050 nm. We used this wavelength sampling (and only plot RP spectra within that limit) because it roughly corresponds to the *Gaia* DR3 RP passband (≈ 620 – 1042 nm, Riello et al., 2021). All spectra were divided by the sum of the fluxes across the entire 600–1050 nm region (i.e. the total flux of normalised spectra is unity). This method of normalisation was chosen because other methods (e.g. dividing by a median flux of a given wavelength regime) could cause non-physical artifacts, especially for noisy spectra. Some *Gaia* RP spectra can exhibit *apparent* negative fluxes, as a result of the projection onto the Hermite base functions during their construction. We sample the wavelengths with a consistent linearly dispersed grid. Ergo, when one normalises all of the *Gaia* RP spectra by dividing by

the sum of the fluxes, the spectra are homogeneous in wavelength and absolute flux calibration, thus are comparable.

Instead of using an absolute magnitude to find outliers, such as the robust M_G to spectral type relation, the *Gaia* DR3 RP spectral sequence follows the optical spectral features which define spectral sub-types for different UCDs. Additionally, as discussed by Gaia Collaboration et al. (2021f), there is a large scatter in *Gaia* colours for UCDs for every spectral type bin. This scatter, present in all photometric selections, means the introduction of a large number of contaminants. Using spectra instead might prove a cleaner selection technique, even at the low resolution of *Gaia* DR3 RP spectra.

In this section, we discuss the additional data gathering used to complement *Gaia* DR3. This includes the cross-matching with external photometry as well our basic spectral typing method. The external photometry was used for validation in Section. 4.3 whilst the spectral typing was used to define bins when searching for outliers. We defined a new colour ratio and used this colour ratio to separate outlying UCDs from normal UCDs.

4.2.1 External cross-matching

Using the *Gaia* data archive, we first performed a ‘left join’ query against the pre-computed cross-matches for Pan-STARRS (Chambers et al., 2016), 2MASS (Skrutskie et al., 2006) and AllWISE (Cutri et al., 2013). A left join query keeps all data entries from the first table (our *Gaia* UCDs), and returns data from the secondary table in the case that there is a match, otherwise a NULL entry. From these cross-matches we noted that the Pan-STARRS join was much less complete than 2MASS or AllWISE. As such, Pan-STARRS was not used in the photometric analysis but was used for the further discussion on our prime candidates. The RP spectral sample was cross-matched with the GUCDS. The GUCDS contains thousands of known objects with spectral types from the literature. Of these, ≈ 270 are known subdwarfs, and are flagged as such within their spectral types. This cross-matched sample between our 21 205 sample, and the GUCDS, is of size 2565. The known subdwarfs and young objects from this GUCDS cross-match are shown in Appendix Table B.1 and were converted into Boolean flags from which we trained our candidate flagging techniques discussed below. Additionally, there exists a list of optical standards for a range of spectral types (see table 1, Sarro et al., 2023), which we use as part of our method and analysis. This list of standards was supplemented with

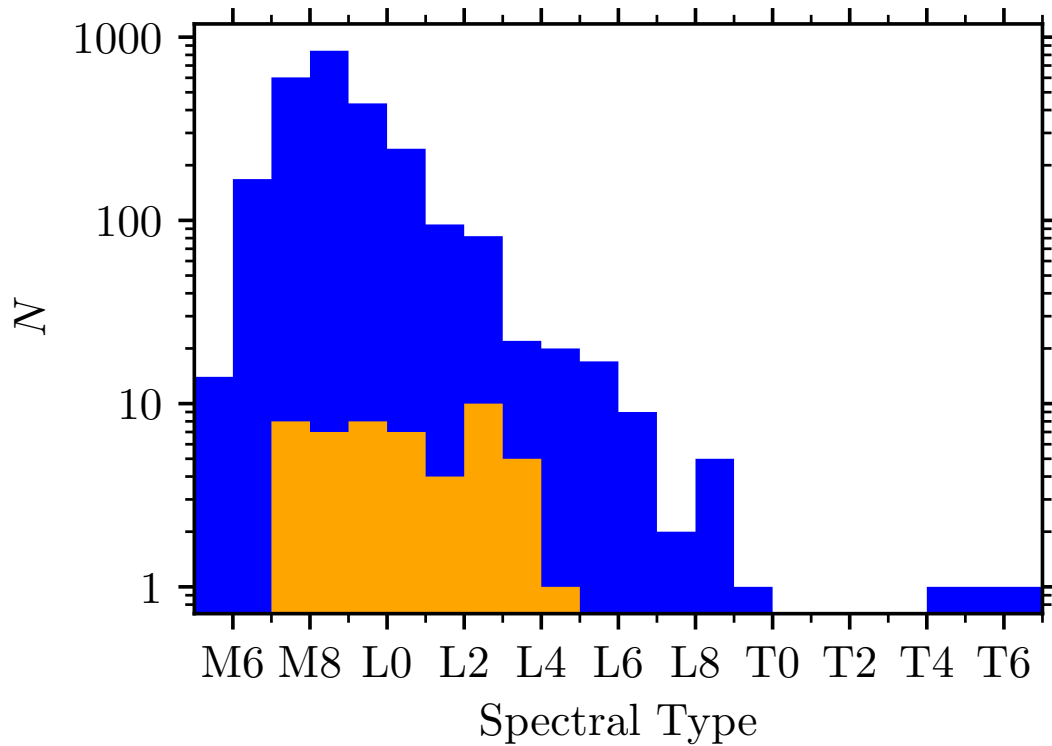


FIGURE 4.2: Histogram of the number of objects in each spectral type bin from the GUCDS. The full GUCDS is shown in blue whilst over plotted in orange is the distribution of the known standards used.

tens of visually selected bright RP spectra which were as similar as possible to each standard; the final list is hereafter referred to as ‘known standards’ and shown in orange in Fig. 4.2.

4.2.2 Estimating a spectral type

For discussing our objects on an individual basis, it is more meaningful to write in terms of spectral type than T_{eff} . As such, we discuss here a simplistic method for estimating spectral type from the T_{eff} values provided by *Gaia* DR3, $\tau_{\text{eff_espucd}}$. These spectral types estimated here were not used for any analysis. To more correctly ascertain spectral types, one would match the features and shapes of the RP spectra to well-known standards. This, however, is similar to our outlier detection technique, hence we seek to avoid any ‘cyclic’ analysis. All sources in our RP spectral sample have a derived effective temperature from *Gaia* DR3. However, known objects, including subdwarfs and young objects, are defined by their spectral types (‘SpT’, as that is a direct measurement) rather than effective temperatures, which are generally inferred from modelling. In the case of *Gaia* DR3, this modelling was trained on an empirical sample not containing any abnormal objects, like subdwarfs and young objects (Creevey et al., 2023; Sarro

TABLE 4.1: Polynomial coefficients for T_{eff} to spectral type relation in equation (4.1). Valid for $1150 < T_{\text{eff}} < 2700$ K or M6–T4.

a	6.38 ± 1.07	10^{-12}	K^{-4}
b	5.61 ± 0.88	10^{-8}	K^{-3}
c	1.83 ± 0.27	10^{-4}	K^{-2}
d	2.71 ± 0.35	10^{-1}	K^{-1}
e	227 ± 17		K

et al., 2023). Spectral type is known to have a direct relation to effective temperature, although there is significant scatter in T_{eff} for every spectral type. To convert the *Gaia* `teff_espucd` into a spectral type we derived a fourth order polynomial between the *Gaia* `teff_espucd` values and the GUCDS optical spectral types. This is shown in Fig. 4.3. This polynomial follows equation (4.1) with coefficients from Table 4.1, where spectral types are converted to numerical values using a code whereby M0=60, L0=70, T0=80, etc.

$$\text{SpT} = aT_{\text{eff}}^4 - bT_{\text{eff}}^3 + cT_{\text{eff}}^2 - dT_{\text{eff}} + e \quad (4.1)$$

4.2.3 Creating a colour ratio

Following literature definitions of spectral indices in the optical regime¹ (Kirkpatrick et al., 1999; Martín et al., 1999b; Geballe et al., 2002), we created a method for measuring a colour ratio (CR). This method used directly the `teff_espucd` values in bins of 100 K. We note here that one spectral type is not equivalent to 100 K, i.e. $\Delta 100\text{K} \neq \Delta 1\text{SpT}$. As for the change in terminology from ‘spectral index’ to ‘colour ratio’, this is because the internally calibrated *Gaia* RP spectra as shown in Fig. 4.1 are too low resolution to use standard spectral typing indices. This method created photometric bands centered on the two primary peaks one can see in the internally calibrated *Gaia* RP spectra (Fig. 4.1). *Gaia* Collaboration et al. (2023f) discuss the creation of synthetic photometry from *Gaia* XP spectra, which inspired our method. Due to the redshifting of these peaks with decreasing effective temperature we define two spectral T_{eff} -specific narrow bands (with width 50 nm), named ‘blue’ and ‘red’ respectively, where the central wavelength shifts with spectral type. These central wavelengths are the vertical dashed lines shown in Fig. 4.1. We linearly interpolate between each manually defined central wavelength against T_{eff} to account for the non-rounded T_{eff} values. The total region possibly

¹ Most spectral indices for UCDs are defined in the near infrared rather than the optical, see Reid et al. (2001); Burgasser et al. (2006); Bardalez Gagliuffi et al. (2014), and references therein.

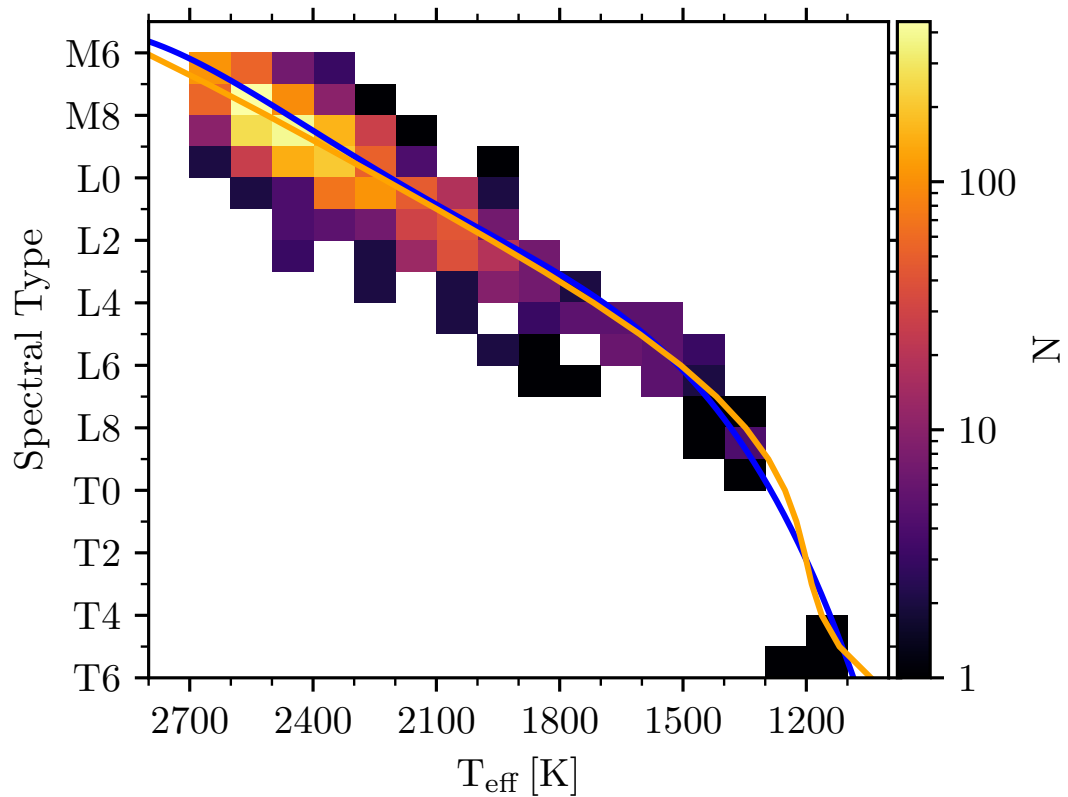


FIGURE 4.3: Spectral type conversion from T_{eff} [K] to spectral type for the GUCDS, as a 2-D histogram. The number of objects in each bin is shown by the colour bar. Our fourth order polynomial is shown as the blue line. By comparison, we plot in orange the fifth order polynomial (equation (4): Stephens et al., 2009) relation, valid from M6–T8. A wider spread of T_{eff} can be seen in the late M and early L dwarfs. This is a natural spread as each known spectral type will have an error margin of 1–2 spectral types.

bound by this relation is 795–995 nm, i.e. the lowest and highest wavelength within 25 nm of the central wavelengths.

These regions were decided by visually inspecting the known standards, subdwarfs and young objects from the literature (Fig. 4.4). The flux summed in blue, divided by the flux summed in red can be deemed a ‘colour’. To create CR we had to compare an object’s observed colour to an ‘expected’ colour.

We constructed a median RP normalised spectrum for every 100 K bin (using the *Gaia* T_{eff} , `teff_espucd`). Then we determined the colour for each median (i.e. the ‘expected’ colour). We created a linear spline relation between T_{eff} and this expected colour. Then, for every object, we measure the observed colour and compare it to the expected colour, extracted from the linear spline for that object’s T_{eff} . CR is each object’s observed colour divided by the expected colour, rounded to two decimal places.

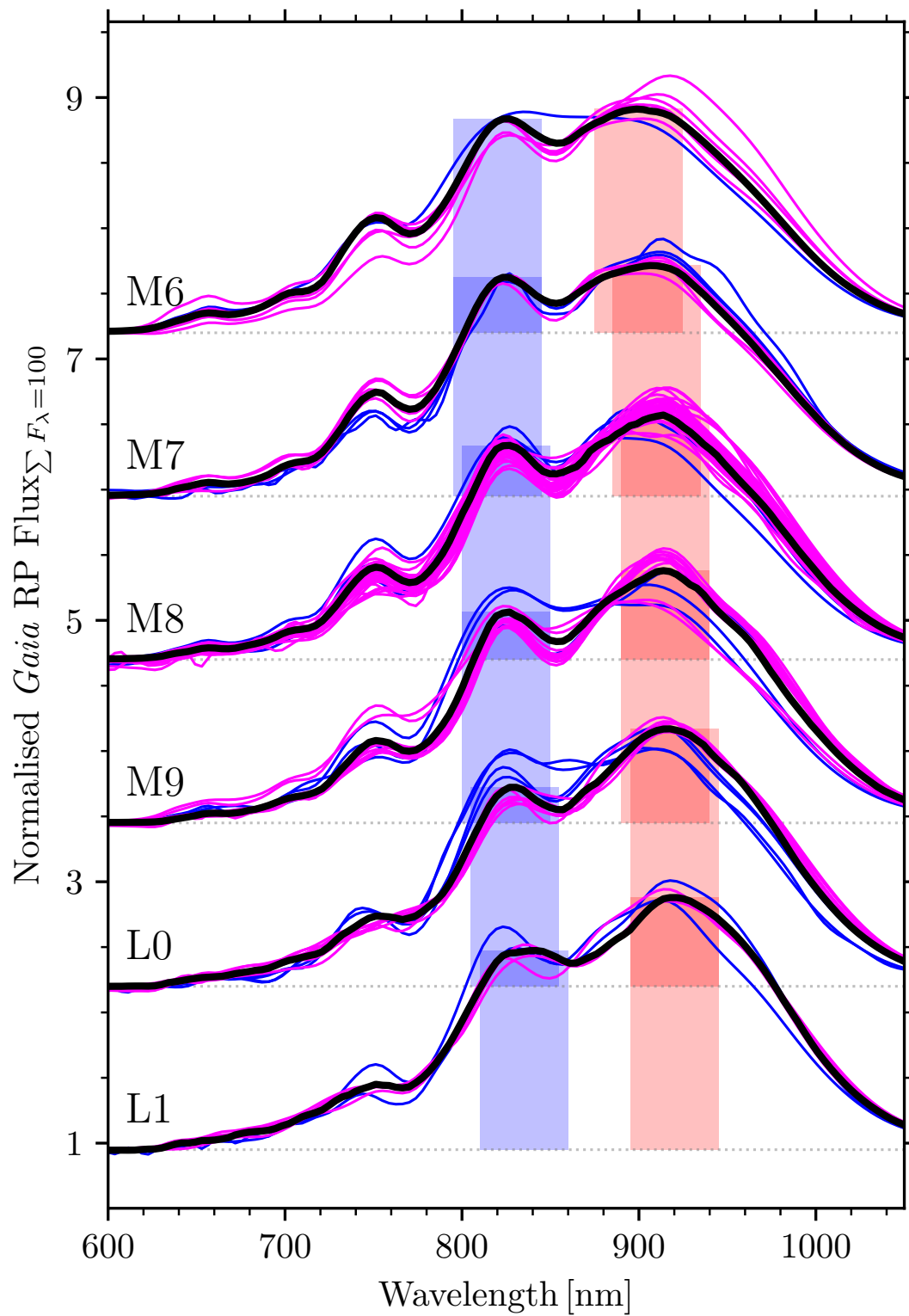


FIGURE 4.4: Internally calibrated RP spectra of known objects, separated by their literature optical spectral types. Magenta spectra are known young objects whilst blue spectra are known subdwarfs. Over-plotted in black is the median RP spectra for a given spectral type from known objects in the GUCDS. The blue and red bands are shown in their respective positions and colours as described in Section. 4.2.3. The normalised spectra were multiplied by a constant value such that the fluxes sum to 100 instead of 1 and are offset by a set value.

We sought outliers from CR to define candidate objects. Values of CR near 1 mean that object is normal. The median RP spectra of known objects are shown in Fig. 4.1, having been selected from the GUCDS by each spectral type bin from M5–T6. We used median RP spectra instead of the known standards in our CR derivation method because of the larger amount of objects and wider spectral coverage, with the numbers of objects per spectral type bin shown in Fig. 4.2. In our colour region, the median RP spectra per spectral type differ from the known standards by $|\Delta F| \leq 10$ per cent. The major caveat for this method is that the `teff_espucd` values were generated from a training set which contained no outliers. Hence, it can be expected to be biased. We may be comparing an observed colour against expectations from an incorrect bin.

4.2.3.1 Determining outliers

For each object, the outliers were defined as the cases where CR was more than 3σ from the average value μ of all elements of CR ($\mu = 0.98 \pm 0.05$). Assuming a Gaussian distribution (z) centered at μ , this $\pm 3\sigma$ equated to the 0.01 per cent and 99.9 per cent percentiles (p) of z_p . In terms of CR, the 0.01 per cent percentile, $z_{-3\sigma}$, equals 0.80 whilst the 99.9 per cent percentile, $z_{3\sigma}$, equals 1.16. To summarise, this outlier selection was $z_{-3\sigma} \geq \text{CR} \geq z_{3\sigma}$ or $0.80 \geq \text{CR} \geq 1.16$ where $p = \pm 3\sigma$. This process went through multiple iterations of different bin sizes, blue and red definitions (e.g. shifting with spectral type and not), numerical methods of creating CR, and different CR cut-off points. We chose the final method parameters such that it only selects the most extreme outliers. Under this selection criteria, subdwarf candidates were the objects with $\text{CR} \geq z_{3\sigma}$ whilst young candidates had $\text{CR} \leq z_{-3\sigma}$.

4.3 Analysis

We discuss here methods of selecting interesting sub-samples of the candidate objects found by the CR in Sect. 4.2.3.1, although we provide the CR measure for every object. This analysis section is intended to produce a list of ‘prime’ candidates, which are the objects passing strict selection criteria. The aforementioned known standard sample was used to calibrate our CR values, and ensure we were not selecting ‘normal’ objects.

We defined any object with $\text{CR} \geq z_{3\sigma}$ as a CR-candidate subdwarf and anything with $\text{CR} \leq z_{-3\sigma}$ as a CR-candidate young object. This selection process is shown in Fig. 4.5.

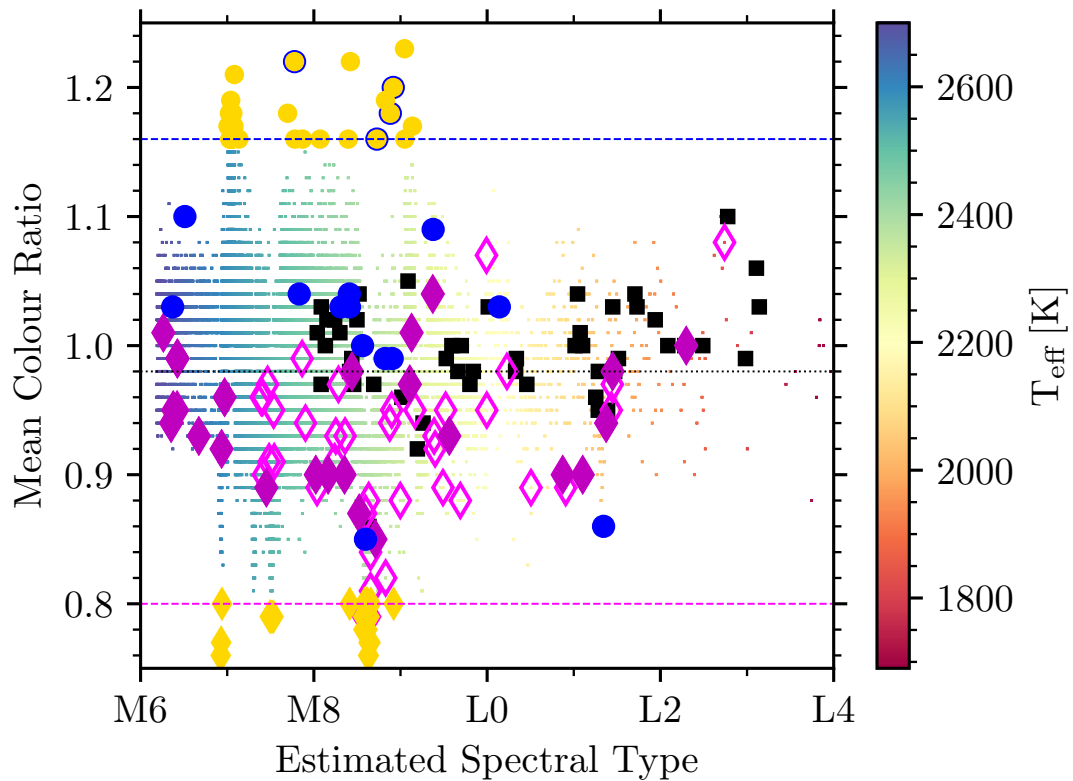


FIGURE 4.5: Colour ratio (CR, Sect. 4.2.3.1) against estimated spectral type (Sect. 4.2.2). We display sources only between M6–L4 (there are no later candidates). The full population is shown as small squares using a colour-code reflecting T_{eff} shown on the right-hand axis. Standards are displayed as black squares whilst known young objects are magenta diamonds (filled if very low gravity, i.e. $\delta / \text{'vl-g'}$) and known subdwarfs are blue circles. Horizontal coloured lines are shown demarcating the selection criteria, magenta for $\text{CR} \leq z_{-3\sigma}$ and blue for $\text{CR} \geq z_{3\sigma}$. A black dotted line is shown at the mean CR. Candidate subdwarfs are yellow circles, candidate young objects are yellow diamonds.

There was an over density of sources around M7–M8, and therefore a less reliable median RP spectrum, hence the larger CR scatter and artifacts shown in Fig. 4.5. This is due to the artificial upper limit of $T_{\text{eff}} < 2700$ K in `teff_espucl`.

Out of 21 205 RP spectra, 44 passed the aforementioned CR cuts. Following the discussion in section. 3 by Sarro et al. (2023), we used internally calibrated RP spectra instead of externally calibrated RP spectra. This is because, as shown by spectral type standards in Fig. 4.6, the external calibration produces non-physical artifacts for some UCDs (Carrasco et al., 2021; Montegriffo et al., 2023). It was not entirely predictable which objects saw the worst performance in the external calibration; however, generally the least bright and least observed (`phot_rp_n_obs`) objects had less reliable spectra. This is due to the external calibration being derived with sources outside of the UCD regime (Pancino et al., 2012). *Gaia* observes internally calibrated

TABLE 4.2: Photometric cuts to select subdwarfs and young objects.

Subdwarf	Young
$M_G > 14.5$	$M_G < 13.5$
$G - J < 4.2$	$G - J > 3.8$
$M_J > 10.5$	$M_J < 9.5$
$J - K_s < 0.8$ ★	$J - K_s \geq 0.8$

★ Slightly more liberal than the $J - K_s < 0.7$ cut by Lodieu et al. (2012).

spectra, not externally calibrated ones. We base our analysis on a set of spectra that has not undergone an additional calibration stage which was not optimised for these red and faint sources. External calibration may introduce systematics upon which we have no control, in the context of a problem where the signal is very weak. The internally calibrated RP spectra showed a much cleaner spectral sequence, which was vital for determining if a given object is ‘typical’ in appearance for a given spectral type, or not. Both the internal and external calibration spectra were converted from physical wavelengths to ‘pseudo-wavelengths’ (used by `gaiaxy`) via the dispersion function shown in fig. 9 from Montegriffo et al. (2023) and discussed in section. 3.1 from De Angeli et al. (2023). This dispersion function is available through `gaiaxy` and documented as `ExternalInstrumentModel.wl_to_pwl`. Flux uncertainties were larger in the external calibration, as shown in Fig. 4.6. One explanation for this is the known issue in *Gaia* DR3 that the internal calibration flux uncertainties are underestimated. The external calibration did have a larger relative range of fluxes from F_{\min} – F_{\max} across our 795–995 nm region (Sect. 4.2.3). Such a larger relative range would produce improved discernment between neighbouring objects.

4.3.1 Photometry checks

In the optical regime of *Gaia*, subdwarfs are known to be typically blue objects whilst young objects are overluminous and red. As such, we constructed a CMD to check that candidate objects are in the same colour-space as known subdwarfs or known young objects. This is shown in Fig. 4.7. To do this, we created a selection of photometric cuts in Table 4.2. These are conservative selections on the two categories, aimed at selecting the bluest known subdwarfs and brightest known young objects. We made the selections conservative in order to avoid contaminant sources, as most contaminants are within the inherent CMD scatter on the UCD main sequence.

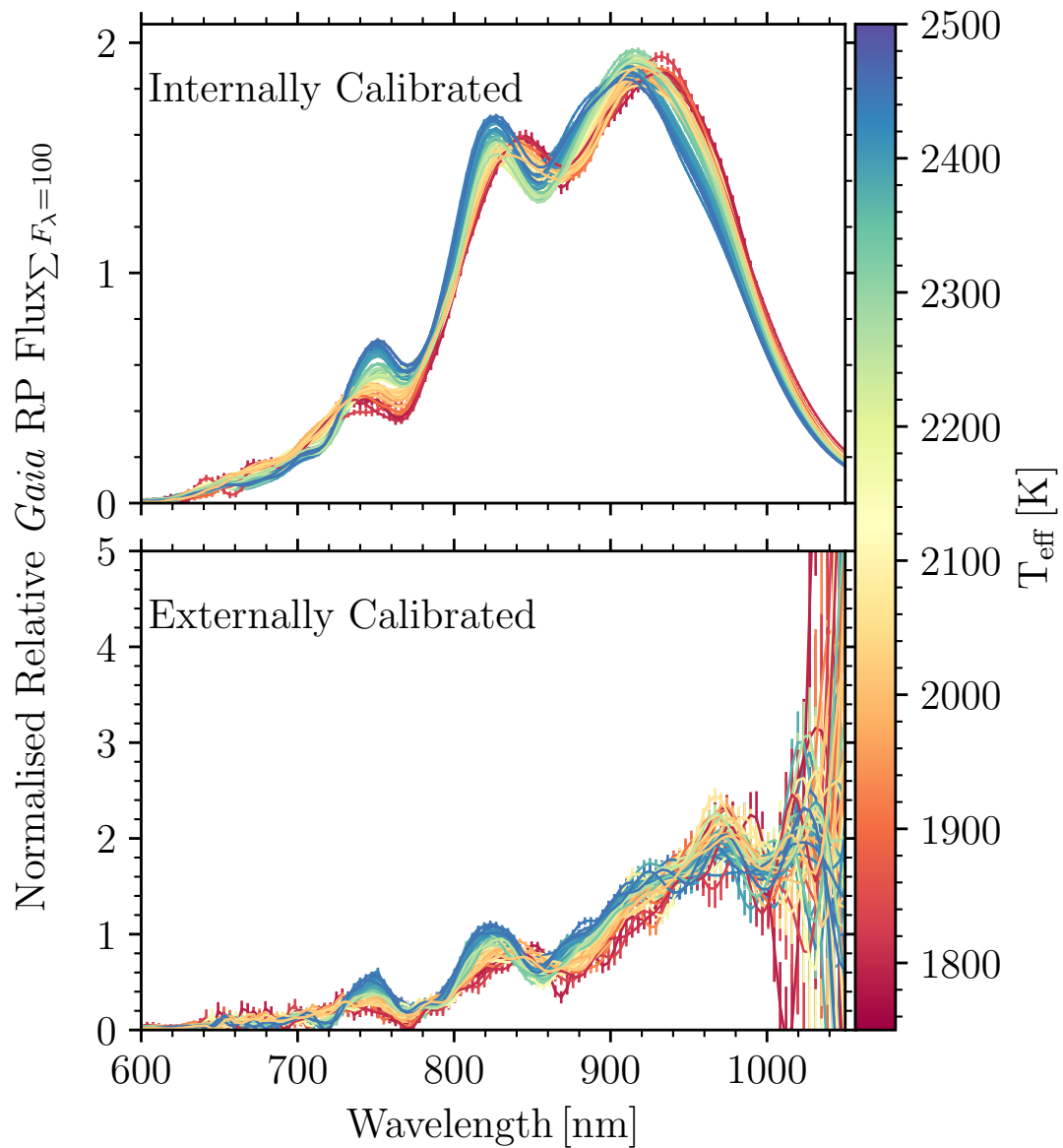


FIGURE 4.6: Spectral comparison between internally and externally calibrated RP spectra of spectral type standards from M7–L4. Spectra are coloured by effective temperature. Internally calibrated RP spectra of spectral type standards in the upper plot. Externally calibrated RP spectra of spectral type standards in the lower plot. The normalised spectra were multiplied by a constant value such that the fluxes sum to 100 instead of 1.

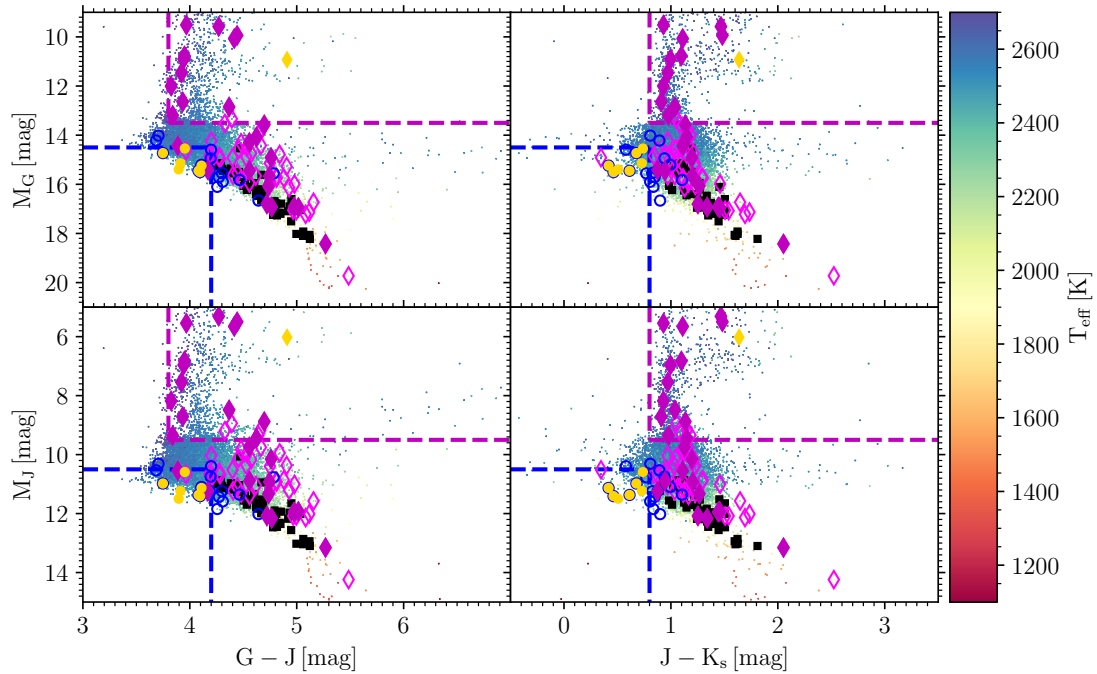


FIGURE 4.7: Four colour-absolute magnitude diagrams with M_G on the top row, M_J on the bottom row, $G - J$ on the left column, and $J - K_s$ on the right column. The full RP spectral sample is shown as small squares using a colour-code reflecting T_{eff} , as shown in the colour bar. Standards are displayed as black squares whilst known young objects are open magenta diamonds (filled if very low gravity $\delta / \text{'v1-g'}$) and known subdwarfs are open blue circles. Candidate subdwarfs are yellow circles, candidate young objects are yellow diamonds. Dashed lines are shown demarcating the cut-offs for the photometric filtering of the candidate selection. Magenta lines are for the young object candidate selection and blue lines are for the subdwarf selection. These lines represent the cuts in Table 4.2.

There are 906 candidate young objects and 260 candidate subdwarfs purely from the photometric cuts in Table 4.2. However, only one object is both a CR candidate, and a photometric young candidate whilst seven objects are both CR candidates, and photometric subdwarf candidates.

4.3.2 Kinematics

We provide a kinematic classification system to indicate thin disc, thick disc, and halo, based on each object's space motions. These motions were calculated using the equations from `astrolibpy`, which follows the work by Johnson and Soderblom (1987), except that U is defined as positive towards the Galactic anti-centre. We used the Local Standard of Rest (LSR) from Coşkunoğlu et al. (2011) with $U, V, W = (-8.50, 13.38, 6.49 \text{ km s}^{-1})$. To create UVW velocities, we needed radial velocities to complement the 5-D astrometry from *Gaia* DR3.

We cross-matched our sample of 21 205 objects with *Gaia* RP spectra with SIMBAD (Wenger et al., 2000). This provided 2187 UCDs with literature radial velocities. For sources without

radial velocities we estimated probability density distributions of the total velocity by assuming a normal radial velocity distribution. This distribution was obtained by a maximum likelihood fit to the values available from the literature, where $\mu = 0.2 \text{ km s}^{-1}$, $\sigma = 52.3 \text{ km s}^{-1}$. We sampled 1000 random radial velocities from this normal distribution for each object in our full sample. Therefore, each object had 1000 different UVW velocities. This converted into 1000 V_{total} values through $V_{\text{total}} = \sqrt{U^2 + V^2 + W^2}$. From each object's range of V_{total} values, we extracted probabilities (P) of Galaxy component membership (thin disk, P_{thin} ; thick disk, P_{thick} ; halo, P_{halo}). This assumes that U , V , W and V_{total} are Gaussian distributions propagated from the normal radial velocity distribution and ignores the impact of metallicity on thick disk/halo discrimination. To do so, we calculated the survival function² of each object's total velocity distribution at two critical velocities: 70 km s^{-1} and 180 km s^{-1} (Nissen and Schuster, 2010). These are checked in descending order: $P_{\text{halo}} = P(V_{\text{total}} > 180 \text{ km s}^{-1})$, $P_{\text{thick}} = \max\{0, P(V_{\text{total}} > 70 \text{ km s}^{-1}) - P_{\text{halo}}\}$, $P_{\text{thin}} = \max\{0, 1 - P_{\text{thick}} - P_{\text{halo}}\}$. We then select the Galaxy component for each object as whichever probability is highest.

Of our candidates, subdwarf candidates were those objects in the halo (28) or thick disk (4057); whilst we required young objects to be in the thin disk (although some known young objects can be in the thick disk). Nevertheless, for young candidates, one object passed all of the respective CR, photometric and kinematic cuts. For the subdwarf candidates, six objects passed all of the respective CR, photometric and kinematic cuts. These seven objects are our prime candidates. We present the surviving candidates on the Toomre diagram in Fig. 4.8, using the mean (of the 1000 total) UVW velocities with propagated uncertainties shown.

4.4 Results

We present the *Gaia* RP spectra of the final, seven prime candidates, having survived all CR, photometric and kinematic cuts in Fig. 4.9 with their astrometry, spectral type and T_{eff} shown in Table 4.3. We also show the stellar energy distribution (SED) difference from a normal SED of the same spectral type, for each object in Fig. 4.10.

We discuss here each object classified as a prime candidate in this work. Four candidates were already known subdwarfs and flagged as such in the GUCDS:

² Equivalent to $1 - \text{CDF}$ (Cumulative Distribution Function).

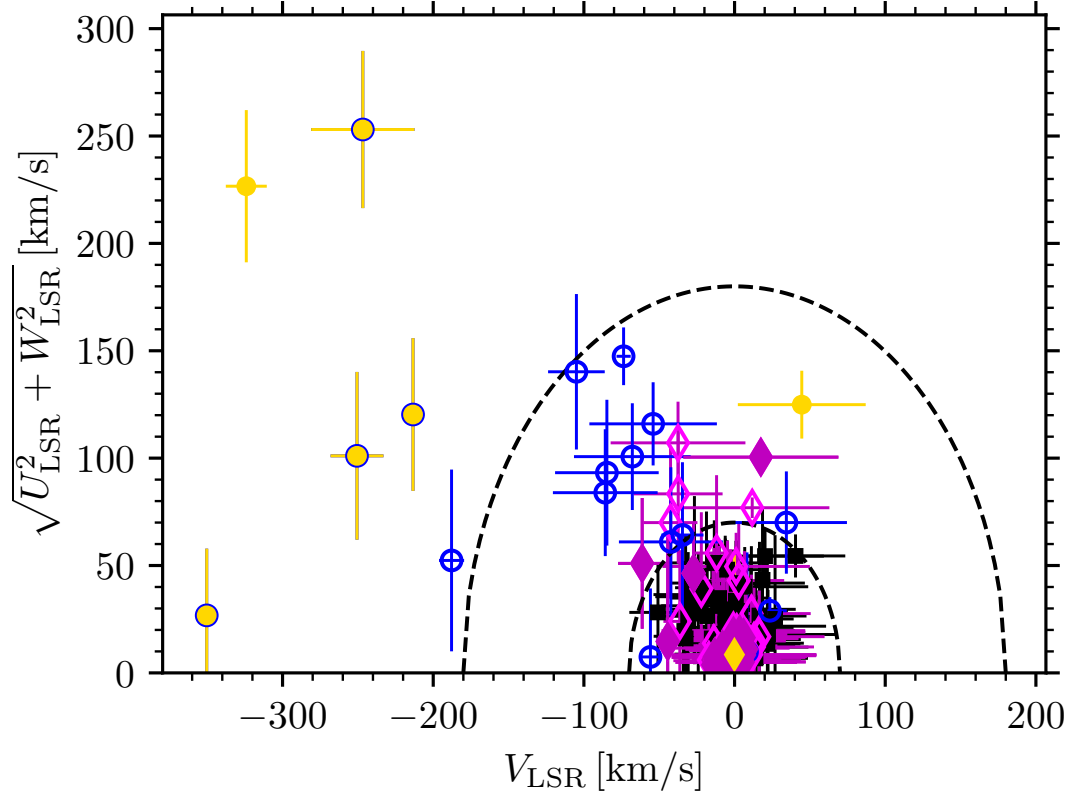


FIGURE 4.8: Toomre diagram (Sandage and Fouts, 1987), corrected for the LSR, of our prime candidates with thick disk and halo selection lines shown at $V_{\text{total}} > 70 \text{ km s}^{-1}$ and $V_{\text{total}} > 180 \text{ km s}^{-1}$ respectively. Standards are displayed as black squares whilst known young objects are open magenta diamonds (filled if very low gravity δ / ‘vl-g’) and known subdwarfs are open blue circles. Candidate subdwarfs are yellow circles, candidate young objects are yellow diamonds. Error-bars in matching colours are also shown.

TABLE 4.3: Unsorted list of candidate subdwarfs and young objects. Astrometry is from *Gaia* DR3 and the T_{eff} values are those produced by the ESP-UCD Apsis module and published as part of the Data Release.

<i>Gaia</i> DR3 Source ID	α [hms]	δ [dms]	ϖ [mas]	Object Name	Spectral Type	T_{eff} [K]
6281432246412503424	14 44 17	-20 19 56.9	58.1 ± 0.1	SSSPM J1444–2019 ¹	sdM9 ²	2352 ± 10
6096164227899898880	14 11 42	-45 24 20.1	19.1 ± 0.2	2MASS J14114474–4524153 ³	sdM9 ⁴	2487 ± 47
144711230753602048	4 35 36	+21 15 03.6	16.7 ± 0.6	2MASS J04353511+2115201 ³	sdL0 ⁵	2371 ± 74
5183457632811832960	3 06 02	-3 31 06.1	24.7 ± 0.3	2MASS J03060140–0330438 ³	sdL0 ⁵	2348 ± 55
70974545020346240	3 40 58	+26 33 40.8	10.6 ± 0.7	2MASS J03405673+2633447 ⁶	sdM8.5 ⁷	2411 ± 111
525463551877051136	1 20 44	+66 23 59.0	12.1 ± 0.4	2MASS J01204397+6623543 ⁶	sdM9 ⁷	2359 ± 106
151130591952773632	4 33 08	+26 16 06.3	6.6 ± 0.2	[BLH2002] KPNO–Tau 14 ⁸	M7.2 ⁹	2385 ± 18

References: 1. Scholz et al. (2004), 2. Winters et al. (2015), 3. Luhman (2014a), 4. Kirkpatrick et al. (2016), 5. Kirkpatrick et al. (2014), 6. Cutri et al. (2003), 7. This Work, 8. Luhman et al. (2003), 9. Zhang et al. (2018a)

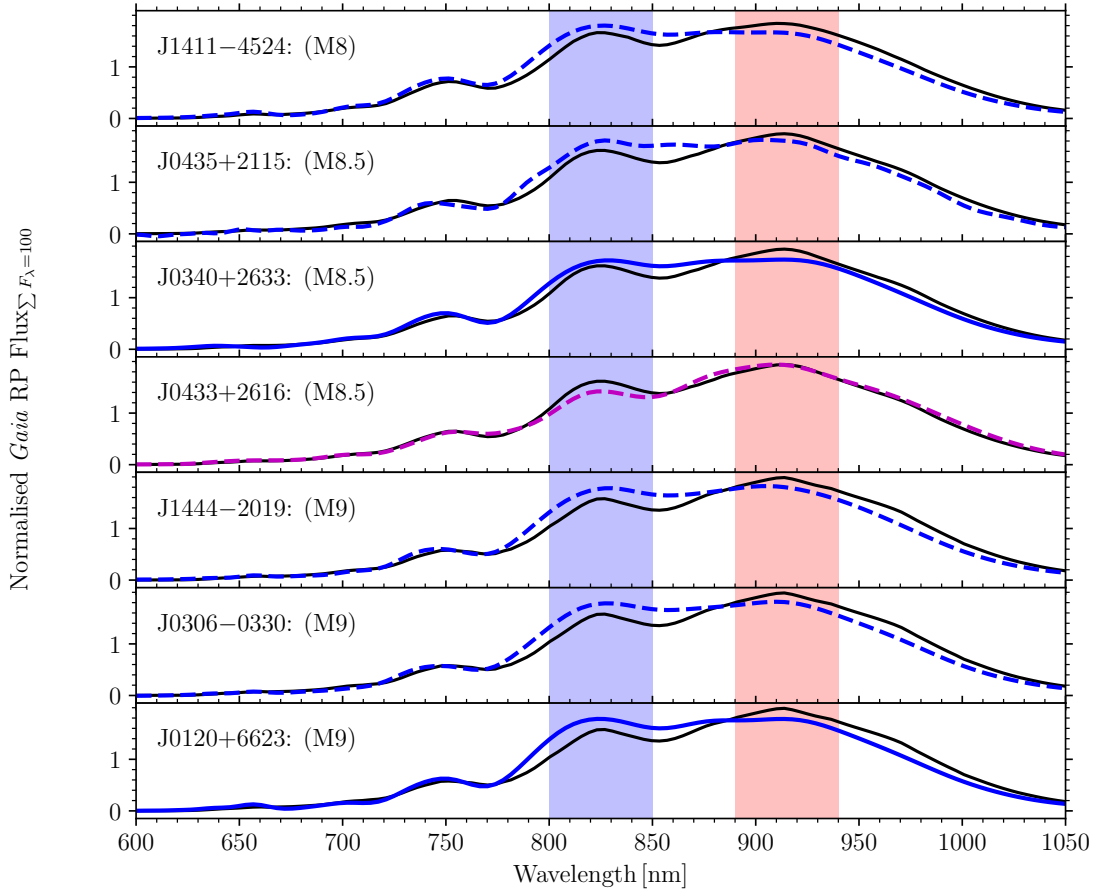


FIGURE 4.9: Internally calibrated RP spectra of our seven prime candidates with estimated spectral type, rounded to 0.5, indicated. Any objects with dashed lines are already known to the literature. Blue lines are subdwarfs whilst magenta lines are young objects. Over-plotted in black is the median RP spectra for the given spectral type from known objects in the GUCDS. Subdwarfs are typically overluminous in blue and underluminous in red (the blue and red bands shown as shaded regions, as described in Sect. 4.2.3) with the inverse true for young objects. The normalised spectra were multiplied by a constant value such that the fluxes sum to 100 instead of 1.

- **SSSPM J1444–2019** (*J1444–2019*): In the literature, this object is an M9 (Bardalez Gagliuffi et al., 2014) or an sdL0 (in both the optical and near-infrared regime, Kirkpatrick et al., 2016). This work estimated a spectral type of M9, $CR = 1.18$ and $P_{\text{halo}} = 1$. Our spectral type agrees with the literature’s modal spectral type and our kinematics combined with it’s blue nature confirm the subdwarf.
- **2MASS J14114474–4524153** (*J1411–4524*): J1411–4524 is an sdM9 (Kirkpatrick et al., 2016). We found a spectral type of M8, $CR = 1.22$ and $P_{\text{halo}} = 1$, hence our agreed classification as a subdwarf.
- **2MASS J04353511+2115201** (*J0435+2115*): An sdL0 (optical) object (Kirkpatrick et al.,

2014), confirmed by Kirkpatrick et al. (2016) with a similar sdM9 from Luhman and Sheppard (2014)³. The spectral type from this work is M8.5, mostly in agreement with the literature, with $CR = 1.16$ and $P_{\text{halo}} = 1.0$. We concur with the subdwarf classification.

- **2MASS J03060140–0330438 (J0306–0330)**: Similarly, an sdL0 (optical) object (Kirkpatrick et al., 2014) with an sdM9 sub-type from Luhman and Sheppard (2014)³. This work estimated a spectral type of M9. $CR = 1.20$ and $P_{\text{halo}} = 1.0$, the high CR value indicates this object is a likely subdwarf.

Two new subdwarf candidates were also found:

- **2MASS J03405673+2633447 (J0340+2633)**: Not known to SIMBAD (besides an entry for *Gaia* DR3 and 2MASS) or the GUCDS⁴. We found a spectral type of M8.5, $CR = 1.16$ and $P_{\text{halo}} = 1.0$. The CR value is on the borderline of the cut-off, however, this is still significant, especially considering that it has the fastest V_{tan} in the sample at 407.3 km s^{-1} . It shows a non detection in PS1 g & r and is generally underluminous in the NIR (Fig. 4.10) but overluminous in the two reddest bands of AllWISE, a similar pattern to J0435+2115 (the known subdwarf of the same estimated spectral type). The missing detection in PS1 is due to the cross-matching, when visually inspected there is a highly red object visible within ≈ 2 arcseconds. J0340+2633 is even more blue in Fig. 4.7 than most of our known subdwarfs, as would be expected for an extreme object.
- **2MASS J01204397+6623543 (J0120+6623)**: Likewise, this object has a lack of information in the literature. This work estimated a spectral type of M9, with $CR = 1.19$ and $P_{\text{thick}} = 1.0$. The very high CR value also indicates this object is also non-standard for an M9. It also shows a non detection in PS1 g & r but additionally no match in AllWISE. This is again due to the cross-matching uncertainties as there is a clear red object in PS1 when visually inspected. It appears in the AllWISE images that the object is hidden by two neighbouring bright stars. However, it is *tending* towards being underluminous in the NIR (Fig. 4.10), as would be expected from the two known subdwarfs of the same estimated spectral type (J1444–2019 and J0306–0330). As with J0340+2633, J0120+6623

³ There appears to be some confusion in the literature bibliography codes (bibcodes) about the origin of this spectral type. There are three very similar bibcodes: Luhman and Sheppard (2014ApJ...787..126L – ‘Characterization of High Proper Motion Objects from the Wide-field Infrared Survey Explorer’ 2014); Luhman (2014ApJ...786L..18L – ‘Discovery of a ~ 250 K Brown Dwarf at 2 pc from the Sun’ 2014b); Luhman (2014ApJ...781....4L – ‘A Search for a Distant Companion to the Sun with the Wide-field Infrared Survey Explorer’ 2014a); the correct reference is Luhman and Sheppard (2014).

⁴ This isn’t unexpected, as the GUCDS is only intended to be complete for L dwarfs.

is notably more blue than other subdwarfs known to the literature in Fig. 4.7. This is therefore classed as a new subdwarf.

Additionally, we found one young object candidate, already known to the literature:

- **[BLH2002] KPNO–Tau 14** (*J0433+2616*): This object is not in the GUCDS⁴ but is an M7.2 (Zhang et al., 2018a) in SIMBAD and classed as M6Ve by Luhman et al. (2003). Kounkel et al. (2019) gives this object a radial velocity of 17.07 ± 0.37 , which combined with the V_{tan} of 13.84 km s^{-1} , suggests it is strongly within the thin disk. It has also been repeatedly shown to be a member of the Taurus star forming complex (Luhman et al., 2006; Kraus and Hillenbrand, 2007; Luhman et al., 2010; Rebull et al., 2010; Luhman, 2018; Rebull et al., 2020) and generally within the Taurus-Auriga ecosystem (Kraus et al., 2017). It is a young stellar object (YSO) with an age (from membership of Taurus) of 1–2 Myr (Gagné et al., 2018). Our spectral type is M8.5, within 2σ of the literature values, which is most likely due to the T_{eff} scatter in that spectral type bin (see Fig. 4.3), in addition to the fact that YSOs are highly variable. The $\text{CR} = 0.83$ and $P_{\text{thin}} = 0.8$. Figure 4.10 shows this object is significantly overluminous for its spectral type, again typical of a YSO.

4.5 Summary

This work has produced a list of 44 objects, which have *Gaia* RP spectral differences greater than 3σ from median RP spectra, derived using the GUCDS and a new colour ratio (CR) specific to internally calibrated *Gaia* RP spectra. We finally produced a list of seven prime candidates, which have passed highly restrictive photometric and kinematic selections, aimed at recovering the most extreme objects in the sample.

Whilst we could have used a more liberal set of cuts, the intention in this work was to produce the most confident candidates. Additionally, part of the publication criteria (see Sect. 4.2) for *Gaia* RP UCD spectra was that the RP spectra had the highest quality flags (`flags_espucd` 0–1). This meant objects with higher Euclidean distances from BT-Settl (Allard et al., 2011)

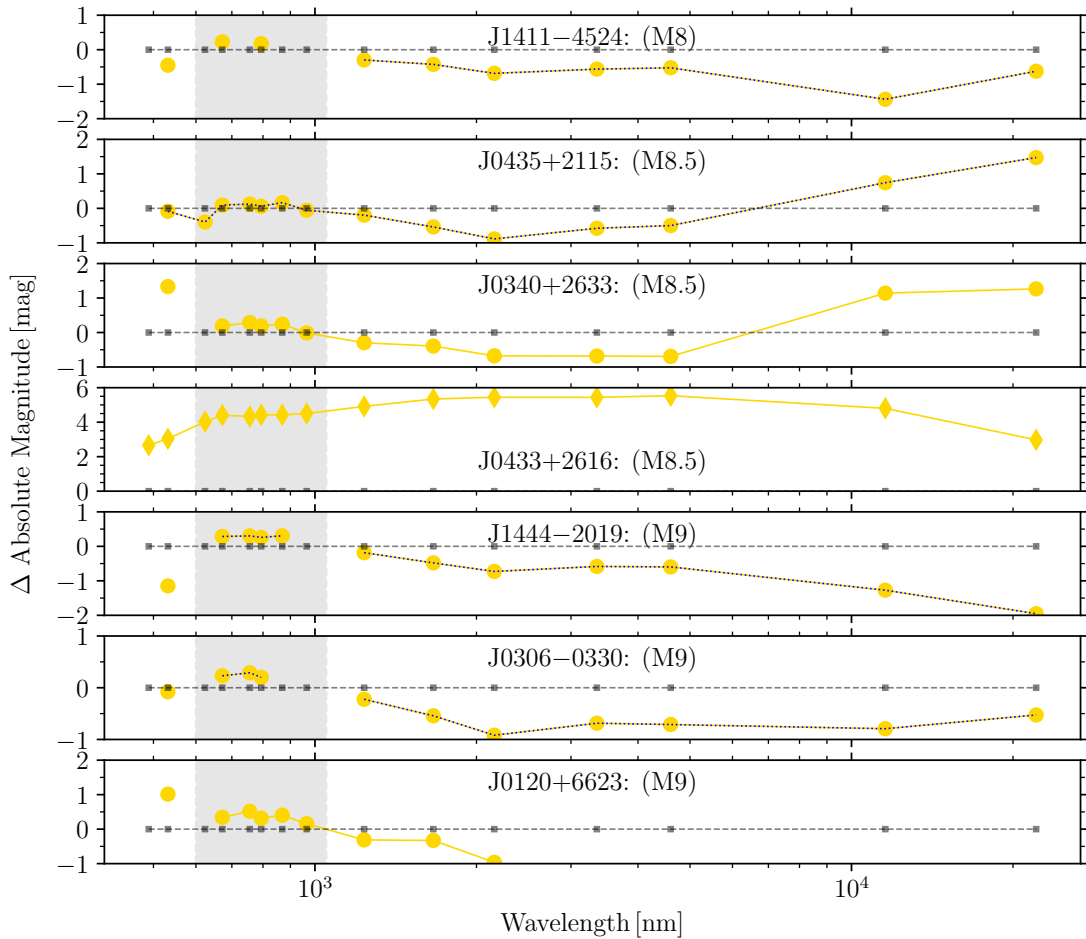


FIGURE 4.10: The Δ SEDs for our seven prime candidates in yellow with estimated spectral type (rounded to 0.5) indicated, as compared with the mean absolute magnitudes for the given spectral type from the GUCDS. Positive values indicate over-brightness and negative values under-brightness. Blue dotted lines are shown on the objects already known to be subdwarfs in the literature. Over-plotted in dark grey at zero are the wavelengths covered. A grey shading is shown in the region covered by *Gaia* RP spectra. The photometry shown is from Pan-STARRS, *Gaia*, 2MASS and AllWISE; converted into an absolute magnitude using the *Gaia* DR3 parallax. The wavelengths plotted correspond to the mean wavelengths ($\bar{\lambda}$) of each photometric band (g , G_{BP} , r , G , i , G_{RP} , z , y , J , H , K_s , $W1$, $W2$, $W3$, $W4$, in increasing $\bar{\lambda}$ order), as extracted from VOSA (Bayo et al., 2008).

models (simulated through the *Gaia* RP transmission function) are not included. In other words, the most extreme objects we seek to classify were precluded from inclusion in *Gaia* DR3⁵.

Several other biases exist, such as the artificial cut of $T_{\text{eff}} < 2700$ K from `teff_espucl`. This caused the over density seen at the M7–M8. The lack of outliers in the empirical training set in *Gaia* DR3 also caused a bias in the creation of expected colour. Also, the sample of known young objects and known subdwarfs in the GUCDS includes many objects, which appear not

⁵ However, the quality flag selections performed by ESP-UCD were very sensible, see discussion by Creevey et al. (2023) and Sarro et al. (2023), as there were many potential contaminants and highly noisy spectra in the lowest quality flag (2).

considerably different from a normal object when visually observed at a resolution as low as *Gaia* RP, see Fig. 4.4. This can be evidenced by Fig. 4.5, where there is little scatter in CR in spectral sub-types beyond L0. These objects are as equally interesting as extreme outliers, but require higher resolution optical and NIR spectroscopy to observe directly the features relating to surface gravity and metallicity. Many of these objects did not pass the CR selection, photometric and kinematic cuts, or both. These reasons combined with the rarity of extreme UCDS are the cause of there being so few prime candidates in our final list. However, the detection of the known extreme UCDS shown here is a highly promising baseline for future analysis. The additional detection of two unknown subdwarf candidates is demonstrative of the fact that existing datasets, like *Gaia* DR3, contain many interesting objects, still to be discovered. This future work could include more advanced selection techniques such as machine learning, more liberal selection criteria and the increased breadth and depth of planned *Gaia* data releases.

Data availability

The data underlying this article will be shared on reasonable request to the corresponding author. It will additionally be available through CDS VizieR.

Chapter 5

Gaia Ultracool Dwarf Sample – V. Database

This chapter is focused on my ‘*Gaia* Ultracool Dwarf Sample – V. Database’ paper. Here, I discuss the creation of the database containing all astronomical data relating to UCDs in the GUCDS.

Abstract

We present here the database description for the data covered by the *Gaia* Ultracool Dwarf Sample. We demonstrate use cases for querying this database via the web interface. Also shown are the representation of spectra as can be interactively plotted.

5.1 Introduction

Many databases and catalogues exist in astronomy. NASA ADS (original form, Eichhorn, 1994) collates all relevant scientific papers. SIMBAD (Wenger et al., 2000) ‘scrapes’ papers for information on astronomical objects. VizieR (Ochsenbein et al., 2000) is a meta database of catalogues, as created under data availability agreements by researchers. There are several disparate catalogues specific to UCDs. These include the Dwarf Archives (Gelino et al., 2009), the UltracoolSheet (Best et al., 2020) and the SpeX Prism Library (Burgasser, 2014). The UCD

field has a lot of intentional overlap with the exoplanet field, which has also seen a recent rise in number of databases. For example, exoplanet.eu (Schneider et al., 2011b), the NASA Exoplanet Archive (Akeson et al., 2013) and EXOPLINES (Gharib-Nezhad et al., 2021). This work will document the GUCDS database. Naturally, there is some overlap between the various UCD catalogues and this GUCDS database. However, the vital distinction is one of nomenclature. One *searches* a catalogue for objects or keywords or matching parameters. One *queries* a database via a Structured Query Language (SQL) to construct selections across any desired combination of attributes.

We will discuss the structure, holdings and use cases in Section. 5.2 before concluding in Section. 5.3.

5.2 Database Description

The GUCDS database was built on MySQL and consists of 19 739 sources, at the time of writing. There are 8 818 published spectra, mostly from SpeX and *Gaia* DR3. Each source has been cross-matched with data from *Gaia*, SIMBAD, 2MASS, AllWISE, PAN-STARRS, SDSS, Spitzer and the MKO filter system. The photometry in the MKO filter columns is a collation from VISTA/VIRCAM (McMahon et al., 2013) and UKIRT/WFCAM (Lawrence et al., 2007). It should be noted that VISTA/VIRCAM does not use utilise MKO filters. Ergo, these columns should not be used for any serious photometric analysis.

The entire description of the database is shown in Table 5.1.

The primary key across the GUCDS is SHORTNAME. As such, SHORTNAME is the only attribute with the ‘NOT NULL’ and ‘UNIQUE’ constraints. This ensures there are no duplicate or missing entries. A common feature of the GUCDS is the referring to numerical spectral types. For clarification, a spectral type of M0 is 60, L0 is 70 and T0 is 80.

TABLE 5.1: The GUCDS description.

Column	Description
SHORTNAME	Short version of object name in the form ‘J1234±5678’.
DISCOVERYNAME	The name given to the object upon discovery.
DISCOVERYREFNAME	The reference code for the object’s discovery.
RA	The object’s right ascension.
DEC	The object’s declination.
POSITIONREFNAME	The reference for the object’s positional data.
POSITIONEPOCH	The epoch of the object’s positional data.
PECULIARNAME	Identifier if the object is peculiar.
PECULIARREFNAME	Reference for the peculiarity.
MGCANDIDACYNAME	Identifier if the object is a candidate for a moving group.
MGCANDIDACYREFNAME	Reference for the moving group candidacy identification.
MULTIPLEFLAGNAME	Flag to identify if the object is in a multiple system.
MULTIPLEFLAGREFNAME	Reference for the multiple system flag.
COMMENTSNAME	Additional comments on the object.
SPTOPTNAME	Optical spectral type designation.
SPTOPTREFNAME	Reference for the optical spectral type.
SPTNIRNAME	Near-infrared spectral type designation.
SPTNIRREFNAME	Reference for the near-infrared spectral type.
SPTPHONAME	Photometric spectral type designation.
SPTPHOREFNAME	Reference for the photometric spectral type.
SPTNUM	Number associated with the spectral type.
PARALLAX	Parallax measurement.
PARALLAXERR	Error in parallax measurement.
PARALLAXREFNAME	Reference for the parallax measurement.
PMRA	Proper motion in right ascension.
PMRAERR	Error in proper motion in right ascension.
PMDEC	Proper motion in declination.
PMDECERR	Error in proper motion in declination.
PMREFNAME	Reference for proper motion measurements.
RV	Radial velocity of the object.
RVERR	Error in radial velocity measurement.

Column	Description
RVREFNAME	Reference for radial velocity.
TMASSJ	J-band magnitude from 2MASS.
TMASSJERR	Error in J-band magnitude from 2MASS.
TMASSH	H-band magnitude from 2MASS.
TMASSHERR	Error in H-band magnitude from 2MASS.
TMASSK	K-band magnitude from 2MASS.
TMASSKERR	Error in K-band magnitude from 2MASS.
TMASSFLAGNAME	Flag for 2MASS data quality.
WISEW1	Magnitude in W1 band from ALLWISE.
WISEW1ERR	Error in W1 band magnitude from ALLWISE.
WISEW2	Magnitude in W2 band from ALLWISE.
WISEW2ERR	Error in W2 band magnitude from ALLWISE.
WISEW3	Magnitude in W3 band from ALLWISE.
WISEW3ERR	Error in W3 band magnitude from ALLWISE.
WISEFLAGNAME	Flag for WISE data quality.
PS1G	G-band magnitude from Pan-STARRS.
PS1GERR	Error in G-band magnitude from Pan-STARRS.
PS1R	R-band magnitude from Pan-STARRS.
PS1RERR	Error in R-band magnitude from Pan-STARRS.
PS1I	I-band magnitude from Pan-STARRS.
PS1IERR	Error in I-band magnitude from Pan-STARRS.
PS1Z	Z-band magnitude from Pan-STARRS.
PS1ZERR	Error in Z-band magnitude from Pan-STARRS.
PS1Y	Y-band magnitude from Pan-STARRS.
PS1YERR	Error in Y-band magnitude from Pan-STARRS.
PS1FLAGNAME	Flag for Pan-STARRS data quality.
PS1REFNAME	Reference for Pan-STARRS1 data.
SDSSG	G-band magnitude from SDSS.
SDSSGERR	Error in G-band magnitude from SDSS.
SDSSR	R-band magnitude from SDSS.
SDSSRERR	Error in R-band magnitude from SDSS.
SDSSI	I-band magnitude from SDSS.

Column	Description
SDSSIERR	Error in I-band magnitude from SDSS.
SDSSZ	Z-band magnitude from SDSS.
SDSSZERR	Error in Z-band magnitude from SDSS.
SDSSFLAGNAME	Flag for SDSS data quality.
SDSSREFNAME	Reference for SDSS data.
IRACCH1	Channel 1 magnitude from Spitzer.
IRACCH1ERR	Error in Channel 1 magnitude from Spitzer.
IRACCH2	Channel 2 magnitude from Spitzer.
IRACCH2ERR	Error in Channel 2 magnitude from Spitzer.
MKOY	Y-band magnitude from MKO system.
MKOYERR	Error in Y-band magnitude from MKO system.
MKOJ	J-band magnitude from MKO system.
MKOJERR	Error in J-band magnitude from MKO system.
MKOH	H-band magnitude from MKO system.
MKOHERR	Error in H-band magnitude from MKO system.
MKOK	K-band magnitude from MKO system.
MKOKERR	Error in K-band magnitude from MKO system.
MKOREFNAME	Reference for MKO system data.
GAIAG	G-band magnitude from <i>Gaia</i> .
GAIAGERR	Error in G-band magnitude from <i>Gaia</i> .
GAIABP	BP-band magnitude from <i>Gaia</i> .
GAIABPERR	Error in BP-band magnitude from <i>Gaia</i> .
GAIARP	RP-band magnitude from <i>Gaia</i> .
GAIARPERR	Error in RP-band magnitude from <i>Gaia</i> .
GAIATOG	Toggle for which <i>Gaia</i> data release the associated values are from.
GAIAREFNAME	Reference for <i>Gaia</i> data.
RA2000	Right Ascension at J2000 epoch.
DEC2000	Declination at J2000 epoch.
SIMBADNAME	Object's name in SIMBAD.
SIMBADTYPENAME	Object type in SIMBAD.
SIMBADRADVEL	Radial velocity according to SIMBAD.
SIMBADSPNAME	Spectral type according to SIMBAD.

Column	Description
SPTOPT	Numerical optical spectral type.
SPTNIR	Numerical near-infrared spectral type.
SPTPHO	Numerical photometric spectral type.
BINSEP	Separation of binary components if applicable.
SOURCE_ID	Unique identifier for the object from <i>Gaia</i> DR3.
SOURCE_ID_DR2	Unique identifier in the <i>Gaia</i> Data Release 2.
SPTGEN	Adopted spectral type drawn from SPTOPT and SPTNIR.
TYPEFLAGNAME	Flag indicating specific types or classifications.
SPECQUALITYNAME	Qualitative assessment of the spectral data.
SPECQUALITY	Numerical rating for spectral data quality.
JGEN	Generated J-band magnitude.
VTAN	Tangential velocity of the object.
EVTAN	Error in tangential velocity.
DMOD	Distance modulus.
GAIASEP	Separation in the <i>Gaia</i> source list if binary.
RA2016	Right Ascension at 2016 epoch.
DEC2016	Declination at 2016 epoch.
LITPARALLAX	Parallax data from literature.
LITPARALLAXERR	Error in literature parallax data.
LITPARALLAXREFNAME	Reference for literature parallax data.
GAIAPOSSVB	Possible visual binary companions to object.
SPECTRAL_COVERAGE	Number of unique spectra for an object in the database.

The screenshot shows the 'gudcs archive data browser, Version 0.2c' interface. At the top, there is a 'Sign out' button and a 'Select by' dropdown menu with options: Short name (selected), Discovery name, J Magnitude, Coords, and WHERE. A search input field contains 'J1234' and a 'Submit' button is next to it. Below the search bar, there are icons for zooming and a '26 rows - Cursor on Objects for info' header. A circular sky image shows the search area with a field of view (FoV) of 174.66°. A 'Reference Catalogue' section shows 'Gaia DR3' selected. A table of 26 rows is displayed, showing search results with columns: ShortName, DiscoveryName, RA, Dec, Parallax, GAIAG, and TMASSJ. The table includes entries like 'No file J1234+3259', '2MASS J12340124+5941520', '2MASS J12340243+2802084', etc. At the bottom, a query is shown: 'SELECT count(*) as n FROM Master_withDR3 WHERE SHORTNAME like '%J1234%' got 26 rows'. A link to retrieve the full JSON table is provided: 'https://gudcs.inaf.it/gudcs/get_log.php?cooaname=J1234&allfields=1'. The footer includes the INAF logo and the text 'L. Nicastro & W. J. Cooper 2019 – 2023'.

FIGURE 5.1: An example search for any objects with a short name like ‘J1234’.

5.2.1 Interfacing with the database

We offer multiple methods of interacting with the database. In Figure 5.1, we show the main search method. Here, a user can search either by short name, full name, J band magnitude or coordinate by using the ‘Select by’ toggle. Furthermore, in Figure 5.2, we show how a user can supplement this search with a SQL WHERE clause. This filters the search results by whatever free text was provided, so long as the keyword corresponds to an existing attribute (Table 5.1). Also shown on this primary page is the sky image, powered by Aladin Lite (Boch and Fernique, 2014). This is wholly interactable and can shown the sky in multiple filters. Clicking on any highlighted source will select that source in the table shown to its side, and vice versa.

The table shown can also be interacted with. Clicking on any hyperlinked text will direct the

The screenshot shows the 'gucds archive data browser, Version 0.2c' interface. The search criteria are set to 'WHERE SPECTRAL_COVERAGE > 4'. The results table lists 11 objects, with 'Wolf 358' highlighted. Below the table is a 'Reference Catalogue' section with a dropdown menu set to 'Gaia DR3'. At the bottom, the SQL query is displayed: `SELECT count(*) as n FROM Master_withDR3 WHERE SHORTNAME like '%J%' AND SPECTRAL_COVERAGE > 4`. A footer bar contains the INAF logo and the text 'L. Nicastro & W. J. Cooper 2019 – 2023'.

ShortName	DiscoveryName	RA	Dec	Parallax	GAIA G	TMASST
J0344+3219	RX J034430.3+321923	56.126667	32.323056	---	---	---
J0539-0059	2MASS J05395200-0059019	84.967404	-0.982315	---	19.157	14.033
J0719+3249	BD+33 1505	109.882472	32.82855	---	9.36045	7.184
J0829+2646	G 51-15	127.450092	26.773286	---	12.1675	8.235
J1050+0648	Wolf 358	162.712964	6.80449	---	10.2908	7.319
J1132-3018	TWA 30B	173.075452	-30.308899	---	18.538	15.35
J1428+3310	LP 271-25	217.178272	33.174412	---	16.6346	11.99
J1655-0823	VB 8	253.893246	-8.398523	---	13.8133	9.776
J1916+0510	HD 180617	289.227652	5.162976	---	8.09991	5.583
J2130-0845	2MASS J21304464-0845205	322.687615	-8.7559	---	18.9536	14.137
J2213-2136	2MASS J22134491-2136079	333.437404	-21.602614	---	20.5316	15.376

FIGURE 5.2: Example query looking for any objects which have at least four spectra in the database.

user to the reference paper for that value. The table presented can be downloaded in multiple file formats. For each row, a download option is provided, this will download all spectra for that object. The magnifying glass icon will open a separate window to display all spectra in an interactable plot (Figure 5.3).

In this spectra display window, a list of filenames are provided at the top of the screen. These can be toggled on and off, and clicking on the hyperlink displays the header data. The plot itself has provided sliders and toggles which can enable/disable error bars and shift the wavelength and flux regimes shown. Each spectrum is normalised by the median flux from a region based on its minimum wavelength (w_{\min}). If $w_{\min} < 0.8 \mu\text{m}$, the normalising regime is $0.81\text{--}0.82 \mu\text{m}$, if $w_{\min} < 1.4 \mu\text{m}$, the normalising regime is $1.45\text{--}1.55 \mu\text{m}$, otherwise it is the median wavelength $\pm 0.1 \mu\text{m}$. The user can select between linear and logarithmic representation of the spectra, and temporarily show/hide any spectra by clicking in the legend. Also in the legend is a ‘Features’ option, the toggling of which enables the presentation of a select few L dwarf features (adapted from SPLAT, Burgasser and Splat Development Team, 2017).

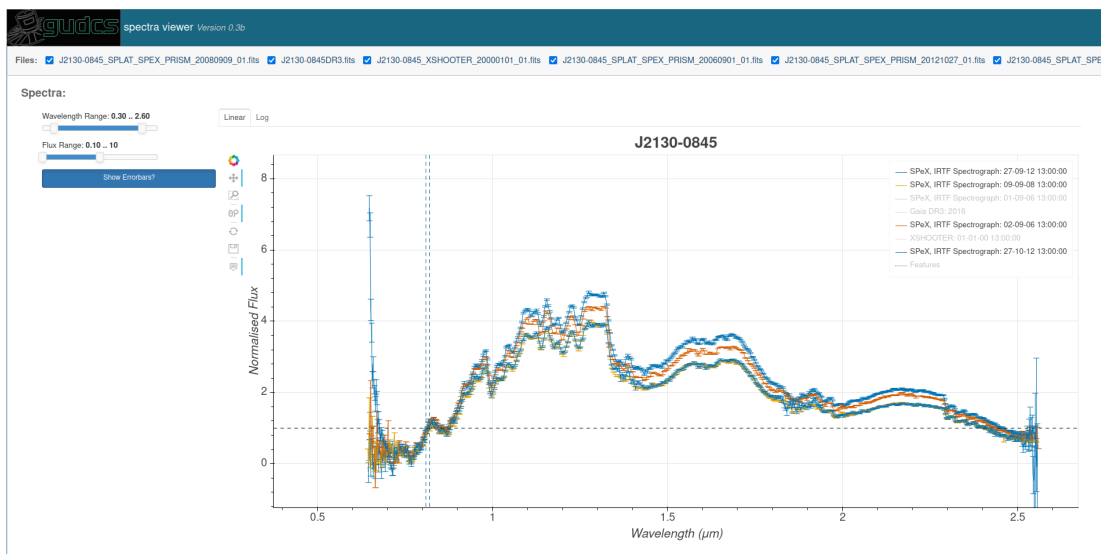


FIGURE 5.3: Example object plotting four spectra, in log space.

5.2.2 Contributing to the database

We strongly support the addition of spectra from the community. Whilst attempting to ensure any additions are convenient to do, we do still require a few manipulations to spectra in order to comply with our ingestion code. Each requirement is due to the plethora of different file formats and standards across decades and data reduction processes.

1. The filename must not already exist in the final directories.
2. The file is a 1D fits file with a header and data card.
3. There are at least 100 data points in the flux.
4. The wavelengths are in units of microns and between $0.3\text{--}10\mu\text{m}$ (this is to check wavelengths are indeed microns).
5. The short name of the object is in the database already.
6. It is not a duplicate of a spectra already in the database (i.e. same date, instrument and object).
7. The following keywords are in the header:
 - `shortname` – The short name of the object as corresponds to the existing database.
 - `instrument` – The instrument name used to observe.

- `mjd-obs` – Mean Julian Date of the observation.
 - `ra-deg` – RA in degrees, and between 0–360 deg.
 - `dec-deg` – Dec in degrees, and between –90–90 deg.
8. It is assumed that the spectra provided are public. If not, provide the `private` keyword set to ‘True’ in the header.

An hourly ‘cronjob’ is operational which shifts spectra from the uploaded directory to a temporary server directory. This triggers an automated script which checks the aforementioned requirements and transfers spectra passing these checks to another temporary directory. There is then a manual script which displays each spectrum in an interactive window, such that a maintainer can confirm that the spectra are visually as expected. Only spectra passing this manual check are added to the database. All processes are logged, with information on each object’s header and list of available spectra stored in ‘json’ files.

5.3 Conclusions

We have presented in this work a description of the GUCDS database. This is following years of gathering observational data across many observatories. Use cases have been presented for the searching and querying of the database one can perform via the web interface. We have demonstrated the interactivity of the spectra plotting.

Chapter 6

Astronomical Software and Observations

I present here the documentation on my work creating databases and astronomical software, for use by the UCD community. I discuss also additional technical work, such as the generation of publication-ready plots and observing targets.

6.1 SIMPLE Database

The SIMPLE database (P.I. Kelle Cruz) has been created to collate information on UCDs. This includes any astrometric, photometric and spectroscopic data. SIMPLE was first conceptualised by Cruz et al. (2021) with further work by L’Heureux et al. (2023). I led the creation of the website, available at simple-bd-archive.org. The entirety of the website is driven by a python codebase I developed, which communicates with the database on the host server via an API. Each webpage is generated by python inserting data into HTML templates I created. I designed the website using Bootstrap-5 to style the pages (CSS). Interactivity of the plots across the website plus additional functionality is driven by client-side javascript, which I also developed. Users can query the database with either coordinates, free text searches (Figure 6.1) or a SQL query.

A user can then view all information on any object, and download spectra and any data (Figure 6.2).

The screenshot shows the SIMPLE website interface. At the top, there is a navigation bar with links: SIMPLE, Home, Search by Object, Query by Coordinates, Full Text Search, Explore the Database, Query using SQL, and About the SIMPLE Archive. The main heading is "Exploring the Database". Below this, there is a search bar with the text "vhs" entered. A "Search" button is visible. Below the search bar, there is a section titled "Results for: vhs" with a sub-heading "Show 10 entries". A table of search results is displayed, with columns: source, ra, dec, epoch, equinox, shortname, reference, other_references, and comments. The table contains 7 rows of data. At the bottom of the table, there is a "Showing 1 to 7 of 7 entries" indicator and navigation buttons for "Previous", "1", and "Next". Below the table, there is a message: "Are we missing any expected data? Please open an [issue!](#)".

source	ra	dec	epoch	equinox	shortname	reference	other_references	comments
2MASS J12560183-1257276	194.007637	-12.957692	None	None	1256-1257b	Gauz15	None	None
2MASS J12560215-1257217	194.007700	-12.956900	None	None	None	Gauz15	None	None
VHS J125804.89-441232.4	194.520500	-44.209100	None	2000	None	Lodi12.53	None	None
VHS J143311.46-083736.3	218.297600	-8.626800	None	2000	None	Lodi12.53	None	None
VHS J154352.78-043909.6	235.970200	-4.652600	None	2000	None	Lodi12.53	None	None
VHS J192934.18-442550.5	292.392400	-44.430700	None	2000	None	Lodi12.53	None	None
VHS J205159.38-550843.9	312.997200	-55.146000	None	2000	None	Lodi12.53	None	None

FIGURE 6.1: An example search performed on the SIMPLE website for any object with a name (not only the main name) including ‘VHS’.

6.2 Public Python packages

I also developed several resources for use by the community to assist with analysis and data gathering.

6.2.1 GaiaXPY Batch

The GaiaXPY (Ruz-Mieres, 2022) package is designed for downloading *Gaia* XP spectra, both internally and externally calibrated. I developed as a complement to this, GaiaXPY-batch (Cooper, 2022a), which allows users to download as many spectra as possible, which was a limitation in GaiaXPY. This is useful as it allows users to retrieve *Gaia* spectra in a ‘big-data’ form, which takes advantage of the homogeneous nature of the spectra.



FIGURE 6.2: An example object results page, with the interactive photometry and spectra plots shown.

6.2.2 RV Fitter

Gathering radial velocities from spectra has historically been challenging due to the often subjective nature of calculating it. This includes the selection of spectral features, the choice of method, the selection of continuum, etc. I developed a code in `rvfitter` (Cooper, 2022b) which has been used by Morris et al. (2022), my ‘The *Gaia* Ultracool Dwarf Sample – IV. GTC/OSIRIS optical spectra of *Gaia* L dwarfs’ work, and other works in preparation. See Figure 2.5 and 2.6 for an example of fitting absorption features. An example of this fitting emission lines is shown in Figure 6.3. This figure was created by me as part of my contribution to the Morris et al. (2022) work.

This code is inspired by older codes such as in IRAF and IDL, and allows a user to interactively fit Gaussian, Lorentzian and Voigt profiles to any provided spectral feature. It also allows a user to manually shift models such as those from BT-Settl (Allard et al., 2012) to the same spectral features as with the line centering technique.

6.2.3 Target List Generator

The gathering of ground-based spectra is a major part of astronomy. I created a code, `targetlistgenerator`, as a time saving tool for observers as it will filter any target list into observable targets, based on sunset/sunrise times. It will also create any finder charts requested via the Aladin (Bonnarel et al., 2000) API. This is demonstrated in Figures 6.4 and 6.5.

Usefully for UCD observations in particular, the code will also intersperse a list of bright standards after each time-ordered target. This is shown in Figure 6.6, with standards selected around an RA 45 minutes after the zenith of each target. The formatted files are designed for typical telescope facilities, including `.cat` files, which are used in useful ‘Star Track’ tools.

6.2.4 Publication-ready Plots

Rybizki et al. (2021) discussed the RVS selection function in *Gaia* DR2. As part of this, I created an interactive, web-accessible all-sky map and CMD which one can explore the effect of the RVS selection function and how it relates to HEALPix, magnitude, colour and sky position. During the preparation of the GCNS (Gaia Collaboration et al., 2021f), I also re-created all

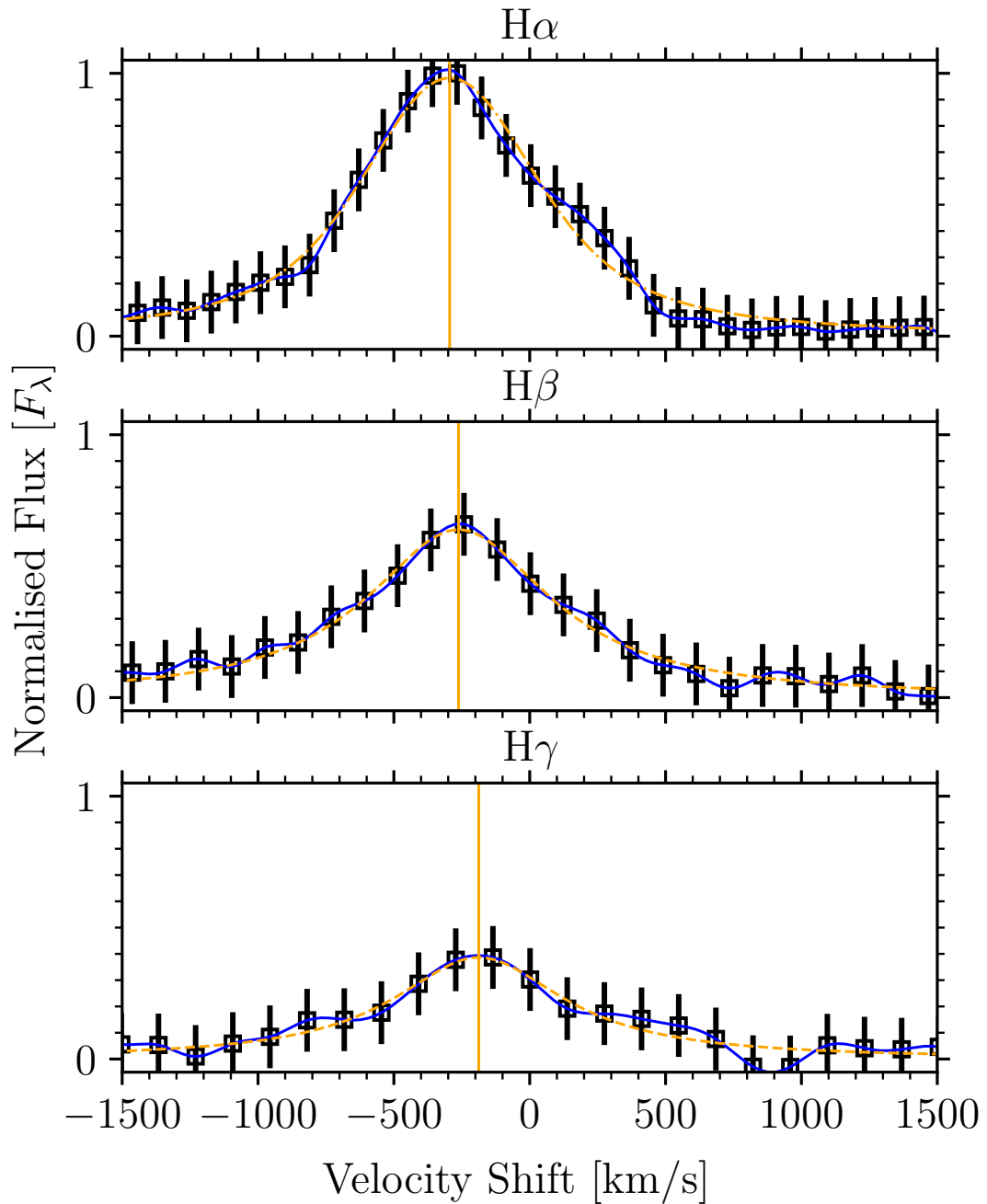


FIGURE 6.3: From Morris et al. (2022), “Fitted line profiles and radial velocities for the hydrogen recombination lines. Points and blue lines are the data, yellow dashed lines are the fits, using a Voigt profile, and converted into velocity space. The median radial velocity of the star was $-283.9 \pm 9.3 \text{ km s}^{-1}$, relative to the Local Standard of Rest. The individual radial velocities fitted to each line are marked with solid yellow lines. Fluxes are normalised with respect to the $\text{HI } 3 \rightarrow 2$ line.”



FIGURE 6.4: An example object finder chart, using Aladin and Pan-STARRS within a 5 arcminute view.

figures made by collaborators. This was to create a unified styling across the entire work. I also heavily assisted with the creation of the figures used by Reylé et al. (2021).

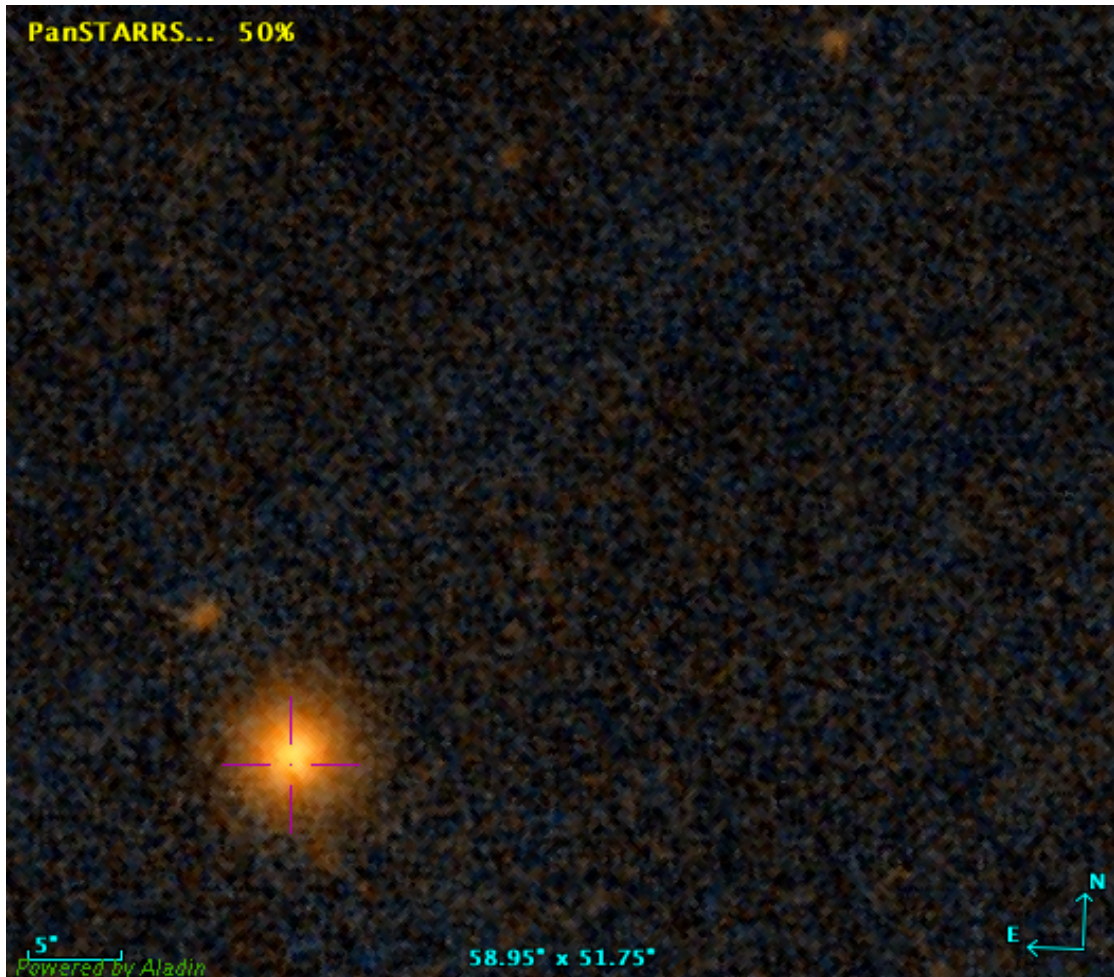


FIGURE 6.5: An example object finder chart, using Aladin and Pan-STARRS within a 1 arcminute view.

#	Index	Name	RA	DEC	Epoch	PMRA	PMDEC	SpT	K2MASS	
1		J0000+3757	0:0:11.58	37:57:0.4		2000	0.0	0.0	L0	14.5
2		HD__952	0:14:2.28	33:12:21.7		2000	0.0	0.0	A1V	6.19
3		J0002+3053	0:2:18.85	30:53:47.0		2000	0.0	0.0	L1	13.93
4		HD__7215	1:12:52.99	32:4:31.6		2000	0.0	0.0	A0V	6.95
5		J0006-5227	0:6:3.52	-52:27:44.8		2000	0.0	0.0	L3	14.06
6		HD__8341	1:21:44.33	-52:4:35.4		2000	0.0	0.0	A0V	8.22
7		J0025-1346	0:25:7.86	-13:46:48.1		2000	0.0	0.0	L2	14.5
8		HD__9399	1:32:12.7	-14:29:32.6		2000	0.0	0.0	A1V	7.88
9		J0029-3119	0:29:0.99	-31:19:37.6		2000	0.0	0.0	L2	14.33
10		HD__7323	1:12:55.04	-35:44:45.3		2000	0.0	0.0	A0V	7.51
11		J0044+4222	0:44:15.18	42:22:35.7		2000	0.0	0.0	L0	14.43
12		HD__9935	1:38:1.66	45:59:54.0		2000	0.0	0.0	A1V	8.4
13		J0048+3022	0:48:22.68	30:22:4.8		2000	0.0	0.0	L1	14.64
14		HD__7215	1:12:52.99	32:4:31.6		2000	0.0	0.0	A0V	6.95
15		J0053-2218	0:53:24.0	-22:18:39.6		2000	0.0	0.0	L1	13.92
16		HD__10161	1:38:49.99	-25:1:19.9		2000	0.0	0.0	B9V	6.84
17		J0056-4036	0:56:14.61	-40:36:3.3		2000	0.0	0.0	L2	14.35
18		HD__10538	1:42:2.99	-36:49:56.3		2000	0.0	0.0	A0V	5.68
19		J0102+5254	1:2:4.58	52:54:10.4		2000	0.0	0.0	M7	0.0
20		HD__11920	1:58:48.18	57:16:55.3		2000	0.0	0.0	A0V	8.65
21		J0103+3429	1:3:16.06	34:29:52.3		2000	0.0	0.0	L1	14.26
22		HD__12381	2:2:17.85	38:37:38.4		2000	0.0	0.0	A0V	8.88

FIGURE 6.6: An example target list of UCDs interspersed with nearby A dwarf standards. This is formatted to the requirements for the Infrared Telescope Facility.

Chapter 7

Conclusions

I have summarised the theory and current population of UCDs, with a focus on late-M and L dwarfs. I presented my work on characterising the 30 pc sample in the GUCDS as following an ongoing observation campaign. Working as part of the *Gaia* DPAC, I helped with the development of astrophysical parameters using the *Gaia* RP spectra. This included ‘downstream’ analysis work on the UCDs within *Gaia*. Utilising my gathering and analysing of ground-based spectra, I contributed to large sample population studies such as in the GCNS. Independently, I created a novel colour ratio specific to *Gaia* RP spectra, to select outlying UCDs. Technical skills were utilised to support the astronomical community and in particular, creating tools suitable for use with UCDs.

I will continue proposing for time on ground and space-based telescopes and observing both interesting UCDs and those within 30 pc as part of the GUCDS. I am expanding on my colour ratio technique, using unsupervised machine learning to select outlying UCDs. I shall assist with the improvement of *Gaia* astrophysical parameters of UCDs for upcoming data releases. There should be much improved data products, due to the longer data baseline and evolved methodology. One change will be that of the expanded use of non-single-star solutions for the photometry.

There are several other *Gaia* and machine learning projects I have planned with collaborators, before *Gaia* DR4 is due to release. These include improving distances determined from *Gaia* parallaxes; classification of sources within 100 pc; mass and age estimates from photometry; analysis of optical variability of UCDs. After *Gaia* DR4, I plan to continue with these machine learning techniques.

Appendix A

GTC/OSIRIS optical spectra of *Gaia* L dwarfs Appendices

Presented here are the appendices from my ‘The *Gaia* Ultracool Dwarf Sample – IV. GTC/OSIRIS optical spectra of *Gaia* L dwarfs’ work, as relates to Chapter 2.

A.0.1 Supplementary Tables

TABLE A.1: Additional information for all observations carried out as part of the two programmes presented here. Note, multiple objects were observed multiple times, with either the same grism or the other. Seeing is given as a range corresponding to reverse wavelength, and is corrected for airmass.

Object Full Name	Object short name	Resolution Grism/ VPH	Programme ID	Date yyyy-mm-dd	Airmass (z)	Humidity [per cent]	Seeing $\lambda_{\max} - \lambda_{\min}$
2MASS J00285545-1927165	J0028-1927	R2500I	GTC8-15ITP	2015-08-30	1.54	27	0.90 - 0.96
2MASS J02354756-0849198	J0235-0849	R2500I	GTC8-15ITP	2015-08-31	1.49	30	0.89 - 0.94
2MASS J04285096-2253227	J0428-2253	R2500I	GTC8-15ITP	2015-08-31	1.82	32	1.12 - 1.19
2MASS J04532647-1751543	J0453-1751	R2500I	GTC8-15ITP	2015-10-01	1.51	11	0.67 - 0.71
2MASS J05021345+1442367	J0502+1442	R2500I	GTC8-15ITP	2015-09-29	1.04	13	0.71 - 0.76
2MASS J0605019-234226	J0605-2342	R2500I	GTC8-15ITP	2015-11-30	1.66	58	1.77 - 1.88
2MASS J07410440+2316377	J0741+2316	R2500I	GTC8-15ITP	2015-12-31	1.05	6	0.90 - 0.95
SDSS J075259.48+413646.8	J0752+4136	R2500I	GTC8-15ITP	2015-11-28	1.04	17	0.98 - 1.04
ULAS J080910.65+231515.7	J0809+2315	R2500I	GTC8-15ITP	2015-12-31	1.10	7	1.20 - 1.27
2MASS J08230316+0240426	J0823+0240	R2500I	GTC8-15ITP	2015-12-31	1.12	7	0.84 - 0.89
2MASS J08230838+6125208	J0823+6125	R2500I	GTC8-15ITP	2015-11-30	1.21	51	1.27 - 1.35
2MASS J08472872-1532372	J0847-1532	R300R	GTC54-15A	2015-04-04	1.40	13	1.49 - 1.73
2MASSW J0918382+213406	J0918+2134	R2500I	GTC8-15ITP	2015-11-30	1.03	52	0.98 - 1.04
2MASS J09352803-2934596	J0935-2934	R2500I	GTC8-15ITP	2015-11-30	1.90	47	1.79 - 1.90
2MASS J09385888+0443438	J0938+0443	R2500I	GTC8-15ITP	2015-12-31	1.18	7	0.67 - 0.72
2MASS J09404793+2946534	J0940+2946	R2500I	GTC8-15ITP	2016-02-26	1.27	13	1.01 - 1.07
2MASS J0953212-101420	J0953-1014	R2500I	GTC54-15A	2015-03-31	1.37	16	1.26 - 1.34
G196-3B	J1004+5022	R2500I	GTC54-15A	2015-04-27	1.09	2	0.83 - 0.88
G196-3B	J1004+5022	R300R	GTC54-15A	2015-04-27	1.08	2	0.82 - 0.95
2MASS J10044030-1318186	J1004-1318	R2500I	GTC8-15ITP	2015-12-31	1.36	8	1.26 - 1.34
DENIS J104731.1-181558	J1047-1815	R300R	GTC54-15A	2015-04-27	1.50	2	1.33 - 1.54
DENIS J104731.1-181558	J1047-1815	R2500I	GTC54-15A	2015-04-27	1.55	2	1.36 - 1.44
DENIS J1058.7-1548	J1058-1548	R300R	GTC54-15A	2015-04-27	1.52	2	1.12 - 1.29
DENIS J1058.7-1548	J1058-1548	R2500I	GTC54-15A	2015-04-27	1.61	1	1.16 - 1.23
2MASS J11092745-1606515	J1109-1606	R2500I	GTC8-15ITP	2015-12-30	1.42	21	1.18 - 1.26
2MASS J11270661+4705481	J1127+4705	R2500I	GTC8-15ITP	2015-12-30	1.05	21	0.63 - 0.67
2MASS J12130336-0432437	J1213-0432	R2500I	GTC54-15A	2015-04-28	1.29	2	0.81 - 0.86
2MASS J12164560+4927452	J1216+4927	R2500I	GTC8-15ITP	2015-12-31	1.07	8	0.73 - 0.77
2MASS J12212770+0257198	J1221+0257	R2500I	GTC54-15A	2015-04-01	1.24	7	0.79 - 0.84
ULAS J122259.30+140750.1	J1222+1407	R300R	GTC8-15ITP	2016-01-19	1.04	6	1.16 - 1.34
DENIS J123218.3-095149	J1232-0951	R2500I	GTC54-15A	2015-05-31	1.32	23	2.06 - 2.19
2MASSW J1246467+402715	J1246+4027	R2500I	GTC54-15A	2015-04-29	1.05	2	0.63 - 0.67
2MASSW J1246467+402715	J1246+4027	R300R	GTC54-15A	2015-04-29	1.03	2	0.53 - 0.61
2MASS J13313310+3407583	J1331+3407	R2500I	GTC54-15A	2015-04-28	1.03	2	0.80 - 0.85
2MASS J13313310+3407583	J1331+3407	R300R	GTC54-15A	2015-04-28	1.01	2	0.79 - 0.91
2MASS J13334540-0215599	J1333-0215	R2500I	GTC8-15ITP	2015-12-31	1.23	7	1.28 - 1.36
2MASS J13460746+0842346	J1346+0842	R2500I	GTC8-15ITP	2016-01-06	1.09	6	1.01 - 1.07
2MASSW J1412244+163312	J1412+1633	R2500I	GTC8-15ITP	2016-01-19	1.06	6	1.26 - 1.34
2MASSW J1412244+163312	J1412+1633	R2500I	GTC54-15A	2015-04-29	1.04	2	0.62 - 0.66
2MASSW J1412244+163312	J1412+1633	R300R	GTC54-15A	2015-04-29	1.03	2	0.62 - 0.72
2MASSW J1421314+182740	J1421+1827	R2500I	GTC54-15A	2015-04-01	1.03	6	0.71 - 0.75
ULAS J143915.10+003941.7	J1439+0039	R300R	GTC8-15ITP	2016-03-29	1.16	10	0.57 - 0.66
DENIS J144137.2-094558	J1441-0945	R300R	GTC54-15A	2015-05-05	1.28	11	1.01 - 1.17
DENIS J144137.2-094558	J1441-0945	R2500I	GTC54-15A	2015-05-05	1.28	11	1.01 - 1.07
ULAS J152722.48+055316.2	J1527+0553	R300R	GTC8-15ITP	2016-03-29	1.15	11	0.76 - 0.88
2MASS J15322338+2611189	J1532+2611	R2500I	GTC8-15ITP	2016-01-29	1.08	17	0.82 - 0.87
2MASS J15394189-0520428	J1539-0520	R2500I	GTC8-15ITP	2016-02-27	1.46	44	1.42 - 1.51
2MASS J15485834-1636018	J1548-1636	R2500I	GTC54-15A	2015-04-01	1.47	10	1.10 - 1.17
2MASS J16170673+7734028	J1617+7733B	R2500I	GTC54-15A	2015-05-29	1.53	47	2.25 - 2.39
2MASS J16170673+7734028	J1617+7733B	R300R	GTC54-15A	2015-05-28	1.58	36	2.29 - 2.65
DENIS J161845.0-132129	J1618-1321	R2500I	GTC54-15A	2015-04-28	1.61	1	0.93 - 0.98
2MASS J16232185+1530393	J1623+1530	R2500I	GTC8-15ITP	2015-09-02	1.29	38	1.02 - 1.08
2MASS J16230740+2908281	J1623+2908	R2500I	GTC8-15ITP	2016-02-12	1.03	21	1.51 - 1.60
2MASS J17054834-0516462	J1705-0516	R300R	GTC54-15A	2015-04-01	1.21	7	1.08 - 1.24
2MASS J17072529-0138093	J1707-0138	R300R	GTC54-15A	2015-05-29	1.21	45	1.76 - 2.03
2MASS J17072529-0138093	J1707-0138	R2500I	GTC54-15A	2015-05-29	1.18	36	1.73 - 1.84
2MASS J17171408+6526221	J1717+6526	R2500I	GTC8-15ITP	2015-08-30	1.51	31	0.89 - 0.95

Object Full Name	Object short name	Resolution Grism/ VPH	Programme ID	Date yyyy-mm-dd	Airmass (z)	Humidity [per cent]	Seeing $\lambda_{\max} - \lambda_{\min}$
2MASS J17171408+6526221	J1717+6526	R300R	GTC54-15A	2015-05-03	1.42	4	0.75 – 0.87
2MASS J17171408+6526221	J1717+6526	R2500I	GTC54-15A	2015-06-01	1.27	39	2.01 – 2.14
Gaia DR2 4569300467950928768	J1724+2336	R300R	GTC8-15ITP	2015-09-01	2.13	28	1.36 – 1.58
DENIS J173342.3–165449	J1733–1654	R300R	GTC54-15A	2015-06-26	1.62	26	1.74 – 2.01
DENIS J174534.6–164053	J1745–1640	R2500I	GTC54-15A	2015-08-04	1.88	17	1.27 – 1.35
2MASS J17502484–0016151	J1750–0016	R2500I	GTC54-15A	2015-04-02	1.15	19	0.95 – 1.01
2MASS J21555848+2345307	J2155+2345	R2500I	GTC8-15ITP	2015-08-30	1.04	28	0.62 – 0.66
2MASS J23392527+3507165	J2339+3507	R2500I	GTC8-15ITP	2015-08-06	1.05	38	0.90 – 0.95

TABLE A.2: Cross-matched absolute photometry from *Gaia*, 2MASS & WISE, using *Gaia* parallaxes.

Object short name	M_G [mag]	M_{RP} [mag]	M_J [mag]	M_H [mag]	M_{K_s} [mag]	M_{W1} [mag]	M_{W2} [mag]	M_{W3} [mag]
J0028–1927	16.03±0.02	14.45±0.03	11.24±0.04	10.38±0.04	9.90±0.04	9.57±0.03	9.31±0.03	8.88±0.27
J0235–0849	17.04±0.09	15.43±0.10	12.26±0.11	11.50±0.11	10.88±0.11	10.47±0.10	10.19±0.10	...
J0428–2253	16.70±0.02	14.79±0.02	11.48±0.03	10.65±0.03	10.10±0.03	9.70±0.03	9.45±0.03	8.93±0.13
J0453–1751	17.73±0.04	16.15±0.04	12.74±0.05	11.66±0.05	11.06±0.05	10.55±0.04	10.20±0.04	9.62±0.21
J0502+1442	15.59±0.03	14.01±0.04	10.96±0.04	10.08±0.04	9.64±0.04	9.34±0.05	9.10±0.04	7.91±0.22
J0605–2342	16.71±0.02	15.16±0.02	11.91±0.04	11.13±0.04	10.54±0.04	10.24±0.03	9.94±0.03	10.05±0.49
J0741+2316	16.40±0.30	14.87±0.32	11.73±0.31	10.75±0.31	10.34±0.31	9.74±0.30	9.43±0.31	>7.16
J0752+4136	13.06±0.03	11.59±0.03	9.35±0.04	8.79±0.04	8.44±0.04	10.36±0.06	10.13±0.09	>7.64
J0823+6125	17.65±0.02	16.09±0.03	12.80±0.04	11.80±0.04	11.18±0.04	10.72±0.03	10.43±0.03	10.39±0.39
J0847–1532	17.18±0.01	15.60±0.01	12.31±0.03	11.43±0.03	10.86±0.02	10.51±0.03	10.26±0.02	9.76±0.11
J0935–2934	16.39±0.02	14.57±0.03	11.42±0.04	10.70±0.04	10.21±0.04	9.80±0.03	9.51±0.03	9.08±0.21
J0938+0443	15.84±0.07	14.31±0.08	11.19±0.09	10.44±0.09	9.95±0.10	9.75±0.08	9.55±0.08	>7.90
J0940+2946	16.57±0.11	14.93±0.12	11.56±0.13	10.61±0.13	10.19±0.12	9.78±0.11	9.52±0.12	>8.78
J0953–1014	15.68±0.02	14.03±0.02	10.71±0.03	9.88±0.03	9.38±0.03	9.01±0.03	8.65±0.03	7.97±0.12
J1004+5022	18.45±0.03	16.86±0.03	13.15±0.05	11.97±0.05	11.10±0.04	10.02±0.03	9.46±0.04	8.60±0.07
J1004–1318	17.87±0.03	16.29±0.04	12.72±0.05	11.92±0.05	11.39±0.05	10.82±0.04	10.53±0.04	10.21±0.43
J1047–1815	16.76±0.02	15.24±0.02	11.96±0.04	11.18±0.04	10.65±0.04	10.34±0.03	10.08±0.03	10.05±0.47
J1058–1548	17.95±0.01	16.39±0.02	12.86±0.04	11.93±0.03	11.24±0.03	10.79±0.03	10.49±0.03	10.40±0.27
J1109–1606	16.56±0.04	15.01±0.05	11.89±0.06	11.26±0.06	10.81±0.07	10.56±0.05	10.26±0.05	9.57±0.48
J1127+4705	16.82±0.05	15.23±0.05	12.08±0.06	11.38±0.06	10.79±0.06	10.49±0.05	10.21±0.06	9.57±0.50
J1213–0432	18.71±0.02	17.15±0.03	13.54±0.04	12.51±0.03	11.87±0.04	11.23±0.03	10.93±0.03	9.91±0.22
J1221+0257	16.52±0.01	14.93±0.01	11.82±0.02	11.06±0.03	10.61±0.03	10.30±0.02	10.02±0.02	9.48±0.15
J1232–0951	16.43±0.28	14.59±0.28	11.42±0.28	10.76±0.28	10.24±0.28	9.92±0.28	9.64±0.28	9.34±0.39
J1246+4027	18.53±0.03	16.95±0.04	13.34±0.06	12.20±0.05	11.53±0.05	10.83±0.04	10.46±0.04	10.21±0.25
J1331+3407	16.72±0.02	15.14±0.02	12.04±0.03	11.11±0.04	10.59±0.03	10.28±0.03	10.05±0.03	9.46±0.23
J1333–0215	17.23±0.07	15.60±0.08	12.50±0.08	11.49±0.08	10.98±0.09	10.66±0.08	10.39±0.08	9.69±0.45
J1346+0842	17.32±0.10	15.78±0.11	12.58±0.13	11.63±0.13	11.00±0.12	10.61±0.11	10.38±0.11	>9.08
J1412–1633	16.15±0.02	14.55±0.02	11.36±0.03	10.63±0.04	10.00±0.03	9.66±0.03	9.40±0.03	8.89±0.13
J1421+1827	16.45±0.01	14.86±0.01	11.85±0.02	11.04±0.02	10.56±0.02	10.18±0.02	9.91±0.02	8.84±0.05
J1441–0945	16.78±0.09	14.86±0.09	11.58±0.09	10.75±0.09	10.22±0.09	9.90±0.09	9.67±0.09	9.67±0.35
J1539–0520	17.85±0.01	16.26±0.02	12.79±0.03	11.92±0.03	11.44±0.03	10.88±0.03	10.61±0.03	10.54±0.28
J1548–1636	16.41±0.02	14.87±0.02	11.76±0.03	10.98±0.03	10.51±0.03	10.16±0.03	9.87±0.03	9.35±0.24
J1617+7733B	12.23±0.01	10.87±0.01	8.79±0.02	8.21±0.02	7.91±0.02	7.62±0.02	7.37±0.02	7.13±0.10
J1618–1321	16.04±0.13	14.14±0.13	10.95±0.13	10.10±0.13	9.62±0.13	9.25±0.13	8.99±0.13	8.55±0.36
J1623+1530	15.65±0.20	14.10±0.20	11.00±0.22	10.20±0.22	9.69±0.22	9.53±0.20	9.26±0.21	7.53±0.54
J1705–0516	16.81±0.01	15.22±0.01	11.94±0.03	11.18±0.03	10.66±0.02	10.31±0.03	10.05±0.03	9.67±0.21
J1707–0138	16.33±0.03	14.72±0.03	11.36±0.04	10.64±0.04	10.14±0.05	9.71±0.04	9.43±0.04	9.32±0.49
J1717+6526	18.56±0.03	16.90±0.03	13.25±0.05	12.14±0.04	11.48±0.04	10.85±0.03	10.52±0.03	9.82±0.07
J1724+2336	16.02±0.07	14.45±0.07	11.50±0.09	10.95±0.11	10.15±0.11	10.03±0.08	9.76±0.08	>7.98
J1733–1654	17.20±0.01	15.46±0.01	12.23±0.05	11.50±0.06	11.05±0.03
J1745–1640	16.98±0.01	15.38±0.01	12.18±0.03	11.41±0.02	10.94±0.02	10.64±0.03	10.40±0.03	10.82±0.46
J1750–0016	>18.47	16.86±0.01	13.47±0.02	12.59±0.02	12.03±0.02	11.36±0.02	11.08±0.02	10.47±0.07
J2339+3507	18.26±0.05	16.74±0.06	13.16±0.07	12.15±0.07	11.38±0.06	10.88±0.05	10.56±0.05	10.32±0.53

A.0.2 Comparison with standard routines

In the reduction we use two procedures based on IRAF and Python packages with a comparison target (J1745–1640, DENIS J174534.6–164053, Phan-Bao et al., 2008) as a sanity check. A full image and spectral reduction was carried out using standard tasks within the IRAF package on one of our target objects (J1745–1640) plus complimentary flux standard (Ross 640). This was done to assess both the quality of the data and to ascertain the necessary required reduction steps to maximise data quality. The results from this bespoke reduction method served as a reliable reference by which to measure the performance of a python pipeline (with support for the GTC/OSIRIS instrument recently added), which was later applied to all objects within our sample.

A.0.2.1 Bespoke IRAF Reduction

Our IRAF reduction was applied to the science and calibration frames of J1745–1640 (L1–1.5) and Ross 640 (DZA6) as appropriate using the following tasks, beginning with basic image

reduction:

CCDPROC: Pre-scan bias level and bias structure removal; flat-fielding; illumination correction; data section trimming.

RESPONSE: Spectroscopic flat-field lamp colour removal (normalisation).

Illumination and CCDPROC: Correction for spatial axis illumination gradients, made from the extensive sky lines of a well exposed object frame.

IDENTIFY , FITCOORDS and TRANSFORM: Correction for geometric image distortion (curvature) along the spatial axis sky background.

For the spectral reduction:

APALL: Trace and extraction using both optimal and fixed-width aperture summing using image distortion corrected arc frames.

IDENTIFY and DISPCOR: Wavelength calibration to a linear wavelength dispersion using image distortion corrected arc frames.

STANDARD, SENSFUNC and CALIBRATE: Flux calibration from the flux standard Ross 640 taken on same night as the target.

In addition to the IRAF tasks mentioned above, two extra reduction software tools were utilised during the reduction process:

DeFringFlat: An IDL routine acquired from the NASA IDL Astronomy library (Landsman, 1993) was used to provide capabilities in de-fringing the flat field frames (DeFringFlat.pro; Rojo and Harrington, 2006)).

SKYCALC : ESO Sky Model Calculator provides additional telluric correction during flux calibration. A telluric sky model was queried using meteorological and astrometric parameters appropriate for the object in question.

During the bias subtraction we discovered that the pre-scan region of the second CCD containing the spectrum displayed a gradient across it in ADU. A carefully chosen restricted section of the

pre-scan region was used (~ 3 pixels wide), which was found to be reliable for row-by-row bias level subtraction, before the 2D image bias structure was removed.

To correct for illumination gradients evident along the spatial axis of the 2D image introduced by the slit illumination function, we utilised the extensive sky lines of the well exposed object frames as a pseudo twilight sky flat (no sky flats were available). The IRAF `ILLUMINATION` task provided this functionality for correction, and we estimate that, after the correction was applied, the error introduced by the slit illumination gradient was reduced to a maximum of ~ 1.5 per cent in the flat-field frames.

The latter, longer wavelength half of the flat-field frames showed evidence of fringing between wavelengths of approximately 8500 to 10,000 Å, coincident with the area of the CCD containing the spectra of interest. We used the IDL routine `DeFringFlat` as mentioned above to attempt to remove as much of the fringing as possible and found the best fit using the Morlet ‘wavemother’ model, and near default parameters. We estimate from measuring the cleaned flat-fielded image that the amplitude of the fringing was reduced from an original level of approximately 7 per cent, to a maximum of about 1.7 per cent.

A combined arc frame was made from the three arcs available from the night of observation to cover the entire wavelength region of the spectrum. An initial wavelength solution was created and applied as part of the geometric image distortion correction, which resulted in a wavelength solution with an RMS error of 0.016 Å. A second wavelength calibration was subsequently made after additional reduction steps to ensure no systematic errors had been introduced, resulting in a more reasonable final RMS to the fitted wavelength solution of 0.025 Å. The final wavelength corrected spectrum had a linear dispersion $1.396 \text{ Å pixel}^{-1}$ over the entire extracted range of 7339–10,155 Å.

Two separate flux calibrations were then made: one used a blackbody to represent the DZ white dwarf flux standard with an effective temperature 8070 K (Blouin et al., 2018) and with an *I*-band magnitude of 13.66 mag (Bergeron et al., 2001); the second used the low resolution calibrated flux standard spectrum of Ross 640 contained in the IRAF database. In both cases, the sensitivity functions were created by interpolating over the affected telluric regions, and regions of intrinsic absorption features. Both of these sensitivity functions provided flux calibrations with almost identical results. A correction for atmospheric extinction and telluric features to the target was included during the flux calibration. An initial extinction correction was made from using a file containing tabulated extinction magnitudes as a function of wavelength applicable to

the observatory site, that was provided on the GTC instrument website. However, an improved extinction correction was obtained from the much higher spectral resolution telluric sky model mentioned above (via the ESO Sky Model Calculator). The improvement is particularly evident over the wavelength regions containing the potassium K I $\lambda\lambda$ 7665,7699 Å doublet and the H₂O band at about 9500 Å.

A.0.3 Radial velocity method validation

The techniques used to measure RVs via the centres of atomic neutral alkali lines and through cross-correlation of spectra were employed by Burgasser et al. (2015), and we adopt a similar twin measurement approach to derive our final RVs. In keeping with our strategy outlined in Section 2.2.3 we again invoked an independent check, this time to validate our methods by helping to identify any problems with our RV measurements relating to the PyPeIt reduced data set. We achieved this through the use of both IRAF and custom prepared routines within IDL to measure the RV via the Fourier cross-correlation and the line centre fitting methods. This analysis was conducted on the bespoke IRAF reduced data of our test object J1745–1640. We then used our validated RVs to classify any objects into young moving groups and stellar associations.

A.0.3.1 Line centres

Two interactive methods were employed here: the first using routines in IDL to measure the 1D centroids of fitted Gaussian profiles to the atomic lines of J1745–1640, while the second used the IRAF task `Sp1ot` to again measure the same lines but via fitting Voigt profiles.

In the first case, sub-sections of the spectrum surrounding the line features to be measured were extracted and interpolated onto a ten times finer wavelength grid, to facilitate the manual fitting of Gaussian profiles with a different number of terms via the `Gaussfit.pro` routine. Best fitting model profiles to spectral features were initially determined by eye, and determined by how closely the profile matched the feature with more emphasis being given around the line centre region. The reported RMS error and Full Width Half-Maximum (FWHM) of fitted profiles were also taken into account for when the different Gaussian profiles produced similar results, such that the number of terms which fitted with the least error and narrowest FWHM were

chosen. The measured wavelength shifts from laboratory rest-frame line centres (in standard air: Kramida et al., 2021) were then converted to Doppler RVs.

Secondly, and by using `Splot`, Voigt profiles were fitted to the same line features of appropriately pseudo-continuum subtracted sub-sections of the spectrum, and Doppler RVs were then found in the same manner as previously from the reported line centres. We obtained results for all eight line features from both measurement sets. However, it was apparent that four of the measurements gave the least error and particularly consistent results between both sets, these being Rb I-a, Rb I-b, Na I-a, Cs I-a with mean values for RV found from these four selected for each measurement set. The RV derived from the Gaussian fitted profiles (IDL) was found to be 35.1 km s^{-1} , and via Voigt profiles (`Splot`) 29.0 km s^{-1} (all test results are Heliocentric: barycentric correction calculated using `baryvel.pro`). From the spread among the individually measured line shifts we place more confidence in the latter result, and assign uncertainties based on the $1\text{-}\sigma$ standard deviation of the respective RV measurements of 4.3 km s^{-1} and 3.8 km s^{-1} .

The RV as measured by our line centering method using the `PyPeIt` reduced data for J1745–1640 is $29.7 \pm 4.2 \text{ km s}^{-1}$ (see Table 2.4) which is in good agreement with those from this independent measurement test. The RV measured via line centre fitting as reported by Burgasser et al. (2015) is $28 \pm 9 \text{ km s}^{-1}$. Thus, we have confidence in our RV results derived from our chosen method, which contribute to the final adopted values.

A.0.3.2 Cross-correlation

To validate this second technique of measuring RVs as part of our adopted method, and to ascertain the best way forward in its application, we used the Fourier cross-correlation task `Fxcor` within IRAF to conduct tests. Our choice of RV rest-frame models were a BT-Settl model spectrum and custom-made synthetic atomic absorption spectra. Our object was again the bespoke IRAF reduced J1745–1640 spectrum.

The BT-Settl spectrum used was the best fitting model with the physical parameters of $T_{\text{eff}} = 2000 \text{ K}$, $\log g = 5 \text{ dex}$ and $\text{Fe}/\text{H} = 0 \text{ dex}$, corresponding to $\simeq \text{L1}$ in spectral type. We smooth the spectrum using a Gaussian kernel to match the dispersion and resolution of the J1745–1640, and appropriate FITS header keywords added for the `Fxcor` task to recognise the template spectrum as rest-frame.

To help highlight any potential systematic wavelength shifts introduced by the use of the BT-Settl model, and therefore to help assess its suitability as an RV template, we measured the line centre locations of the most reliable Rb I-b and Cs I-a lines by fitting Voigt profiles in `Sp1ot`. A maximum difference compared to laboratory rest-frame line centres of 0.13 \AA was found, corresponding to 4.5 km s^{-1} . This shift is similar to the uncertainty found earlier from the fitted line profiles suggesting that the BT-Settl model is reliable for use as a template, however, we add this uncertainty in velocity units in quadrature to the subsequent `Fxcor` individual RV region measurements.

To facilitate the most accurate RV measurements we extracted sections of both object and template spectra into discrete spectral regions, each covering the main atomic absorption features as well as the FeH Wing-Ford band at $\sim 9900 \text{ \AA}$, then each region was appropriately pseudo-continuum subtracted and normalised.

During the RV measurements, we interactively adjusted the sample test wavelength range around the features of interest to reduce noise in Fourier space domain. Next, the width of the cross-correlation function (CCF) fit was changed to facilitate a best-fit (Gaussian fit to the CCF was used). The results of these changes to the CCF height, the goodness-of-fit ‘R-value’ and fit error were noted, until the best RV estimate was obtained. The shape of the CCF profile was also informative to this end. No Fourier filtering was applied as it was not found to be beneficial.

For this test, three regions gave consistent results covering both of the rubidium lines, the first caesium line and the FeH band. The average of these individual results gave an RV of $21.2 \pm 5.2 \text{ km s}^{-1}$.

For our second test, we created a noise-free synthetic absorption spectrum of unity continuum with line widths and depths as measured by Voigt profiles of the neutral atomic lines in of J1745–1640, with no attempt to include the FeH band. The line centres were fixed to the laboratory rest-frame wavelength values. Results from all four regions were averaged which covered both of the rubidium lines, the sodium doublet and both caesium lines. Including the potassium doublet gave a similar result for that region but gave a very large increase in uncertainty, so was not included. We find a resulting RV of $24.6 \pm 1.7 \text{ km s}^{-1}$.

Our final test was conducted to ascertain the intrinsic level of uncertainty in RV from the application of this method through the use of `Fxcor` on a representation of our spectral data. This involved making a cross-correlation between two noise-free synthetic absorption spectra: the

same RV rest-frame template as used above in the second test, and with the object being a wavelength shifted version of the same synthetic spectrum, with the FITS header updated accordingly. The shift in wavelength was set at a value corresponding to the adopted RV presented in Burgasser et al. (2015), of $26.2 \pm 2.3 \text{ km s}^{-1}$. We found the average combined RV of the four measured regions used to be $26.7 \pm 1.2 \text{ km s}^{-1}$, indicating that 1.2 km s^{-1} is our base level uncertainty in using this method. This is, however, in addition to any uncertainty introduced from a real object spectrum (i.e. J1745–1640).

Both of these cross-correlation RV test results for J1745–1640 are in agreement with the equivalent value presented in Burgasser et al. (2015), within their respective uncertainties. The measured RV for J1745–1640 using the cross-correlation package we adopted and apply to our data set (see Section §2.3.3) has a value of $28.8 \pm 4.7 \text{ km s}^{-1}$. Again, the results of this cross-correlation test validate our method and provide us with confidence in the separately derived RVs as well as in our final adopted values combined from both methods (see Section §2.3.3.3).

A.0.4 Spectral sequence

We compare here in Figures A.1 and A.2 the sequence of R2500I spectra, as in Figures 2.2 and 2.3, to their appropriate standards and best-fitting BT-Settl models. All spectra are normalised by the median flux from 8100–8200 Å. The standards and BT-Settl models have been interpolated onto the wavelength grid of the spectra from this work. BT-Settl models have been additionally smoothed by a 2σ Gaussian kernel, so as to not “dominate” the plot. These models are only plotted within $\pm 100 \text{ Å}$ of each spectral line listed in Table 2.2.

A.0.5 PypeIt Configuration Files

A.0.5.1 Reduction

```
slitspatnum = 2:240
[calibrations]
  [[biasframe]]
    exprng = None, 1
  [[[process]]]
    apply_gain = False
    combine = median
    use_biasimage = False
    use_overscan = False
```

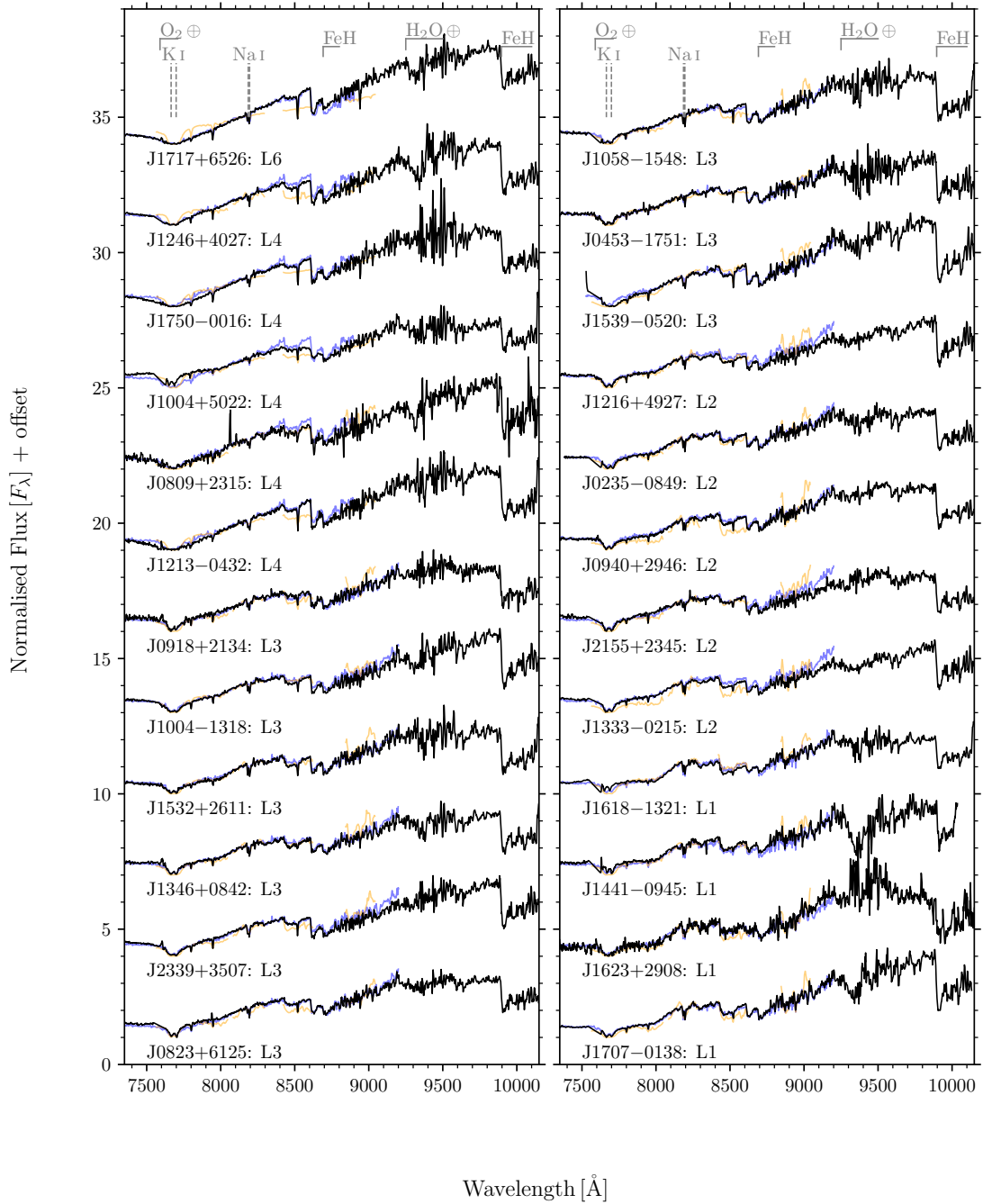


FIGURE A.1: Same as Figure 2.2 with additional comparison spectra. Light blue shows the corresponding standard optical spectra whilst light orange is the best-fitting BT-Settl model around the relevant spectral lines.

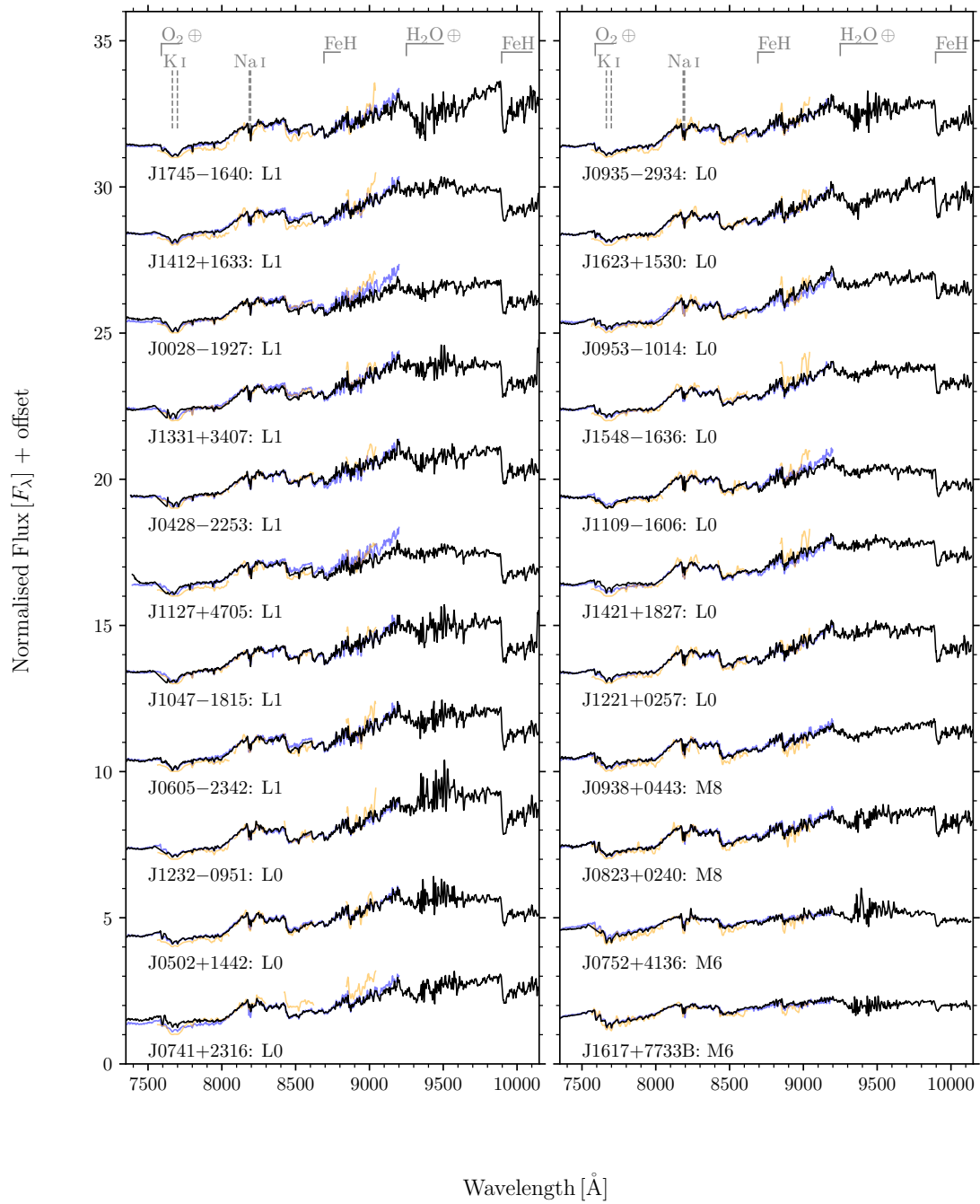


FIGURE A.2: Same as Figure A.1 but for the second half of the R2500I VPHG spectral sample.

```
        use_pixelflat = False
        use_illumflat = False
[[darkframe]]
    exprng = 999999, None
    [[process]]
        apply_gain = False
        use_biasimage = False
        use_overscan = False
        use_pixelflat = False
        use_illumflat = False
[[arcframe]]
    [[process]]
        clip = False
        comb_sigrej = None
        use_overscan = False
        use_pixelflat = False
        use_illumflat = False
[[tiltframe]]
    [[process]]
        comb_sigrej = None
        use_overscan = False
        use_pixelflat = False
        use_illumflat = False
[[pixelflatframe]]
    [[process]]
        combine = median
        satpix = nothing
        use_overscan = False
        use_pixelflat = False
        use_illumflat = False
[[pinholeframe]]
    exprng = 999999, None
    [[process]]
        use_overscan = False
[[alignframe]]
    [[process]]
        satpix = nothing
        comb_sigrej = None
        use_overscan = False
        use_pixelflat = False
        use_illumflat = False
[[traceframe]]
    [[process]]
        use_overscan = False
        use_pixelflat = False
        use_illumflat = False
[[illumflatframe]]
    [[process]]
```

```
        satpix = nothing
        use_overscan = False
        use_pixelflat = False
        use_illumflat = False
    [[skyframe]]
        [[process]]
            mask_cr = True
            use_overscan = False
    [[standardframe]]
        exprng = None, 600
        [[process]]
            combine = median
            spat_flexure_correct = True
            mask_cr = True
            use_overscan = False
    [[wavelengths]]
        reid_arxiv =
        method = full_template
        lamps = XeI,HgI,NeI,ArI
        fwhm_fromlines = True
        ech_fix_format = False
        n_first = 5
        n_final = 6
        match_toler = 2.
    [[slitedges]]
        sync_predict = nearest
        bound_detector = True
[scienceframe]
    exprng = 600, None
    [[process]]
        mask_cr = True
        use_overscan = False
        combine = median
        spat_flexure_correct = True
[reduce]
    [[findobj]]
        maxnumber = 2
[flexure]
    spec_method = slitcen
```

A.0.5.2 Sensitivity Function

```
[sensfunc]
    algorithm = IR
    mask_abs_lines = True
    polyorder = 5
```

```
samp_fact = 1.0
extrap_blu = 0.5
extrap_red = 0.5
[[IR]]
  objmodel = poly
  polyorder = 3
  delta_redshift = 0.
  fit_wv_min_max = [7350, 7550, 7750,
                    8000, 8350, 8900, 9850, 10150]
```

A.0.5.3 Flux Calibration

```
[fluxcalib]
  extinct_correct = False

flux read
  ../Science/<spec1d-standard.fits> sensfunc.fits
  ../Science/<spec1d-object.fits> sensfunc.fits
flux end
```

A.0.5.4 Coadding

```
[coadd1d]
  coaddfile = ../Science/<standard.fits>

coadd1d read
  ../Science/<spec1d-standard.fits>
  SPAT0240-SLIT0457-DET02
coadd1d end
```

```
[coadd1d]
  coaddfile = ../Science/<object.fits>

coadd1d read
  ../Science/<spec1d-object.fits>
  SPAT0240-SLIT0457-DET02
coadd1d end
```

A.0.5.5 Telluric Correction

```
[telluric]
  objmodel = poly
```

```
polyorder = 5
fit_wv_min_max = 7350, 7550, 7750,
                 8000, 8350, 8900, 9850, 10150
maxiter = 1
popsize = 300
pix_shift_bounds = -10., 10.
```

Appendix B

Ultracool Outliers in *Gaia* DR3

Appendices

Presented here are the appendices from my ‘Ultracool Spectroscopic Outliers in *Gaia* DR3’ work, as relates to Chapter 4.

B.1 Ultracool Outliers in *Gaia* DR3 Training Sample

TABLE B.1: List of subdwarfs and young objects used to train our colour ratio. Astrometry is from *Gaia* DR3 and the T_{eff} values are those produced by the ESP-UCD Apsis module and published as part of the Data Release.

<i>Gaia</i> DR3	α	δ	ϖ	Object	Spectral	T_{eff}
Source ID	[hms]	[dms]	[mas]	Name	Type	[K]
164802984685384320	4 15 41	+29 15 07.6	6.5 ± 0.1	2MASS J04154131+2915078 ¹	M8 γ^2	2664 ± 13
4406489184157821952	16 10 28	-0 41 13.7	33.5 ± 0.3	LSR J1610-0040 ³	d/sdM6 ⁴	2651 ± 11
152466120624336896	4 26 45	+27 56 42.9	7.4 ± 0.1	2MASS J04264449+2756433 ¹	M7 γ^2	2674 ± 19
3406128761895775872	4 44 02	+16 21 32.1	6.9 ± 0.1	2MASS J04440164+1621324 ¹	M7 γ^1	2670 ± 14
52039511681854208	4 10 28	+20 51 50.5	7.7 ± 0.4	2MASS J04102834+2051507 ¹	M7 γ^1	2688 ± 20
6412696995416769536	22 02 58	-56 05 10.0	14.4 ± 0.3	2MASS J22025794-5605087 ⁵	M6.2 γ^6	2322 ± 27
3311992669430199168	4 22 14	+15 30 52.6	3.5 ± 0.1	Cl* Melotte 25 LH 190 ⁷	M6: γ^8	2527 ± 19
6154629964132559104	12 57 45	-36 35 43.4	12.3 ± 0.2	2MASS J12574463-3635431 ⁵	M6: γ^6	2523 ± 40
6246004053326362368	16 17 43	-18 58 18.3	16.7 ± 0.5	2MASS J16174255-1858179 ⁹	s/sdM7 ⁹	2350 ± 224
152917298349085824	4 25 16	+28 29 27.1	7.2 ± 0.1	2MASS J04251550+2829275 ¹⁰	M7 γ^2	2628 ± 8
4364702279101281024	17 12 51	-5 07 36.8	43.5 ± 0.1	G 19-16B ¹¹	M7 β^{12}	2410 ± 55
6246979972975055360	15 57 52	-19 56 39.5	19.9 ± 0.4	UScoCTIO 135 ¹³	d/sdM7 ⁹	2391 ± 37
2497288672467622912	2 50 12	-1 51 30.4	19.7 ± 0.1	TVLM 831-154910 ¹⁴	M7.3 γ^6	2664 ± 20
638128236336998016	9 24 31	+21 43 51.9	9.9 ± 0.5	2MASS J09243114+2143536 ¹⁵	M7 β^{15}	2534 ± 61
5682841554856156160	9 17 11	-16 50 05.3	13.7 ± 0.3	SIPS J0917-1649 ¹⁶	M7 β^{15}	2532 ± 57
1191334936190541184	15 56 19	+13 00 53.4	10.9 ± 0.7	2MASS J15561873+1300527 ¹⁷	M8 β^{17}	2387 ± 153
1250625276082413568	13 54 43	+21 50 29.4	11.1 ± 0.3	2MASS J13544271+2150309 ¹⁵	M8 γ^{15}	2593 ± 49
1597899151767870208	15 41 24	+54 25 58.7	7.8 ± 0.4	2MASS J15412408+5425598 ¹⁷	sdM7.5 ¹⁸	2480 ± 140
1310888340170379136	16 39 08	+28 39 00.6	9.3 ± 0.5	2MASS J16390818+2839015 ¹⁷	M8 β^{15}	2516 ± 54
4562040220870331520	17 03 36	+21 19 03.1	12.8 ± 0.5	2MASS J17033593+2119071 ¹⁵	M8 β^{15}	2416 ± 135
6442586188225229312	20 11 57	-62 01 18.9	12.8 ± 0.4	2MASS J20115649-6201127 ¹⁹	sdM8 ²⁰	2422 ± 51
4588438567346043776	18 26 08	+30 14 07.9	90.1 ± 0.1	LSR J1826+3014 ²¹	sdM8.5 ¹⁸	2360 ± 14
147786354323787008	4 34 06	+24 18 50.4	7.5 ± 0.2	2MASS J04340619+2418508 ²²	M8 γ^2	2440 ± 67
1938820873903912448	23 36 38	+45 23 30.4	8.0 ± 0.7	2MASS J23363834+4523306 ¹⁷	M8 β^{17}	2531 ± 83
4693823801926111360	2 21 29	-68 31 40.1	14.4 ± 0.2	2MASS J02212859-6831400 ²³	M8 ²³	2471 ± 63
4708433867622492416	0 38 15	-64 03 53.7	21.8 ± 0.3	2MASS J00381489-6403529 ⁵	M8.2 β^6	2252 ± 63
5734132118729087488	8 56 14	-13 42 24.6	18.6 ± 0.2	2MASS J08561384-1342242 ⁶	M8.6 β^6	2380 ± 32
6258149537937551232	15 20 17	-17 55 34.5	21.5 ± 0.3	SIPS J1520-1755 ¹⁶	M8 β^{15}	2353 ± 63
4815936868977501568	4 36 28	-41 14 46.3	25.3 ± 0.1	2MASS J04362788-4114465 ²⁴	M8 $\beta\gamma^{25}$	2429 ± 15
373562923829421440	1 14 58	+43 18 57.6	21.1 ± 0.4	2MASS J01145788+4318561 ²⁶	M8 β^{26}	2213 ± 102
5203361404618057984	9 45 14	-77 53 14.0	15.4 ± 0.1	2MASS J09451445-7753150 ⁶	M8.2 β^6	2425 ± 20
6407490636060550400	22 35 36	-59 06 32.0	21.3 ± 0.2	2MASS J22353560-5906306 ⁵	M8.6 β^6	2289 ± 80
1349492949336359936	17 50 13	+44 24 06.7	32.5 ± 0.3	LSPM J1750+4424 ²⁷	M8 β^{28}	2525 ± 26
6468916639853825664	20 28 22	-56 37 03.5	15.2 ± 0.2	2MASS J20282203-5637024 ⁵	M8 γ^6	2417 ± 41
553593388644803968	5 38 17	+79 31 05.4	43.1 ± 0.0	LP 16-36 ²⁹	sdM ²⁹	2671 ± 10
6568517687360642816	22 22 56	-44 46 22.5	21.3 ± 0.3	SIPS J2222-4446 ¹⁶	M8 β^{15}	2383 ± 59
6551233295852532096	23 36 07	-35 41 50.5	21.7 ± 0.5	SIPS J2336-3541 ¹⁶	M8.6 γ^6	2268 ± 66
5401822669314874240	11 02 10	-34 30 35.8	16.9 ± 0.1	TWA 28 ³⁰	M8.5 γ^{31}	2382 ± 42
2861861847492765568	0 08 28	+31 25 58.0	11.4 ± 0.6	2MASS J00082822+3125581 ²⁶	M8 γ^{26}	2292 ± 203
5657734928392398976	9 38 40	-27 48 21.2	35.3 ± 0.1	SIPS J0938-2748 ¹⁶	M8 β^{15}	2476 ± 11
656167618671591424	8 19 46	+16 58 53.3	33.0 ± 0.3	2MASS J08194602+1658539 ³²	M8 β^{18}	2350 ± 43
5432903251692290944	9 39 59	-38 17 18.1	16.4 ± 0.3	2MASS J09395909-3817217 ¹⁵	M8 γ^{15}	2406 ± 34
147614422487144960	4 36 33	+24 21 39.4	6.3 ± 0.1	2MASS J04363248+2421395 ¹	M8 γ^2	2457 ± 11
3313381382679891456	4 32 51	+17 30 08.9	6.9 ± 0.4	2MASS J04325119+1730092 ³³	M8 γ^{34}	2373 ± 67
1952664279346269056	21 40 39	+36 55 55.3	9.9 ± 0.4	2MASS J21403907+3655563 ¹⁵	M8 β^{15}	2517 ± 42
3459372646830687104	12 07 33	-39 32 54.4	15.5 ± 0.1	TWA 27 ³⁵	M8 β^{36}	2430 ± 13
3459725624422311424	12 03 59	-38 21 40.6	12.2 ± 0.2	TWA 38 ⁵	M8 γ^{31}	2455 ± 22
6281432246412503424	14 44 17	-20 19 56.9	58.1 ± 0.1	SSSPM J1444-2019 ³⁷	sdM9 ³⁸	2352 ± 10
5399990638128330752	11 06 45	-37 15 11.7	9.8 ± 0.3	2MASS J11064461-3715115 ⁵	M9.4 γ^6	2396 ± 65
2898019875782441856	6 08 53	-27 53 58.2	22.6 ± 0.2	DENIS J060852.8-275358 ³²	M9 β^{25}	2359 ± 102
216704503361774080	3 45 21	+32 18 17.6	3.1 ± 0.1	2MASS J03452106+3218178 ³⁹	M9 γ^{40}	2588 ± 12
6152893526035165312	12 47 44	-38 16 46.8	11.9 ± 0.3	2MASS J12474428-3816464 ⁴¹	M9 ⁶	2380 ± 98
6236753694496012544	15 47 47	-24 23 51.7	29.3 ± 0.3	DENIS J154747.2-242349 ²³	L0 β^{36}	2273 ± 74
6358389917097619968	21 54 49	-74 59 14.9	21.3 ± 0.2	2MASS J21544859-7459134 ⁵	M9.8 γ^6	2325 ± 32
6366726276822544768	20 00 49	-75 23 08.8	34.0 ± 0.1	SIPS J2000-7523 ⁴²	M9 γ^{43}	2338 ± 32
365582359196918656	0 41 22	+35 47 12.5	9.3 ± 1.1	2MASS J00412179+3547133 ¹⁷	sdM9 ⁴⁴	2194 ± 145
2969695320811729280	5 26 43	-18 24 31.9	18.6 ± 0.1	2MASS J05264316-1824315 ⁵	M6.2 γ^6	2663 ± 12
6845967936118138752	20 13 52	-28 06 03.3	21.0 ± 0.3	2MASS J20135152-2806020 ²³	L0 β^{36}	2277 ± 68

<i>Gaia</i> DR3	α	δ	ϖ	Object	Spectral	Teff
Source ID	[hms]	[dms]	[mas]	Name	Type	[K]
3230008650057256960	4 43 38	+0 02 03.4	47.6 ± 0.1	2MASS J0443376+000205 ⁴⁵	M9 β ⁴⁶	2290 ± 35
6096164227899898880	14 11 42	-45 24 20.1	19.1 ± 0.2	2MASS J14114474-4524153 ⁴⁷	sdM9 ⁴⁸	2487 ± 47
3478519134297202560	11 39 51	-31 59 21.8	21.4 ± 0.2	TWA 26 ³⁵	M9 γ ³⁵	2390 ± 17
1320853355787534848	15 52 59	+29 48 47.5	48.9 ± 0.2	2MASS J15525906+2948485 ⁴⁹	L0 γ ⁵⁰	2097 ± 49
6132672029732817024	12 45 14	-44 29 08.1	12.2 ± 0.3	TWA 29 ⁵¹	L0 γ ³⁶	2317 ± 41
1458522725665649536	13 47 50	+33 36 01.5	13.0 ± 0.7	2MASS J13474972+3336019 ⁵²	sdL0 ⁵³	2387 ± 70
4568719543555702272	17 11 13	+23 26 32.5	30.9 ± 0.3	2MASS J17111135+232633 ⁴⁶	L1 γ ³⁶	2065 ± 90
2328674716056981888	23 22 47	-31 33 32.1	50.2 ± 0.2	2MASS J23224684-3133231 ²³	L0 γ ²³	2017 ± 46
144711230753602048	4 35 36	+21 15 03.6	16.7 ± 0.6	2MASS J04353511+2115201 ⁴⁷	sdL0 ⁵⁴	2371 ± 74
5183457632811832960	3 06 02	-3 31 06.1	24.7 ± 0.3	2MASS J03060140-0330438 ⁴⁷	sdL0 ⁵⁴	2348 ± 55
4954323704550180352	1 41 58	-46 33 58.1	27.3 ± 0.4	2MASS J01415823-4633574 ⁵⁵	L0 γ ²⁵	2146 ± 153
4980384088633481216	0 32 56	-44 05 07.3	29.0 ± 0.4	EROS-MP J0032-4405 ⁵⁶	L0 γ ⁵⁰	2092 ± 83
4841448081361281920	3 57 27	-44 17 30.5	21.3 ± 0.3	2MASS J03572695-4417305 ⁵⁷	L0 β ²⁵	2213 ± 115
2358397882610264960	1 16 39	-16 54 20.1	16.1 ± 0.5	2MASS J01163865-1654210 ⁵⁸	sdL0 ⁵³	2291 ± 96
2802623115925093760	0 43 26	+22 21 21.9	15.0 ± 0.3	2MASS J00432610+2221295 ⁴⁷	sdL1 ⁵⁴	2410 ± 36
4584405146372926720	17 56 10	+28 15 16.8	28.9 ± 0.3	2MASS J17561080+2815238 ¹⁵	sdL1 ⁵⁴	2032 ± 108
1047188004010109440	10 22 47	+58 25 33.6	54.0 ± 0.2	2MASS J10224821+5825453 ⁵⁹	L1 γ ²⁵	2028 ± 68
1060313492785021312	11 08 30	+68 30 13.5	61.8 ± 0.1	LSPM J1108+6830 ²⁷	L1 γ ⁶	2019 ± 55
2955015805492793088	5 18 46	-27 56 45.8	18.3 ± 0.6	2MASS J0518461-275645 ⁴⁶	L1 β ⁴⁶	2183 ± 164
2781513733917711616	0 45 22	+16 34 44.0	65.4 ± 0.2	2MASS J00452143+1634446 ⁶⁰	L2 β ⁵⁰	2018 ± 39
824017070904063488	10 04 20	+50 22 56.1	46.2 ± 0.5	G 196-3B ⁶¹	L3 γ ²⁵	1899 ± 100
3303349202364648320	3 55 24	+11 33 33.7	109.1 ± 0.5	2MASS J03552337+1133437 ⁶²	L5 γ ⁵⁰	1839 ± 140

References: 1. Esplin et al. (2014), 2. Luhman et al. (2017), 3. Lépine et al. (2003), 4. Reiners and Basri (2006), 5. Gagné et al. (2015b), 6. Gagné et al. (2015a), 7. Gliese and Jahreiß (1991), 8. Faherty et al. (2012), 9. Luhman et al. (2018), 10. Rebull et al. (2010), 11. Schneider et al. (2011a), 12. Aganze et al. (2016), 13. Ardila et al. (2000), 14. Tinney (1993), 15. Kirkpatrick et al. (2010), 16. Deacon and Hambly (2007), 17. Burgasser et al. (2004), 18. Bardalez Gagliuffi et al. (2014), 19. Andrei et al. (2011), 20. Marocco et al. (2013), 21. Lépine et al. (2002a), 22. Magazzù et al. (2003), 23. Reid et al. (2008), 24. Phan-Bao et al. (2003), 25. Kirkpatrick et al. (2008), 26. Kellogg et al. (2017), 27. Gizis et al. (2000), 28. Dupuy and Liu (2012), 29. Liebert et al. (1979), 30. Scholz et al. (2005), 31. Gagné et al. (2017), 32. Cruz et al. (2003), 33. Leggett and Hawkins (1989), 34. Luhman et al. (2009), 35. Gizis (2002), 36. Allers and Liu (2013), 37. Scholz et al. (2004), 38. Winters et al. (2015), 39. Cieza and Baliber (2006), 40. Luhman et al. (2016), 41. Gagné et al. (2014a), 42. Ménard et al. (2002), 43. Gálvez-Ortiz et al. (2014), 44. Burgasser (2004), 45. Hawley et al. (2002), 46. Cruz et al. (2007), 47. Luhman (2014a), 48. Kirkpatrick et al. (2016), 49. Wilson et al. (2003), 50. Cruz et al. (2009), 51. Looper et al. (2007), 52. West et al. (2008), 53. Zhang et al. (2017b), 54. Kirkpatrick et al. (2014), 55. Kirkpatrick et al. (2006), 56. EROS Collaboration et al. (1999), 57. Bouy et al. (2003), 58. Schneider et al. (2016), 59. Schmidt et al. (2007), 60. Salim et al. (2003), 61. Hellemans (1998), 62. Reid et al. (2006)

Bibliography

- Abazajian, K.N., Adelman-McCarthy, J.K., Agüeros, M.A., et al., 2009. The Seventh Data Release of the Sloan Digital Sky Survey. *ApJ*, 182(2):543.
- Aganze, C., Burgasser, A.J., Faherty, J.K., et al., 2016. Characterization of the Very-low-mass Secondary in the GJ 660.1AB System. *AJ*, 151(2):46.
- Akeson, R.L., Chen, X., Ciardi, D., et al., 2013. The NASA Exoplanet Archive: Data and Tools for Exoplanet Research. *PASP*, 125(930):989.
- Allard, F., Homeier, D., and Freytag, B., 2011. Model Atmospheres From Very Low Mass Stars to Brown Dwarfs. In C. Johns-Krull, M.K. Browning, and A.A. West, editors, *16th Cambridge Workshop on Cool Stars, Stellar Systems, and the Sun*, volume 448 of *Astronomical Society of the Pacific Conference Series*, page 91.
- Allard, F., Homeier, D., and Freytag, B., 2012. Models of very-low-mass stars, brown dwarfs and exoplanets. *Philosophical Transactions of the Royal Society of London Series A*, 370:2765.
- Allers, K.N. and Liu, M.C., 2013. A Near-infrared Spectroscopic Study of Young Field Ultra-cool Dwarfs. *ApJ*, 772(2):79.
- Almendros-Abad, V., Mužić, K., Moitinho, A., et al., 2022. Youth analysis of near-infrared spectra of young low-mass stars and brown dwarfs. *A&A*, 657:A129.
- Anders, F., Khalatyan, A., Queiroz, A.B.A., et al., 2023. Parameters for \sim 300 million Gaia stars: Bayesian inference vs. machine learning. *arXiv e-prints*, arXiv:2302.06995.
- Andrae, R., Fouesneau, M., Sordo, R., et al., 2023a. Gaia Data Release 3. Analysis of the Gaia BP/RP spectra using the General Stellar Parameterizer from Photometry. *A&A*, 674:A27.

- Andrae, R., Rix, H.W., and Chandra, V., 2023b. Robust Data-driven Metallicities for 175 Million Stars from Gaia XP Spectra. *ApJ*, 267(1):8.
- Andrei, A.H., Smart, R.L., Penna, J.L., et al., 2011. Parallaxes of Southern Extremely Cool Objects. I. Targets, Proper Motions, and First Results. *AJ*, 141(2):54.
- Andrews, S.M., Huang, J., Pérez, L.M., et al., 2018. The Disk Substructures at High Angular Resolution Project (DSHARP). I. Motivation, Sample, Calibration, and Overview. *ApJ*, 869(2):L41.
- Ardila, D., Martín, E., and Basri, G., 2000. A Survey for Low-Mass Stars and Brown Dwarfs in the Upper Scorpius OB Association. *AJ*, 120(1):479.
- Baraffe, I., Chabrier, G., Allard, F., et al., 1997. Evolutionary models for metal-poor low-mass stars. Lower main sequence of globular clusters and halo field stars. *A&A*, 327:1054.
- Baraffe, I., Chabrier, G., Allard, F., et al., 1998. Evolutionary models for solar metallicity low-mass stars: mass-magnitude relationships and color-magnitude diagrams. *A&A*, 337:403.
- Baraffe, I., Homeier, D., Allard, F., et al., 2015. New evolutionary models for pre-main sequence and main sequence low-mass stars down to the hydrogen-burning limit. *A&A*, 577:A42.
- Bardalez Gagliuffi, D., Ward-Duong, K., Faherty, J., et al., 2019. Substellar Multiplicity Throughout the Ages. *arXiv e-prints*, page arXiv:1903.06699.
- Bardalez Gagliuffi, D.C., Burgasser, A.J., Gelino, C.R., et al., 2014. SpeX Spectroscopy of Unresolved Very Low Mass Binaries. II. Identification of 14 Candidate Binaries with Late-M/Early-L and T Dwarf Components. *ApJ*, 794(2):143.
- Baron, F., Lafrenière, D., Artigau, É., et al., 2015. Discovery and Characterization of Wide Binary Systems with a Very Low Mass Component. *The Astrophysical Journal*, 802(1):37.
- Barrado y Navascues, D., 1998. The Castor moving group. The age of Fomalhaut and VEGA. *A&A*, 339:831.
- Barrado Y Navascués, D., 2006. On the age of the TW Hydrae association and 2M1207334-393254. *A&A*, 459(2):511.
- Basri, G., 1998. The Lithium Test for Young Brown Dwarfs (invited review). In R. Rebolo, E.L. Martín, and M.R. Zapatero Osorio, editors, *Brown Dwarfs and Extrasolar Planets*, volume 134 of *Astronomical Society of the Pacific Conference Series*, page 394.

- Bayo, A., Rodrigo, C., Barrado Y Navascués, D., et al., 2008. VOSA: virtual observatory SED analyzer. An application to the Collinder 69 open cluster. *A&A*, 492(1):277.
- Becklin, E.E. and Zuckerman, B., 1988. A low-temperature companion to a white dwarf star. *Nature*, 336:656.
- Bensby, T., Feltzing, S., Lundström, I., et al., 2005. α -, r-, and s-process element trends in the Galactic thin and thick disks. *A&A*, 433(1):185.
- Bergeron, P., Leggett, S.K., and Ruiz, M.T., 2001. Photometric and Spectroscopic Analysis of Cool White Dwarfs with Trigonometric Parallax Measurements. *ApJ*, 133(2):413.
- Best, W.M.J., Dupuy, T.J., Liu, M.C., et al., 2020. The UltracoolSheet: Photometry, Astrometry, Spectroscopy, and Multiplicity for 3000+ Ultracool Dwarfs and Imaged Exoplanets. Version 1.0.1 – added stripped down versions of UltracoolSheet to make it easier to plot different populations on color-magnitude diagrams, etc. The new files are named plot-cmd-*.dat.
- Best, W.M.J., Liu, M.C., Magnier, E.A., et al., 2020. The Hawaii Infrared Parallax Program. IV. A Comprehensive Parallax Survey of L0-T8 Dwarfs with UKIRT. *AJ*, 159(6):257.
- Best, W.M.J., Liu, M.C., Magnier, E.A., et al., 2021. A Volume-limited Sample of Ultracool Dwarfs. I. Construction, Space Density, and a Gap in the L/T Transition. *AJ*, 161(1):42.
- Best, W.M.J., Magnier, E.A., Liu, M.C., et al., 2018. Photometry and Proper Motions of M, L, and T Dwarfs from the Pan-STARRS1 3π Survey. *ApJ*, 234(1):1.
- Binks, A.S. and Jeffries, R.D., 2016. Spectroscopic confirmation of M-dwarf candidate members of the Beta Pictoris and AB Doradus Moving Groups. *MNRAS*, 455(3):3345.
- Blake, C.H., Charbonneau, D., and White, R.J., 2010. The NIRSPEC Ultracool Dwarf Radial Velocity Survey. *ApJ*, 723(1):684.
- Blouin, S., Dufour, P., and Allard, N.F., 2018. A New Generation of Cool White Dwarf Atmosphere Models. I. Theoretical Framework and Applications to DZ Stars. *ApJ*, 863(2):184.
- Boch, T. and Fernique, P., 2014. Aladin Lite: Embed your Sky in the Browser. In N. Manset and P. Forshay, editors, *Astronomical Data Analysis Software and Systems XXIII*, volume 485 of *Astronomical Society of the Pacific Conference Series*, page 277.
- Bochanski, J.J., West, A.A., Hawley, S.L., et al., 2007. Low-Mass Dwarf Template Spectra from the Sloan Digital Sky Survey. *AJ*, 133(2):531.

- Bohlin, R.C., Colina, L., and Finley, D.S., 1995. White Dwarf Standard Stars: G191-B2B, GD 71, GD 153, HZ 43. *AJ*, 110:1316.
- Bohlin, R.C., Gordon, K.D., and Tremblay, P.E., 2014. Techniques and Review of Absolute Flux Calibration from the Ultraviolet to the Mid-Infrared. *PASP*, 126(942):711.
- Bonnarel, F., Fernique, P., Bienaymé, O., et al., 2000. The ALADIN interactive sky atlas. A reference tool for identification of astronomical sources. *Astronomy & Astrophysics Supplement*, 143:33.
- Bouy, H., Brandner, W., Martín, E.L., et al., 2003. Multiplicity of Nearby Free-Floating Ultracool Dwarfs: A Hubble Space Telescope WFPC2 Search for Companions. *AJ*, 126(3):1526.
- Burgasser, A., 2021. kastredux.
- Burgasser, A.J., 2004. Discovery of a Second L Subdwarf in the Two Micron All Sky Survey. *ApJ*, 614(1):L73.
- Burgasser, A.J., 2014. The SpeX Prism Library: 1000+ low-resolution, near-infrared spectra of ultracool M, L, T and Y dwarfs. In *Astronomical Society of India Conference Series*, volume 11 of *Astronomical Society of India Conference Series*, pages 7–16.
- Burgasser, A.J., Cruz, K.L., Cushing, M., et al., 2010. SpeX Spectroscopy of Unresolved Very Low Mass Binaries. I. Identification of 17 Candidate Binaries Straddling the L Dwarf/T Dwarf Transition. *ApJ*, 710(2):1142.
- Burgasser, A.J., Cruz, K.L., and Kirkpatrick, J.D., 2007. Optical Spectroscopy of 2MASS Color-selected Ultracool Subdwarfs. *ApJ*, 657(1):494.
- Burgasser, A.J., Geballe, T.R., Leggett, S.K., et al., 2006. A Unified Near-Infrared Spectral Classification Scheme for T Dwarfs. *ApJ*, 637(2):1067.
- Burgasser, A.J., Kirkpatrick, J.D., Brown, M.E., et al., 2002. The Spectra of T Dwarfs. I. Near-Infrared Data and Spectral Classification. *ApJ*, 564(1):421.
- Burgasser, A.J., Kirkpatrick, J.D., McElwain, M.W., et al., 2003. The 2Mass Wide-Field T Dwarf Search. I. Discovery of a Bright T Dwarf within 10 Parsecs of the Sun. *AJ*, 125(2):850.
- Burgasser, A.J., Logsdon, S.E., Gagné, J., et al., 2015. The Brown Dwarf Kinematics Project (BDKP). IV. Radial Velocities of 85 Late-M and L Dwarfs with MagE. *ApJ*, 220(1):18.

- Burgasser, A.J., McElwain, M.W., Kirkpatrick, J.D., et al., 2004. The 2MASS Wide-Field T Dwarf Search. III. Seven New T Dwarfs and Other Cool Dwarf Discoveries. *AJ*, 127(5):2856.
- Burgasser, A.J. and Splat Development Team, 2017. The SpeX Prism Library Analysis Toolkit (SPLAT): A Data Curation Model. In *Astronomical Society of India Conference Series*, volume 14 of *Astronomical Society of India Conference Series*, pages 7–12.
- Burgasser, A.J., Wilson, J.C., Kirkpatrick, J.D., et al., 2000. Discovery of a Bright Field Methane (T-Type) Brown Dwarf by 2MASS. *AJ*, 120(2):1100.
- Burningham, B., Marley, M.S., Line, M.R., et al., 2017. Retrieval of atmospheric properties of cloudy L dwarfs. *MNRAS*, 470(1):1177.
- Burrows, A., Marley, M., Hubbard, W.B., et al., 1997. A Nongray Theory of Extrasolar Giant Planets and Brown Dwarfs. *ApJ*, 491(2):856.
- Caballero, J.A., 2009. Reaching the boundary between stellar kinematic groups and very wide binaries. The Washington double stars with the widest angular separations. *A&A*, 507(1):251.
- Calamari, E., Faherty, J.K., Burningham, B., et al., 2022. An Atmospheric Retrieval of the Brown Dwarf Gliese 229B. *ApJ*, 940(2):164.
- Cantat-Gaudin, T., Anders, F., Castro-Ginard, A., et al., 2020. Painting a portrait of the Galactic disc with its stellar clusters. *A&A*, 640:A1.
- Canty, J.I., Lucas, P.W., Yurchenko, S.N., et al., 2015. Methane and ammonia in the near-infrared spectra of late-T dwarfs. *Monthly Notices of the Royal Astronomical Society*, 450:454.
- Carrasco, J.M., Weiler, M., Jordi, C., et al., 2021. Internal calibration of Gaia BP/RP low-resolution spectra. *A&A*, 652:A86.
- Carroll, B. and Ostlie, D., 2007. *An introduction to modern astrophysics*. Addison-Wesley, San Francisco, CA., 2 edition.
- Castro, P.J. and Gizis, J.E., 2012. Discovery of a Late L Dwarf: WISEP J060738.65+242953.4. *ApJ*, 746(1):3.
- Castro, P.J., Gizis, J.E., Harris, H.C., et al., 2013. Discovery of Four High Proper Motion L Dwarfs, Including a 10 pc L Dwarf at the L/T Transition. *ApJ*, 776(2):126.

- Cayrel, R., 1988. Data Analysis. In G. Cayrel de Strobel and M. Spite, editors, *The Impact of Very High S/N Spectroscopy on Stellar Physics*, volume 132 of *Symposium of the International Astronomical Union*, page 345.
- Cepa, J., 1998. OSIRIS Imaging and Spectroscopy for the GTC. *Astrophysics and Space Science*, 263:369.
- Chabrier, G., 2003. Galactic Stellar and Substellar Initial Mass Function. *PASP*, 115(809):763.
- Chabrier, G. and Baraffe, I., 1997. Structure and evolution of low-mass stars. *A&A*, 327:1039.
- Chabrier, G., Baraffe, I., Allard, F., et al., 2000. Deuterium Burning in Substellar Objects. *ApJ*, 542(2):L119.
- Chambers, K.C., Magnier, E.A., Metcalfe, N., et al., 2016. The Pan-STARRS1 Surveys. *arXiv e-prints*, arXiv:1612.05560.
- Cieza, L. and Baliber, N., 2006. Testing the Disk Regulation Paradigm with Spitzer Observations. I. Rotation Periods of Pre-Main-Sequence Stars in the IC 348 Cluster. *ApJ*, 649(2):862.
- Coşkunoğlu, B., Ak, S., Bilir, S., et al., 2011. Local stellar kinematics from RAVE data - I. Local standard of rest. *MNRAS*, 412(2):1237.
- Cooper, W.J., 2022a. gaiaxy-batch. If you use this software, please cite it as below.
- Cooper, W.J., 2022b. rvfitter.
- Cooper, W.J., 2022c. Will-Cooper/targetlist-generator.
- Cooper, W.J., Smart, R.L., Jones, H.R.A., et al., 2023. Ultracool Spectroscopic Outliers in Gaia DR3. *arXiv e-prints*, arXiv:2310.01576.
- Couture, D., Gagné, J., and Doyon, R., 2023. Addressing Systematics in the Traceback Age of the β Pictoris Moving Group. *ApJ*, 946(1):6.
- Creevey, O.L., Sordo, R., Pailer, F., et al., 2023. Gaia Data Release 3. Astrophysical parameters inference system (Apsis). I. Methods and content overview. *A&A*, 674:A26.
- Crifo, F., Phan-Bao, N., Delfosse, X., et al., 2005. New neighbours. VI. Spectroscopy of DENIS nearby stars candidates. *A&A*, 441(2):653.

- Cruz, K., Rodriguez, D.R., Whiteford, N.P., et al., 2021. SIMPLE Archive of Complex Objects: A new collaborative archive of low mass stars, brown dwarfs, and planetary mass objects. In *The 20.5th Cambridge Workshop on Cool Stars, Stellar Systems, and the Sun (CS20.5)*, Cambridge Workshop on Cool Stars, Stellar Systems, and the Sun, page 248.
- Cruz, K.L., Galindo, C., Faherty, J.K., et al., 2016. Comparative Analysis of Age Indicators in Young M and L dwarfs. In *American Astronomical Society Meeting Abstracts #227*, volume 227 of *American Astronomical Society Meeting Abstracts*, page 145.03.
- Cruz, K.L., Kirkpatrick, J.D., and Burgasser, A.J., 2009. Young L Dwarfs Identified in the Field: A Preliminary Low-Gravity, Optical Spectral Sequence from L0 to L5. *AJ*, 137(2):3345.
- Cruz, K.L., Reid, I.N., Kirkpatrick, J.D., et al., 2007. Meeting the Cool Neighbors. IX. The Luminosity Function of M7-L8 Ultracool Dwarfs in the Field. *AJ*, 133(2):439.
- Cruz, K.L., Reid, I.N., Liebert, J., et al., 2003. Meeting the Cool Neighbors. V. A 2MASS-Selected Sample of Ultracool Dwarfs. *AJ*, 126(5):2421.
- Culpan, R., Geier, S., Reindl, N., et al., 2022. The population of hot subdwarf stars studied with Gaia. IV. Catalogues of hot subluminous stars based on Gaia EDR3. *A&A*, 662:A40.
- Cushing, M.C., Kirkpatrick, J.D., Gelino, C.R., et al., 2011. The Discovery of Y Dwarfs using Data from the Wide-field Infrared Survey Explorer (WISE). *ApJ*, 743(1):50.
- Cutri, R.M., Skrutskie, M.F., van Dyk, S., et al., 2003. VizieR Online Data Catalog: 2MASS All-Sky Catalog of Point Sources (Cutri+ 2003). *VizieR Online Data Catalog*, II/246.
- Cutri, R.M., Wright, E.L., Conrow, T., et al., 2013. VizieR Online Data Catalog: AllWISE Data Release (Cutri+ 2013). *VizieR Online Data Catalog*, II/328.
- Czekaj, M.A., Robin, A.C., Figueras, F., et al., 2014. The Besançon Galaxy model renewed. I. Constraints on the local star formation history from Tycho data. *A&A*, 564:A102.
- Dahn, C.C., Harris, H.C., Vrba, F.J., et al., 2002. Astrometry and Photometry for Cool Dwarfs and Brown Dwarfs. *AJ*, 124(2):1170.
- Damone, L., Barbagallo, M., Mastromarco, M., et al., 2018. ${}^7\text{Be}(n,p){}^7\text{Li}$ reaction and the cosmological lithium problem: Measurement of the cross section in a wide energy range at n_tof at cern. *Phys. Rev. Lett.*, 121:042701.

- De Angeli, F., Weiler, M., Montegriffo, P., et al., 2023. Gaia Data Release 3. Processing and validation of BP/RP low-resolution spectral data. *A&A*, 674:A2.
- de la Reza, R., Torres, C.A.O., Quast, G., et al., 1989. Discovery of New Isolated T Tauri Stars. *ApJ*, 343:L61.
- Deacon, N.R. and Hambly, N.C., 2006. The possibility of detection of ultracool dwarfs with the UKIRT Infrared Deep Sky Survey. *Monthly Notices of the Royal Astronomical Society*, 371(4):1722.
- Deacon, N.R. and Hambly, N.C., 2007. Southern infrared proper motion survey. II. A sample of low mass stars with $\mu \geq 0.1''/\text{yr}$. *A&A*, 468(1):163.
- Deacon, N.R., Liu, M.C., Magnier, E.A., et al., 2014. Wide Cool and Ultracool Companions to Nearby Stars from Pan-STARRS 1. *The Astrophysical Journal*, 792(2):119.
- Delchambre, L., Bailer-Jones, C.A.L., Bellas-Velidis, I., et al., 2023. Gaia Data Release 3. Apsis. III. Non-stellar content and source classification. *A&A*, 674:A31.
- Delfosse, X., Forveille, T., Beuzit, J.L., et al., 1999. New neighbours. I. 13 new companions to nearby M dwarfs. *A&A*, 344:897.
- Delfosse, X., Tinney, C.G., Forveille, T., et al., 1997. Field brown dwarfs found by DENIS. *A&A*, 327:L25.
- Desai, B., 2010. *Quantum mechanics with basic field theory*. Cambridge University Press, Cambridge, UK, 1 edition.
- Draine, B.T., 2003. Interstellar Dust Grains. *Annual Review of Astronomy & Astrophysics*, 41:241.
- Dupuy, T.J. and Liu, M.C., 2012. The Hawaii Infrared Parallax Program. I. Ultracool Binaries and the L/T Transition. *ApJ*, 201(2):19.
- Edlen, B., 1953. The dispersion of standard air. *Journal of the Optical Society of America (1917-1983)*, 43(5):339.
- Eichhorn, G., 1994. An Overview of the Astrophysics Data System. *Experimental Astronomy*, 5(3-4):205.
- Elmegreen, B.G., 2000. Star Formation in a Crossing Time. *ApJ*, 530(1):277.

- Epchtein, N., de Batz, B., Capoani, L., et al., 1997. The deep near-infrared southern sky survey (DENIS). *The Messenger*, 87:27.
- EROS Collaboration, Goldman, B., Delfosse, X., et al., 1999. EROS 2 proper motion survey: a field brown dwarf, and an L dwarf companion to LHS 102. *A&A*, 351:L5.
- Esplin, T.L., Luhman, K.L., and Mamajek, E.E., 2014. A WISE Survey of Circumstellar Disks in Taurus. *ApJ*, 784(2):126.
- Faherty, J.K., Burgasser, A.J., Cruz, K.L., et al., 2009. The Brown Dwarf Kinematics Project I. Proper Motions and Tangential Velocities for a Large Sample of Late-Type M, L, and T Dwarfs. *AJ*, 137(1):1.
- Faherty, J.K., Burgasser, A.J., Walter, F.M., et al., 2012. The Brown Dwarf Kinematics Project (BDKP). III. Parallaxes for 70 Ultracool Dwarfs. *ApJ*, 752(1):56.
- Faherty, J.K., Gagné, J., Popinchalk, M., et al., 2021. A Wide Planetary Mass Companion Discovered through the Citizen Science Project Backyard Worlds: Planet 9. *ApJ*, 923(1):48.
- Faherty, J.K., Riedel, A.R., Cruz, K.L., et al., 2016. Population Properties of Brown Dwarf Analogs to Exoplanets. *ApJ*, 225(1):10.
- Fan, X., Knapp, G.R., Strauss, M.A., et al., 2000. L Dwarfs Found in Sloan Digital Sky Survey Commissioning Imaging Data. *AJ*, 119(2):928.
- Filippazzo, J.C., Rice, E.L., Faherty, J., et al., 2015. Fundamental Parameters and Spectral Energy Distributions of Young and Field Age Objects with Masses Spanning the Stellar to Planetary Regime. *ApJ*, 810(2):158.
- Forgan, D.H., Hall, C., Meru, F., et al., 2018. Towards a population synthesis model of self-gravitating disc fragmentation and tidal downsizing II: the effect of fragment-fragment interactions. *Monthly Notices of the Royal Astronomical Society*, 474(4):5036.
- Fouesneau, M., Frémat, Y., Andrae, R., et al., 2023. Gaia Data Release 3. Apsis. II. Stellar parameters. *A&A*, 674:A28.
- Gagné, J. and Faherty, J.K., 2018. BANYAN. XIII. A First Look at Nearby Young Associations with Gaia Data Release 2. *ApJ*, 862(2):138.
- Gagné, J., Faherty, J.K., Cruz, K., et al., 2014a. The Coolest Isolated Brown Dwarf Candidate Member of TWA. *ApJ*, 785(1):L14.

- Gagné, J., Faherty, J.K., Cruz, K.L., et al., 2015a. BANYAN. VII. A New Population of Young Substellar Candidate Members of Nearby Moving Groups from the BASS Survey. *ApJ*, 219(2):33.
- Gagné, J., Faherty, J.K., Mamajek, E.E., et al., 2017. BANYAN. IX. The Initial Mass Function and Planetary-mass Object Space Density of the TW HYA Association. *ApJ*, 228(2):18.
- Gagné, J., Lafrenière, D., Doyon, R., et al., 2014b. BANYAN. II. Very Low Mass and Substellar Candidate Members to Nearby, Young Kinematic Groups with Previously Known Signs of Youth. *ApJ*, 783(2):121.
- Gagné, J., Lafrenière, D., Doyon, R., et al., 2015b. BANYAN. V. A Systematic All-sky Survey for New Very Late-type Low-mass Stars and Brown Dwarfs in Nearby Young Moving Groups. *ApJ*, 798(2):73.
- Gagné, J., Mamajek, E.E., Malo, L., et al., 2018. BANYAN. XI. The BANYAN Σ Multivariate Bayesian Algorithm to Identify Members of Young Associations with 150 pc. *ApJ*, 856(1):23.
- Gaia Collaboration, Antoja, T., McMillan, P.J., et al., 2021a. Gaia Early Data Release 3. The Galactic anticentre. *A&A*, 649:A8.
- Gaia Collaboration, Arenou, F., Babusiaux, C., et al., 2023a. Gaia Data Release 3. Stellar multiplicity, a teaser for the hidden treasure. *A&A*, 674:A34.
- Gaia Collaboration, Babusiaux, C., van Leeuwen, F., et al., 2018a. Gaia Data Release 2. Observational Hertzsprung-Russell diagrams. *A&A*, 616:A10.
- Gaia Collaboration, Brown, A.G.A., Vallenari, A., et al., 2018b. Gaia Data Release 2. Summary of the contents and survey properties. *A&A*, 616:A1.
- Gaia Collaboration, Brown, A.G.A., Vallenari, A., et al., 2021b. Gaia Early Data Release 3. Summary of the contents and survey properties. *A&A*, 649:A1.
- Gaia Collaboration, Brown, A.G.A., Vallenari, A., et al., 2021c. Gaia Early Data Release 3. Summary of the contents and survey properties (Corrigendum). *A&A*, 650:C3.
- Gaia Collaboration, Creevey, O.L., Sarro, L.M., et al., 2023b. Gaia Data Release 3. A golden sample of astrophysical parameters. *A&A*, 674:A39.
- Gaia Collaboration, De Ridder, J., Ripepi, V., et al., 2023c. Gaia Data Release 3. Pulsations in main sequence OBAF-type stars. *A&A*, 674:A36.

- Gaia Collaboration, Drimmel, R., Romero-Gómez, M., et al., 2023d. Gaia Data Release 3. Mapping the asymmetric disc of the Milky Way. *A&A*, 674:A37.
- Gaia Collaboration, Galluccio, L., Delbo, M., et al., 2023e. Gaia Data Release 3. Reflectance spectra of Solar System small bodies. *A&A*, 674:A35.
- Gaia Collaboration, Klioner, S.A., Lindegren, L., et al., 2022. Gaia Early Data Release 3. The celestial reference frame (Gaia-CRF3). *A&A*, 667:A148.
- Gaia Collaboration, Klioner, S.A., Mignard, F., et al., 2021d. Gaia Early Data Release 3. Acceleration of the Solar System from Gaia astrometry. *A&A*, 649:A9.
- Gaia Collaboration, Luri, X., Chemin, L., et al., 2021e. Gaia Early Data Release 3. Structure and properties of the Magellanic Clouds. *A&A*, 649:A7.
- Gaia Collaboration, Montegriffo, P., Bellazzini, M., et al., 2023f. Gaia Data Release 3. The Galaxy in your preferred colours: Synthetic photometry from Gaia low-resolution spectra. *A&A*, 674:A33.
- Gaia Collaboration, Prusti, T., de Bruijne, J.H.J., et al., 2016. The Gaia mission. *A&A*, 595:A1.
- Gaia Collaboration, Recio-Blanco, A., Kordopatis, G., et al., 2023g. Gaia Data Release 3. Chemical cartography of the Milky Way. *A&A*, 674:A38.
- Gaia Collaboration, Schultheis, M., Zhao, H., et al., 2023h. Gaia Data Release 3. Exploring and mapping the diffuse interstellar band at 862 nm. *A&A*, 674:A40.
- Gaia Collaboration, Smart, R.L., Sarro, L.M., et al., 2021f. Gaia Early Data Release 3. The Gaia Catalogue of Nearby Stars. *A&A*, 649:A6.
- Gaia Collaboration, Vallenari, A., Brown, A.G.A., et al., 2023i. Gaia Data Release 3. Summary of the content and survey properties. *A&A*, 674:A1.
- Gálvez-Ortiz, M.C., Kuznetsov, M., Clarke, J.R.A., et al., 2014. Spectroscopic signatures of youth in low-mass kinematic candidates of young moving groups. *MNRAS*, 439(4):3890.
- Geballe, T.R., Knapp, G.R., Leggett, S.K., et al., 2002. Toward Spectral Classification of L and T Dwarfs: Infrared and Optical Spectroscopy and Analysis. *ApJ*, 564(1):466.
- Gelino, C.R., Kirkpatrick, J.D., and Burgasser, A.J., 2009. Dwarf Archives: A Compendium of M, L, and T Dwarf Data. In E. Stempels, editor, *15th Cambridge Workshop on Cool*

- Stars, Stellar Systems, and the Sun*, volume 1094 of *American Institute of Physics Conference Series*, pages 924–927.
- Gharib-Nezhad, E., Iyer, A.R., Line, M.R., et al., 2021. EXOPLINES: Molecular Absorption Cross-section Database for Brown Dwarf and Giant Exoplanet Atmospheres. *ApJ*, 254(2):34.
- Gizis, J.E., 1997. M-Subdwarfs: Spectroscopic Classification and the Metallicity Scale. *AJ*, 113:806.
- Gizis, J.E., 2002. Brown Dwarfs and the TW Hydrae Association. *ApJ*, 575(1):484.
- Gizis, J.E., Monet, D.G., Reid, I.N., et al., 2000. New Neighbors from 2MASS: Activity and Kinematics at the Bottom of the Main Sequence. *AJ*, 120(2):1085.
- Gizis, J.E. and Reid, I.N., 1999. M Subdwarfs: The Population II Luminosity Function. *AJ*, 117(1):508.
- Gliese, W., 1957. Katalog der Sterne näher ALS 20 Parsek für 1950.0. *Astronomisches Rechen-Institut Heidelberg Mitteilungen Serie A*, 8:1.
- Gliese, W. and Jahreiß, H., 1991. Preliminary Version of the Third Catalogue of Nearby Stars. On: The Astronomical Data Center CD-ROM: Selected Astronomical Catalogs, Vol. I; L.E. Brodzmann, S.E. Gesser (eds.), NASA/Astronomical Data Center, Goddard Space Flight Center, Greenbelt, MD.
- Golovin, A., Reffert, S., Just, A., et al., 2023. The Fifth Catalogue of Nearby Stars (CNS5). *A&A*, 670:A19.
- Gomes, J.I., Pinfield, D.J., Marocco, F., et al., 2013. Two new ultracool benchmark systems from WISE+2MASS. *Monthly Notices of the Royal Astronomical Society*, 431:2745.
- González Egea, E., Raddi, R., Koester, D., et al., 2021. Serendipitous discovery of a dusty disc around WDJ181417.84-735459.83. *MNRAS*, 501(3):3916.
- Gorlova, N.I., Meyer, M.R., Rieke, G.H., et al., 2003. Gravity Indicators in the Near-Infrared Spectra of Brown Dwarfs. *ApJ*, 593(2):1074.
- Grether, D. and Lineweaver, C.H., 2006. How Dry is the Brown Dwarf Desert? Quantifying the Relative Number of Planets, Brown Dwarfs, and Stellar Companions around Nearby Sun-like Stars. *The Astrophysical Journal*, 640(2):1051.

- Hall, P.B., 2002. 2MASS 1315-2649: A High Proper-Motion L Dwarf with Strong H α Emission. *ApJ*, 580(1):L77.
- Hamuy, M., Suntzeff, N.B., Heathcote, S.R., et al., 1994. Southern Spectrophotometric Standards. II. *PASP*, 106:566.
- Hamuy, M., Walker, A.R., Suntzeff, N.B., et al., 1992. Southern Spectrophotometric Standards. I. *PASP*, 104:533.
- Hartmann, L., Ballesteros-Paredes, J., and Bergin, E.A., 2001. Rapid Formation of Molecular Clouds and Stars in the Solar Neighborhood. *ApJ*, 562(2):852.
- Hawley, S.L., Covey, K.R., Knapp, G.R., et al., 2002. Characterization of M, L, and T Dwarfs in the Sloan Digital Sky Survey. *AJ*, 123(6):3409.
- Hellemans, A., 1998. ASTRONOMY:Binaries Answer Riddle of Brown Dwarf Origins. *Science*, 282:1240.
- Henry, T.J., Kirkpatrick, J.D., and Simons, D.A., 1994. The Solar Neighborhood. I. Standard Spectral Types (K5-M8) for Northern Dwarfs Within Eight Parsecs. *AJ*, 108:1437.
- Hiranaka, K., Cruz, K.L., Douglas, S.T., et al., 2016. Exploring the Role of Sub-micron-sized Dust Grains in the Atmospheres of Red L0-L6 Dwarfs. *ApJ*, 830(2):96.
- Horne, K., 1986. An optimal extraction algorithm for CCD spectroscopy. *PASP*, 98:609.
- Hsu, C.C., Burgasser, A.J., Theissen, C.A., et al., 2021. The Brown Dwarf Kinematics Project (BDKP). V. Radial and Rotational Velocities of T Dwarfs from Keck/NIRSPEC High-resolution Spectroscopy. *ApJ*, 257(2):45.
- Johnson, D.R.H. and Soderblom, D.R., 1987. Calculating Galactic Space Velocities and Their Uncertainties, with an Application to the Ursa Major Group. *AJ*, 93:864.
- Kanodia, S. and Wright, J., 2018. Python Leap Second Management and Implementation of Precise Barycentric Correction (barycorrpy). *Research Notes of the American Astronomical Society*, 2(1):4.
- Karalidi, T., Marley, M., Fortney, J.J., et al., 2021. The Sonora Substellar Atmosphere Models. II. Cholla: A Grid of Cloud-free, Solar Metallicity Models in Chemical Disequilibrium for the JWST Era. *ApJ*, 923(2):269.

- Kastner, J.H., Zuckerman, B., Weintraub, D.A., et al., 1997. X-ray and molecular emission from the nearest region of recent star formation. *Science*, 277:67.
- Katz, D., Sartoretti, P., Guerrier, A., et al., 2023. Gaia Data Release 3. Properties and validation of the radial velocities. *A&A*, 674:A5.
- Kellogg, K., Metchev, S., Miles-Páez, P.A., et al., 2017. A Statistical Survey of Peculiar L and T Dwarfs in SDSS, 2MASS, and WISE. *AJ*, 154(3):112.
- Kendall, T.R., Delfosse, X., Martín, E.L., et al., 2004. Discovery of very nearby ultracool dwarfs from DENIS. *A&A*, 416:L17.
- Kendall, T.R., Jones, H.R.A., Pinfield, D.J., et al., 2007a. New nearby, bright southern ultracool dwarfs. *MNRAS*, 374(2):445.
- Kendall, T.R., Maun, N., Azzopardi, M., et al., 2003. Serendipitous discovery of seven new southern L-dwarfs. *A&A*, 403:929.
- Kendall, T.R., Tamura, M., Tinney, C.G., et al., 2007b. Two T dwarfs from the UKIDSS early data release. *A&A*, 466(3):1059.
- Kesseli, A.Y., West, A.A., Veyette, M., et al., 2017. An Empirical Template Library of Stellar Spectra for a Wide Range of Spectral Classes, Luminosity Classes, and Metallicities Using SDSS BOSS Spectra. *ApJ*, 230(2):16.
- Kiman, R., Schmidt, S.J., Angus, R., et al., 2019. Exploring the Age-dependent Properties of M and L Dwarfs Using Gaia and SDSS. *AJ*, 157(6):231.
- Kirkpatrick, J.D., 2005. New Spectral Types L and T. *Annual Review of Astronomy and Astrophysics*, 43(1):195.
- Kirkpatrick, J.D., Barman, T.S., Burgasser, A.J., et al., 2006. Discovery of a Very Young Field L Dwarf, 2MASS J01415823-4633574. *ApJ*, 639(2):1120.
- Kirkpatrick, J.D., Cruz, K.L., Barman, T.S., et al., 2008. A Sample of Very Young Field L Dwarfs and Implications for the Brown Dwarf “Lithium Test” at Early Ages. *ApJ*, 689(2):1295.
- Kirkpatrick, J.D., Gelino, C.R., Faherty, J.K., et al., 2021. The Field Substellar Mass Function Based on the Full-sky 20 pc Census of 525 L, T, and Y Dwarfs. *ApJ*, 253(1):7.

- Kirkpatrick, J.D., Henry, T.J., and Irwin, M.J., 1997. Ultra-Cool M Dwarfs Discovered by QSO Surveys.I: The APM Objects. *AJ*, 113:1421.
- Kirkpatrick, J.D., Henry, T.J., and McCarthy, Donald W., J., 1991. A Standard Stellar Spectral Sequence in the Red/Near-Infrared: Classes K5 to M9. *ApJ*, 77:417.
- Kirkpatrick, J.D., Kellogg, K., Schneider, A.C., et al., 2016. The AllWISE Motion Survey, Part 2. *ApJ*, 224(2):36.
- Kirkpatrick, J.D., Looper, D.L., Burgasser, A.J., et al., 2010. Discoveries from a Near-infrared Proper Motion Survey Using Multi-epoch Two Micron All-Sky Survey Data. *ApJ*, 190(1):100.
- Kirkpatrick, J.D., Martin, E.C., Smart, R.L., et al., 2019. Preliminary Trigonometric Parallaxes of 184 Late-T and Y Dwarfs and an Analysis of the Field Substellar Mass Function into the “Planetary” Mass Regime. *ApJ*, 240(2):19.
- Kirkpatrick, J.D., Reid, I.N., Liebert, J., et al., 1999. Dwarfs Cooler than M: The Definition of Spectral Type L” Using Discoveries from the 2 Micron All-Sky Survey (2MASS). *ApJ*, 519(2):802.
- Kirkpatrick, J.D., Reid, I.N., Liebert, J., et al., 2000. 67 Additional L Dwarfs Discovered by the Two Micron All Sky Survey. *AJ*, 120(1):447.
- Kirkpatrick, J.D., Schneider, A., Fajardo-Acosta, S., et al., 2014. The AllWISE Motion Survey and the Quest for Cold Subdwarfs. *ApJ*, 783(2):122.
- Klutsch, A., Freire Ferrero, R., Guillout, P., et al., 2014. Reliable probabilistic determination of membership in stellar kinematic groups in the young disk. *A&A*, 567:A52.
- Knapp, G.R., Leggett, S.K., Fan, X., et al., 2004. Near-Infrared Photometry and Spectroscopy of L and T Dwarfs: The Effects of Temperature, Clouds, and Gravity. *AJ*, 127(6):3553.
- Koppelman, H., Helmi, A., and Veljanoski, J., 2018. One Large Blob and Many Streams Frosting the nearby Stellar Halo in Gaia DR2. *ApJ*, 860(1):L11.
- Kounkel, M., Covey, K., Moe, M., et al., 2019. Close Companions around Young Stars. *AJ*, 157(5):196.
- Kramida, A., Ralchenko, Y., Reader, J., et al., 2021. Nist atomic spectra database (version 5.9).

- Kraus, A.L., Herczeg, G.J., Rizzuto, A.C., et al., 2017. The Greater Taurus-Auriga Ecosystem. I. There is a Distributed Older Population. *ApJ*, 838(2):150.
- Kraus, A.L. and Hillenbrand, L.A., 2007. The Role of Mass and Environment in Multiple-Star Formation: A 2MASS Survey of Wide Multiplicity in Three Young Associations. *ApJ*, 662(1):413.
- Kroupa, P., 2001. On the variation of the initial mass function. *MNRAS*, 322(2):231.
- Kroupa, P., 2002. The Initial Mass Function of Stars: Evidence for Uniformity in Variable Systems. *Science*, 295:82.
- Lagarde, N., Reyl , C., Chiappini, C., et al., 2021. Deciphering the evolution of the Milky Way discs: Gaia APOGEE Kepler giant stars and the Besan on Galaxy Model. *A&A*, 654:A13.
- Landsman, W.B., 1993. The IDL Astronomy User's Library. In R.J. Hanisch, R.J.V. Brissenden, and J. Barnes, editors, *Astronomical Data Analysis Software and Systems II*, volume 52 of *Astronomical Society of the Pacific Conference Series*, page 246.
- Lanzafame, A.C., Brugaletta, E., Fr mat, Y., et al., 2023. Gaia Data Release 3. Stellar chromospheric activity and mass accretion from Ca II IRT observed by the Radial Velocity Spectrometer. *A&A*, 674:A30.
- Lawrence, A., Warren, S.J., Almaini, O., et al., 2007. The UKIRT Infrared Deep Sky Survey (UKIDSS). *MNRAS*, 379(4):1599.
- Leggett, S.K., 1992. Infrared Colors of Low-Mass Stars. *ApJ*, 82:351.
- Leggett, S.K., Golimowski, D.A., Fan, X., et al., 2002. Infrared Photometry of Late-M, L, and T Dwarfs. *ApJ*, 564(1):452.
- Leggett, S.K. and Hawkins, M.R.S., 1989. Low mass stars in the region of the Hyades cluster. *MNRAS*, 238:145.
- L pine, S., 2008. New High Proper Motion Stars from the Digitized Sky Survey. Iv. Completion of the Southern Survey and 170 Additional Stars with $\mu \gtrsim 0.45'' \text{ yr}^{-1}$. *AJ*, 135(6):2177.
- L pine, S., Rich, R.M., Neill, J.D., et al., 2002a. Discovery of an M8.5 Dwarf with Proper Motion $\mu = 2.38''$ per Year. *ApJ*, 581(1):L47.
- L pine, S., Rich, R.M., and Shara, M.M., 2003. LSR 1610-0040: The First Early-Type L Subdwarf. *ApJ*, 591(1):L49.

- Lépine, S. and Shara, M.M., 2005. A Catalog of Northern Stars with Annual Proper Motions Larger than $0.15''$ (LSPM-NORTH Catalog). *AJ*, 129(3):1483.
- Lépine, S., Shara, M.M., and Rich, R.M., 2002b. New High Proper Motion Stars from the Digitized Sky Survey. I. Northern Stars with $0.5'' \text{ yr}^{-1} \leq \mu \leq 2.0'' \text{ yr}^{-1}$ at Low Galactic Latitudes. *AJ*, 124(2):1190.
- L'Heureux, J., Cruz, K., and Alejandro, S., 2023. Standardizing Spectra in the SIMPLE Archive. In *American Astronomical Society Meeting Abstracts*, volume 55 of *American Astronomical Society Meeting Abstracts*, page 203.17.
- Liebert, J., Dahn, C.C., Gresham, M., et al., 1979. New results from a survey of faint proper-motion stars: a probable deficiency of very low luminosity degenerates. *ApJ*, 233:226.
- Liu, M.C., Dupuy, T.J., and Allers, K.N., 2016. The Hawaii Infrared Parallax Program. II. Young Ultracool Field Dwarfs. *ApJ*, 833(1):96.
- Lodieu, N., Espinoza Contreras, M., Zapatero Osorio, M.R., et al., 2012. New ultracool subdwarfs identified in large-scale surveys using Virtual Observatory tools. I. UKIDSS LAS DR5 vs. SDSS DR7. *A&A*, 542:A105.
- Lodieu, N., Espinoza Contreras, M., Zapatero Osorio, M.R., et al., 2017. New ultracool subdwarfs identified in large-scale surveys using Virtual Observatory tools. *A&A*, 598:A92.
- Lodieu, N., Rebolo, R., and Pérez-Garrido, A., 2018. Lithium in the Hyades L5 brown dwarf 2MASS J04183483+2131275. *A&A*, 615:L12.
- Lodieu, N., Scholz, R.D., McCaughrean, M.J., et al., 2005. Spectroscopic classification of red high proper motion objects in the Southern Sky. *A&A*, 440(3):1061.
- Lodieu, N., Smart, R.L., Pérez-Garrido, A., et al., 2019. A 3D view of the Hyades stellar and sub-stellar population. *A&A*, 623:A35.
- Looper, D.L., Burgasser, A.J., Kirkpatrick, J.D., et al., 2007. Discovery of an M9.5 Candidate Brown Dwarf in the TW Hydrae Association: DENIS J124514.1-442907. *ApJ*, 669(2):L97.
- Looper, D.L., Kirkpatrick, J.D., Cutri, R.M., et al., 2008. Discovery of Two Nearby Peculiar L Dwarfs from the 2MASS Proper-Motion Survey: Young or Metal-Rich? *ApJ*, 686(1):528.
- Luhman, K.L., 2013. Discovery of a Binary Brown Dwarf at 2 pc from the Sun. *ApJ*, 767:L1.

- Luhman, K.L., 2014a. A Search for a Distant Companion to the Sun with the Wide-field Infrared Survey Explorer. *ApJ*, 781(1):4.
- Luhman, K.L., 2014b. Discovery of a ~250 K Brown Dwarf at 2 pc from the Sun. *ApJ*, 786(2):L18.
- Luhman, K.L., 2018. The Stellar Membership of the Taurus Star-forming Region. *AJ*, 156(6):271.
- Luhman, K.L., Allen, P.R., Espaillat, C., et al., 2010. The Disk Population of the Taurus Star-forming Region. *ApJ*, 186(1):111.
- Luhman, K.L., Briceño, C., Stauffer, J.R., et al., 2003. New Low-Mass Members of the Taurus Star-forming Region. *ApJ*, 590(1):348.
- Luhman, K.L., Esplin, T.L., and Loutrel, N.P., 2016. A Census of Young Stars and Brown Dwarfs in IC 348 and NGC 1333. *ApJ*, 827(1):52.
- Luhman, K.L., Herrmann, K.A., Mamajek, E.E., et al., 2018. New Young Stars and Brown Dwarfs in the Upper Scorpius Association. *AJ*, 156(2):76.
- Luhman, K.L., Mamajek, E.E., Allen, P.R., et al., 2009. An Infrared/X-Ray Survey for New Members of the Taurus Star-Forming Region. *ApJ*, 703(1):399.
- Luhman, K.L., Mamajek, E.E., Shukla, S.J., et al., 2017. A Survey for New Members of the Taurus Star-forming Region with the Sloan Digital Sky Survey. *AJ*, 153(1):46.
- Luhman, K.L. and Sheppard, S.S., 2014. Characterization of High Proper Motion Objects from the Wide-field Infrared Survey Explorer. *ApJ*, 787(2):126.
- Luhman, K.L., Whitney, B.A., Meade, M.R., et al., 2006. A Survey for New Members of Taurus with the Spitzer Space Telescope. *ApJ*, 647(2):1180.
- Luyten, W.J., 1955. Luyten's Five Tenths. *Luyten's Five Tenths*. (1955, page 0.
- Luyten, W.J., 1979. *LHS catalogue. A catalogue of stars with proper motions exceeding 0"5 annually*.
- Magazzù, A., Dougados, C., Licandro, J., et al., 2003. Infrared Spectra of Brown Dwarf Candidates in Taurus. In E. Martín, editor, *Brown Dwarfs*, volume 211 of *Proceedings of IAU Symposium*, page 75.

- Makarov, V.V. and Urban, S., 2000. A moving group of young stars in Carina-Vela. *MNRAS*, 317(2):289.
- Mamajek, E.E., 2009. Initial Conditions of Planet Formation: Lifetimes of Primordial Disks. In T. Usuda, M. Tamura, and M. Ishii, editors, *Exoplanets and Disks: Their Formation and Diversity*, volume 1158 of *American Institute of Physics Conference Series*, pages 3–10.
- Mamajek, E.E. and Bell, C.P.M., 2014. On the age of the β Pictoris moving group. *MNRAS*, 445(3):2169.
- Mamajek, E.E., Marocco, F., Rees, J.M., et al., 2018. WISE J064336.71-022315.4: A Thick-disk L8 Brown Dwarf Discovered by Gaia DR2 at 13.9 pc. *Research Notes of the American Astronomical Society*, 2(4):205.
- Marley, M.S., Saumon, D., Visscher, C., et al., 2021. The Sonora Brown Dwarf Atmosphere and Evolution Models. I. Model Description and Application to Cloudless Atmospheres in Rainout Chemical Equilibrium. *ApJ*, 920(2):85.
- Marley, M.S., Seager, S., Saumon, D., et al., 2002. Clouds and Chemistry: Ultracool Dwarf Atmospheric Properties from Optical and Infrared Colors. *ApJ*, 568(1):335.
- Marocco, F., Andrei, A.H., Smart, R.L., et al., 2013. Parallaxes of Southern Extremely Cool Objects (PARSEC). II. Spectroscopic Follow-up and Parallaxes of 52 Targets. *AJ*, 146(6):161.
- Marocco, F., Day-Jones, A.C., Lucas, P.W., et al., 2014. The extremely red L dwarf ULAS J222711-004547 - dominated by dust. *MNRAS*, 439(1):372.
- Marocco, F., Eisenhardt, P.R.M., Fowler, J.W., et al., 2021. The CatWISE2020 Catalog. *ApJ*, 253(1):8.
- Marocco, F., Jones, H.R.A., Day-Jones, A.C., et al., 2015. A large spectroscopic sample of L and T dwarfs from UKIDSS LAS: peculiar objects, binaries, and space density. *Monthly Notices of the Royal Astronomical Society*, 449(4):3651.
- Marocco, F., Pinfield, D.J., Cook, N.J., et al., 2017. Ultracool dwarf benchmarks with Gaia primaries. *MNRAS*, 470(4):4885.
- Marocco, F., Smart, R.L., Mamajek, E.E., et al., 2020. The Gaia Ultra-Cool Dwarf Sample - III: seven new multiple systems containing at least one Gaia DR2 ultracool dwarf. *MNRAS*, 494(4):4891.

- Martín, E.L., Basri, G., and Zapatero Osorio, M.R., 1999a. The Lithium Test in Young Brown Dwarf Candidates. *AJ*, 118(2):1005.
- Martín, E.L., Delfosse, X., Basri, G., et al., 1999b. Spectroscopic Classification of Late-M and L Field Dwarfs. *AJ*, 118(5):2466.
- Martín, E.L., Lodieu, N., Pavlenko, Y., et al., 2018. The Lithium Depletion Boundary and the Age of the Hyades Cluster. *ApJ*, 856(1):40.
- Martín, E.L., Phan-Bao, N., Bessell, M., et al., 2010. Spectroscopic characterization of 78 DENIS ultracool dwarf candidates in the solar neighborhood and the Upper Scorpii OB association. *A&A*, 517:A53.
- McCleery, J., Tremblay, P.E., Gentile Fusillo, N.P., et al., 2020. Gaia white dwarfs within 40 pc II: the volume-limited Northern hemisphere sample. *MNRAS*, 499(2):1890.
- McGovern, M.R., Kirkpatrick, J.D., McLean, I.S., et al., 2004. Identifying Young Brown Dwarfs Using Gravity-Sensitive Spectral Features. *ApJ*, 600(2):1020.
- McLean, I.S., Prato, L., McGovern, M.R., et al., 2007. The NIRSPEC Brown Dwarf Spectroscopic Survey. II. High-Resolution J-Band Spectra of M, L, and T Dwarfs. *ApJ*, 658(2):1217.
- McMahon, R.G., Banerji, M., Gonzalez, E., et al., 2013. First Scientific Results from the VISTA Hemisphere Survey (VHS). *The Messenger*, 154:35.
- McMahon, R.G., Banerji, M., Gonzalez, E., et al., 2021. VizieR Online Data Catalog: The VISTA Hemisphere Survey (VHS) catalog DR5 (McMahon+, 2020). *VizieR Online Data Catalog*, II/367.
- Meisner, A.M., Caselden, D., Schlafly, E.F., et al., 2023. unTimely: a Full-sky, Time-domain unWISE Catalog. *AJ*, 165(2):36.
- Ménard, F., Delfosse, X., and Monin, J.L., 2002. Optical linear polarimetry of ultra cool dwarfs. *A&A*, 396:L35.
- Minniti, D., Lucas, P.W., Emerson, J.P., et al., 2010. VISTA Variables in the Via Lactea (VVV): The public ESO near-IR variability survey of the Milky Way. *NewA*, 15(5):433.
- Montegriffo, P., De Angeli, F., Andrae, R., et al., 2023. Gaia Data Release 3. External calibration of BP/RP low-resolution spectroscopic data. *A&A*, 674:A3.

- Montegriffo et al., 2022. External calibration of the photometric and low-resolution spectroscopic data. *A&A in prep.*
- Mordasini, C., Alibert, Y., Benz, W., et al., 2009. Extrasolar planet population synthesis. II. Statistical comparison with observations. *Astronomy & Astrophysics*, 501(3):1161.
- Morris, C., Maccarone, T.J., Lucas, P.W., et al., 2022. UGPS J194310+183851: an unusual optical and X-ray faint cataclysmic variable? *MNRAS*, 514(4):6002.
- Mužić, K., Radigan, J., Jayawardhana, R., et al., 2012. Discovery of Two Very Wide Binaries with Ultracool Companions and a New Brown Dwarf at the L/T Transition. *The Astrophysical Journal*, 144:180.
- Nissen, P.E. and Schuster, W.J., 2010. Two distinct halo populations in the solar neighborhood. Evidence from stellar abundance ratios and kinematics. *A&A*, 511:L10.
- Ochsenbein, F., Bauer, P., and Marcout, J., 2000. The VizieR database of astronomical catalogues. *A&A Supp.*, 143:23.
- Oke, J.B., 1974. Absolute Spectral Energy Distributions for White Dwarfs. *ApJ*, 27:21.
- Oke, J.B., 1990. Faint Spectrophotometric Standard Stars. *AJ*, 99:1621.
- Padoan, P., Haugbølle, T., and Nordlund, Å., 2012. A Simple Law of Star Formation. *The Astrophysical Journal Letters*, 759(2):L27.
- Pancino, E., Altavilla, G., Marinoni, S., et al., 2012. The Gaia spectrophotometric standard stars survey - I. Preliminary results. *MNRAS*, 426(3):1767.
- Perryman, M.A.C., Brown, A.G.A., Lebreton, Y., et al., 1998. The Hyades: distance, structure, dynamics, and age. *A&A*, 331:81.
- Perryman, M.A.C., Lindegren, L., Kovalevsky, J., et al., 1997. The HIPPARCOS Catalogue. *A&A*, 323:L49.
- Phan-Bao, N., Bessell, M.S., Martín, E.L., et al., 2008. Discovery of new nearby L and late-M dwarfs at low Galactic latitude from the DENIS data base. *MNRAS*, 383(3):831.
- Phan-Bao, N., Crifo, F., Delfosse, X., et al., 2003. New neighbours. V. 35 DENIS late-M dwarfs between 10 and 30 parsecs. *A&A*, 401:959.

- Phan-Bao, N., Lee, C.F., Ho, P.T.P., et al., 2011. Molecular Outflows in the Substellar Domain: Millimeter Observations of Young Very Low Mass Objects in Taurus and ρ Ophiuchi. *ApJ*, 735(1):14.
- Pinfield, D.J., Jones, H.R.A., Lucas, P.W., et al., 2006. Finding benchmark brown dwarfs to probe the substellar initial mass function as a function of time. *MNRAS*, 368(3):1281.
- Pollack, J.B., Hubickyj, O., Bodenheimer, P., et al., 1996. Formation of the Giant Planets by Concurrent Accretion of Solids and Gas. *Icarus*, 124(1):62.
- Prochaska, J.X., Hennawi, J.F., Westfall, K.B., et al., 2020. Pypeit: The python spectroscopic data reduction pipeline. *Journal of Open Source Software*, 5(56):2308.
- Ranc, C., Cassan, A., Albrow, M.D., et al., 2015. MOA-2007-BLG-197: Exploring the brown dwarf desert. *Astronomy & Astrophysics*, 580:A125.
- Rebolo, R., Martin, E.L., and Magazzu, A., 1992. Spectroscopy of a Brown Dwarf Candidate in the alpha Persei Open Cluster. *ApJ*, 389:L83.
- Rebull, L.M., Padgett, D.L., McCabe, C.E., et al., 2010. The Taurus Spitzer Survey: New Candidate Taurus Members Selected Using Sensitive Mid-Infrared Photometry. *ApJ*, 186(2):259.
- Rebull, L.M., Stauffer, J.R., Cody, A.M., et al., 2020. Rotation of Low-mass Stars in Taurus with K2. *AJ*, 159(6):273.
- Recio-Blanco, A., de Laverny, P., Palicio, P.A., et al., 2023. Gaia Data Release 3. Analysis of RVS spectra using the General Stellar Parametriser from spectroscopy. *A&A*, 674:A29.
- Reid, I.N., Burgasser, A.J., Cruz, K.L., et al., 2001. Near-Infrared Spectral Classification of Late M and L Dwarfs. *AJ*, 121(3):1710.
- Reid, I.N., Cruz, K.L., Kirkpatrick, J.D., et al., 2008. Meeting the Cool Neighbors. X. Ultracool Dwarfs from the 2MASS All-Sky Data Release. *AJ*, 136(3):1290.
- Reid, I.N. and Gizis, J.E., 2005. Probing the LHS Catalog. II. Faint Proper-Motion Stars. *PASP*, 117(833):676.
- Reid, I.N., Kirkpatrick, J.D., Gizis, J.E., et al., 2000. Four Nearby L Dwarfs. *AJ*, 119(1):369.
- Reid, I.N., Lewitus, E., Allen, P.R., et al., 2006. A Search for Binary Systems among the Nearest L Dwarfs. *AJ*, 132(2):891.

- Reiners, A. and Basri, G., 2006. The First High-Resolution Spectra of 1.3 L Subdwarfs. *AJ*, 131(3):1806.
- Reiners, A., Homeier, D., Hauschildt, P.H., et al., 2007. A high resolution spectral atlas of brown dwarfs. *A&A*, 473(1):245.
- Reipurth, B. and Clarke, C., 2001. The Formation of Brown Dwarfs as Ejected Stellar Embryos. *The Astronomical Journal*, 122(1):432.
- Reyl , C., 2018. New ultra-cool and brown dwarf candidates in Gaia DR2. *A&A*, 619:L8.
- Reyl , C., Jardine, K., Fouqu , P., et al., 2021. The 10 parsec sample in the Gaia era. *A&A*, 650:A201.
- Richert, A.J.W., Getman, K.V., Feigelson, E.D., et al., 2018. Circumstellar disc lifetimes in numerous galactic young stellar clusters. *MNRAS*, 477(4):5191.
- Riedel, A.R., Blunt, S.C., Lambrides, E.L., et al., 2017. LACEwing: A New Moving Group Analysis Code. *AJ*, 153(3):95.
- Riello, M., De Angeli, F., Evans, D.W., et al., 2021. Gaia Early Data Release 3. Photometric content and validation. *A&A*, 649:A3.
- Robert, J., Gagn , J., Artigau,  ., et al., 2016. A Brown Dwarf Census from the SIMP Survey. *ApJ*, 830(2):144.
- Rojo, P.M. and Harrington, J., 2006. A Method to Remove Fringes from Images Using Wavelets. *ApJ*, 649(1):553.
- Ruz-Mieres, D., 2022. *gaia-dpci/gaiaxy*: Gaiaxy 1.1.4.
- Ryan, Russell E., J., Thorman, P.A., Schmidt, S.J., et al., 2017. The Effect of Atmospheric Cooling on Vertical Velocity Dispersion and Density Distribution of Brown Dwarfs. *ApJ*, 847(1):53.
- Rybizki, J., Rix, H.W., Demleitner, M., et al., 2021. Characterizing the Gaia radial velocity sample selection function in its native photometry. *MNRAS*, 500(1):397.
- Salim, S., L pine, S., Rich, R.M., et al., 2003. LSR 0602+3910: Discovery of a Bright Nearby L-Type Brown Dwarf. *ApJ*, 586(2):L149.
- Salpeter, E.E., 1955. The Luminosity Function and Stellar Evolution. *ApJ*, 121:161.

- Sandage, A. and Fouts, G., 1987. New Subdwarfs. VI. Kinematics of 1125 High-Proper-Motion Stars and the Collapse of the Galaxy. *AJ*, 93:74.
- Sarro, L.M., Berihuete, A., Smart, R.L., et al., 2023. Ultracool dwarfs in Gaia DR3. *A&A*, 669:A139.
- Sartoretti, P., Marchal, O., Babusiaux, C., et al., 2023. Gaia Data Release 3. G_{RVS} photometry from the RVS spectra. *A&A*, 674:A6.
- Saumon, D., Hubbard, W.B., Burrows, A., et al., 1996. A Theory of Extrasolar Giant Planets. *ApJ*, 460:993.
- Saumon, D. and Marley, M.S., 2008. The Evolution of L and T Dwarfs in Color-Magnitude Diagrams. *ApJ*, 689(2):1327.
- Scalo, J.M., 1986. The Stellar Initial Mass Function. , 11:1.
- Schiavon, R.P., Barbuy, B., Rossi, S.C.F., et al., 1997a. The Near-Infrared Na I Doublet Feature in M Stars. *ApJ*, 479(2):902.
- Schiavon, R.P., Barbuy, B., and Singh, P.D., 1997b. The FeH Wing-Ford Band in Spectra of M Stars. *ApJ*, 484(1):499.
- Schlafly, E.F., Meisner, A.M., and Green, G.M., 2019. The unWISE Catalog: Two Billion Infrared Sources from Five Years of WISE Imaging. *ApJ*, 240(2):30.
- Schlieder, J.E., Lépine, S., and Simon, M., 2012a. Cool Young Stars in the Northern Hemisphere: β Pictoris and AB Doradus Moving Group Candidates. *AJ*, 143(4):80.
- Schlieder, J.E., Lépine, S., and Simon, M., 2012b. Likely Members of the β Pictoris and AB Doradus Moving Groups in the North. *AJ*, 144(4):109.
- Schmidt, S.J., Cruz, K.L., Bongiorno, B.J., et al., 2007. Activity and Kinematics of Ultracool Dwarfs, Including an Amazing Flare Observation. *AJ*, 133(5):2258.
- Schmidt, S.J., West, A.A., Hawley, S.L., et al., 2010. Colors and Kinematics of L Dwarfs from the Sloan Digital Sky Survey. *AJ*, 139(5):1808.
- Schneider, A., Melis, C., Song, I., et al., 2011a. Hunting the Coolest Dwarfs: Methods and Early Results. *ApJ*, 743(2):109.

- Schneider, A.C., Cushing, M.C., Kirkpatrick, J.D., et al., 2014. Discovery of the Young L Dwarf WISE J174102.78-464225.5. *AJ*, 147(2):34.
- Schneider, A.C., Greco, J., Cushing, M.C., et al., 2016. A Proper Motion Survey Using the First Sky Pass of NEOWISE-reactivation Data. *ApJ*, 817(2):112.
- Schneider, J., Dedieu, C., Le Sidaner, P., et al., 2011b. Defining and cataloging exoplanets: the exoplanet.eu database. *A&A*, 532:A79.
- Scholz, R.D., 2020. New ultracool dwarf neighbours within 20 pc from Gaia DR2. *A&A*, 637:A45.
- Scholz, R.D., Lodieu, N., and McCaughrean, M.J., 2004. SSSPM J1444-2019: An extremely high proper motion, ultracool subdwarf. *A&A*, 428:L25.
- Scholz, R.D., McCaughrean, M.J., Zinnecker, H., et al., 2005. SSSPM J1102-3431: A probable new young brown dwarf member of the TW Hydrae Association. *A&A*, 430:L49.
- Scholz, R.D. and Meusinger, H., 2002. SSSPM J0829-1309: a new nearby L dwarf detected in SuperCOSMOS Sky Surveys. *MNRAS*, 336(3):L49.
- Schönrich, R. and Binney, J., 2009. Origin and structure of the Galactic disc(s). *MNRAS*, 399(3):1145.
- Shkolnik, E.L., Anglada-Escudé, G., Liu, M.C., et al., 2012. Identifying the Young Low-mass Stars within 25 pc. II. Distances, Kinematics, and Group Membership. *ApJ*, 758(1):56.
- Skrutskie, M.F., Cutri, R.M., Stiening, R., et al., 2006. The Two Micron All Sky Survey (2MASS). *AJ*, 131(2):1163.
- Smart, R.L., Bucciarelli, B., Jones, H.R.A., et al., 2018. Parallaxes of Southern Extremely Cool objects III: 118 L and T dwarfs. *MNRAS*, 481(3):3548.
- Smart, R.L., Marocco, F., Caballero, J.A., et al., 2017. The Gaia ultracool dwarf sample - I. Known L and T dwarfs and the first Gaia data release. *MNRAS*, 469:401.
- Smart, R.L., Marocco, F., Sarro, L.M., et al., 2019. The Gaia ultracool dwarf sample - II. Structure at the end of the main sequence. *MNRAS*, 485(3):4423.
- Smette, A., Sana, H., Noll, S., et al., 2015. Molecfit: A general tool for telluric absorption correction. I. Method and application to ESO instruments. *A&A*, 576:A77.

- Smith, L., Lucas, P.W., Burningham, B., et al., 2014. A 1500 deg² near infrared proper motion catalogue from the UKIDSS Large Area Survey. *MNRAS*, 437(4):3603.
- Smith, L.C., Lucas, P.W., Contreras Peña, C., et al., 2015. Discovery of a brown dwarf companion to the A3V star β Circini. *MNRAS*, 454(4):4476.
- Smith, L.C., Lucas, P.W., Kurtev, R., et al., 2018. VIRAC: the VVV Infrared Astrometric Catalogue. *MNRAS*, 474(2):1826.
- Stephens, D.C. and Leggett, S.K., 2004. JHK Magnitudes for L and T Dwarfs and Infrared Photometric Systems. *PASP*, 116(815):9.
- Stephens, D.C., Leggett, S.K., Cushing, M.C., et al., 2009. The 0.8-14.5 μ m Spectra of Mid-L to Mid-T Dwarfs: Diagnostics of Effective Temperature, Grain Sedimentation, Gas Transport, and Surface Gravity. *ApJ*, 702(1):154.
- Tinney, C.G., 1993. The Faintest Stars: The Luminosity and Mass Functions at the Bottom of the Main Sequence. *ApJ*, 414:279.
- Tinney, C.G. and Reid, I.N., 1998. High-resolution spectra of very low-mass stars. *MNRAS*, 301(4):1031.
- Torres, C.A.O., Quast, G.R., Melo, C.H.F., et al., 2008. Young Nearby Loose Associations. In B. Reipurth, editor, *Handbook of Star Forming Regions, Volume II*, volume 5, page 757. Astronomical Society of the Pacific.
- Tremblay, P.E., Bergeron, P., and Gianninas, A., 2011. An Improved Spectroscopic Analysis of DA White Dwarfs from the Sloan Digital Sky Survey Data Release 4. *ApJ*, 730(2):128.
- van Dokkum, P.G., 2001. Cosmic-Ray Rejection by Laplacian Edge Detection. *PASP*, 113(789):1420.
- Venn, K.A., Irwin, M., Shetrone, M.D., et al., 2004. Stellar Chemical Signatures and Hierarchical Galaxy Formation. *AJ*, 128(3):1177.
- Vrba, F.J., Henden, A.A., Luginbuhl, C.B., et al., 2004. Preliminary Parallaxes of 40 L and T Dwarfs from the US Naval Observatory Infrared Astrometry Program. *AJ*, 127(5):2948.
- Vrijmoet, E.H., Tokovinin, A., Henry, T.J., et al., 2022. The Solar Neighborhood. XLIX. New Discoveries and Orbits of M-dwarf Multiples with Speckle Interferometry at SOAR. *AJ*, 163(4):178.

- Wagner, K., Apai, D., and Kratter, K.M., 2019. On the Mass Function, Multiplicity, and Origins of Wide-Orbit Giant Planets. *arXiv e-prints*, page arXiv:1904.06438.
- Weinberger, A.J., Boss, A.P., Keiser, S.A., et al., 2016. Trigonometric Parallaxes and Proper Motions of 134 Southern Late M, L, and T Dwarfs from the Carnegie Astrometric Planet Search Program. *AJ*, 152(1):24.
- Wenger, M., Ochsenbein, F., Egret, D., et al., 2000. The SIMBAD astronomical database. The CDS reference database for astronomical objects. *A&A Supp.*, 143:9.
- West, A.A., Hawley, S.L., Bochanski, J.J., et al., 2008. Constraining the Age-Activity Relation for Cool Stars: The Sloan Digital Sky Survey Data Release 5 Low-Mass Star Spectroscopic Sample. *AJ*, 135(3):785.
- West, A.A., Morgan, D.P., Bochanski, J.J., et al., 2011. The Sloan Digital Sky Survey Data Release 7 Spectroscopic M Dwarf Catalog. I. Data. *AJ*, 141(3):97.
- Whitworth, A.P. and Stamatellos, D., 2006. The minimum mass for star formation, and the origin of binary brown dwarfs. *Astronomy & Astrophysics*, 458(3):817.
- Whitworth, A.P. and Zinnecker, H., 2004. The formation of free-floating brown dwarves and planetary-mass objects by photo-erosion of prestellar cores. *Astronomy & Astrophysics*, 427:299.
- Wilson, J.C., Miller, N.A., Gizis, J.E., et al., 2003. New M and L Dwarfs Confirmed with COR-MASS. In E. Martín, editor, *Brown Dwarfs*, volume 211 of *Proceedings of IAU Symposium*, page 197.
- Winters, J.G., Henry, T.J., Lurie, J.C., et al., 2015. The Solar Neighborhood. XXXV. Distances to 1404 m Dwarf Systems Within 25 pc in the Southern Sky. *AJ*, 149(1):5.
- Wright, E.L., Eisenhardt, P.R.M., Mainzer, A.K., et al., 2010. The Wide-field Infrared Survey Explorer (WISE): Mission Description and Initial On-orbit Performance. *AJ*, 140(6):1868.
- Yao, Y., Ji, A.P., Koposov, S.E., et al., 2023. 188,000 Candidate Very Metal-poor Stars in Gaia DR3 XP Spectra. *arXiv e-prints*, arXiv:2303.17676.
- York, D.G., Adelman, J., Anderson, John E., J., et al., 2000. The Sloan Digital Sky Survey: Technical Summary. *AJ*, 120(3):1579.

- Zapatero Osorio, M.R., Rebolo, R., Bihain, G., et al., 2010. Infrared and Kinematic Properties of the Substellar Object G 196-3 B. *ApJ*, 715(2):1408.
- Zechmeister, M., Dreizler, S., Ribas, I., et al., 2019. The CARMENES search for exoplanets around M dwarfs. Two temperate Earth-mass planet candidates around Teegarden's Star. *A&A*, 627:A49.
- Zhang, H.W. and Zhao, G., 2006. Chemical abundances of 32 mildly metal-poor stars. *A&A*, 449(1):127.
- Zhang, X., Green, G.M., and Rix, H.W., 2023. Parameters of 220 million stars from Gaia BP/RP spectra. *MNRAS*.
- Zhang, Z., 2018. The Substellar Transition Zone: A Stretched Temperature Canyon in Brown Dwarf Population due to Unsteady Hydrogen Fusion. In *20th Cambridge Workshop on Cool Stars, Stellar Systems and the Sun, Cambridge Workshop on Cool Stars, Stellar Systems, and the Sun*, page 44.
- Zhang, Z., Liu, M.C., Best, W.M.J., et al., 2018a. The Pan-STARRS1 Proper-motion Survey for Young Brown Dwarfs in Nearby Star-forming Regions. I. Taurus Discoveries and a Reddening-free Classification Method for Ultracool Dwarfs. *ApJ*, 858(1):41.
- Zhang, Z.H., Burgasser, A.J., and Smith, L.C., 2019. Primeval very low-mass stars and brown dwarfs - V. A halo L3 subdwarf with prograde eccentric orbit in the Galactic plane. *MNRAS*, 486(2):1840.
- Zhang, Z.H., Galvez-Ortiz, M.C., Pinfield, D.J., et al., 2018b. Primeval very low-mass stars and brown dwarfs - IV. New L subdwarfs, Gaia astrometry, population properties, and a blue brown dwarf binary. *MNRAS*, 480(4):5447.
- Zhang, Z.H., Homeier, D., Pinfield, D.J., et al., 2017a. Primeval very low-mass stars and brown dwarfs - II. The most metal-poor substellar object. *MNRAS*, 468(1):261.
- Zhang, Z.H., Pinfield, D.J., Gálvez-Ortiz, M.C., et al., 2017b. Primeval very low-mass stars and brown dwarfs - I. Six new L subdwarfs, classification and atmospheric properties. *MNRAS*, 464(3):3040.
- Zuckerman, B., Bessell, M.S., Song, I., et al., 2006. The Carina-Near Moving Group. *ApJ*, 649(2):L115.

Zuckerman, B., Song, I., and Bessell, M.S., 2004. The AB Doradus Moving Group. *ApJ*, 613(1):L65.

Zuckerman, B., Song, I., Bessell, M.S., et al., 2001. The β Pictoris Moving Group. *ApJ*, 562(1):L87.